Fakultät für Physik
Institut für Theoretische Festkörperphysik

Aspects of Complex Magnetism: Vortex Phases, Skyrmion Dynamics, and Chaotic Nano-Oscillators

Zur Erlangung des akademischen Grades eines

DOKTORS DER NATURWISSENSCHAFTEN
(Dr. rer. nat.)

von der KIT-Fakultät für Physik des
Karlsruher Instituts für Technologie (KIT)
angenommene

DISSERTATION

von

M.SC. BENJAMIN BERTHOLD WOLBA

Contents

Abstracts

Project I Vortex Phase in Spiral Antiferromagnets

Spiral antiferromagnets are characterized by a Dzyaloshinskii-Moriya interaction that stabilizes spatially modulated phases of the staggered order parameter. In the framework of a Ginzburg-Landau theory, it is shown that a magnetic field leads to the formation of a topological phase constituting a square lattice of vortices and antivortices. An orthogonal alignment of the antiferromagnetic staggered order parameter with an external magnetic field is energetically favorable since both sublattices of a spiral antiferromagnet cannot minimize their Zeeman energy simultaneously, and energy can be gained from spin canting. This spin-flop mechanism has the same effect as easy-plane anisotropy, which leads the vortices to form topological defects with vanishing core. Thus, the vortex phase is only stable close to the Néel temperature.

At lower temperatures, the square-lattice vortex phase undergoes spontaneous symmetry breaking into a rectangular phase. We investigate the stability of this rectangular phase with respect to mixed DMI and in-plane magnetic fields. Since any modulated magnetic texture induces a ferroelectric polarization, the vortices of both the vortex and the rectangular phase carry an electrical charge which makes them amenable to the manipulation with in-plane electric fields. Finally, the relevance of these results for the chiral antiferromagnet $Ba_2CuGe_2O_7$ is discussed.

Project II High-Energy Magnons of a Skyrmion Lattice

The energy bands of magnons in the skyrmion lattice phase of a chiral magnet, which were recently measured experimentally, show a peculiar, parabola-shaped superstructure when plotted in an extended zone scheme. They are described theoretically in the continuum approximation by a bosonic Bogoliubov-de Gennes equation. In this project, a high-energy approximation is developed, which takes the form of a Schrödinger equation, describing these magnons as charged particles in the emergent magnetic field of the skyrmion lattice.

It is known that charged particles in a periodically modulated magnetic field can form runaway orbits, skipping between regions of positive and regions of negative magnetic field values and effectively behaving as free particles. A semiclassical analysis shows the magnon eigenfunctions corresponding to the parabola-shaped superstructures focus on the runaway orbits in the periodically modulated emergent magnetic field experienced by the magnons in this high-energy description. Hence, they can be explained by classical runaway orbits, skipping along the high-symmetry directions of the skyrmion lattice phase, which may be used as magnon waveguides.

Project III Chaotic Spin-Torque Nano-Oscillator

A spin current transversing a magnetic material exerts a spin-transfer torque onto the magnetic textures, which may lead to oscillations of the magnetization, which constitutes a so-called spin-torque nano-oscillator. Understanding the dynamics of spin-torque nano-oscillators is a prerequisite for applications in reservoir and stochastic computing and designing hardware that emulates artificial neural networks with low power consumption.

This project analyses a specific setup for an antiferromagnetic spin-torque nano-oscillator, where a spin current drives a collinear easy-axis antiferromagnet, including damping, and with an external magnetic field applied perpendicular to it. First, it characterizes the static, uniform states and their excitations, yielding the eigenfrequencies of the nano-oscillator. Next, it analyzes the regular dynamics, investigating the stability of a limit cycle at the spin-flop field. Finally, it is shown by calculating the Lyapunov spectrum that this model features chaotic dynamics intrinsically. The transition to chaos is analyzed using bifurcation diagrams, and it is shown that for large damping, chaos is controlled by period-halving bifurcations.

1 General Introduction

Spiral magnets, also called helimagnets, are magnetic materials that host periodically modulated magnetic textures, which break inversion symmetry. Thus, they either emerge from spontaneous symmetry breaking or if the crystal lattice itself lacks inversion symmetry. In the latter case, this allows for the presence of antisymmetric exchange interactions, most prominently the so-called Dzyaloshinskii-Moriya interaction (DMI), which favors a canted alignment of neighboring spins. It competes with the symmetric exchange interaction, which tries to align all spin in parallel.

Their competition leads to the formation of long-range magnetic spirals or even a so-called skyrmion lattice, described by the twisting of the magnetization order parameter as a continuous function of space. Depending on the type of DMI, these magnetic textures may feature a particular chirality in how they wind. In this case, their host material is called a chiral magnet. In addition, they are characterized by a winding number, capturing their topological nature. We will introduce these characteristics in the first section before taking a closer look at skyrmions in the second section.

In the limit of small DMI, these textures extend over several unit cells of the crystal lattice, which is why it is convenient to describe them by an effective Ginzburg-Landau theory, as we will introduce in the third section. It will allow us to predict the phase diagram, i.e. which magnetic state is thermodynamically most favorable for given external parameters like temperature or an applied magnetic field. Finally, we will use Ginzburg-Landau theory in the fourth section to describe the ferroelectric polarization that is induced by periodically modulated magnetic texture in insulating, multiferroic spiral magnets.

1.1 Chirality and Topology

Chirality characterizes the asymmetry between an object and its mirror image: if both are distinguishable, i.e. if mere translations or rotations cannot superimpose them, they are chiral. One familiar example are human hands, which is why it is also called handedness. Other examples are chiral molecules in chemistry [1], where all bonds are formed with different (groups of) atoms, left- and right-handed circularly polarized electromagnetic waves [2], or left- and right-handed quarks in quantum chromodynamics [3].

Finally, also magnetic materials can host chiral spin textures, i.e. that are distinguishable from their mirror image. Thus, they break both inversion symmetry and mirror symmetry. If also the inversion symmetry of the crystal lattice is broken, this allows for the presence of the antisymmetric DMI, whose competition with the symmetric exchange interaction makes neighboring spins assume a finite tilt angle and form long-range magnetic textures: e.g. different types of spin spirals and so-called skyrmions that are two-dimensional, whirling textures.

However, not all spiral textures are chiral. For example, a cycloidal spiral or Néel skyrmions – as introduced below – are non-chiral textures, as one can superimpose them with their mirror image. Thus, broken inversion symmetry is a necessary but not sufficient condition for chirality. In addition, mirror symmetry needs to be broken, as is the case for certain types of DMI that lead to spiral textures with a certain helicity, e.g. helical/conical spiral or Bloch skyrmions (also introduced below).

For example, helical spirals, where the plane of spin rotation is perpendicular to the propagation direction, are chiral in how they wind as they propagate – either left-handed or right-handed. Human hands can visualize this: The thumb points in the direction of propagation, the fingers curl into the palm as the direction of rotation of the spiral. A mirror reflection will invert the winding direction, i.e. turning a left-handed into a right-handed spiral.

Another intriguing feature of these textures is their topological nature, which means that they possess topological properties that are invariant under a continuous deformation of the magnetization order parameter. It is a field $\vec{m}(\vec{r})$, that constitutes a mapping from position space, typically $\mathbb{R}^2$ or $\mathbb{R}^3$, to the order parameter manifold M

$$\vec{m} : \mathbb{R}^3 \to M, \quad \vec{r} \mapsto \vec{m}(\vec{r}) \tag{1.1}$$

It is topologically non-trivial if the magnetization field is smooth at every point in real space and if it features a non-zero winding number W

$$\int \mathrm{d}^3 r \, \rho_{\text{top}}(\hat{m}) = W \tag{1.2}$$

The form of the topological density ρ_{top} depends on the dimensionality of the texture and will be given in the following sections. In addition, we introduced the unit magnetization $\hat{m} = \vec{m}/|\vec{m}|$. This is justified, as deep within the ordered phase, the magnitude of the magnetization will be almost constant.

This assumption breaks down close to the Curie temperature, and the magnetization may even vanish at singular points. In analogy to the terminology developed for superconductors, we will call these points topological defects [4–6].

Example: One-Dimensional Cycloid

As an example for a one-dimensional, non-chiral topological texture, we consider a one-dimensional cycloid of length L in an XY-magnet (see Figure 1.1 a)). Here, the magnetization is a mapping

$$\hat{m} : [0, L] \to S^1, \quad x \mapsto (\cos(\vartheta(x)), \sin(\vartheta(x)))^T \tag{1.3}$$

4
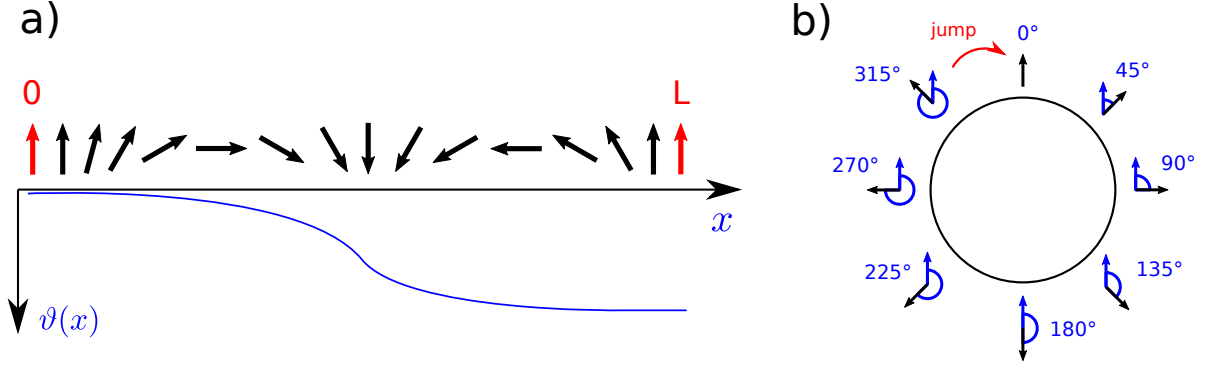
Figure 1.1.: One-dimensional, non-chiral cycloid of an XY-magnet: The fixed boundary magnetic moments (left plot a) or periodic boundary conditions (right plot b) make the cycloid topological.

with the boundary conditions $\hat{m}(0) = \hat{m}(L) = (0,1)^T$ and the position-dependent turning angle $\vartheta(x)$. Fixing these boundary conditions is crucial in this example because only then there is no continuous transformation to unwind the spiral into a collinear ferromagnet while leaving both magnetic moments at the boundary fixed. This can also be seen from the winding number $W = -1$, with the topological density $\rho_{\text{top}} = \partial_x \vartheta(x)/2\pi$ and

$$\int \mathrm{d}x \, \frac{\partial}{\partial x} \vartheta(x) = \vartheta(x_f) - \vartheta(x_i) = 2\pi W \tag{1.4}$$

A variant of this example would be a cycloid with periodic boundary conditions $\vartheta(0) = \vartheta(2\pi)$, which is equivalent to placing all the magnetic moments on a circle (see Fig. 1.1 b)). Again, to turn this texture into a collinear ferromagnetic state, every magnetic moment needs to be turned by the polar angle of their respective position on the circle. At the top, this transformation requires a discontinuity, as there is a jump in the turning angle between the top-most moment, being turned zero degrees, and its counter-clockwise neighboring moments, being turned almost 360 degrees. Thus, there is no continuous transformation between the cycloid with periodic boundary conditions and the topologically trivial, collinear ferromagnetic state.

Types of Spirals

We consider 'spiral' an umbrella term for various textures described by a curve that moves farther apart as it winds around its winding axis. Various types of spirals may occur in a spiral magnet:

- (non-chiral) cycloid: the plane of spin rotation is aligned with the propagation direction, e.g. $\hat{m}(x) = (\cos(Qx), 0, \sin(Qx))^T$

- (chiral) helix: the plane of spin rotation is perpendicular to the propagation direction, e.g. $\hat{m}(x) = (0, \cos(Qx), \sin(Qx))^T$

- (chiral) conical spiral: a helical spiral with a constant component m_0 in the direction of propagation, e.g. $\hat{m}(x) = (m_0, \cos(Qx), \sin(Qx))^T$

Based on the complex representation of sine and cosine, one can classify these spiral structures according to their Fourier components. E.g. for a cycloidal texture we get:

$$
\begin{pmatrix} \cos(Qx) \\ 0 \\ \sin(Qx) \end{pmatrix} = \frac{1}{2}\left(\begin{pmatrix} 1 \\ 0 \\ \frac{1}{i} \end{pmatrix} e^{iQx} + \begin{pmatrix} 1 \\ 0 \\ \frac{1}{-i} \end{pmatrix} e^{-iQx} \right)
\tag{1.5}
$$

In addition, every complex pair of Fourier components spans a plane $\vec{E}(\vec{u}, \vec{v})$, which is characterized by its normal vector $\vec{n} = \vec{u} \times \vec{v}$ (with some $r_1, r_2, r_3, i_1, i_2, i_3 \in \mathbb{R}$)

$$
2\left(\frac{1}{2} \begin{pmatrix} r_1 - \frac{1}{i}i_1 \\ r_2 - \frac{1}{i}i_2 \\ r_3 - \frac{1}{i}i_3 \end{pmatrix} e^{-iQx} + \frac{1}{2} \begin{pmatrix} r_1 + \frac{1}{i}i_1 \\ r_2 + \frac{1}{i}i_2 \\ r_3 + \frac{1}{i}i_3 \end{pmatrix} e^{iQx} \right)
$$

$$
= 2 \begin{pmatrix} r_1 \\ r_2 \\ r_3 \end{pmatrix} \cos(Qx) + 2 \begin{pmatrix} i_1 \\ i_2 \\ i_3 \end{pmatrix} \sin(Qx) \overset{!}{=} \varepsilon\vec{u} + \lambda\vec{v} = \vec{E}(\vec{u}, \vec{v})
\tag{1.6}
$$

Two-Dimensional Topological Textures

In two dimensions, the topological charge density is given by

$$
\rho_{\text{top}} = \frac{1}{4\pi}\hat{m} \cdot (\partial_x \hat{m} \times \partial_y \hat{m})
\tag{1.7}
$$

and the winding number W is obtained by integrating over the solid angle $\mathrm{d}\Omega = \sin(\vartheta)\,\mathrm{d}\vartheta\,\mathrm{d}\varphi$

$$
\int \mathrm{d}\Omega = \int \hat{m} \cdot (\partial_x \hat{m} \times \partial_y \hat{m})\,\mathrm{d}x\,\mathrm{d}y = 4\pi W
\tag{1.8}
$$

This means, for a two-dimensional texture to have a non-zero winding number W and be topological, it needs to wrap the unit sphere. If all the magnetic moments fall on a great

circle of the sphere, by choosing local coordinates along the great circle and perpendicular to it, the partial derivative in the direction perpendicular to it vanishes, and so does the topological charge density. It explains mathematically why spirals in two dimensions are topologically trivial: they fall on a great circle. Intuitively speaking, one can contract every circle on the surface of a sphere to a point. Since this is a continuous deformation, a circle is topologically equivalent to a point, i.e. topologically trivial.

Note that these topological concepts apply strictly speaking only to mathematical objects. For any real physical system, this description breaks down on the length scale of the atomic lattice constant, as the order parameter cannot be regarded anymore as a smooth function. In addition, it will always be possible to transition from a topological to a trivial state, given enough energy. However, this energy barrier makes topological textures such as a skyrmion lattice exceptionally stable [7]. Thus, the notion of topology is helpful in order to classify different magnetic states.

1.2 Skyrmions

This section explores one specific, particularly intriguing type of magnetic textures: skyrmions. Magnetic skyrmions are two-dimensional magnetic whirls with a quantized topological charge and particle-like properties. They can be regarded as a stereographic projection from a hedgehog configuration on a unit sphere (Bloch point) into the two-dimensional plane (see Fig. 1.2).

Two examples for skyrmions are: non-chiral Néel-skyrmions, which originate from the aforementioned stereographic projection of a Bloch point: The spin at the north-pole is mapped onto a far-off edge circle at infinity, while the spin at the south-pole is mapped onto the center of the disk. And Bloch-skyrmions, which originate from a Bloch point by first combing the hedgehog around the axis through north and south pole and only then projecting it into the two-dimensional plane. The combing leads to a certain chirality of Bloch-type skyrmions, i.e. this type is observed in chiral magnets. Both types are depicted in Fig. 1.3, featuring a winding number of $Q = -1$ as their center spin points downwards. There is an analogy to domain walls, since cutting through the center of a Néel-/Bloch-skyrmion yields a Néel-/Bloch-domain wall.

Figure 1.2.: Unfolding of a Bloch point yields a (non-chiral) Néel-skyrmion. The arrows indicate the local magnetization direction $\hat{m} = \frac{\vec{m}}{|\vec{m}|}$; the color code captures the direction of the out-of-plane component. All rights with AIP Publishing LLC [8].

Skyrmions are not only interesting for potential applications in spintronics [9, 10], as we are going to see below, but also from a fundamental point. Skyrmion solutions were first explored by Tony Skyrme in 1961, before the advent of quantum chromodynamics, to explain the stability of baryons as soliton solutions of a so-called non-linear sigma model [11–14]. His Skyrme model did not involve the DMI, and considered skyrmion solutions

Figure 1.3.: Visualization of the spin vector field of a) a Néel-skyrmion and b) a Bloch-skyrmion using the same color code as in Fig. 1.2. CC-BY-SA Karin Everschor-Sitte and Matthias Sitte [27].

as mappings from S^3 onto itself. As magnetic skyrmions are described by mappings from $\mathbb{R}^2$ to S^2, they are also called 'baby-skyrmions' [15, 16].

A non-linear sigma model is a (quantum) field theory describing a field, which takes values on a non-linear target manifold. It was originally developed by Gell-Mann and Levy to describe the spinless σ-meson [17]. Non-linear sigma models also emerge in the field-theoretic description of magnets: deep within the ordered phase (i.e. at low temperatures), variations in the magnetization strength can be neglected. The magnetization vector can then be normalized to unity and thus it resides on a unit sphere, which constitutes the non-linear target manifold.

Thus, also magnetic skyrmions can be regarded mathematically as topologically stable field configurations ('topological solitons') of certain non-linear sigma models [18, 19]. As topologically non-trivial magnetic configurations, they are localized in space and possess intrinsic stability over a topologically trivial ferromagnetic state (see remarks about 'topological protection' and energy barriers in the previous section).

Magnetic skyrmions had been first envisioned theoretically by Bogdanov and collaborators in the late 1980s [20–23], showing that terms in the free energy density of a Ginzburg-Landau model that are linear in the first spatial derivatives of the magnetization (also known as Lifshitz invariants [24]), may stabilize a skyrmion lattice as the thermodynamically most favorable ground state. One example of such a term originates from the DMI [25, 26], which we will discuss in the next section.

Skyrmions may also appear as excitations of a ferromagnetic ground state, but since they are only metastable, in practice, they vanish after a certain lifetime [28–30]. On the contrary, Bogdanov et al. predicted [20–23], that skyrmions may appear – for suitable external parameters – as the actual ground state of a magnetic material. Once it is thermodynamically favorable to have one skyrmion, it is also favorable to have two, three, and, finally, many skyrmions, forming a densely packed, typically hexagonal skyrmion lattice.

Such a skyrmion lattice phase was finally discovered also experimentally about three decades later in 2009 when Mühlbauer and collaborators could probe a skyrmion lattice phase in the cubic chiral magnet MnSi using small-angle neutron scattering (SANS). Soon after its initial discovery in MnSi [31–33], the skyrmion lattice phase was also found in other chiral B20 compounds such as $Fe_{1-x}Co_xSi$ [34–36], FeGe [37] and $Mn_{1-x}Fe_xGe$ [38]. A lattice of non-chiral Néel skyrmions was probed a few years later in the polar magnetic

semiconductor GaV_4S_8 [39].

Generally, the skyrmion lattice was probed using different experimental techniques such as neutron scattering [31–34], and via real space images obtained from Lorentz transmission electron microscopy (LTEM) [36–38] and magnetic force microscopy [35].

Cu_2OSeO_3 was the first cubic chiral magnet for which a skyrmion phase was observed, but that does not belong to the B20 group and is insulating [40–42]. Magnetic skyrmions were found in materials with various electronic properties, such as metals, insulators, semiconductors, or even multi-ferroics. Thus, their formation is independent of the electronic properties of a material, and there are different mechanisms that may stabilize a skyrmion lattice [41]:

1) The competition between the antisymmetric exchange interaction, most prominently the DMI, and the symmetric exchange interaction [20–23]. For a finite DMI to be present, the inversion symmetry of the crystal lattice needs to be broken, i.e., the material needs to be non-centrosymmetric [25, 26].

2) The competition between magnetic dipolar interactions and easy-axis anisotropy in centrosymmetric materials, which leads to larger skyrmions, in the range of 3 - 100 μm, but may also produce topologically trivial magnetic bubbles [43–46].

3) Frustrated exchange interactions [47] and four-spin interactions [48], which lead to atomically small skyrmions.

This thesis will focus on spiral magnets and topological textures stabilized by the first mechanism, the competition between the DMI and the symmetric exchange interaction.

Example: Phase Diagram of MnSi

We will take a closer look at the phase diagram of manganese silicide (MnSi), a prototypical chiral magnet and one of the most studied materials [31–33, 49–51], due to the availability of high-quality single crystals.

It is one of the cubic B20 compounds, lacking inversion symmetry and being described by the space group $P2_13$. It features a hierarchy of three competing energy scales, which produce a Curie temperature of $T_c = 29.5$ K: The strongest energy scale is set by the ferromagnetic (symmetric) exchange interaction, favoring a uniform spin alignment. The second strongest energy scale is set by the Dzyaloshinsky-Moriya interaction [25, 26], originating from relativistic spin-orbit coupling with the strength $\lambda_{SO} \sim 10^{-2}$ [52–55]. It is the lowest order antisymmetric exchange interaction. Finally, the weakest energy scale is set by crystalline field interactions, which break rotational symmetry and tend to align the wave vector of magnetic textures with the [111] direction [54]. The interplay of these three energy scales produces a rich phase diagram, which is plotted in Fig. 1.4 over the temperature T and the external magnetic field B.

At high temperatures, a paramagnetic phase is present, where the local magnetic moments point in arbitrary directions and the resulting magnetization is zero. This phase is adiabatically connected to a field-polarized phase at larger magnetic fields, where the latter orients the local magnetic moments and thereby induces a finite magnetization.

When lowering the temperature, one enters a fluctuation disordered crossover regime,
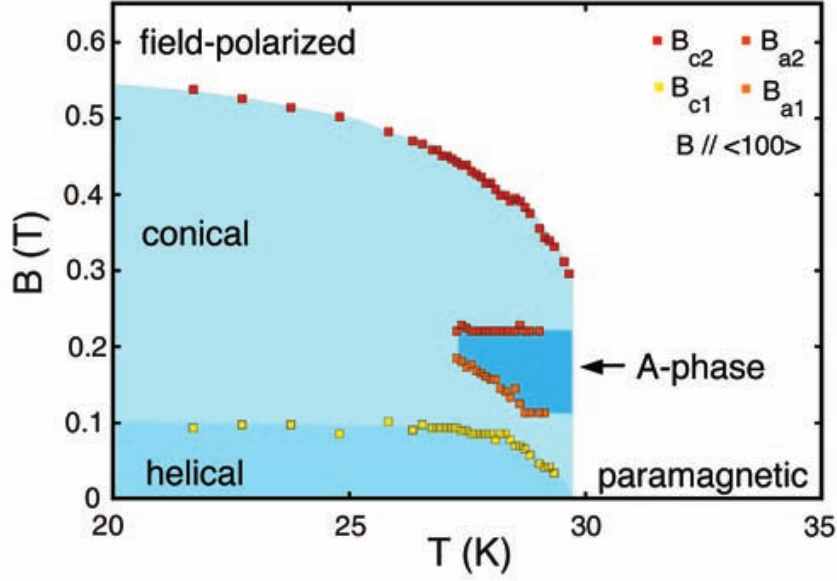
Figure 1.4.: Magnetic phase diagram of MnSi over temperature T and magnetic field B probed by Mühlbauer et al. using small angle neutron scattering (SANS). The magnetic field was applied in [100] direction. All rights with the American Association for the Advancement of Science [31].

which mitigates between the paramagnetic and the ordered phases (not shown in Fig. 1.4). On the mean-field level, the phase transition ought to be of second-order, but in practice, the fluctuations drive it to be a first-order transition (in a so-called Brazovskii scenario) [33, 50, 56, 57].

At zero or small magnetic fields, one enters the helical phase, which features helical magnetic spirals. Since the local magnetic moments are perpendicular to the helix pitch, there is no net magnetization. The orientation of the helix is determined by cubic anisotropies, preferably along the [111] axes, so that four domains with different pitch orientation may form [52–55]. The wavelength of $\lambda_h = \frac{2\pi}{k} \sim 180\,\text{Å}$ is large compared to the lattice constant $a \sim 4.56\,\text{Å}$ [52, 55], which effectively decouples the magnetic texture from the atomic lattice, leading to a huge correlation length $10^4\,\text{Å}$ [58, 59].

Applying a small external magnetic field orients the helical spirals toward the internal magnetic field, which is formed from the external magnetic field, the demagnetization field, and anisotropies. At $B_{c1} \sim 0.1\,\text{T}$, this orientation process is concluded, and for further increasing magnetic fields, the local magnetic moments tilt toward the internal magnetic field, building up a uniform magnetization component, and turning the helix into a conical spiral [60–62]. Generally, this is a crossover, unlike when the magnetic field is applied along a high-symmetry direction, like the [111]-direction, when an actual, second-order phase transition occurs.

For large magnetic fields, a second-order phase transition to the field-polarized phase is observed, where the cone angle goes smoothly to zero, and thus the local magnetic moments become collinear at $B_{c2} \approx 0.6\,\mathrm{T}$.

In a small pocket of the phase diagram, close to the Curie temperatures and at finite magnetic fields, sits the skyrmion lattice phase, which was discovered by Mühlbauer et al. in 2009 using small-angle neutron scattering [31]. As its nature was unknown before, it was simply called A-phase [60, 62].

It is reached by a first-order transition from the conical phase, forming a hexagonal lattice of skyrmions with lattice constant $2\lambda_h/\sqrt{3}$. Thus, also the skyrmion lattice decouples from the atomic structures, orienting itself in the plane perpendicular to the magnetic field and forming skyrmion tubes in the magnetic field's direction, like flux tubes in type-II superconductors. Its in-plane orientation is determined by crystalline field interactions [63], as well as the orientation of the magnetic field. For specific magnetic field directions, the skyrmion lattice orientation is particularly sensitive, in agreement with the "hairy-ball theorem," again similar to flux tubes in type-II superconductors [4, 63, 64].

Integrating the topological charge over a two-dimensional unit cell yields $W = -1$ as the winding number (1.8) of a single skyrmion, i.e. the magnetic moment at the skyrmion center is antiparallel to the applied magnetic field.

The skyrmion lattice phase is missed in a mean-field analysis, as is it stabilized by fluctuations. Only when taking Gaussian thermal fluctuations into account, its energy can be lowered below the energy of the conical phase [31]. Using Monte-Carlo simulations and thereby accounting for fluctuations in a fully non-perturbative way, the A-phase can be reproduced with decent accuracy [65].

For three-dimensional samples, the A-phase pocket is small, and thus the skyrmion lattice phase is rather unstable. On the other hand, for two-dimensional samples, i.e., thin-films, its stability can be significantly enhanced, even down to very low temperatures: When the film thickness becomes less than the helical wavelength, the conical spirals is destabilized for magnetic fields perpendicular to the film, and the skyrmion lattice gains relative stability [36, 66, 67].

Skyrmion Creation and Dynamics

Since their discovery, magnetic skyrmions have evolved into an aspiring research field, as more of their dynamical properties have been investigated, and potential applications were envisioned subsequently. Several review papers [68–71] and books [41, 72, 73] give a decent overview of the field.

The skyrmion lattice may appear not only as the true ground state of a chiral magnet, as we have just seen for MnSi, but also single skyrmions may be produced as excitations of a ferromagnetic state. Simulations showed that this could be achieved, for example, by applying an electrical current to a square notch of a stripline-shape system [74] or by injecting a spin-polarized current into a nano-disk [75]. In these constricted geometries, the spin-transfer torque of the electrical current leads to a swelling of the spin texture, eventually producing a single skyrmion. This was also realized experimentally, using local

spin-polarized currents from a scanning tunneling microscope that allowed for controlled writing and deleting of single skyrmions [76].

Over time, various ways were identified to create single skyrmions, e.g. using nanosecond current pulses [77], exploiting edge instabilities [78, 79], utilizing surface acoustic waves [80] and many more. Creating and moving single skyrmions is crucial for applications, as they were envisioned as information carriers, e.g. in a so-called racetrack memory [69, 81–83]. Therefore, it is crucial to understand how they can be pushed by small readout currents, so we will give a short summary of their interaction with electrical currents in the following.

When an electron flow transverses a skyrmion lattice, an electron's spin aligns adiabatically with the local magnetization direction of the skyrmion textures, picking up a so-called Berry phase [84]. It can be interpreted as an emergent gauge field, leading to emergent magnetic and electric fields that bend the electron's trajectory, as shown by Schulz et al. [85]:

$$B_i = \frac{\hbar}{4e} \varepsilon_{ijk} \hat{m} \cdot (\partial_j \hat{m} \times \partial_k \hat{m}) \tag{1.9}$$

$$E_i = \frac{\hbar}{2e} \hat{m} \cdot (\partial_i \hat{m} \times \partial_t \hat{m}) \tag{1.10}$$

Here, $\hat{m}(\vec{r})$ is the unit magnetization order parameter, $i, j, k \in \{1, 2, 3\}$ are coordinate labels, ∂_t is a time-derivative, e is the electron charge and $\hbar$ is the reduced Planck's constant.

This emergent electrodynamics is not only a nice description of the Berry phases influence but leads to an actual Lorentz force that can be measured in experiments. For example, it leads to an additional contribution to the Hall signal, called the topological Hall effect, which was measured e.g. for MnSi [49, 86–88].

Vice versa, as the electrons are deflected by the emergent magnetic field, the skyrmion lattice experiences a counter-force, the so-called Magnus force, pushing them into the opposite direction due to momentum conservation. This way, the skyrmion lattice is not only pushed in the direction of the electron flow, due to the electrons spin-transfer torque onto the magnetic texture [89] but also perpendicular to it, due to the Magnus force. As a result, for tiny electrical currents, the skyrmion lattice starts to rotate, as it is still pinned by impurities [90–93]. For larger electrical currents, e.g. in the range of $10^6 \, \mathrm{A \, m^{-2}}$ for bulk samples of MnSi [85, 94], it moves at an angle to the electron flow, the so-called skyrmion Hall angle, which is known as the skyrmion Hall effect [8, 68, 95].

The coupling between an electrical current and the skyrmion lattice is very efficient since the critical current densities to unpin and move the skyrmion lattice are about five orders of magnitudes lower than for moving magnetic domain walls [96, 97]. The skyrmion Hall effect in magnetic layers has been probed experimentally by Jian et al. [98], using magneto-optical Kerr microscopy, and by Litzius et al. [99], using time-resolved scanning transmission X-ray microscopy. Both studies found that the skyrmion Hall angle depends on the skyrmion size as well as its velocity.

An emergent electric field (1.10) is only observed for a time-varying magnetic texture, which can be achieved by pushing a single skyrmion or even an entire skyrmion lattice exploiting the spin-transfer torque generated by a sufficiently large, spin-polarized current. The emergent electric field leads to a reduction in the Hall signal since its effective force on the conduction electrons is opposite to the Lorenz force of the emergent magnetic field [85, 95]. Lately, it was suggested that the helical spiral state of a chiral magnet might be used as an inductor, based on the emergent electric field generated when a spin current moves the helices [100–103].

Another exciting feature is the interaction of a skyrmion with magnons, leading to rainbow scattering [104], as well as their internal excitation spectrum [104, 105]. We will skip an extended discussion at this point and get back to it in the introduction to the second project in chapter 8, which deals with a high-energy approximation to the magnon energy band spectrum of the skyrmion lattice phase.

1.3 Theoretical Description: Ginzburg-Landau Theory

In this section we introduce Ginzburg-Landau Theory as a theoretical tool to describe phases and phase transitions at the mean-field level [24, 106, 107].

A phase is a region of a thermodynamic system with qualitatively uniform properties. Consequently, a phase transitions is an abrupt change in these qualitative properties as an external control parameter is tuned: For example decreasing temperature (the control parameter) leads to the freezing of liquid water into ice (the qualitative change). They result from the tendency of every physical system to, on the one hand, minimize its internal energy and, on the other hand, maximize its entropy. The competition of these opposing tendencies defines the critical point, e.g., a critical transition temperature T_c, where the qualitative change in the system's properties unfolds.

Phase transitions can be described by an order parameter, which is typically zero in the high-symmetry (usually high-temperature) phase but assumes a finite value below the transition point in the broken-symmetry (usually low-temperature) phase of the system. They can be classified according to how the thermodynamic free energy F behaves as a function of the control parameter: If the first/second derivative with respect to the control parameter is discontinuous, the phase transition is called a first/second-order phase transition.

For first-order phase transitions, the order parameter assumes a non-zero value immediately upon entering the symmetry-broken phase, while for second-order phase transitions, its value increases continuously from zero. Generally, for second-order phase transitions, the system's correlation length diverges at the transition point, i.e. long-range fluctuations occur that drive the phase transition across the entire system simultaneously.

These long-range fluctuations extend over many lattice sites, and thus the properties of the phase transition are independent of the microscopic details that account for each phase's characteristics. An effective, phenomenological theory can describe these universal properties of continuum phase transitions well.

Such a theory was developed by Landau for a spatially uniform order parameter ϕ [24, 108]. Since the latter is small in the vicinity of a phase transition, one can develop the (a

priori unknown) free energy into a power series

$$F(\phi) = F_0 + A\phi + B\phi^2 + C\phi^3 + D\phi^4 + \ldots \tag{1.11}$$

This power series is capped after all terms have been included, that capture the physics of the respective system. In the example above, it is capped at the fourth-order, which requires $D > 0$ to ensure the stability of the theory, as the minimization of F would otherwise lead to a diverging order parameter.

Typically, symmetries such as time-reversal or inversion symmetry further restrict the terms allowed in the expansion, which in our case lead to $A = C = 0$. Now, the phase transition is governed by B, which has to be chosen e.g. for a temperature-dependent phase transition in a way that $B < 0$ for $T < T_c$ and $B > 0$ for $T > T_c$, which is fulfilled by the linear approximation $B = B_c(T - T_c)$.

Mean-field Approximation and Fluctuations

Landau theory was later extended to allow for spatial variations and fluctuations of the order parameter $\phi(\vec{r})$. This so-called Ginzburg-Landau theory was first developed to describe superconductors [109], but it also applies to a broad range of phase transitions, including magnetic ones.

Here, the state of a physical system is determined by the condition that the (Gibbs) free energy G is minimized. The partition function Z is given by

$$Z = e^{-\beta G} = \int \mathcal{D}\phi \, e^{-\beta F[\phi]} \tag{1.12}$$

with the Ginzburg-Landau free energy functional $F[\phi]$ and the inverse temperature $\beta = \frac{1}{k_B T}$. Note that this functional not necessarily corresponds to the thermodynamic free energy but to the thermodynamic potential that becomes extremal at the phase transition for the respective physical system.

In the mean-field approximation, one determines the value of the order parameter for which the Gibbs free energy becomes minimal: the so-called mean-field ϕ_{MF}. It corresponds to a stationary point of the free energy functional when neglecting fluctuations:

$$G \sim \min F[\phi] = F[\phi_{\mathrm{MF}}] \tag{1.13}$$
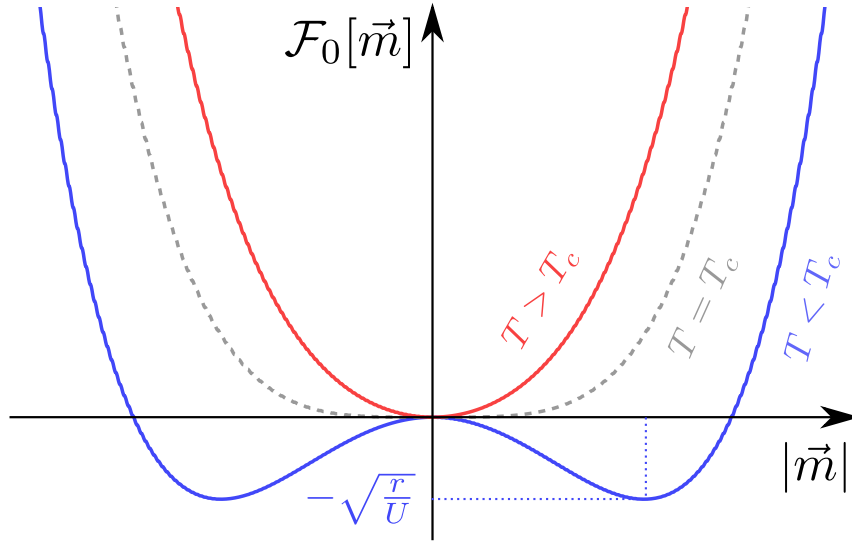
Figure 1.5.: Ginzburg-Landau terms of a ferromagnet's free energy density: For $T < T_c$, i.e. $r < 0$ it forms a so-called Mexican hat potential, which assumes its minimum for a finite magnetization $m_0 = \sqrt{\frac{-r}{U}}$. At $T = T_c$ the systems transitions into a paramagnetic state: for $T \geq T_c$, i.e. $r \geq 0$, free energy density gets minimal for vanishing magnetization.

Application to Ferromagnets

A ferromagnet is described by the three-dimensional magnetization vector $\vec{m} = \vec{m}(\vec{r})$ as its order parameter. The free energy functional takes the typical form

$$F[\vec{M}] = \int \mathrm{d}^3 r \, \mathcal{F} = \int \mathrm{d}^3 r \left[\frac{r}{2} \vec{m}^2 + \frac{U}{4} \vec{m}^4 + \frac{J}{2} (\nabla \vec{m})^2 - \vec{B} \cdot \vec{m} \right] \tag{1.14}$$

Without an external magnetic field $\vec{B}$, time-reversal symmetry $t \to t' = -t$ and spatial inversion symmetry of an isotropic ferromagnet restrict the free energy density $\mathcal{F}$ to even terms in $\vec{m}$. Here, $\vec{m}^4 = (\vec{m} \cdot \vec{m})^2$ and $U > 0$ is required to ensure the theory's stability.

The first two terms form the typical Mexican hat potential $\mathcal{F}_0 = \frac{r}{2} \vec{m}^2 + \frac{U}{4} \vec{m}^4$, which control the magnetization's magnitude (see Fig. 1.5). For $T < T_c$ we have $r < 0$ and in the absence of an external magnetic field $\vec{B}$ minimizing $F[\vec{m}]$ leads to

$$|\vec{m}| = m_0 = \sqrt{\frac{-r}{U}} \tag{1.15}$$

For $T \geq T_c$ we have $r \geq 0$ and $F[\vec{m}]$ gets minimal for vanishing magnetization, i.e. the system becomes paramagnetic. Thus, for T close to T_c one can make a linear approximation $r = A(T - T_c)$ with some constant A.

The third term involves the shorthand $(\nabla \vec{m})^2 = \partial_i m_j \partial_i m_j$, where Einstein sum convention applies. It accounts for ferromagnetic, isotropic exchange, which makes spatial variations in $\vec{m}(\vec{r})$ energetically costly and aligns all the magnetic moments within a ferromagnetic domain in the same direction.

Last but not least, an external magnetic field $\vec{B}$ may break time-reversal symmetry and introduce a linear Zeeman term. It reduces the symmetry of the theory from $O(3)$ to $O(2)$, as the direction of $\vec{B}$ gets distinguished.

The terms allowed in the free energy density depend on the actual physical system and the present symmetries. In the following section, we will go one step further and break inversion symmetry.

Non-Centrosymmetric Magnets

Inversion symmetry is broken in so-called non-centrosymmetric magnets, where neither the crystal lattice, nor the free energy density is invariant under spatial inversion $\vec{r} \rightarrow \vec{r}' = -\vec{r}$. Spatial inversion translates non-centrosymmetric magnets with different handedness, i.e. chirality, into each other.

Broken inversion symmetry allows several additional terms in the free energy density, as it was first shown by Dzyaloshinskii [25] in order to explain the appearance of weak ferromagnetism in antiferromagnets. The most important contribution is linear in the gradient $\nabla \vec{m}$ and one possible form of it is

$$\mathcal{F}_{\mathrm{DMI}} = D \, \vec{m} \times (\nabla \vec{m}) \tag{1.16}$$

The physical origin of this term was subsequently demonstrated by Moriya [26], as it arises in the second-order perturbation theory of the spin-orbit coupling $\vec{L} \cdot \vec{S}$ between two magnetic ions i, j in Anderson's superexchange formalism [110]. The coupling constant is proportional to the spin-orbit coupling $D \sim \lambda_{\mathrm{SO}}$ and the resulting energy correction takes the form $\delta E = \vec{D}_{ij} \cdot [\vec{S}_i \times \vec{S}_j]$.

Since this term is antisymmetric with respect to the exchange of the two spins $\vec{S}_i, \vec{S}_j$, it is also called 'antisymmetric exchange' or simply 'Dzyaloshinskii-Moriya interaction' (DMI). This can also be seen by considering a Heisenberg model, where the exchange is described most generally by a matrix $\hat{J}$. The Hamiltonian of just two spins $\vec{S}_1, \vec{S}_2$ reads

$$\hat{H}_{\mathrm{ex}} = \vec{S}_1 \hat{J} \vec{S}_2 \tag{1.17}$$

Every matrix can be decomposed into a symmetric and asymmetric part.

$$\hat{J} = \frac{\hat{J} + \hat{J}^T}{2} + \frac{\hat{J} - \hat{J}^T}{2} = \hat{J}^S + \hat{J}^A \tag{1.18}$$

For three-dimensional spin vectors, we have

$$\hat{J}^S = \begin{pmatrix} J & 0 & 0 \\ 0 & J & 0 \\ 0 & 0 & J \end{pmatrix}, \quad \hat{J}^A = \begin{pmatrix} 0 & D_{12} & D_{13} \\ -D_{12} & 0 & D_{23} \\ -D_{13} & -D_{23} & 0 \end{pmatrix} \tag{1.19}$$

for isotropic symmetric exchange, and also the Hamiltonian decomposes into two parts

$$\begin{aligned} \hat{H}_{\text{ex}} &= \vec{S}_1 \hat{J}^S \vec{S}_2 + \vec{S}_1 \hat{J}^A \vec{S}_2 \\ &= J S_1^x S_2^x + J S_1^y S_2^y + J S_1^z S_2^z \\ &\quad + S_1^x D_{12} S_2^y - S_1^y D_{12} S_2^x + S_1^x D_{13} S_2^z - S_1^z D_{13} S_2^x + S_1^y D_{23} S_2^z - S_1^z D_{23} S_2^y \\ &= J \vec{S}_1 \cdot \vec{S}_2 + \vec{D} \cdot \vec{S}_1 \times \vec{S}_2 \end{aligned} \tag{1.20}$$

The second term is the antisymmetric exchange, where $D = (D_{23}, -D_{13}, D_{12})^T$, which we have encountered just before when discussing the results of Moriya. It breaks inversion symmetry, as its sign depends on the relative orientation of the spins to the DMI vector $\vec{D}_{ij}$ and it gets minimal for an orthogonal alignment of $\vec{S}_1$, $\vec{S}_2$.

Therefore, the DMI competes with the isotropic exchange, which likes to align all spins in parallel, leading to canted spin configurations and topological textures such as spirals or skyrmions, as we have seen in the first section. For small DMI, these textures span over many unit cells of the crystal lattice, which justifies their treatment in a continuum theory such as Ginzburg-Landau theory. Here, the most general form of the DMI reads

$$\mathcal{F}_{\text{DMI}} = \frac{1}{D}(\hat{D}\hat{e}_\mu) \cdot (\vec{m} \times (\partial_\mu \vec{m})) \tag{1.21}$$

where the DMI tensor $\hat{D}$ depends on the crystal symmetry, D is the DMI strength, $\vec{m}$ the magnetization order parameter and Einstein summation taken over the index μ.

Its symmetry properties and their influence on the resulting phase diagram were analyzed for 3D chiral magnets by Bogdanov in [20] and for 2D chiral magnets by Güngördü et al. in [111]. The key results are summarized in appendix A.

1.4 Ferroelectricity in Chiral Magnets

Any incommensurate magnetic texture breaks inversion symmetry and therefore in principal allows for the presence of ferroelectric polarization. Indeed, it has been shown in the past [112, 113] that magnetic spirals induce a ferroelectric polarization. While it is screened in metallic materials, the ferroelectric polarization may actually be observed for insulating multiferroics.

Microscopically, the origin of the induced polarization for spiral magnets lies in the competition between symmetric exchange interaction and DMI (so-called 'exchange striction') [112]. The DMI between two transition metal ions is usually mediated by ligand O^{2-} ions. Its strength is proportional to the offset x of the O^{2-} ion. The lattice relaxation in the presence of an incommensurate magnetic texture pushes the O^{2-} ion away from the line of transition metal ions, i.e. x increases, and thus it induces a ferroelectric polarization.

An expression for this induced polarization was derived within a Ginzburg-Landau theory and based on general symmetry considerations by Mostovoy [113]

$$\vec{P} = \gamma \chi_e \left((\vec{m} \cdot \nabla)\vec{m} - \vec{m}(\nabla \cdot \vec{m}) \right) \tag{1.22}$$

Here, χ_e is the dielectric susceptibility in the absence of magnetism, and γ is the magneto-electric coupling constant.

As also shown by Mostovoy in [113], helices and conical spirals induce a sign-alternating polarization, which results in zero net polarization. On the contrary, cycloids induce a constant average polarization. Similarly, the total polarization of a Bloch domain wall is zero, while a Néel domain wall carries a nonzero polarization, which we are showing in the following as an example.

The magnetization of a Néel domain wall across x-direction can be described by the ansatz $\vec{m} = m \left(\cos(\phi(x)), \sin(\phi(x)), 0 \right)^T$ with the rotation angle $\phi(x) \in [0, 2\pi[$. The polarization $\vec{P}(x)$ is then given by

$$\vec{P} = \gamma \chi_e \left((\vec{m} \cdot \nabla)\vec{m} - \vec{m}(\nabla \cdot \vec{m}) \right) = \gamma \chi_e \sum_i m_i \frac{\partial \vec{m}}{\partial x_i} - \frac{\partial m_i}{\partial x_i} \vec{m}$$

$$= \gamma \chi_e m^2 \begin{pmatrix} -\cos(\phi)\sin(\phi)\phi' - (-\sin(\phi)\phi')\cos(\phi) \\ \cos^2(\phi)\phi' + \sin^2(\phi)\phi' \\ 0 \end{pmatrix} = \gamma \chi_e m^2 \begin{pmatrix} 0 \\ \phi' \\ 0 \end{pmatrix} \tag{1.23}$$

where $\phi' = \frac{\partial \phi}{\partial x}$. The total polarization of the domain wall is given by

$$\int_{-\infty}^{\infty} dx \, \vec{P}(x) = \gamma \chi_e m^2 \left[\phi(\infty) - \phi(-\infty) \right] \hat{e}_2 \qquad (1.24)$$

In addition, Mostovoy predicted in [113] that vortices of the magnetization carry an electrical charge. Since this is directly relevant to our results, we are going to reproduce this calculation as well.

Here, a vortex with winding number n is described by

$$\vec{m} = m \left(\cos(n\phi + \phi_0), \sin(n\phi + \phi_0), 0 \right)^T \qquad (1.25)$$

where $\phi = \arctan\left(\frac{y}{x}\right)$ and ϕ_0 is an arbitrary angle, which we put to zero. The calculation for $\vec{P}$ goes completely analogously as before, resulting in

$$\vec{P}(x, y) = \gamma \chi_e m^2 n \left(-\partial_y \phi, -\partial_x \phi, 0 \right)^T \qquad (1.26)$$

It is convenient to use polar coordinates (ρ, φ) and Gauss law to determine the charge Q carried by the vortex and enclosed by the surface A

$$Q = -\oint_A \vec{P} \cdot d\vec{A} = -\int_0^{2\pi} R \, d\varphi \, \vec{P} \cdot \vec{e}_\rho \qquad (1.27)$$

with $\vec{e}_\rho = \frac{1}{R}(\cos(\varphi), \sin(\varphi), 0)^T$ and $R = \sqrt{x^2 + y^2}$. Using the explicit expression given above for ϕ we get

$$\partial_x \phi = -\frac{y}{R^2}, \quad \partial_y \phi = \frac{x}{R^2} \quad \Rightarrow \quad \vec{P} = \frac{\gamma \chi_e m^2 n}{R^2} (-x, -y, 0)^T \qquad (1.28)$$

Thus

$$\vec{P} \cdot \vec{e}_\rho = \gamma \chi_e m^2 n \frac{-x^2 - y^2}{R^3} = \frac{-\gamma \chi_e m^2 n}{R} \qquad (1.29)$$

and

$$Q = -\int_0^{2\pi} d\varphi \, R \frac{-\gamma \chi_e m^2 n}{R} = 2\pi \gamma \chi_e m^2 n \qquad (1.30)$$

The charge is quantized in terms of the winding number n.

Part I

Vortex Phase in Spiral Antiferromagnets

2 Introduction to Spiral Antiferromagnets

2.1 Two-Dimensional Spiral Antiferromagnets

As we have seen in the previous chapter, the competition between the symmetric exchange interaction, aiming to align spins in parallel, and the antisymmetric DMI, which leads to spin canting, is at the heart of stabilizing topological magnetic textures [25, 26, 114]. The interplay of these interactions, together with magnetic anisotropy and external magnetic fields, leads to a wide variety of different topological phases in spiral magnets.

In this respect, two-dimensional (2D) materials are fascinating, as they are more amenable to the stabilization of topological phases [37, 115, 116]. They can be described in the continuum limit by a non-linear sigma model of the unit magnetization $\hat{m}$, where the free energy density describing a typical 2D chiral magnet reads [21, 22, 111, 115, 117–119]

$$\mathcal{F}[\vec{m}] = \frac{J}{2} \sum_i (\partial_i \hat{m})^2 - D\hat{m} \cdot (\nabla \times \hat{m}) + \frac{A_\mathrm{s}}{2} m_z^2 - \vec{h} \cdot \hat{m} \tag{2.1}$$

The first term captures an isotropic, symmetric exchange interaction. The second term stems from DMI, which in this example has SO(2)-symmetry as is the case e.g. for the chiral magnet MnSi [31, 41, 53, 66]. The third term accounts for uniaxial anisotropy, and the last term is a Zeeman term, describing the coupling of the magnetization to an external magnetic field $\vec{h}$.

The resulting phase diagram depends on the symmetry class of the DMI and features in general three distinct topological phases (see Fig. 2.2 for an example, taken from [111]): A spiral phase (SP) for small external magnetic fields, a skyrmion crystal phase (SkX) extending into the realm of easy-plane anisotropy, and a vortex-antivortex phase forming a square cell lattice for large easy-plane anisotropy before the system is transitioning into a tilted ferromagnetic phase. This vortex-antivortex phase (square cell phase – SC) has been missed initially [115]. It was first reported in a semi-quantitative analysis of the phase diagram [119] and finally established by Monte Carlo simulations and solving the Landau-Lifshitz-Gilbert (LLG) equations in [111].

While much research in the past was dedicated to chiral ferromagnets, chiral antiferromagnets just recently moved closer to the focus of possible applications in antiferromagnetic spintronics [120–126]. They feature much faster dynamics than ferromagnets, produce weaker stray fields, and antiferromagnetic skyrmions pushed by a spin current move in straight lines, which is desirable for applications [127–137].

Past research has shown that a skyrmion crystal phase is present for the antiferromagnetic Heisenberg model on a triangular lattice, involving either longer-ranged interactions [47] or a DMI [138]. Yet, their experimental realization remains a challenge, being so far achieved only for synthetic antiferromagnets composed of magnetic multilayers [139] and as a fractional skyrmion lattice in the centrosymmetric spinel $MnSc_2S_4$ [140]. Recently, also merons, antimerons and bimerons were stabilized in a thin film of antiferromagnetic α-Fe_2O_3 tuned across its Morin transition [141].

Bipartite antiferromagnets can be described as a composition of two ferromagnetic sublattices A and B of opposite magnetization $\vec{m}_A$ and $\vec{m}_B$. Based on this description one can define the antiferromagnetic, staggered order parameter $\hat{n} = \frac{\vec{m}_A - \vec{m}_B}{2M_s}$.

In the continuum limit, antiferromagnets can be described as well by a free energy model for $\hat{n}$. Applying an external magnetic field $\vec{h}$ to an antiferromagnet induces easy-plane anisotropy, which is described by a term in the free energy density reading $\mathcal{F}_h \sim (\hat{n} \cdot \vec{h})^2$.

It arises within the derivation of such a free energy model from a Heisenberg model (see next section 2.2), which shows, that also for antiferromagnets a small magnetization $\vec{m}$ may be present. It can be expressed entirely in terms of the staggered order parameter $\hat{n}$ (see for example (2.4)), which involves a term

$$\vec{m} = -\hat{n} \times (\hat{n} \times \vec{h}) = \vec{h} \underbrace{(\hat{n} \cdot \hat{n})}_{=1} - \hat{n}(\hat{n} \cdot \vec{h}) \tag{2.2}$$

Thus, a Zeeman term in the free energy density leads to the coupling below of the staggered order parameter to an external magnetic field

$$\mathcal{F}_h = -\vec{h} \cdot \vec{m} = (\hat{n} \cdot \vec{h})^2 - \vec{h}^2 \tag{2.3}$$

$\vec{h}^2$ is just a constant offset and can be neglected.

The resulting term $\mathcal{F}_h \sim (\hat{n} \cdot \vec{h})^2$ can be understood intuitively: If the staggered order parameter is parallel to the magnetic field, one sublattice gains maximum Zeeman energy, while the other loses maximum Zeeman energy since its orientation is antiparallel. Overall, this is energetically unfavorable and leads to a positive contribution to the free energy density (see Fig. 2.1). If both sublattices, and thus also the staggered order parameter, are oriented perpendicular to the magnetic field, this is an energetic compromise, as the corresponding term $\mathcal{F}_h$ vanishes. In addition, Zeeman energy can be gained from spin canting towards the magnetic field.

The term $\mathcal{F}_h \sim (\hat{n} \cdot \vec{h})^2$ is of the same form, as a term $\mathcal{F}_{\text{anisotropy}} \sim A_s m_z^2$ describing uniaxial anisotropy in the continuum model description of a chiral ferromagnet with magnetization $\hat{m}$, where a positive anisotropy constant $A_s > 0$ corresponds to easy-plane anisotropy.

For a 2D chiral ferromagnet, the magnetic anisotropy, i.e. the value of A_s, is determined by the material properties. By tuning the magnetic field, one can reach the skyrmion phase, but one might easily miss the vortex-antivortex phase (compare with the left-hand side of Fig. 2.2 taken from [111]).
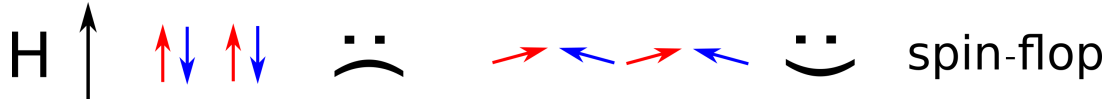
Figure 2.1.: Cartoon visualizing the spin-flop physics: If the two sublattices (red and blue) of a bipartite antiferromagnet are aligned perpendicular to an external magnetic field H energy can be gained from spin canting towards the latter.
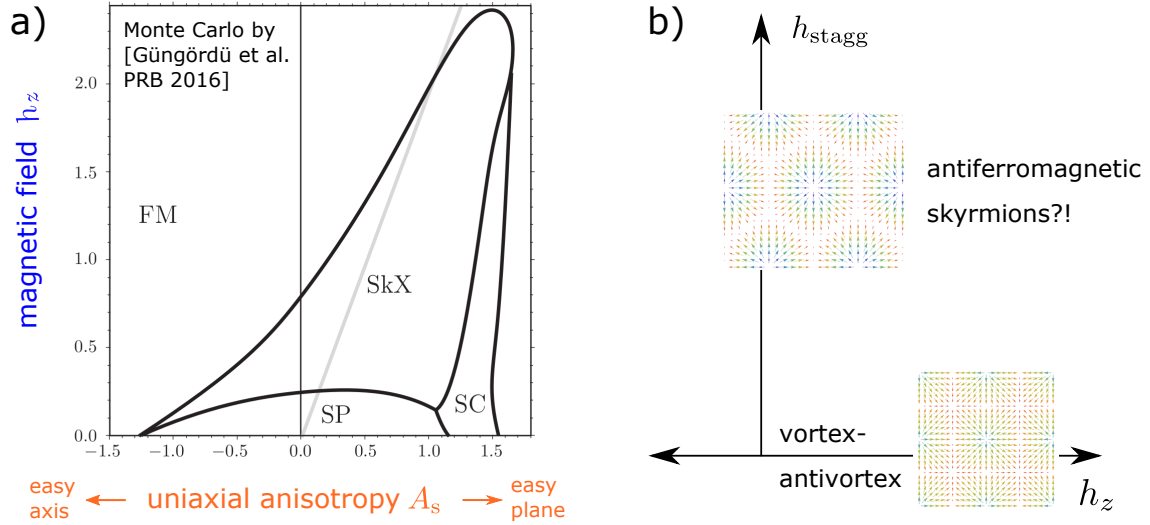
Figure 2.2.: Plot a): Phase diagram of 2D chiral ferromagnets with Rashba-/Dresselhaus-type DMI. It hosts three distinct magnetic phases, a spiral phase (SP), a skyrmion crystal phase (SkX), and a square-cell vortex-antivortex phase (SC). All rights with the American Physical Society [111]. Sketch b): Applying a magnetic field to an antiferromagnet is equivalent to increasing easy-plane anisotropy. Therefore one could reach and stabilize the vortex-antivortex phase for 2D chiral antiferromagnets.

The case is different for 2D chiral antiferromagnets. As staggered magnetic fields are impossible to realize in an experiment, reaching an antiferromagnetic skyrmion phase remains tricky in practice. However, tuning the magnetic field now corresponds to tuning the value A_s towards stronger easy-plane anisotropy, and thus one can stabilize the vortex-antivortex phase.

This project shows that an external magnetic field leads to the stabilization of a vortex phase for 2D chiral antiferromagnets by inducing easy-plane anisotropy. The results are directly relevant to the spiral antiferromagnet $Ba_2CuGe_2O_7$, which is discussed in detail alongside other candidate materials. Also, it draws a connection between previous results on $Ba_2CuGe_2O_7$ [142, 143] and the generic phase diagram of 2D chiral magnets, which suggest that Güngördü et al. missed a conical phase in the phase diagram displayed in Fig. 2.2 a), taken from their analysis in [111].

2.2 Ba$_2$CuGe$_2$O$_7$

Ba$_2$CuGe$_2$O$_7$ is an insulating, spiral antiferromagnet, which crystallizes in the non-centrosymmetric, non-polar, tetragonal space group P42$_1$m (point group D_{2d}). Non-centrosymmetric means that spatial inversion symmetry is broken, but not necessarily mirror symmetry; hence, Ba$_2$CuGe$_2$O$_7$ is a spiral rather than a chiral antiferromagnet. Also, a point group is polar, if every of its symmetry operations leaves more than one common point unmoved – so for non-polar point groups, there is just a single such point. The unit cell is displayed in Fig. 2.3 a); it features the lattice parameters $a = b = 8.466$ Å, $c = 5.445$ Å [144].

The magnetic properties of Ba$_2$CuGe$_2$O$_7$ stem from a square-lattice arrangement of Cu^{2+} cations (lattice constant $d = \frac{a}{\sqrt{2}} \approx 6$ Å) carrying localized $s = \frac{1}{2}$ spins in the (a, b)-plane. One can introduce coordinate axes x, y, and z by a 45° azimuthal rotation of the original crystal axes a, b, and c [142]. The antiferromagnetic in-plane coupling of these cations of $J_{||} \approx 0.96$ meV per bond sets an energy scale convenient to neutron scattering experiments. The inter-plane coupling $J_\perp \approx -0.026$ meV is only weakly ferromagnetic, i.e. the material can be treated effectively as a 2D spiral antiferromagnet [145].

The DMI in Ba$_2$CuGe$_2$O$_7$ possesses an in-plane component $\vec{D}_y$, pointing along the diagonal of the (a,b)-plane along Cu^{2+}-bonds. It is of Dresselhaus type, results from broken bulk inversion symmetry, and stabilizes non-chiral, cycloidal magnetic textures. In addition, there is an out-of-plane component D_z, which is parallel to the c-axis, sign-alternating for different Cu^{2+}-bonds, and thus leading to weak ferromagnetism [127].

Below the Néel temperature of $T_N = 3.2$ K, the in-plane DMI component stabilizes an almost harmonic cycloidal magnetic phase, which was established by neutron scattering [145–149]. Even at zero magnetic field, it is slightly distorted [145, 150], due to the presence of easy-plane anisotropy induced by Kaplan, Shekhtman, Entin-Wohlman, and Aharony (KSEA) interaction [151, 152]. For larger magnetic fields, it features an incommensurate-to-commensurate (IC) phase transition to a commensurate antiferromagnet, which had been at the center of interest for neutron scattering experiments in the late 1990s [145, 146, 148, 149].

Previous theoretical work by Chovan et al. described the phase diagram, and in particular the IC-transition of Ba$_2$CuGe$_2$O$_7$, within the scope of a non-linear sigma model for the free energy density [142, 143, 153]. It also predicted the occurrence of a conical phase, which was eventually found a decade later also in neutron scattering experiments by Mühlbauer et al. [144, 154].

The non-linear sigma model was derived in [142], starting from an effective Heisenberg model: The planes of Cu^{2+} cations can be regarded as a two-dimensional, square-lattice antiferromagnet, which is composed of two ferromagnetic sublattices A and B, which label the respective (classical) spins by $\vec{S}_A$ and $\vec{S}_B$. Next, one can introduce the magnetization $\vec{m} = \frac{\vec{S}_A + \vec{S}_B}{2s}$ and the staggered magnetization $\vec{n} = \frac{\vec{S}_A - \vec{S}_B}{2s}$, with the classical constraints $\vec{m} \cdot \vec{n} = 0$ and $\vec{m}^2 + \vec{n}^2 = 1$. Since the model describes an antiferromagnet $|\vec{m}| \ll |\vec{n}|$, and thus $|\vec{n}| \approx 1$. We will therefore treat the staggered magnetization as a unit vector $\hat{n}$.

It is further assumed that all anisotropies, and especially the in-plane DMI $D_\perp = |\vec{D}_y|$, are small compared to the strength of the in-plane antiferromagnetic exchange interaction
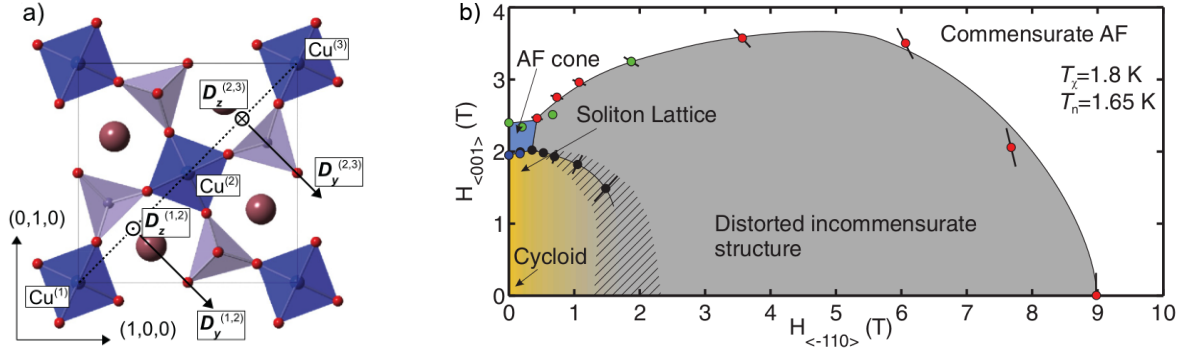
Figure 2.3.: Phase diagram of $Ba_2CuGe_2O_7$ for canted magnetic fields determined by Mühlbauer et al using neutron scattering. All rights with the American Physical Society [144].

J, i.e. the period of the observed magnetic textures is much greater than one unit cell. With this in mind, one can take the continuum limit of the model by introducing the small, dimensionless expansion parameter $\varepsilon = \frac{D_\perp}{J}$ and making a systematic expansion of the Landau-Lifshitz equations in powers of ε. Taking only terms linear in ε into account, one can express the magnetization $\vec{m}$ by the staggered order parameter $\hat{n}$

$$\vec{m} = \frac{\varepsilon}{2\sqrt{2}}[\hat{n} \times (\dot{\hat{n}} + \vec{d}_z - \hat{n} \times \vec{h})] - \frac{\varepsilon}{2}\partial_1\hat{n} \tag{2.4}$$

where $\vec{d}_z$ stems from the sign-alternating component of the DMI, $\vec{h}$ is the dimensionless, external magnetic field and ∂_1 is the derivative along x-direction (which was defined in [142] based on the orientation of the Cu^{2+} bonds.)

The resulting equation of motion for $\hat{n}$ can be regarded as the Euler-Lagrange equation of the non-linear sigma model

$$\mathcal{L} = \mathcal{L}_0 - \mathcal{F}; \quad \mathcal{L}_0 = \frac{1}{2}\partial_0\hat{n} \cdot \partial_0\hat{n} + \vec{h} \cdot (\hat{n} \times \partial_0\hat{n});$$

$$\mathcal{F} = \frac{1}{2}\left(\partial_1\hat{n} - \vec{e_2} \times \hat{n}\right)^2 + \frac{1}{2}\left(\partial_2\hat{n} - \vec{e_1} \times \hat{n}\right)^2 + \frac{1}{2}(\hat{n} \cdot \vec{h})^2 + d_z(\vec{h} \times \vec{e_3}) \cdot \hat{n} \tag{2.5}$$

where all quantities were expressed as in [142] using dimensionless units and ∂_0 represents the time derivative.

The ground state can be obtained by minimization of $\int d^3r \, \mathcal{F}$, either by discretizing $\hat{n}(\vec{r})$ on a lattice or by using variational minimization. The latter approach was followed analytically and numerically, in real space, by Chovan et al. [142, 143, 153], and the results agree qualitatively well with the phase diagram of $Ba_2CuGe_2O_7$.

The state-of-the-art phase diagram of $Ba_2CuGe_2O_7$, based on neutron scattering experiments by Mühlbauer et al., is displayed in plot b) of Fig. 2.3 (taken from [144]).

It shows various magnetic phases, depending on the magnetic field applied within the plane of Cu^{2+} cations $h_\perp = H_{<110>}$ and the out-of-plane magnetic field $h_z = H_{<001>}$. We summarize their characteristics in the following based on [143, 144].

At zero in-plane field $h_\perp$ and for small out-of-plane field h_z, an almost harmonic cycloidal spiral is present. It is just slightly distorted due to the KSEA interaction [151, 152]; its analytical derivation is reviewed in appendix C.

In addition, the model (2.5) possesses a $U(1)$-symmetry [142, 143], where an azimuthal rotation by an angle ϕ in real space is followed by a corresponding rotation of the staggered order parameter in spin-space according to

$$x + iy \rightarrow (x + iy)e^{i\phi}, \quad n_1 + in_2 \rightarrow (n_1 + in_2)e^{-i\phi} \tag{2.6}$$

I.e. the plane of spin rotation turns by $-\phi$. It is aligned with the propagation direction only for propagation in x- or y-direction (therefore also called 'flat' spiral).

A finite in-plane magnetic field $h_\perp$ breaks this $U(1)$-symmetry and orients the propagation direction of the flat spiral perpendicular to it. Thanks to the underlying, broken $U(1)$-symmetry, the solutions for different directions of h_{bot} can be related to each other [143]. Therefore, without restricting the generality of the foregoing, we may assume $h_y = h_\perp$. The flat spiral then propagates along x-direction, while its plane of spin rotation is tilted off the z-axis by an angle in the y-z-plane, in order to minimize the Zeeman energy $\sim (\hat{n} \cdot \vec{h})^2$. Thus, the cycloidal spiral becomes non-flat and develops a finite n_2-component, whose average over one period of the cycloid $\langle n_2 \rangle = 0$ vanishes.

As the diagonal terms of the Zeeman energy $n_2^2 h_\perp^2$, $n_3^2 h_z^2$ are always positive, energy can only be gained from the off-diagonal term $h_\perp h_z n_2 n_3$, and since $h_\perp > 0$, $h_z > 0$ the n_2-component must have opposite sign to the n_3 component. Therefore, as the flat spiral evolves over one period L, the n_2-component fulfills the property $n_2(x) = -n_2(L - x)$, which is why Chovan et al. labeled this state as 'antisymmetric phase'.

The weak-ferromagnetic term $d_z(\vec{h} \times \vec{e_3}) \cdot \hat{n} = d_z n_1 h_\perp$ makes the orientation along the x-axis nonequivalent, favoring $\langle n_1 \rangle < 0$, where the average is taken over one period L. This leads to a distortion of the spiral with increasing in-plane fields, which was indicated by Mühlbauer et al. in the phase diagram Fig. 2.3 b) in grey as 'distorted, incommensurate structure.' It is reached by a crossover from the cycloidal spiral, indicated in yellow. The crossover line also marks the boundary, where the uniform spin-flop state becomes thermodynamically unstable. However, it does not reach this boundary, as the distorted, incommensurate structure phase becomes energetically more favorable before. Together, the cycloidal spiral phase and the distorted, incommensurate structure constitute the antisymmetric phase described by Chovan et al. For sufficiently large in-plane fields, the IC-transition to a commensurate spin-flop state $\hat{n} = (-1, 0, 0)^T$ occurs, as the spiral period L diverges.

The scenario is similar with increasing h_z for a fixed, but large $h_\perp$: this time, the spiral distorts due to the easy-plane anisotropy induced by the magnetic field, trying to minimize the diagonal Zeeman term $n_3^2 h_z^2$. The expectation value $\langle n_2 n_3 \rangle < 0$ over one period L is negative due to the off-diagonal Zeeman term $h_\perp h_z n_2 n_3$. Again, the period L

diverges with h_z, and above the IC-transition only the spin-flop state $\hat{n} = (-1, 0, 0)^T$ is present.

The scenario is different for small $h_\perp$, as another phase – predicted by Chovan in [142] – occurs when increasing h_z: the antiferromagnetic (AF) cone phase. The transition between cycloidal spiral and AF cone phase is of first-order, and a $\pi/2$-reorientation takes place. As we consider the cycloidal spiral propagating in x-direction, the conical spiral within the AF cone phase propagates in y-direction but nutates around $-x$. The $\pi/2$-reorientation is due to the weak-ferromagnetic term $d_z n_1 h_\perp$, which dominates for small $h_\perp$ over the diagonal Zeeman term $n_2^2 h_\perp^2$.

In practice, the $U(1)$-symmetry is broken even for $h_\perp = 0$ by a tetragonal anisotropy originating from discreteness effects [148, 153]. There are four degenerate states of the conical spiral: propagation in x-direction with nutation in $\pm y$-direction or propagation in y-direction with nutation in $\pm x$-direction. A finite in-plane field $h_\perp$ selects via the weak-ferromagnetic term one of these four states, making propagation in y-direction with nutation in $-x$-direction in the setup we consider energetically most favorable.

The AF cone phase is also called symmetric phase, as the n_1 component fulfills the relation $n_1(y) = n_1(L/2 + y)$. For increasing h_z, the magnitude of n_1 increases, and similar as before an IC-transition to the uniform spin-flop state $\hat{n} = (-1, 0, 0)^T$ occurs. For increasing $h_\perp$, the propagation in y-direction becomes energetically more costly, as it is off the easy plane induced by the magnetic field. Eventually, a first-order transition occurs, with the distorted, incommensurate cycloid emerging as the true ground state.

As mentioned, the results of Chovan [142, 143, 153] capture the characteristics of the various magnetic phases of $Ba_2CuGe_2O_7$ qualitatively well – and they predicted the AF cone phase about a decade before its discovery. The quantitative agreement is almost perfect considering just out-of-plane magnetic field. There are minor quantitative disagreements, e.g. in the extent of the IC-transition (compare Fig. 2.3 with Fig. 4 in [143]) and the critical field values for a purely in-plane or canted magnetic field, which may be due to a) approximations made by Chovan's model for d_z, and b) the non-linear sigma model providing a mean-field treatment, disregarding possible fluctuations in the strength of the staggered order parameter, which may occur as the neutron scattering experiments by Mühlbauer et al. [144, 154] were carried out at about one half to two-thirds of the Néel temperature $T_N = 3.2\,\mathrm{K}$.

Apart from the weak-ferromagnetic term and the zero-field easy-plane anisotropy induced by the KSEA-interaction, the non-linear sigma model by Chovan corresponds to a general free energy model describing two-dimensional, spiral ferro- and antiferromagnets, as introduced in the previous section. For such a general free energy model, the AF cone spiral was also found by Rowland et al. [118], but it seems to be missing in a subsequent paper by Güngördü et al. [111].

Vice versa, the square-lattice vortex phase elucidated in these papers [111, 118, 119] seems to be missing in the analysis by Chovan et al. for $Ba_2CuGe_2O_7$. In addition, a Monte-Carlo study by Keesman et el. [155] suggests the existence of such a phase independently. Thus, the motivation of this project is to develop a linear sigma model in order to predict the occurrence of the square-lattice vortex phase in the phase diagram of $Ba_2CuGe_2O_7$.

3 Modelling & Numerics

3.1 Model Definition

In this project, we consider the following general continuum model for 2D spiral anti-ferromagnets (AFM)

$$
\begin{aligned}
\mathcal{F}[\vec{\phi}] ={}& \frac{\tilde{r}}{2}\vec{\phi}^2 + \frac{U}{4}(\vec{\phi}^2)^2 + \frac{A}{2}(\vec{\phi}\cdot\vec{h})^2 \\
& + \frac{J}{2}\left[\left(\partial_1\vec{\phi}\right)^2 + \left(\partial_2\vec{\phi}\right)^2\right] - D\left[\partial_1\vec{\phi}\cdot\left(\hat{e}_2\times\vec{\phi}\right) + \partial_2\vec{\phi}\cdot\left(\hat{e}_1\times\vec{\phi}\right)\right]
\end{aligned}
\tag{3.1}
$$

As it is a linear sigma model, the staggered order parameter $\vec{\phi} = |\vec{\phi}|\,\hat{n} = \phi\,\hat{n} \in \mathbb{R}^3$, with $\hat{n}^2 = 1$, is allowed to vary in strength. Its strength is determined by the first two terms, which constitute the usual Mexican hat potential with $U > 0$. The parameter $\tilde{r}$ captures the effect of temperature and is given to a linear approximation by

$$
\tilde{r} = r_0 \frac{T - T_N}{T_N}
\tag{3.2}
$$

with $r_0 > 0$, and T_N being the Néel temperature of the respective antiferromagnet. In the limit $\tilde{r} \to -\infty$, variations in the order parameter strength are suppressed, which results in a non-linear sigma model for $\hat{n}$.

The third term captures the coupling of the AFM order parameter $\vec{\phi}$ to an external magnetic field $\vec{h}$, which was introduced in section 2.1 (see formulas (2.2) and (2.3)).

The fourth term represents isotropic exchange in the $x-y-$plane, competing with the last term, the Dresselhaus type DMI (compare with [111]). Dresselhaus and Rashba DMI are related by a global rotation and yield the same phase diagram, but the two-dimensional topological magnetic textures they stabilize will have opposite topological charges.

Dimensionless Units

The linear sigma model can be non-dimensionalized by rescaling lengths (the position vector $\vec{r}$), the AFM order parameter $\vec{\phi}$, and the external magnetic field $\vec{h}$

$$
\vec{r} \to \frac{J}{D}\,\vec{r}, \quad \vec{\phi} \to \sqrt{\frac{D^2}{UJ}}\,\vec{\phi}, \quad \vec{h} \to \sqrt{\frac{D^2}{AJ}}\,\vec{h}
\tag{3.3}
$$

and by introducing the new parameters

$$r = \frac{J}{D^2}\,\tilde{r}, \quad \gamma = \frac{JD}{U} \tag{3.4}$$

An educational introduction to this procedure can be found in [104]. The linear sigma model in dimensionless units finally assumes the form

$$
F[\vec{\phi}] = \int \mathrm{d}^2 r\, \mathcal{F}[\phi] = \gamma \int \mathrm{d}^2 r\, \frac{r}{2}\vec{\phi}^2 + \frac{1}{4}(\vec{\phi}^2)^2 + \frac{1}{2}(\vec{\phi}\cdot\vec{h})^2
$$
$$
+ \frac{1}{2}\left[\left(\partial_1\vec{\phi}\right)^2 + \left(\partial_2\vec{\phi}\right)^2\right] - \left[\partial_1\vec{\phi}\cdot\left(\hat{e}_2 \times \vec{\phi}\right) + \partial_2\vec{\phi}\cdot\left(\hat{e}_1 \times \vec{\phi}\right)\right] \tag{3.5}
$$

Throughout the entire project, we will use this rescaled linear sigma model and quote our results in dimensionless units.

3.2 Variational Minimization in Fourier Space

Variational minimization is based on the idea, that the free energy functional $F = \int \mathrm{d}^3 r\, \mathcal{F}$ becomes minimal for the ground state solution. Thus, varying an ansatz for the ground state solution to minimize F yields an approximation to the true ground state.

While this can be done straightforwardly in real space by discretizing F on a lattice, we will pursue a different route and minimize the free energy functional in Fourier space. This works particularly well for periodic textures that a handful of Fourier components can describe. Therefore, we are developing the AFM order parameter into a Fourier series

$$\vec{\phi}(\vec{r}) = \sum_{\vec{k}} e^{i\vec{k}\cdot\vec{r}}\vec{\phi}_{\vec{k}} \quad \text{with} \quad \vec{\phi}_{\vec{k}}^* = \vec{\phi}_{-\vec{k}} \tag{3.6}$$

Next, the integration over space in the free energy functional corresponds to a Fourier transform, and thus the free energy in Fourier space is an algebraic expression. Standard algorithms can minimize it.

The actual Fourier transform is performed in appendix B. The resulting free energy decomposes into a quadratic and a quartic part

$$\mathcal{F}[\vec{\phi}_{\vec{k}}] = \mathcal{F}_0[\vec{\phi}_{\vec{k}}] + \mathcal{F}_i[\vec{\phi}_{\vec{k}}], \quad \mathcal{F}_i[\vec{\phi}_{\vec{k}}] = \frac{1}{4}\sum_{\vec{k}_1,\vec{k}_2,\vec{k}_3}\vec{\phi}_{\vec{k}_1}\vec{\phi}_{\vec{k}_2}\vec{\phi}_{\vec{k}_3}\vec{\phi}_{-\vec{k}_1-\vec{k}_2-\vec{k}_3} \tag{3.7}$$

The quadratic terms simplify considerably and depend effectively only on $\vec{k} = (k_1, k_2, k_3)^T$.

Using $\vec{\phi}_{-\vec{k}} = \vec{\phi}_{\vec{k}}^*$ we get

$$\mathcal{F}_0[\vec{\phi}_{\vec{k}}] = \sum_{\vec{k}} \left[\frac{r + k_1^2 + k_2^2}{2} |\vec{\phi}_{\vec{k}}|^2 + \frac{1}{2}(\vec{\phi}_{\vec{k}} \cdot \vec{h})(\vec{\phi}_{-\vec{k}} \cdot \vec{h}) \right.$$

$$\left. -i(k_1)\vec{\phi}_{\vec{k}} \cdot (\vec{e}_2 \times \vec{\phi}_{-\vec{k}}) - i(k_2)\vec{\phi}_{\vec{k}} \cdot (\vec{e}_1 \times \vec{\phi}_{-\vec{k}}) \right] \tag{3.8}$$

The quartic part does not simplify further and contributes the bulk part of the numerical effort. Depending on the ansatz, the vector $\vec{k}$ is expanded on a lattice, but only a finite number of Fourier components can be taken into account. For this project

- 1D solutions $\vec{k} = m\, q_x\, \vec{e}_1$ with $m \in \mathbb{Z}$ were expanded up to order $|m| = 9$

- 2D solutions were expanded on a rectangular lattice $\vec{k} = n_x\, q_x\, \vec{e}_x + n_y\, q_y\, \vec{e}_y$ up to 5th order, i.e. $\sqrt{n_x^2 + n_y^2} \le 5$ and $n_x, n_y \in \mathbb{Z}$

Using $\vec{\phi}_{\vec{k}}^* = \vec{\phi}_{-\vec{k}}$, the number of distinct Fourier modes reduces significantly, i.e. in 1D there are now $m + 1$ distinct modes, with three complex components each. In 2D and for $q_x = q_y$, the Gauss circle problem describes the number of Fourier mode, which was determined numerically by applying the cut-off. We also tried in this project a hexagonal lattice but did not find any ground state solution that would have been more favorable in energy.

Note that the k-values are entirely determined by the Fourier components: Let $\vec{k} = n_x\, q_x\, \vec{e}_x + n_y\, q_y\, \vec{e}_y$ be expanded on a rectangular lattice we see that

$$\frac{\partial}{\partial k_x} \mathcal{F}[\vec{\phi}_{\vec{k}}] = \sum_{n_x} n_x k_x |\vec{\phi}_{\vec{k}}|^2 - i n_x \vec{\phi}_{\vec{k}} \cdot (\vec{e}_2 \times \vec{\phi}_{-\vec{k}}) \overset{!}{=} 0 \tag{3.9}$$

so that

$$k_x = \frac{\sum_{n_x} n_x |\vec{\phi}_{\vec{k}}|^2}{\sum_{n_x} i\, n_x \vec{\phi}_{\vec{k}} \cdot (\vec{e}_2 \times \vec{\phi}_{-\vec{k}})} \tag{3.10}$$

The algebraic expression (3.8) is minimized finally using the python library SciPy and its standard minimization routine `optimize.minimize()` with both the Fourier components and the k-parameters as variational parameters.

To determine the phase diagram over a range of physical parameters, one first determines the ground state solution at an initial point by choosing initial variational parameters corresponding to different possible magnetic textures and then optimizing the free energy. The main challenge is to find the global minimum since the competition of symmetric exchange, DMI, and anisotropies allows for various magnetic textures with very similar energies.

Once a ground state solution is found, the variational parameters of this solution can be used as initial variational parameters again, and then the same energy minimum can be tracked over the whole range of physical parameters. Caution needs to be taken, as this minimum may evolve from a global into a local minimum or even vanish entirely. Therefore, various initial points need to be chosen and iterated over the parameter region, always storing only the lowest energy solution. Phase boundaries are the intersections of the energy surfaces of different magnetic states over the parameter region.

Different phases need to be discriminated against each other based on their characteristics and how the Fourier components reflect these. The result is a rough phase diagram, giving an overview of the competition between different magnetic states.

The phase boundaries can then be determined accurately by a more dedicated procedure based on a bisection method: Starting at two points, each in a different phase and well apart from each other, the ground state is determined for the mid-point, taking the variational parameters at either of the two points as ansatz. Once the ground state at the mid-point is obtained, it needs to be classified. Depending on which phase it belongs to, it replaces either of the two initial points. Then the procedure is repeated until the distance between the two points falls below a threshold of $\epsilon = 10^{-6}$.

4 Emergence of the Vortex Phase

4.1 Phase Diagram

At first, we consider the phase diagram for magnetic fields parallel to the c-axis $\vec{h} = h_z \hat{e}_3$. In this case the model (3.1) fulfills the $U(1)$-symmetry

$$x + iy \to (x + iy)e^{i\psi} \quad \phi_1 + i\phi_2 \to (\phi_1 + i\phi_2)e^{-i\psi} \tag{4.1}$$

A rotation in x-y-plane by an angle ψ is followed by a rotation of the AFM order parameter by $-\psi$. This symmetry allows us to fix the propagation direction of spiral states along the x-axis for demonstration purposes as we go ahead and calculate the phase diagram in r and h_z using variational minimization (see section 3.2).

The result is displayed in Fig. 4.2, where the distinct magnetic phases are depicted color-coded. Taking just one-dimensional solutions into account, a flat spiral state is present at zero magnetic field $h_z = 0$, i.e. the system forms a cycloid confined to x-z-plane and propagating in x-direction (see Fig. 4.1 a)).

A finite magnetic field h_z induces easy-plane anisotropy and distorts the flat spiral, as pointing along the z-axis gets energetically unfavorable. It is still confined to x-z-plane but spends a larger share of its evolution near the x-axis and increasingly avoids pointing in z-direction.

As the magnetic field h_z is increased further, the flat spiral state undergoes a first-order phase transition at the dotted line into the AF cone state. The AF cone phase constitutes a conical spiral, propagating in x-direction while rotating around the y-axis (see Fig. 4.1 b)). Therefore, it spontaneously breaks the mirror symmetry across the x-z-plane of the flat spiral state by developing a y-component. Note that there is no $\frac{\pi}{2}$-rotation of the spiral propagation direction, as described for the phase diagram of $Ba_2CuGe_2O_7$ in section 2.2, since there are no in-plane magnetic fields yet, and thus all in-plane propagation directions are still energetically equivalent.

Figure 4.1.: Visualization of a) the flat spiral phase at $r = -1.0$ and $h_z = 0.0$ and b) the AF cone phase at $r = -3.0$ and $h_z = 1.4$.

By further increasing h_z, the conical spiral's pitch length diverges, while its commensurate Fourier component gains strength, and at the critical magnetic field $h_{z,c_2} = 2.0$ a phase transition into a collinear AFM state occurs. This phase boundary, as well as the one to the paramagnetic state (representing the magnetic field dependence of Néel temperature), has been calculated analytically from fluctuations (see section 4.2). Both are of second-order, and therefore they are displayed in bold.

For $r \to -\infty$, the phase boundary between flat spiral and AF cone state (dotted line) tends toward the critical magnetic field value $h_{z,c_1} = 1.42$, which has been predicted by Chovan et al. [142, 143] within a non-linear sigma model and was checked numerically. For $r \to 0$, the phase boundary to the AF cone phase vanishes at the triple point $r = 0$ and $h_z = 2.0$, as the flat spiral state gains flexibility to cope with the easy-plane anisotropy.

Figure 4.2.: Phase diagram of the linear sigma model (3.1) in the tuning parameter r and the magnetic field h_z applied along the c-axis. At low h_z, a cycloidal spiral confined to x-z-plane constitutes the ground state, which gets increasingly more distorted as h_z is ramped up and eventually transitions into a conical spiral (dotted line), which propagates along x-direction, but rotates around the y-axis. This phase transition is intervened by two 2D phases, forming the true ground state of the system. Close to Néel temperature, depicted in orange, a vortex phase is present, forming a square lattice of topological defects. At lower r, this square-lattice vortex phase undergoes spontaneous symmetry breaking into a rectangular phase (depicted in lavender), which removes the topological defects and strives towards the former phase boundary between flat spiral and AF cone spiral for $r \to \infty$. For large h_z, the system transitions into an collinear AFM lying in x-y-plane, while for positive r the system gets paramagnetic $|\vec{\phi}| = 0$. The corresponding phase boundaries in bold were obtained analytically from fluctuation calculations, while the other thin boundaries were determined numerically by variational minimization in Fourier space and using a bisection method.

Remarkably, the flat spiral state is stable even for slightly positive r, as the gain in DMI energy still outweighs the influence of thermal disorder, leading to an overall negative coefficient of the ϕ^2-term in our linear sigma model (3.1), until reaching the high-temperature boundary.

This picture changes substantially as we are now considering also two-dimensional solutions and predict the emergence of two other phases intervening in the phase transition between the flat spiral and AF cone phase.

The first one is the vortex phase, whose extent is depicted in Fig. 4.2 in orange. It constitutes a superposition of two cycloids, one propagating along x in x-z-plane and the other one propagating along y in y-z-plane. The resulting state constitutes a square lattice of vortices and antivortices, where the vortices constitute topological defects, i.e. the order parameter strength goes to zero at the vortex core.

The vortex phase is stable only close to Néel temperature, and as r is lowered, variations in the order parameter strength get energetically punished, and thus topological defects get energetically costly. Depending on the external magnetic field h_z, a second-order phase transition occurs with lower r into a rectangular phase, depicted in Fig. 4.2 in lavender, featuring two distinct k-vectors in x- and y-direction. As r is further lowered, its extent shrinks and approaches the transition line between the flat spiral and AF cone phase for $r \to -\infty$. We will discuss both phases in more detail below in in section 4.3 and 4.4.

All the phase transitions between one- and two-dimensional phases are of first order. They are depicted in Fig. 4.2 as thin lines, and were calculated using a bisection method and variational minimization – like the dotted line.

4.2 Fluctuations of the Collinear AFM Phase

Mean-Field Solution without In-Plane Fields

The mean-field solution of the collinear AFM for magnetic fields oriented along the c-axis $\vec{h} = h_z \hat{e}_3$ can be described analytically by

$$\vec{\phi}_{\mathrm{MF}}(\vec{r}) = \phi \left(\cos\varphi, \sin\varphi, 0\right)^T \tag{4.2}$$

with some polar angle $\varphi \in [0, 2\pi[$. The free energy density (3.5) evaluated at $\vec{\phi}_{\mathrm{MF}}$ reads

$$\mathcal{F}[\vec{\phi}_{\mathrm{MF}}] = \frac{r}{2}\phi^2 + \frac{1}{4}\phi^4 \tag{4.3}$$

The ground state solution is found by minimizing $\mathcal{F}$

$$\frac{\partial \mathcal{F}[\vec{\phi}_{\mathrm{MF}}]}{\partial \phi} = r\phi + \phi^3 = 0 \tag{4.4}$$

and by excluding the trivial/paramagnetic solution $\phi = 0$ the non-trivial solution reads

$$\phi^2 = -r \tag{4.5}$$

and the free energy density becomes

$$\mathcal{F}[\vec{\phi}_{\mathrm{MF}}] = \frac{r}{2}\,(-r) + \frac{1}{4}\,(-r)^2 = -\frac{r^2}{4} \tag{4.6}$$

Derivation of the Fluctuation Matrix

Using $\vec{\nabla} = (\partial_1, \partial_2)^T$ and $\vec{h} = h_z \hat{e}_3$, we can shape the free energy density (3.5) into matrix form

$$\mathcal{F}[\phi] = \frac{1}{2}\,\vec{\phi}^T \begin{pmatrix} r - \vec{\nabla}^2 & 0 & 2\partial_1 \\ 0 & r - \vec{\nabla}^2 & -2\partial_2 \\ -2\partial_1 & 2\partial_2 & r + h_z^2 - \vec{\nabla}^2 \end{pmatrix} \vec{\phi} + \frac{1}{4}(\vec{\phi}^2)^2 \tag{4.7}$$

Here, partial integration was used for shifting the derivatives between factors

$$\int \mathrm{d}^2 r\,(\partial_1 \vec{\phi}) \cdot (\partial_1 \vec{\phi}) = \left[(\partial_1 \vec{\phi}) \cdot \vec{\phi}\right] - \int \mathrm{d}^2 r\,(\partial_1^2 \vec{\phi}) \cdot \vec{\phi}$$

The term in square brackets (surface term) will be neglected, as just the bulk's interior is of interest. As a next step, we consider fluctuations around the mean-field solution and determine the fluctuation matrix

$$\chi_{ij}^{-1}(\vec{r}, \vec{r}') = \left.\frac{\delta^2 F}{\delta\phi_i(\vec{r})\delta\phi_j(\vec{r}')}\right|_{\vec{\phi}(\vec{r})=\phi_{\mathrm{MF}}} \tag{4.8}$$

from the free energy functional $F = \int \mathrm{d}^2 r\, \mathcal{F}$ in momentum space ($\vec{\nabla} \to i\vec{k}$), resulting in

$$
\chi_{ij}^{-1} = \begin{pmatrix} r + \vec{k}^2 & 0 & 2ik_1 \\ 0 & r + \vec{k}^2 & -2ik_2 \\ -2ik_1 & 2ik_2 & r + h_z^2 + \vec{k}^2 \end{pmatrix}_{ij} + 2\phi_i\phi_j + \vec{\phi}^2\delta_{ij} \tag{4.9}
$$

The derivation used the relations

$$
\frac{\delta}{\delta\phi_i}\left(\frac{1}{4}\vec{\phi}^4\right) = \frac{1}{4}\frac{\delta}{\delta\phi_i}\left((\phi_1^2 + \phi_2^2 + \phi_3^2)^2\right) = \frac{1}{4}\left(2(\phi_1^2 + \phi_2^2 + \phi_3^2)\cdot 2\phi_i\right) = \phi_i\vec{\phi}^2 \tag{4.10}
$$

$$
\frac{\delta^2}{\delta\phi_i\delta\phi_j}\left(\frac{1}{4}\vec{\phi}^4\right) = \phi_i(2\phi_j) + \delta_{ij}\vec{\phi}^2 = 2\phi_i\phi_j + \delta_{ij}\vec{\phi}^2 \tag{4.11}
$$

Transition to the Collinear AFM

Inserting the mean-field solution for the collinear AFM $\vec{\phi}_{\mathrm{MF}}(\vec{r}) = \phi\,(\cos\varphi, \sin\varphi, 0)^T$, with $\phi^2 = -r$, into (4.9) leads to

$$
\chi^{-1} = \begin{pmatrix} r + \vec{k}^2 - r(2\cos^2\varphi + 1) & -2r\sin\varphi\cos\varphi & 2ik_1 \\ -2r\sin\varphi\cos\varphi & r + \vec{k}^2 - r(2\sin^2\varphi + 1) & -2ik_2 \\ -2ik_1 & 2ik_2 & h_z^2 + \vec{k}^2 \end{pmatrix} \tag{4.12}
$$

Importantly, the transition into the AF cone phase occurs for $\vec{k}$ perpendicular to the in-plane AFM order parameter. We fix the $U(1)$-symmetry by setting $\varphi = 0$, to remove redundancy in our description, and transform to polar coordinates $k_1 \to k\cos(\chi)$, $k_2 \to k\sin(\chi)$. Next, we choose $\chi = \frac{\pi}{2}$ in order for $\vec{k}$ be perpendicular to $\vec{\phi}$. The resulting matrix reads

$$
\chi^{-1} = \begin{pmatrix} k^2 - 2r & 0 & 0 \\ 0 & k^2 & -2ik \\ 0 & 2ik & h_z^2 + k^2 \end{pmatrix} \tag{4.13}
$$

To find the boundary of stability, we determine the eigenvalues of the fluctuation matrix:

$$\lambda_1 = k^2 - 2r, \quad \lambda_{2,3} = \frac{h^2}{2} + k^2 \pm \frac{\sqrt{h^4 + 16k^2}}{2} \tag{4.14}$$

Only the third eigenvalue can turn negative, where $\lambda_3 = 0$ leads to the condition

$$h^2 + k^2 - 4 = 0 \tag{4.15}$$

Expanding λ_3 in a Taylor series

$$\lambda_3 = \left(1 - \frac{4}{h^2}\right) k^2 + \frac{16}{h^6} k^4 + \mathcal{O}(k^6) \tag{4.16}$$

one can see that at the critical magnetic field $h_{z,c_2} = 2$ the quadratic term is changing sign, i.e. the collinear AFM phase becomes unstable for $h < h_{z,c_2}$. The transition occurs at $k = 0$, which one could see also from the condition (4.15), i.e. remarkably, it is the Goldstone mode that becomes unstable.

Field-Dependence of Néel Temperature

Analogously, we can calculate the paramagnetic phase's boundary, where the order parameter becomes zero and thus $\phi = 0$. Now, the fluctuation matrix reads

$$\left(\chi_{ij}^{-1}\right) = \begin{pmatrix} k^2 + r & 0 & 2ik\cos\chi \\ 0 & k^2 + r & -2ik\sin\chi \\ -2ik\cos\chi & 2ik\sin\chi & h_z^2 + k^2 + r \end{pmatrix} \tag{4.17}$$

where we have applied the same transformation to polar coordinates $k_1 \to k\cos(\chi)$, $k_2 \to k\sin(\chi)$. Its eigenvalue are given by

$$\lambda_1 = k^2 + r, \quad \lambda_{2,3} = \frac{h_z^2}{2} + k^2 + r \pm \frac{\sqrt{h_z^4 + 16k^2}}{2} \tag{4.18}$$

The third eigenvalue as a function of momentum $\lambda_3(k)$ is minimal at $k_{\min} = 0$ for $h_z > 2$ and at $k_{\min} = \sqrt{1 - \left(\frac{h_z}{2}\right)^4}$ for $h_z \leq 2$, signalling the tendency to develop spiral order.

The minimum value is

$$\lambda_3 = \begin{cases} r & h_z > 2 \\ r - \left(1 - \left(\frac{h_z}{2}\right)^2\right)^2 & h_z \leq 2 \end{cases} \tag{4.19}$$

This minimum value vanishes at the phase transition and we obtain

$$r(h) = \begin{cases} 0 & h_z > 2 \\ \left(1 - \left(\frac{h_z}{2}\right)^2\right)^2 & h_z \leq 2 \end{cases} \tag{4.20}$$

as the high-temperature phase boundary, beyond which the systems becomes paramagnetic, i.e. which corresponds to the field-dependence of Néel temperature.

4.3 Vortices on a Lattice

After performing the mean-field analysis, we now take a closer look at the vortex phase. It can be described by the superposition of two cycloids, one propagating along x in x-z-plane and the other one propagating along y in y-z-plane. The resulting state constitutes a square lattice of vortices and antivortices, and is displayed in Fig. 4.3 a). The maximum gain in DMI energy determines the relative orientation of both cycloids, rendering vortices into topological defects for which the AFM order parameter strength goes to zero, as the two cycloids interfere destructively (see Fig. 4.3 b)).

The vortex phase possesses full D_{2d} symmetry, which is the symmetry class of Dresselhaus DMI, involving

- a C_2 rotation axis given by the z-axis

- C_2' axes that are the x- and y- axis

- a S_4 symmetry, where a rotation by $\pi/2$ around the z-axis is followed by an inversion in z

- two diagonal mirror planes σ_d

If the vortices were absent, the magnetic texture would constitute a square-lattice of merons and antimerons, where the former vortices form the edges. Merons are like half a skyrmion, topological textures that wrap half of the unit sphere, which recently moved into the focus of research as an alternative to skyrmions [156]. As Fig. 4.3 a) shows, they feature a vorticity $m = -1$ (rotation direction of the in-plane component of the staggered order parameter), which is consistent with the D_{2d}-symmetry of the Dresselhaus DMI [157].

For the normalized staggered order parameter, the winding number W can be defined (excluding the vanishing vortex cores), which is given by the product of vorticity and the

orientation at the core [68]. This results in $W = -\frac{1}{2}$ for core-up merons (red-colored center) and $W = \frac{1}{2}$ for core-down antimerons (blue-colored center). Merons and antimerons are distinguished by the sign of W [156]. Also for Rashba-DMI, this phase would, without vortices, constitute a square lattice of merons and antimerons, but with opposite vorticity, and thus opposite winding numbers.

A square lattice of merons and antimerons was already observed in the chiral ferromagnet $Co_8Zn_9Mn_3$ using Lorentz TEM by Yu et al. [158]. It is chiral and shows no vanishing vortex cores, which is due to the linear Zeeman term in chiral ferromagnets. In spiral antiferromagnets, this term is absent, and the easy-plane anisotropy induced by an external magnetic field makes the orientation of the staggered order parameter along the magnetic field unfavorable, leading to vanishing vortex cores.
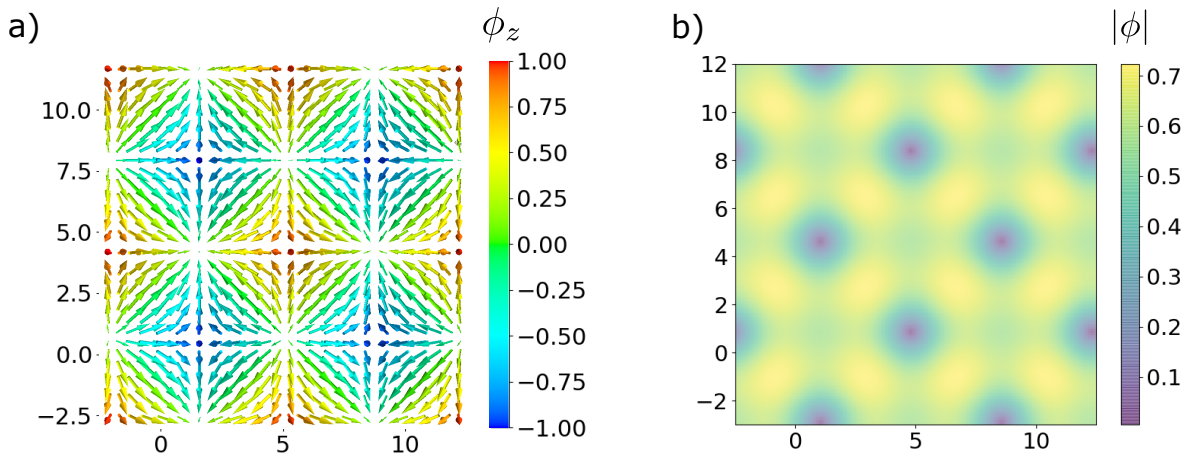
Figure 4.3.: Properties of the vortex phase for the parameters $r = -1.2$ and $h_z = 1.49$. Plot (a) shows the staggered order parameter $\vec{\phi}$, where the z-component ϕ_z is plotted color-coded: Red indicates the staggered order parameter pointing out of the paper-plane. Plot (b) depicts the absolute value $|\vec{\phi}|$ going to zero at the vortex core.

Both cycloids are almost harmonic, as higher-order Fourier components are negligibly weak. The following represents a minimum ansatz for the vortex phase:

$$\vec{\phi} = \phi \left[\begin{pmatrix} \sin(kx) \\ 0 \\ \cos(kx) \end{pmatrix} + \begin{pmatrix} 0 \\ \cos(ky) \\ \sin(ky) \end{pmatrix} \right] \tag{4.21}$$

The relative shift and orientation of both cycloids is determined by the maximum gain in DMI energy; yet this ansatz is sufficient to understand the key properties of the vortex

phase. The first two components fix the position of vortices and antivortices by

$$\sin(kx_{n_x}) = 0 \rightarrow x_{n_x} = \frac{\pi \, n_x}{k}, \quad \cos\bigl(ky_{n_y}\bigr) = 0 \rightarrow y_{n_y} = \frac{\pi \, n_y + \frac{1}{2}}{k} \qquad (4.22)$$

and $n_x, n_y \in \mathbb{Z}$. The third component now distinguishes vortices at positions with $n_x + n_y$ being uneven and antivortices with $n_x + n_y$ being even.

4.4 Spontaneous Symmetry Breaking

As r is lowered even further, a second-order phase transition from the vortex phase into a rectangular phase occurs. It is depicted in Fig. 4.4 and features two distinct k-vectors in x- and y-direction. The S_4-symmetry of the vortex phase gets spontaneously broken and reduced to C_2-symmetry. Thus, the overall symmetry class changes from D_{2d} of the vortex phase to C_{2v} for the rectangular phase.

Getting back to the simple ansatz for the vortex phase (4.21), one can see that for two distinct $k_x \neq k_y$ the third component of the AFM order parameter does not vanish anymore, due to a misalignment of both cycloids, and thus the topological defects are removed, and the vortex cores are rendered finite. The increase in strength of the AFM order parameter $\vec{\phi}$ at the vortex cores follows a square root behavior $\phi_{\min} \sim \sqrt{-r}$ and is shown in Fig. 4.5 a), while subfigure b) shows the bifurcation in the k-values, where one of the k-vectors remains almost constant after bifurcation, and the other one is steadily decreasing in strength. The rectangular phase is a two-domain state, with the k_x-vector being either the larger or the smaller one. Its in-plane orientation is arbitrary, thanks to the $U(1)$-symmetry of our model.

As r is further lowered, the extent of the rectangular phase in Fig. 4.2 shrinks and approaches the transition line between flat spiral and AF cone phase for $r \rightarrow -\infty$, which was checked numerically. The rectangular phase resembles the flat spiral state more and more, given that one of the k-vectors is vanishing while the other survives.
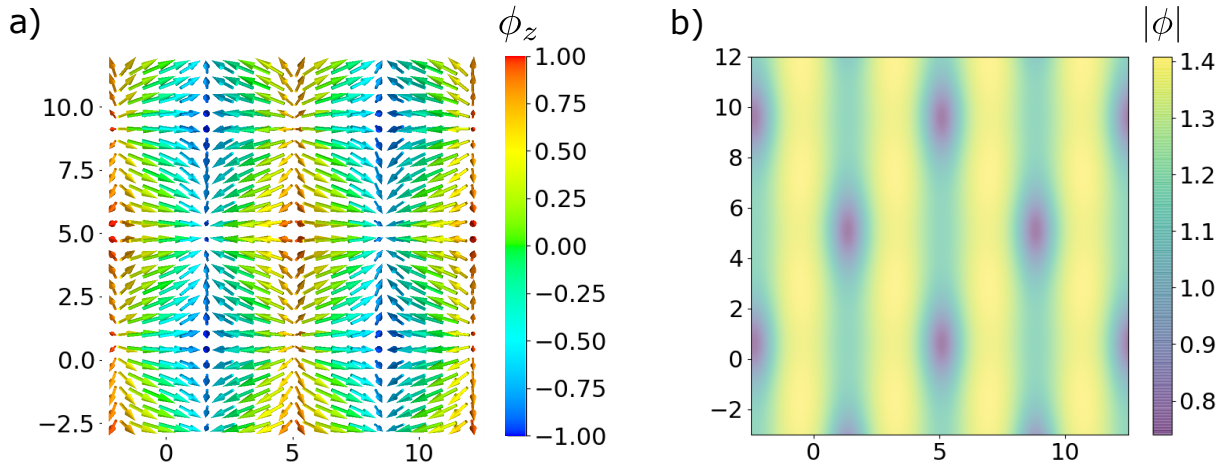
Figure 4.4.: Properties of the rectangular phase for the parameters $r = -2.5$ and $h_z = 1.12$. Plot (a) shows the staggered order parameter $\vec{\phi}$, where the z-component ϕ_z is plotted color-coded: Red indicates the staggered order parameter pointing out of the paper-plane. Plot (b) depicts the order parameter strength, which is finite everywhere and resembling a mix between a spiral and the vortex phase.
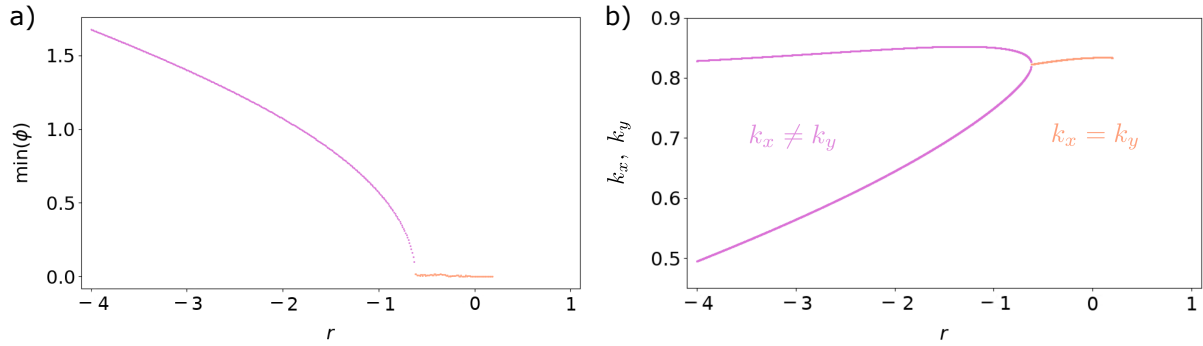
Figure 4.5.: Transition from the vortex to the rectangular phase upon decreasing r along $h_z = 1.1$: In a), the minimum of the absolute value $\phi = |\vec{\phi}|$ shows an increase according to a square-root law. In b), the transition is indicated by a bifurcation in the components of the $\vec{k}$-vector.

5 Broken Symmetry

5.1 Mixed DMI

More generally, one can consider a mixed DMI of Rashba and Dresselhaus type, reading

$$
F_{\mathrm{DMI}}[\vec{\phi}] = - \left(\cos(\beta) - \sin(\beta) \right) \partial_1 \vec{\phi} \cdot \left(\hat{e}_2 \times \vec{\phi} \right)
$$
$$
- \left(\cos(\beta) + \sin(\beta) \right) \partial_2 \vec{\phi} \cdot \left(\hat{e}_1 \times \vec{\phi} \right)
$$

(5.1)

where $D_D = \cos(\beta)$ and $D_R = \sin(\beta)$ are the respective strengths of Dresselhaus and Rashba DMI (compare with [111, 118]).

If the mixing angle β acquires a non-zero value, i.e. the Dresselhaus DMI acquires a small Rashba-DMI contribution, the $U(1)$-symmetry of the linear sigma model 3.1 gets broken and the D_{2d}-symmetry of the vortex phase is reduced to C_{2v}-symmetry of the rectangular phase. As β gets larger, a flat spiral in y-direction becomes energetically more favorable as compared to the rectangular phase, which can be seen in Fig. 5.1.
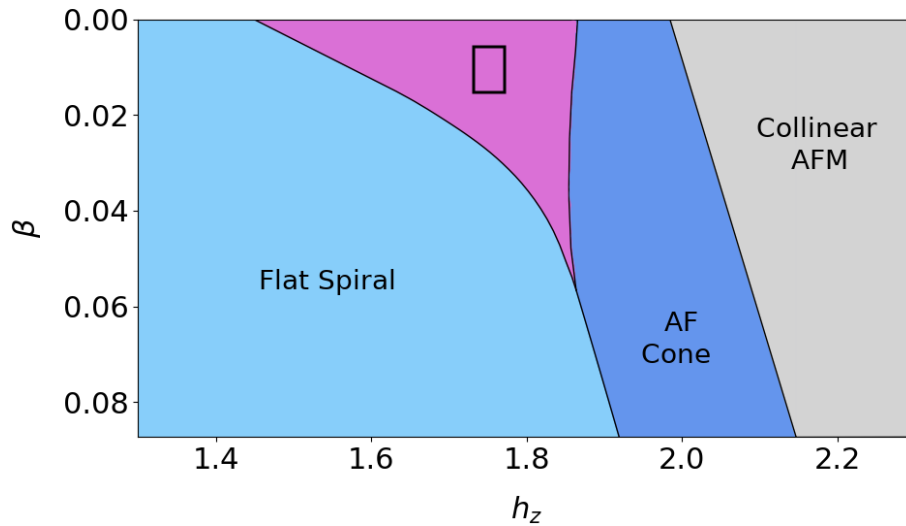
Figure 5.1.: Evolution of phases at $r = -0.2$ for different mixing angles β (in radians) between Dresselhaus and Rashba DMI. As soon as β acquires a non-zero value, the D_{2d}-symmetry of the vortex phase is reduced to C_{2v}-symmetry of the rectangular phase. For increasing β, the rectangular phase vanishes as it is energetically more favorable to spiral just in y-direction than spiraling in both x- and y-direction.

5.2 Canted Magnetic Fields
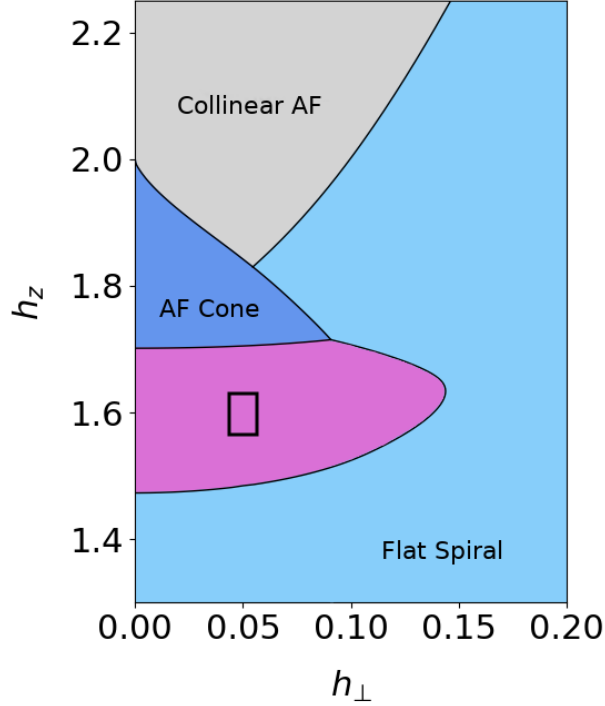
Figure 5.2.: Lateral Stability of different phases at $r = -1.5$ under the application of an in-plane magnetic field $h_\perp$.

Next, we consider the application of an in-plane magnetic field $h_\perp$ in addition to the magnetic field in z-direction h_z, which tilts the easy-plane by an angle $\tan(\alpha) = \frac{h_\perp}{h_z}$.

As an example, we let $h_\perp$ point along y-direction, which makes spiral propagation along x-direction favorable. The solution for an arbitrary in-plane direction of the magnetic field can be obtained by making use of the underlying, broken $U(1)$.symmetry as described in [143]. The resulting phase diagram at $r = -1.5$, i.e. well below Néel temperature, is depicted in Fig. 5.2.

The phase diagram becomes primarily dominated by the flat spiral state, which gets increasingly distorted for larger magnetic fields. Despite the distortion, the in-plane magnetic field stabilizes the flat spiral state: For any h_z, there is a sufficiently large $h_\perp$ so that the flat spiral state becomes energetically favorable over a collinear antiferromagnet.

Both the AF cone and the rectangular phase survive for small in-plane fields in a pocket of the phase diagram. The rectangular phase has slightly greater lateral stability up to an angle of $\alpha = 4.9°$. In-plane magnetic fields also break the two-domain degeneracy of the rectangular phase, favoring the state, whose larger k-vector is aligned perpendicular to $h_\perp$, i.e. pointing in x-direction and aligning the principal plane of spin rotation with the easy-plane.

5.3 In-Plane Electric Fields

Since the ferroelectric polarization induced by an incommensurate magnetic texture depends quadratically on the magnetization $\vec{m}$, it does not depend on the orientation of $\vec{m}$. This means that formula (1.22) suggested by Mostovoy [112, 113] for spiral ferromagnets also describes the ferroelectric polarization induced by the staggered order parameter $\vec{\phi}$ of spiral antiferromagnets

$$\vec{P} = \gamma \chi_e \left((\vec{\phi} \cdot \nabla)\vec{\phi} - \vec{\phi}(\nabla \cdot \vec{\phi}) \right) \tag{5.2}$$

where γ is the magneto-electric coupling and χ_e is the dielectric susceptibility.

Cycloids induce an average polarization $\vec{P} \sim \hat{e}_n \times \vec{Q}$, where $\vec{e}_n$ is the unit vector of the plane of spin rotation [113]. Correspondingly, the flat spiral state for $\vec{e}_n = \hat{e}_y$ and $\vec{Q} = q_x \hat{e}_y$ induces a polarization along $-\vec{e}_z$ of varying strength, so that the average polarization is pointing also in the direction of $-\vec{e}_z$ (see Fig. 5.3 a) and b)).

The AF cone spiral features an additional nutation around the y-axis; the polarization starts tilting towards the x-y-plane, while the y-component alternates in sign. Therefore, no further average polarization is induced by the nutation around y, and when h_z increases, the average polarization vanishes quickly due to this sign-alternation. As the spin-flop transition into a collinear AFM state unfolds, the sign-alternating polarization vanishes entirely.

The ferroelectric polarization induced by the vortex state forms a square lattice of vortices and antivortices, where both vortices and antivortices constitute topological defects.
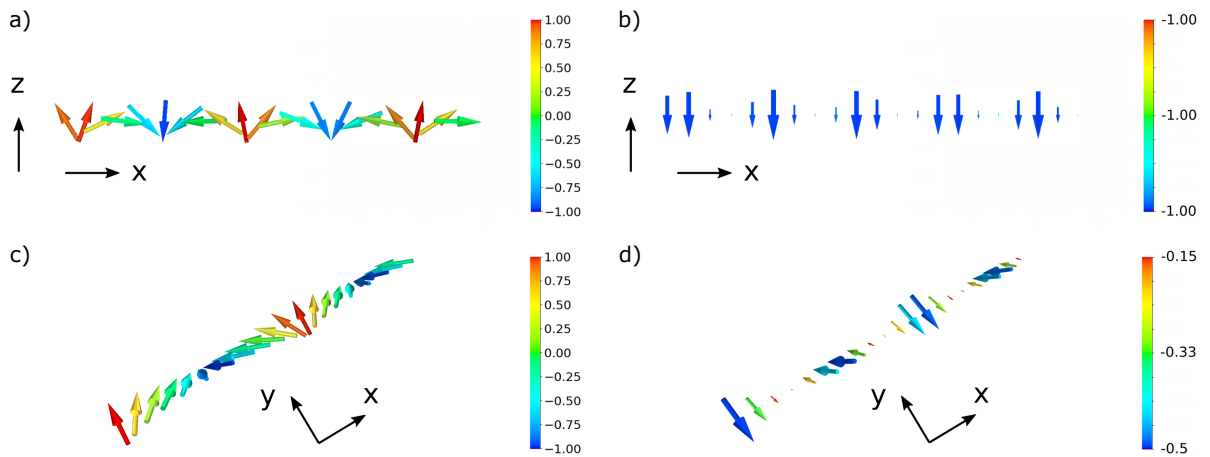
Figure 5.3.: a) Evolution of the staggered order parameter $\vec{\phi}$ for the flat spiral state at $r = -0.2$, $h_z = 0.0$. b) Polarization $\vec{P}$ induced by the flat spiral state from a), with an average polarization in the direction of $-\vec{e}_z$. c) Evolution of the staggered order parameter for the AF cone state at $r = -0.2$, $h_z = 1.64$. d) Polarization $\vec{P}$ induced by the AF cone state from c), tilting into the x-y-plane, while the average polarization almost vanishes.
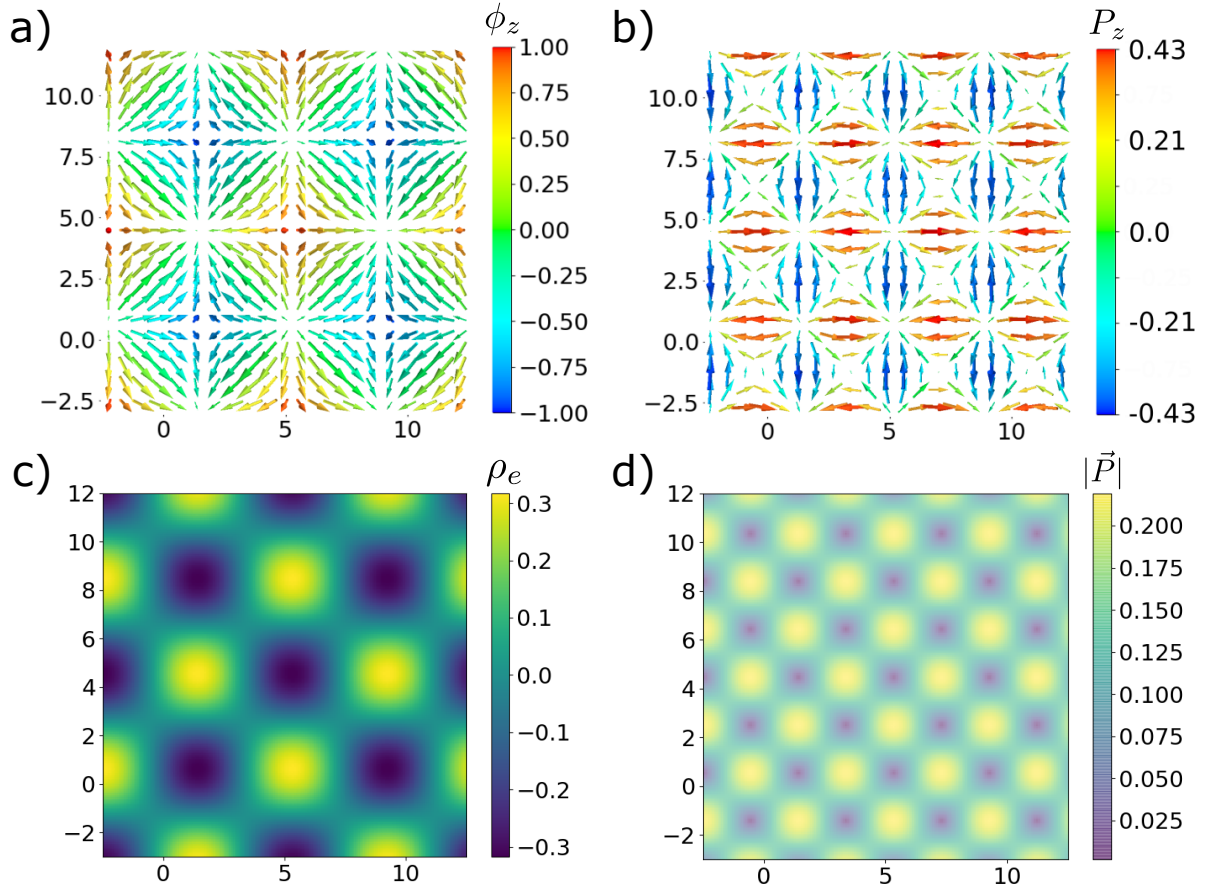
Figure 5.4.: Plot a) depicts the AFM order parameter at $r = -0.2$ and $h_z = 1.56$, while plot b) shows the induced electrical polarization $\vec{P}$ of the vortex phase. Beneath, plot c) shows its electrical charge density $\rho_e = -\nabla \cdot \vec{P}$, which indicates that vortices and antivortices in plot a) are charged oppositely. Plot d) displays the absolute polarization value $|\vec{P}|$, showing that both vortices and antivortices are topological defects.

An example is depicted in Fig. 5.4; plot a) shows the AFM order parameter, plot b) the corresponding induces polarization $\vec{P}$, and plot d) displays its strength $|\vec{P}|$.

As Mostovoy has shown in [113], topological defects of the polarization carry an electrical charge. This can be directly seen from computing the electrical charge density $\rho_e = -\nabla \cdot \vec{P}$. As shown in Fig. 5.4 c), vortices and antivortices carry exactly opposite electrical charge, the integrated charge density vanishes.

Finally, the induced ferroelectric polarization of the rectangular phase constitutes a rectangular lattice, shown in Fig. 5.5 a) and b). The vortex cores are rendered finite (see d)), but they remain charged (see c)). Again, the integrated charge vanishes. The average polarization is finite and could be used in experiments as a handle to switch the rectangular phase between different domains, as it was already done for the flat spiral state [159].
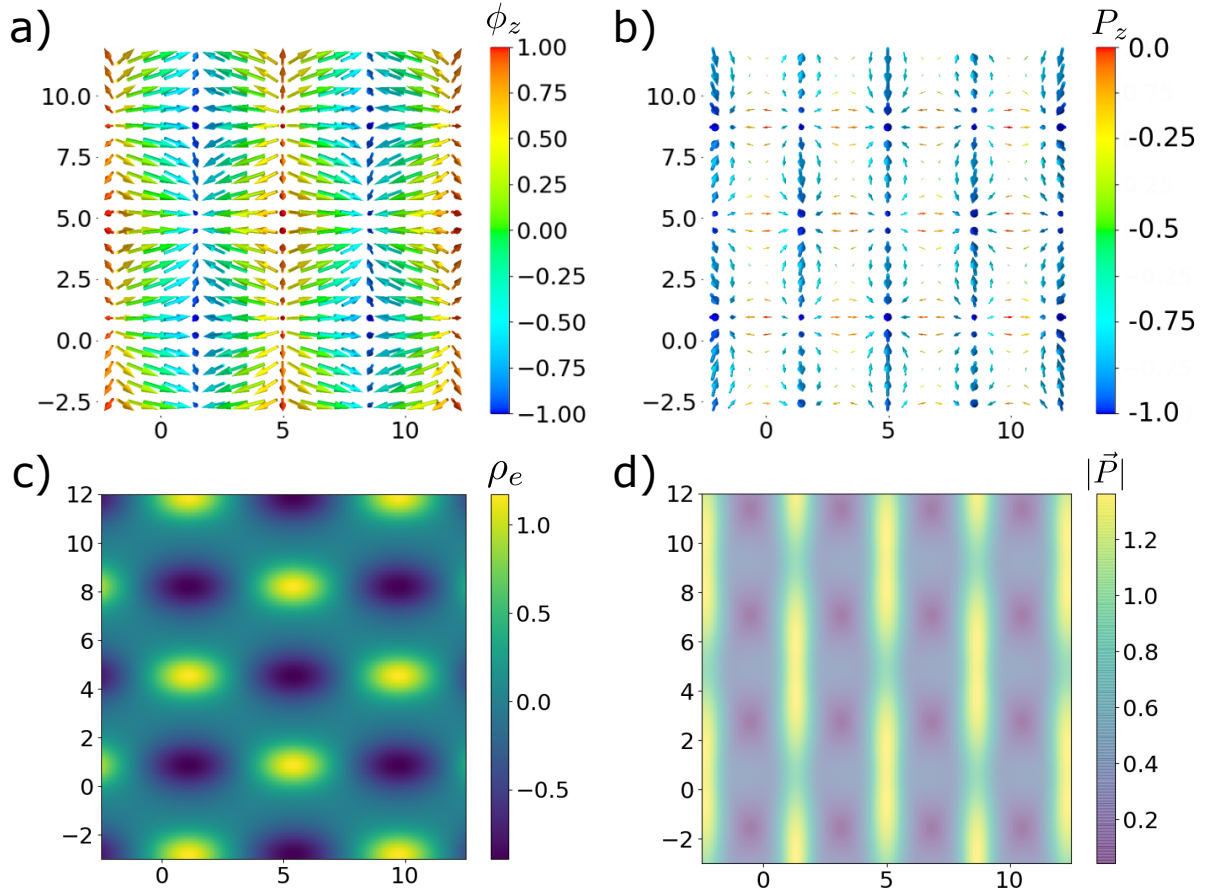
Figure 5.5.: Example for the rectangular phase at $r = -0.2$, $h_z = 1.49$ depicted in a). The more its distorted from the vortex phase, the more it resembles the behaviour of the flat spiral state, which is also reflected by the induced polarization shown in b). Plot c) shows the electrical charge density, which demonstrates, that also for the rectangular phase vortices and antivortices remain charged and plot d) depicts the strength of the induced polarization, showing that the vortex cores of the polarization are rendered finite.

Applying an in-plane electric field leads to an additional term in the free energy density

$$\mathcal{F}_{\mathrm{E}}[\vec{\phi}] = -\vec{P} \cdot \vec{E} \tag{5.3}$$

On the one hand, it couples to any non-zero average polarization, which could be used as a handle as mentioned. On the other hand, it pulls vortices and antivortices apart in different directions since they have opposite charges. Thus, the $U(1)$-symmetry of the model gets broken, and the symmetry of the resulting phase is reduced to only mirror symmetry. An example is shown in Fig. 5.6 a) for an electric field of $E = 0.07$ applied in x-direction $\vec{E} = E\hat{x}$, and therefore the mirror plane being the x-z-plane.
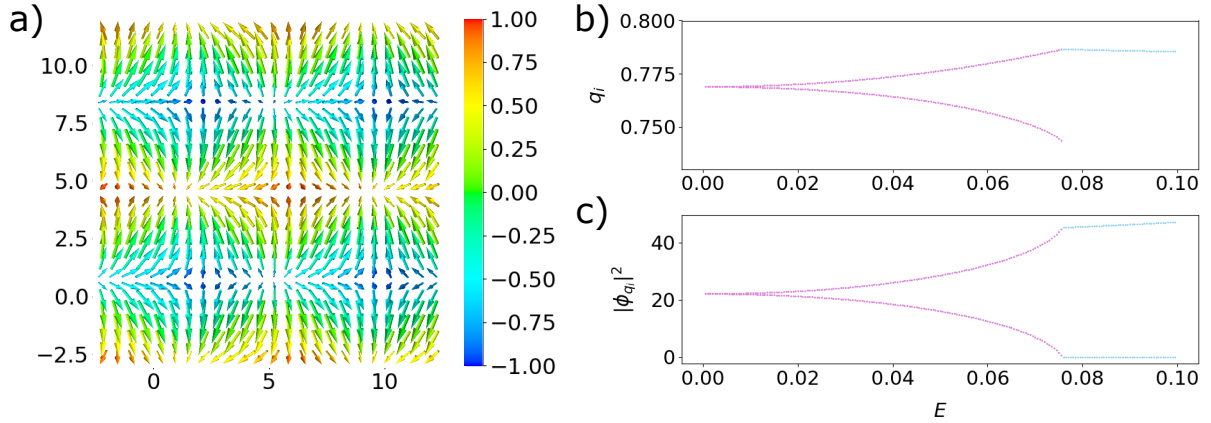
Figure 5.6.: a) Distorted rectangular phase at $r = -0.2$, $h_z = 1.6$ with an electric field $E = 0.07$ applied in x-direction. b) and c): Strengths q_i of the $\vec{k}$-components and the respective Fourier components $|\phi_{q_i}|^2$ with $i = x, y$, when ramping up an electrical field in x-direction at $r = -1.5$, $h_z = 1.6$. For zero electric field the vortex phase is present, which immediately turns into a distorted rectangular phase of only mirror symmetry upon a finite in-plane electrical field. Once the distortion is becoming too large, a distorted spiral in y-direction becomes more stable.

Tuning the electrical in-plane field turns the vortex phase immediately into a distorted rectangular phase of only mirror symmetry. With increasing electric field both the difference in the strengths q_i of the $\vec{k}$-components and the respective Fourier components $|\phi_{q_i}|^2$ increases ($i = x, y$), as shown in plot b) and c) of Fig. 5.6. Once the in-plane electrical field gets too large, the rectangular phase vanishes, and a distorted flat spiral in y-direction becomes energetically more favorable.

6 Predictions for Ba$_2$CuGe$_2$O$_7$

Our results are directly relevant to the 2D spiral antiferromagnet Ba$_2$CuGe$_2$O$_7$, which was introduced in section 2.2. As a specialty, it features weak ferromagnetism [127], and easy-plane anisotropy [145, 150–152, 160], even for zero external magnetic field, which need to be taken into account by our model.

Ba$_2$CuGe$_2$O$_7$ features an incommensurate-to-commensurate (IC) phase transition, which had been at the center of interest for a series of experiments in the late 1990s [145, 146, 148, 149]. Previous theoretical work has described the phase diagram within the scope of a non-linear sigma model of the free energy density, predicting the occurrence of an intermediate phase [142, 143, 153], which was found a decade later also in experiment [144, 154]. We predict the occurrence of two other phases in the phase diagram of Ba$_2$CuGe$_2$O$_7$: the vortex and the rectangular phase.

6.1 Extended Linear sigma model

In order to obtain an appropriate model for the 2D spiral antiferromagnet Ba$_2$CuGe$_2$O$_7$, two additional terms need to be taken into account in our free energy density model:

$$\mathcal{F}[\vec{\phi}] = \frac{D^2}{2J}(\vec{\phi} \cdot \hat{e}_3)^2 + \tilde{d}_z(\vec{h} \times \hat{e}_3) \cdot \vec{\phi} \tag{6.1}$$

The first one accounts for easy-plane anisotropy, which is already present in zero-field for this material. Effectively, this leads to a shift $h_z^2 \to 1 + h_z^2$ as compared to the phase diagram we obtained previously (see Fig. 4.2). The value of the respective coefficient is determined entirely by the strength of exchange interaction and DMI within the so-called KSEA-limit [145, 150–152, 160]. So far, Ba$_2$CuGe$_2$O$_7$ is the only pure KSEA-system known [143].

The second term stems from the bond-alternating component of the DMI, leading to a weak ferromagnetic term. Its Fourier transform is derived in appendix B.

The model can be non-dimensionalized using the same transformation of units (3.3), leading to

$$d_z = \sqrt{\frac{UJ^2}{D^4}}\, \tilde{d}_z \tag{6.2}$$

Thus, the full non-dimensionalized model for $Ba_2CuGe_2O_7$ reads

$$F[\vec{\phi}] = \gamma \int d^3r \, \frac{r}{2}\vec{\phi}^2 + \frac{1}{4}(\vec{\phi}^2)^2 + \frac{1}{2}(\vec{\phi} \cdot \vec{h})^2 + \frac{1}{2}(\vec{\phi} \cdot \hat{e}_3)^2 + d_z(\vec{h} \times \hat{e}_3) \cdot \vec{\phi}$$
$$+ \frac{1}{2}\left[\left(\partial_1\vec{\phi}\right)^2 + \left(\partial_2\vec{\phi}\right)^2\right] - \left[\partial_1\vec{\phi} \cdot \left(\hat{e}_2 \times \vec{\phi}\right) + \partial_2\vec{\phi} \cdot \left(\hat{e}_1 \times \vec{\phi}\right)\right] \tag{6.3}$$

Relation to Chovan's Model

The phase diagram of $Ba_2CuGe_2O_7$ was described previously by Chovan et al. [142, 143] using a non-linear sigma model. With $\vec{\phi} = \phi\hat{n}$, $\hat{n}^2 = 1$ Chovan's non-linear sigma model is obtained from our model in the limit $r \to -\infty$.

$$\mathcal{F}[\phi] = \frac{r-1}{2}\phi^2 + \frac{U}{4}\phi^4 + \frac{\phi^2}{2}\mathcal{F}_{Ch}[\hat{n}, \vec{h}] \tag{6.4}$$

$$\mathcal{F}_{Ch}[\hat{n}, \vec{h}] = \left[(\partial_1\hat{n})^2 + (\partial_2\hat{n})^2\right] - \left[\partial_1\hat{n} \cdot (\hat{e}_2 \times \hat{n}) + \partial_2\hat{n} \cdot (\hat{e}_1 \times \hat{n})\right]$$
$$+ (\hat{n} \cdot \hat{e}_3)^2 + \frac{1}{2}(\hat{n} \cdot \vec{h})^2 + \frac{d_z}{\phi}(\vec{h} \times \hat{e}_3) \cdot \hat{n} + 1 \tag{6.5}$$

Thus, for a constant amplitude ϕ, as it is the case deep within the ordered phase, the linear sigma model (6.3) effectively reduces to Chovan's non-linear sigma model. The orientation of the AFM order parameter in space $\hat{n}$ is then determined by minimization of $\mathcal{F}_{Ch}[\hat{n}, \vec{h}]$. The amplitude ϕ can be determined fields $\vec{h} = h_z\hat{e}_3$ along the c-axis from

$$\frac{\partial \mathcal{F}}{\partial \phi} = \left(r - 1 + \mathcal{F}_{Ch}[\hat{n}, \vec{h}]\right)\phi + U\phi^3 = 0 \tag{6.6}$$

Excluding the trivial solution $\phi = 0$, the amplitude ϕ is given by

$$\phi^2 = -\frac{1}{U}\left(r - 1 + \mathcal{F}_{Ch}[\hat{n}, \vec{h}]\right) \tag{6.7}$$

and the free energy density takes the form

$$\mathcal{F} = -\frac{1}{4U}\left(r - 1 + \mathcal{F}_{Ch}[\hat{n}, \vec{h}]\right)^2 \tag{6.8}$$

6.2 Prediction of the Vortex Phase

Magnetic Field along c-Axis
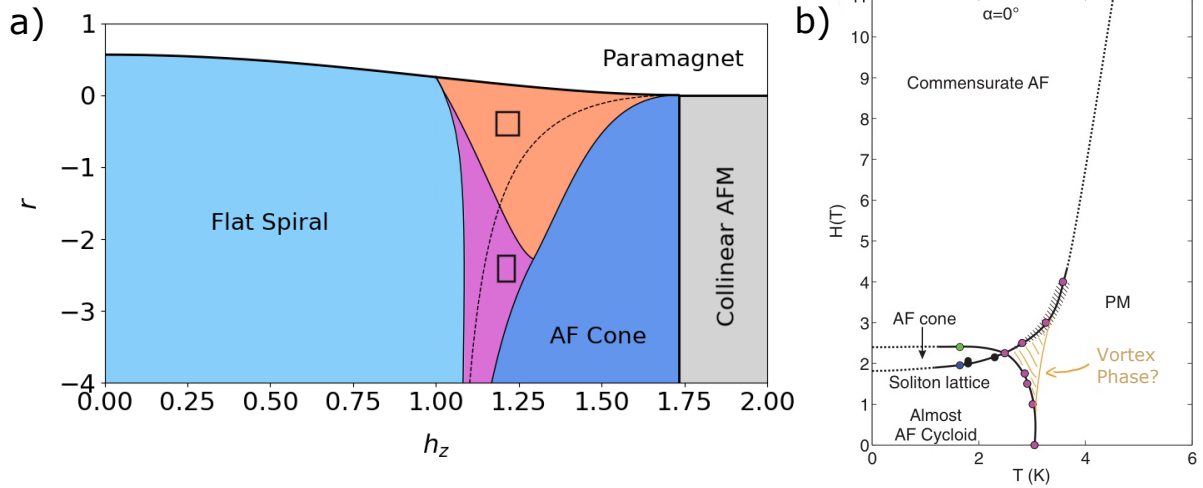
Figure 6.1.: a) Proposed phase diagram for $Ba_2CuGe_2O_7$, which corresponds to the general phase diagram in Fig. 4.2 with a shift $h_z^2 \rightarrow 1 + h_z^2$. b) Phase diagram of $Ba_2CuGe_2O_7$ based on neutron scattering and heat capacity measurements, taken from Fig. 12 a) in [144] (all rights with the American Physical Society). Our model suggests, that the phase boundary marked by magenta dots from measurements of the heat capacity corresponds to the phase transition into the vortex phase and that there will be another phase transition into the paramagnetic phase as sketched in orange.

For magnetic fields along c, i.e. $\vec{h} = h_z \hat{e}_3$, the weak ferromagnetic term drops and the phase diagram depicted in Fig. 6.1 a) remains largely unchanged apart from a shift $h_z^2 \rightarrow 1 + h_z^2$ as compared to the general linear sigma model (3.1) and Fig. 4.2. See section 4.1 for an in-depth discussion.

Due to the KSEA-interaction [145, 150–152] already at zero field, an easy-plane anisotropy is present in $Ba_2CuGe_2O_7$, and thus the flat spiral is not entirely harmonic at zero field, i.e. it has already some contributions from higher-order Fourier components.

The occurrence of the AF cone phase, also called 'intermediate phase', was predicted in earlier studies by Chovan et al. [142, 143]. However, since the staggered order parameter was constrained to unity, the vortex phase and the rectangular phase were overlooked. This suggests that in the experimental phase diagram obtained by Mühlbauer et al., displayed in Fig. 6.1 b), the phase boundary marked by magenta dots from measurements of the heat capacity corresponds to the phase transition into the vortex phase and that there will be another phase transition into the paramagnetic phase as sketched in orange.

Canted Magnetic Fields
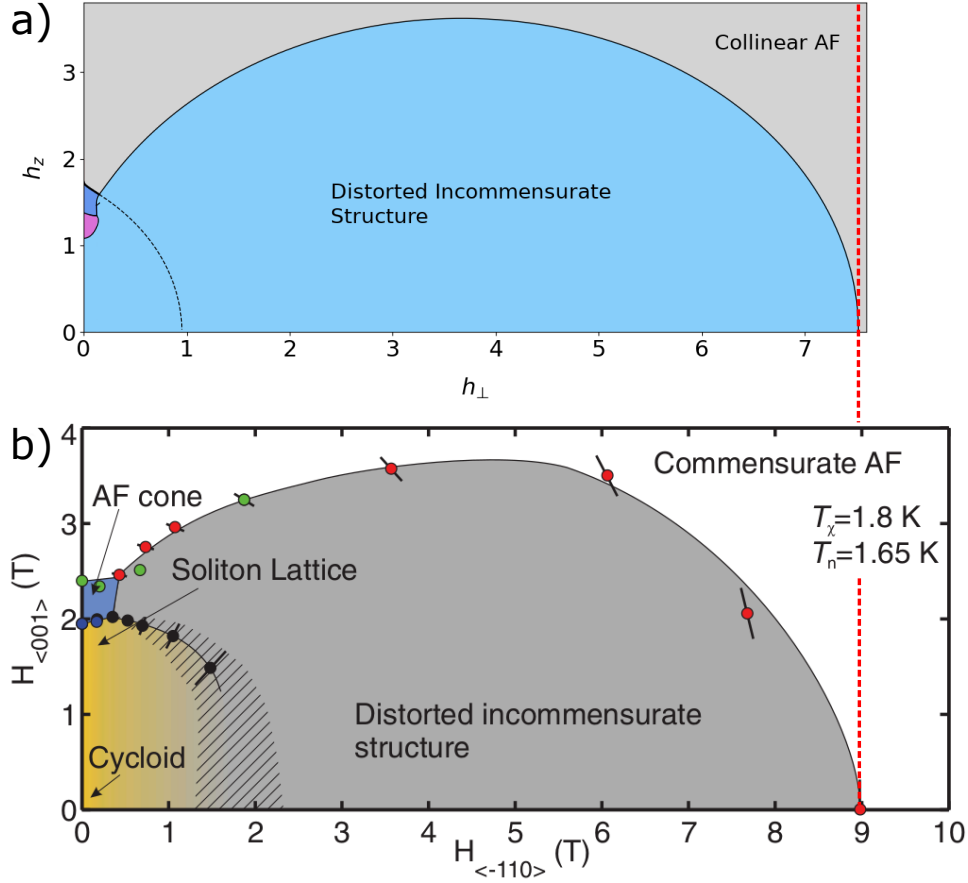
Figure 6.2.: a) Phase diagram in canted magnetic fields at $r = -1.5$, which reproduces qualitatively well experimental findings by Mühlbauer et al. in b), taken from FIG: 11 (a) in [144]. All rights with the American Physical Society.

Next, we consider the phase diagram in canted magnetic fields, where an additional in-plane field $h_\perp$ is present, breaking the $U(1)-$symmetry of our model. For demonstration purpose we will let $h_\perp$ point in y-direction. The solution for a magnetic field in an arbitrary in-plane direction can be obtained by making use of the underlying, broken $U(1)-$symmetry as described in [143].

On the one hand, the spin-flop term $(\vec{h} \cdot \vec{\phi})^2$ tilts the easy-plane by an angle $\tan(\alpha) = \frac{h_\perp}{h_z}$. On the other hand, the weak ferromagnetic term $d_z(\vec{h} \times \hat{e}_3) \cdot \vec{\phi} = d_z h_\perp \phi_1$ leads to a linear coupling of $h_\perp$ to the AFM order parameter, which dominates over the quadratic terms for small in-plane fields. The value $d_z = 0.06$ is chosen in comparison to previous work by Chovan et al. [143].

The phase diagram at $r = -1.5$ in canted fields is displayed in Fig. (6.2) a). It is dominated by the evolution of the flat spiral state into a distorted, incommensurate structure, which eventually undergoes an incommensurate-to-commensurate (IC) transition to the collinear AFM state at sufficiently high magnetic fields. The extent and curvature of this

arch-shaped IC transition are determined by d_z. For $d_z = 0$, the flat spiral prevails for any $h_\perp$, and the arch does not wind back to the x-axis (compare with Fig. 5.2).

The AF cone phase, as well as the rectangular phase, occur only in a small pocket of the phase diagram, where the out-of-plane field h_z is sufficiently strong to render the flat spiral state energetically unfavorable, but in-plane fields $h_\perp$ are sufficiently weak not to destroy these phases.

This pocket is shown more closely in Fig. 6.3 a). While the symmetry of the vortex phase is immediately broken for a non-zero in-plane field, resulting into the rectangular phase, the rectangular phase possesses lateral stability comparable to the AF cone state.

In-plane fields also break the two-domain degeneracy of the rectangular phase, favoring the state, whose larger k-vector is aligned perpendicular to $h_\perp$, i.e. aligning the principal plane of spin rotation with the easy plane.

The bold transition line between the AF cone phase and the collinear AFM phase has been calculated from fluctuations (see below), while the dotted line marks the boundary of stability of the collinear state.

These findings complement qualitatively well the phase diagram of $Ba_2CuGe_2O_7$, depicted in Fig. 6.2 b), which was reported by Mühlbauer et al. [144]. One of the main experimental challenges for finding the rectangular phase will be the distinction between the flat spiral state, being a single-k state but with two domains, and the rectangular phase, being a two-k single domain state.

6.3 Vortex Phase Properties

Evolution of Fourier Components

We show the evolution of Fourier components and k-vectors along a representative cut through the phase diagram for comparison with neutron scattering experiments. The inset Fig. 6.3 a) suggest that the tilt angle of the magnetic field $\tan(\alpha) = h_\perp/h_z$ must not exceed 2° to reach the vortex phase and must not exceed 6° to hit the rectangular phase still, respectively. For demonstration purpose, the cut is chosen at an ideal angle of $\alpha = 0°$, i.e. along the y-axis in Fig. 6.3 a).

Plot b) in Fig. 6.3 shows the strength of the commensurate and first-order Fourier components as the circle radius at the value of the respective k-vector, depending on the field strength $h = \sqrt{h_z^2 + h_\perp^2}$. In addition, plots c) and d) show the absolute strength of the commensurate and first-order Fourier components, respectively.

The flat spiral state is present at low fields, which is described by its first-order Fourier components. At the first-order phase transition into the rectangular phase, a second, smaller k_y-vector develops and an additional, first-order Fourier component. The second-order phase transition into the vortex phase is marked by a bifurcation point in both the $q-$value and the first-order Fourier components' strength. Then, at the first-order phase transition into the AF cone phase, the q_x value drops to zero, alongside the respective first-order Fourier component. At the same time, both the q_y-value and the respective first-order Fourier component diminish continuously with increasing h, and a non-zero

commensurate Fourier component develops suddenly. These transitions can also be seen in the incommensurability parameter $\xi = L(0)/L(h) = q(h)/q(0)$ plotted in Fig. 6.4.
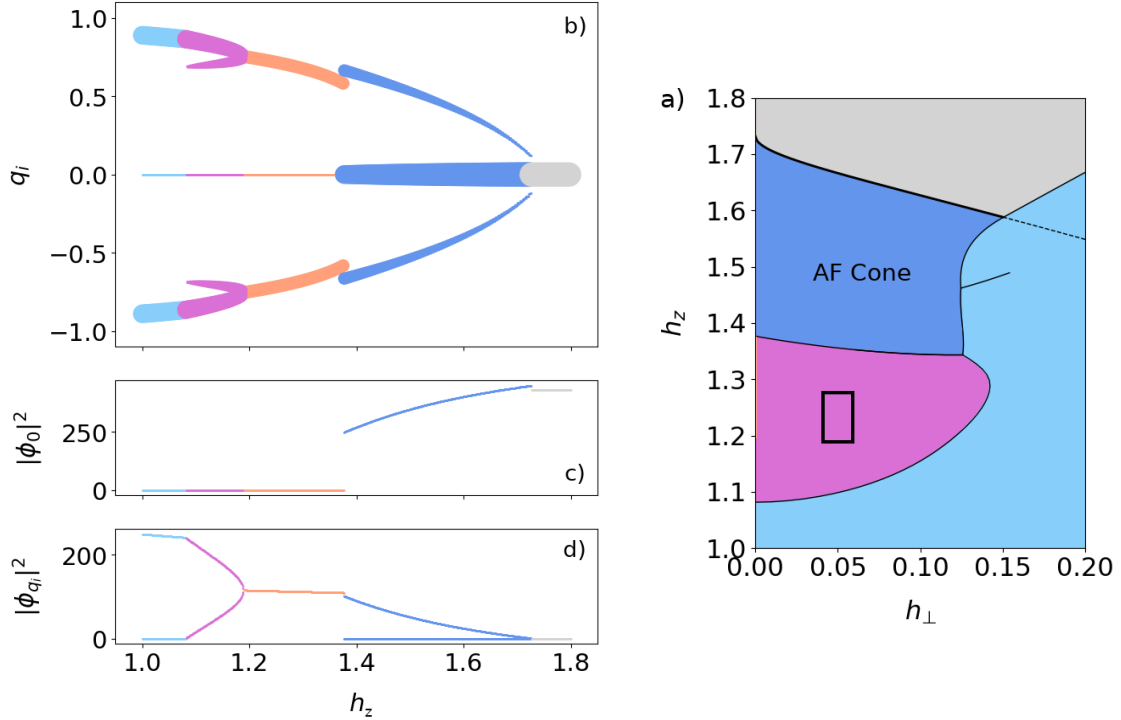
Figure 6.3.: Cut through the phase diagram in canted fields at $r = -1.5$ along the angle $\alpha = 0°$ (plot a)). Plot b) depicts the strength of the commensurate and first-order Fourier components as the radius of a circle at the corresponding q-value. Their absolute strength is shown at the same time in plot c) and d).
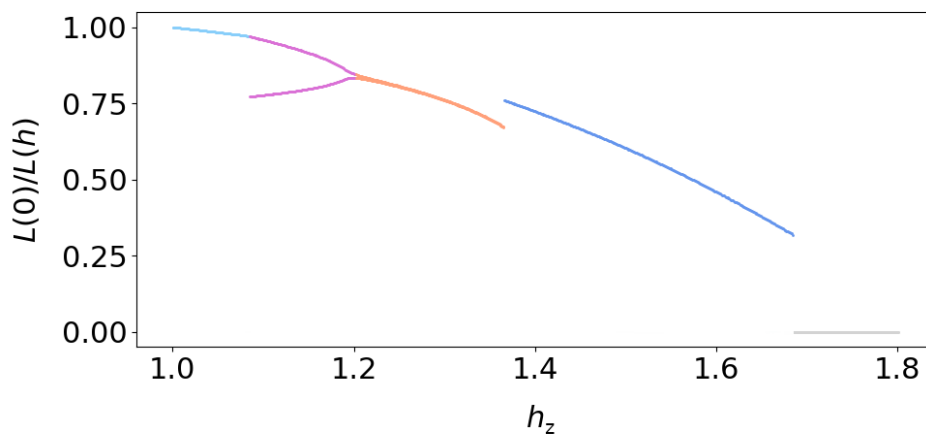
Figure 6.4.: Incommensurability parameter ξ, comparing a spirals pitch length L at the magnetic field h with the one in zero-field: $\xi = L(0)/L(h) = q(h)/q(0)$ with $L = 1/q$ and $h = h_z$ in our case.

No Emergent Electrodynamics

Electrons flowing through a spiral magnet adapt their spin adiabatically to the background magnetic texture [161]. If this texture is topological, e.g. for a skyrmion lattice, the electron's wave function picks up a topological Berry phase, which acts like an Aharanov-Bohm phase. Its impact on the electron's trajectory can be described by (fictitious) emerging electric and magnetic fields [85]. This leads to a skyrmion Hall effect, where the electron flow is deflected by the skyrmion lattice [49, 86–88]. An overview and educational introduction to this emergent electrodynamics is given by [8, 68, 90].

We investigated whether there is an emergent electrodynamics for the vortex phase. Here, a perfect antiferromagnet can be described by two ferromagnetic sublattices A and B, which will be differentiated by an index $\mu = A, B = \pm 1$. Solving the Schrödinger equation for an electron in a topological antiferromagnet leads to the known expressions for the emergent electric and magnetic field [85], including an additional prefactor μ

$$E_{\mu,i} = \mu \frac{\hbar}{2e} \hat{m}_\mu \cdot (\partial_i \hat{m}_\mu \times \partial_t \hat{m}_\mu) \tag{6.9}$$

$$B_{\mu,i} = \mu \frac{\hbar}{4e} \varepsilon_{ijk} \hat{m}_\mu \cdot (\partial_j \hat{m}_\mu \times \partial_k \hat{m}_\mu) \tag{6.10}$$

Here, $i = x, y, z$ counts the spatial dimensions and e is the electron charge. As $\mu = \pm 1$ enters as a prefactor, the fields emerging from different sublattices cancel each other, and no emergent electrodynamics is expected in this adiabatic approximation. However, $Ba_2CuGe_2O_7$ hosts as well weak ferromagnetism, described by

$$\mathcal{F}[\vec{\phi}] = d_z(\vec{h} \times \hat{e}_3) \cdot \vec{\phi} = -\vec{h} \cdot \delta\vec{m}, \quad \delta\vec{m} = d_z(\vec{\phi} \times \hat{e}_3) \tag{6.11}$$

For a static magnetic texture the emergent electric field is zero and since $\partial_3 \delta\vec{m} = 0$ we have $B_1 = B_2 = 0$. For the z-component of the emerging magnetic field we obtain

$$B_3 = \frac{\hbar}{2e} \delta\vec{m} \cdot (\partial_1 \delta\vec{m} \times \partial_2 \delta\vec{m}) = \frac{\hbar}{2e} d_z^2 (\vec{\phi} \times \hat{e}_3) \cdot (\partial_1(\vec{\phi} \times \hat{e}_3) \times \partial_2(\vec{\phi} \times \hat{e}_3)) \tag{6.12}$$

Using $(\vec{a} \times \vec{b}) \times (\vec{a} \times \vec{c}) = \det\left(\vec{a}, \vec{b}, \vec{c}\right)\vec{a}$ we get

$$B_3 = \frac{\hbar}{2e} d_z^2 \underbrace{(\vec{\phi} \times \hat{e}_3) \cdot \hat{e}_3}_{= \det\left(\hat{e}_3, \vec{\phi}, \hat{e}_3\right) = 0} \det\left(\hat{e}_3, \partial_1\vec{\phi}, \partial_2\vec{\phi}\right) = 0 \tag{6.13}$$

Hence, also from weak ferromagnetism we do not expect an emergent electrodynamics in an adiabatic approximation. It does not preclude a topological Hall effect in $Ba_2CuGe_2O_7$.

Ferroelectricity

In a previous experimental study by Murakawa et al. [159], the polarization induced by the flat spiral state was used as a handle to switch the flat spiral between different domains, which are due to an additional tetragonal crystal anisotropy. In a recent study, the spin-current mechanism was proposed as the microscopic origin of this polarization for $Ba_2CuGe_2O_7$ within the superexchange theory [162].

Similarly, the polarization induced by the vortex phase and rectangular phase may be used as a handle. An in-plane electric field picks the domain of the rectangular phase whose k-vector points perpendicular to it. Thus, an in-plane magnetic field $h_\perp$, which favors the domain with larger $\vec{k}$ along x-direction and an in-plane electric field in x-direction, which favors the domain with larger $\vec{k}$ along y-direction, can be balanced against each other.

When tuning the electrical field strength E, as demonstrated in Fig. 6.5 b) and c), one may reach a point that balances in-plane electric field and in-plane magnetic field. This would result in a distorted square-lattice phase (see Fig. 6.5 a)) and may allow to determine the magnetoelectric coupling experimentally.
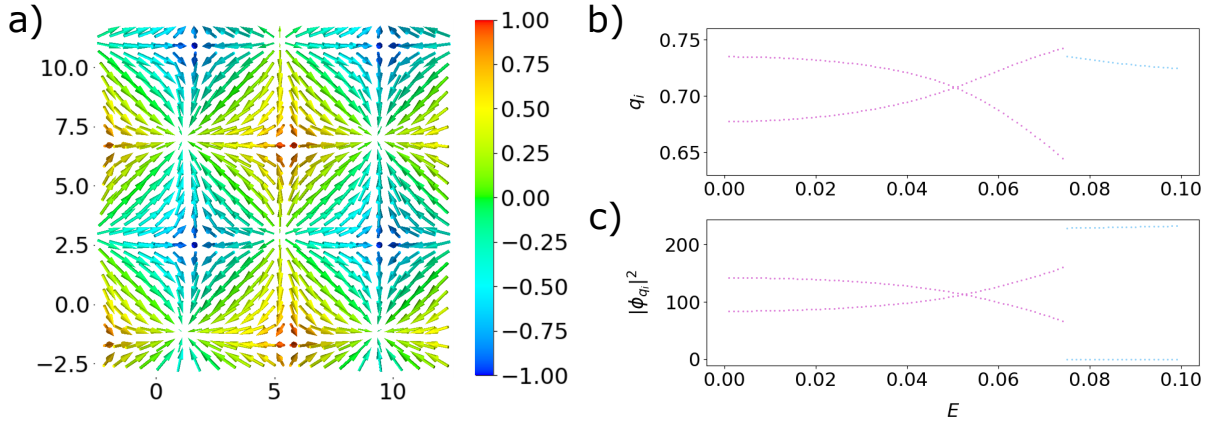
Figure 6.5.: a) Distorted vortex phase at $r = -0.2$, $h_z = 1.25$ at the point, where an in-plane magnetic field $h_\perp = 0.1$ in y-direction is balanced by an in-plane electric field $E = 0.055$ in x-direction. b) and c): Strength of the $\vec{k}$-components q_i and the respective Fourier components $|\phi_{q_i}|^2$ with $i = x, y$, when tuning an electrical field in x-direction against an in-plane magnetic field of $h_\perp = 0.1$ in y-direction at $r = -1.5$, $h_z = 1.25$. For zero electric field the larger k-vector points along x-direction, at $E = 0.055$ both q-vectors are roughly equally large, and for larger E the larger k-vector points along y-direction. Again, for even larger E a distorted spiral state develops.

6.4 Fluctuations of the Collinear AFM

For completeness, we revisit the fluctuations of the collinear AFM when in-plane magnetic fields are present.

Mean Field Solution with In-Plane Fields

If also in-plane magnetic fields $\vec{h} = h_y \vec{e}_y + h_z \vec{e}_z$ are present, the free energy density for the collinear AFM (4.2) is given by

$$\mathcal{F}_{\mathrm{MF}}(\vec{r}) = \frac{1}{4}\phi^4 + \frac{r}{2}\,\phi^2 + \phi\,d_z\,h_y \tag{6.14}$$

The mean-field solution is found by setting its derivative to zero

$$\frac{\partial \mathcal{F}_{\mathrm{MF}}}{\partial \phi} = \phi^3 + r\,\phi + d_z\,h_y = 0 \tag{6.15}$$

which results into three non-trivial solutions.

Fluctuations with In-Plane Fields

The matrix form of the free energy density (6.3) now reads

$$\mathcal{F}[\phi] = \frac{1}{2}\,\vec{\phi}^T \begin{pmatrix} r - \vec{\nabla}^2 & 0 & 2\,\partial_1 \\ 0 & r - \vec{\nabla}^2 + h_y^2 & -2\,\partial_2 + h_y h_z \\ -2\,\partial_1 & 2\,\partial_2 + h_z h_y & r + h_z^2 - \vec{\nabla}^2 \end{pmatrix} \vec{\phi} + \frac{u}{4}(\vec{\phi}^2)^2 + d_z(\vec{h} \times \vec{e}_3) \cdot \vec{\phi} \tag{6.16}$$

The fluctuation matrix in Fourier space (with $-i\vec{\nabla} \to \vec{k}$) is then given by

$$\chi_{ij}^{-1} = \begin{pmatrix} r + \vec{k}^2 & 0 & 2\,ik_1 \\ 0 & r + h_y^2 + \vec{k}^2 & -2ik_2 + h_y h_z \\ -2ik_1 & 2\,ik_2 + h_z h_y & r + h_z^2 + \vec{k}^2 \end{pmatrix}_{ij} + u\left(\vec{\phi}^2 \delta_{ij} + 2\,\phi_i \phi_j\right) \tag{6.17}$$

We have used (4.11) and also it is

$$d_z(\vec{h} \times \hat{e}_3) \cdot \vec{\phi} = d_z \phi h_y \hat{e}_1 \quad \Rightarrow \quad \frac{\delta^2}{\delta \phi_i \delta \phi_j}(d_z h_y \phi_1) = 0 \tag{6.18}$$

Inserting the mean-field state solution (4.2), the fluctuation matrix is finally given by

$$\left(\chi_{ij}^{-1}\right) = \begin{pmatrix} r + \vec{k}^2 & 0 & 2\,ik_1 \\[2mm] 0 & r + h_y^2 + \vec{k}^2 & -2ik_2 + h_y h_z \\[2mm] -2ik_1 & 2\,ik_2 + h_z h_y & r + h_z^2 + \vec{k}^2 \end{pmatrix} + u\,\phi^2 \left(\hat{1} + 2\,\vec{e}_\varphi \cdot \vec{e}_\varphi^T\right) \tag{6.19}$$

We set $\varphi = 0$, do the transformation $k_1 \to k\cos(\chi)$, $k_2 \to k\sin(\chi)$, and set $\chi = \frac{\pi}{2}$. The resulting matrix reads

$$\chi_{ij}^{-1} = \begin{pmatrix} 3\phi^2 + k^2 + r & 0 & 0 \\[2mm] 0 & h_y^2 + k^2 + \phi^2 + r & h_y h_z - 2ik \\[2mm] 0 & h_y h_z + 2ik & h_z^2 + k^2 + \phi^2 + r + 1 \end{pmatrix} \tag{6.20}$$

The eigenvalues are

$$\lambda_1 = 3\phi^2 + k^2 + r,$$

$$\lambda_{2/3} = \frac{h_y^2}{2} + \frac{h_3^2}{2} + k^2 + \phi^2 + r + \frac{1}{2} \pm \frac{1}{2}\sqrt{h_y^4 + 2h_y^2 h_3^2 - 2h_y^2 + h_3^4 + 2h_3^2 + 16k^2 + 1}$$

Only the third eigenvalue can turn negative,

$$\lambda_3 = \frac{h_y^2}{2} + \frac{h_3^2}{2} + k^2 + \phi^2 + r + \frac{1}{2} - \frac{1}{2}\sqrt{h_y^4 + 2h_y^2 h_3^2 - 2h_y^2 + h_3^4 + 2h_3^2 + 16k^2 + 1}$$

so, at first, we need to figure out at which k-value this happens. We set the derivative with respect to k to zero

$$\frac{d\lambda_3}{dk} = k \left(2 - \frac{8}{\sqrt{h_y^4 + 2h_y^2 h_3^2 - 2h_y^2 + h_3^4 + 2h_3^2 + 16k^2 + 1}} \right) = 0$$

and, while excluding $k = 0$, this results in

$$k = \pm\sqrt{-\frac{1}{16}h_y^4 - \frac{2}{16}h_y^2 h_3^2 + \frac{2}{16}h_y^2 - \frac{1}{16}h_3^4 - \frac{2}{16}h_3^2 + \frac{15}{16}}$$

We insert k into the expression for the eigenvalue and determine its root

$$\lambda_3 = -\frac{1}{16}h_y^4 - \frac{2}{16}h_y^2 h_3^2 + \frac{10}{16}h_y^2 - \frac{1}{16}h_3^4 + \frac{6}{16}h_3^2 + \phi^2 + r - \frac{9}{16} = 0$$

As ϕ itself depends on h_y via (6.15), we solve this for h_z

$$h_z = \pm\sqrt{-h_y^2 \pm 2.0\sqrt{h_y^2 + 4\phi^2 + 4r} + 3}$$

As h_z is positive, all solutions with negative sign can be neglected, and

$$h_z = \sqrt{-h_y^2 - 2.0\sqrt{h_y^2 + 4\phi^2 + 4rr} + 3}$$

describes the boundary between the field-polarized and the AF cone phase for finite in-plane fields. The critical field is given by $h_{z,c} = \sqrt{3}$ for $h_y = 0$, because then $\phi^2 = -r$, which agrees with $h_{z,c} = 2$ for the general model (3.5) due to the shift $h_z^2 \rightarrow 1 + h_z^2$ (see section 6.1).

7 Summary and Outlook

In summary, we have developed a linear sigma model to describe two-dimensional spiral antiferromagnets, in particular $Ba_2CuGe_2O_7$. The phase diagram was determined using variational minimization in Fourier space, revealing a vortex-antivortex phase close to Néel temperature, intervening the phase transition between a flat cycloid and a conical spiral. The vortices constitute a square lattice of topological defects, where the staggered order parameter's strength is going to zero at the vortex cores. If the vortices were absent, the texture could be regarded as a meron-antimeron lattice.

This is consistent with previous work on spiral ferromagnets [118, 119] and a Monte-Carlo study on spiral antiferromagnets [155], hinting at the existence of such a square-lattice vortex-antivortex phase.

At lower temperatures, the vortex phase undergoes spontaneous symmetry breaking into a rectangular phase, rendering the staggered order parameter's strength finite at the vortex cores and thus removing the topological defects. It persists even at very low temperatures, mediating the transition between flat cycloid and conical spiral, but vanishes as the temperature approaches zero.

The vortex phase's symmetry could also be broken actively by introducing a mixed DMI (i.e. choosing a material with mixed Rashba and Dresselhaus DMI) or applying an in-plane magnetic field. In both cases, the vortex phase evolves immediately into a rectangular phase. With respect to in-plane magnetic fields, its lateral stability is comparable to the conical spiral. We predict the strength of the $\vec{k}$-vector and the Fourier components, which can be checked by neutron scattering experiments to establish both the vortex and the rectangular phase.

Experiments by the group of Sebastian Mühlbauer from TU Munich provide preliminary evidence of an additional phase in $Ba_2CuGe_2O_7$ (see Fig. 7.1). Plot A shows the measurement setup, where a magnetic field was applied, tilted 1.5° off the c-axis and 1.2° off the b-axis, with the central peak and two pairs of satellite peaks.

Their intensities were measured by Mühlbauer's group at the D23 diffractometer of the ILL (Institut Laue-Langevin) in Grenoble on a dense grid in reciprocal space. The results are shown in plots C - F at various magnetic fields, ranging from 0 T to 3 T. The central peak displayed in plot F was fitted by two 2D Gaussians (both with independent rotation angles and different centroids) to capture the resolution's shape which was used as a fitting curve for each peak in plots C - E to determine their amplitudes.

Finally, plot B shows the amplitudes of the respective central and satellite peaks color-coded. At zero magnetic field (plot C), the flat spiral state is present, with both of the two domains being populated (orange and purple markers). For a finite magnetic field of 1.5 T (plot D), one of the domains (orange markers) gets favored over the other due to the anisotropy induces by the tilted magnetic field. However, for a magnetic field of 2.2 T, both satellite peaks feature almost identical relative intensities, as expected for the vortex/rectangular phase. A commensurate AF state is present for even larger magnetic fields of 3 T (plot F), resulting in a single central peak.
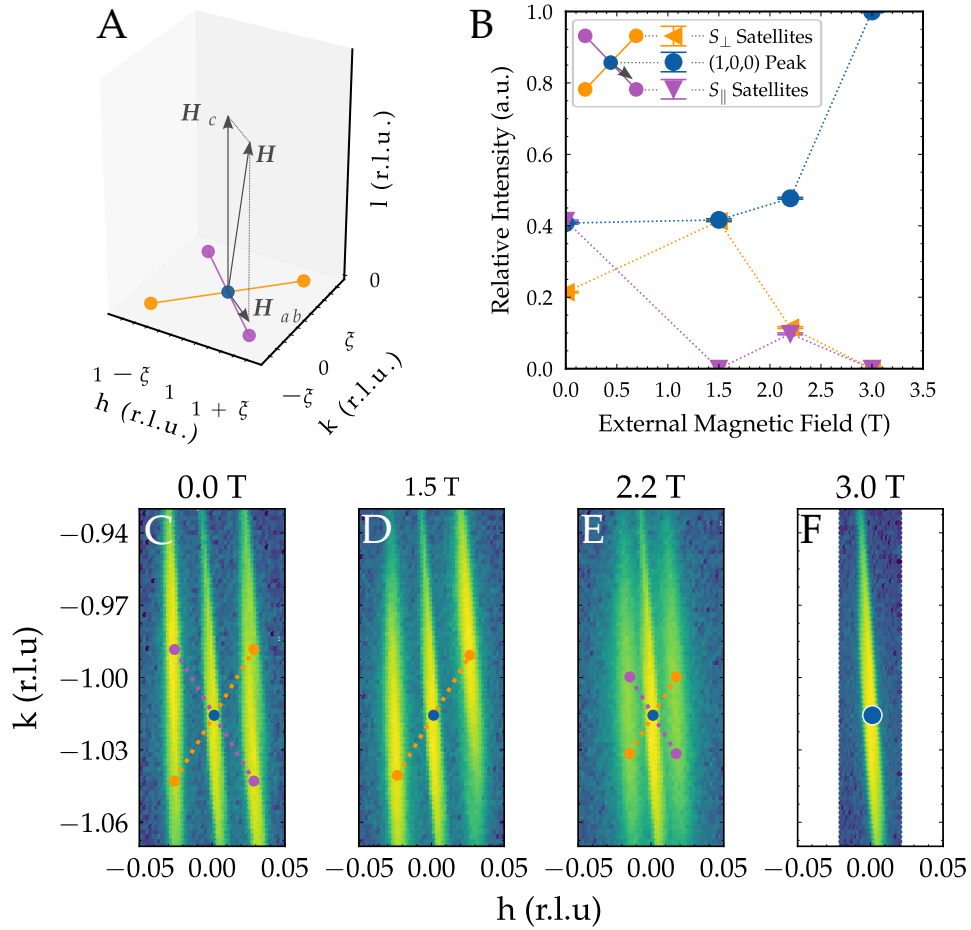
Figure 7.1.: Preliminary neutron scattering results by Michal Dembski-Villalta from the research group of Sebastian Mühlbauer at TU Munich. Plot A shows a sketch of the measurement setup, while plot B shows the intensities of the central peak and the satellites. They were extracted from the neutron scattering data displayed in plots C-F at various magnetic fields ranging from 0 T to 3 T according to the color encoding.

All in all, this gives a strong indication for a two-k, single domain texture like the vortex/rectangular phase being present at 2.2 T rather than a two-domain, single-k texture, where one of the domains would have been suppressed.

So far, no thermodynamic signature e.g. in the specific heat capacity or magnetic susceptibility, was observed in experiments. However, it may be that these signatures are rather small, and further investigations with a better resolution are needed.

In addition, also the multiferroic properties of $Ba_2CuGe_2O_7$ will be of interest to experiments. Since modulated magnetic textures in insulators induce a ferroelectric polarization, vortices and antivortices ought to carry opposite electrical charges. Applying an in-plane electrical field, pulling both in opposite directions, is another way to break the vortex phase's symmetry, which one may detect using neutron scattering. Balancing an in-plane electrical field with an in-plane magnetic field, one could determine this way the electromagnetic coupling.

Our predictions were made specifically for $Ba_2CuGe_2O_7$, but our model should apply to 2D spiral antiferromagnets in general. As a magnetic field induces easy-plane anisotropy, even an easy-axis antiferromagnet could be tuned into a regime where the vortex phase should be present. A candidate material would be the easy-axis antiferromagnet $K_2V_3O_8$, which belongs to the C_{4v} symmetry class, featuring Rashba-DMI, and exhibiting both spiral magnetic textures and weak ferromagnetism [127, 153, 163].

Future research could study the vortices in real space or via Monte-Carlo, studying the formation of single vortices and investigating fluctuations and the dynamical properties of the vortex phase. Just recently, the potential of spin waves in antiferromagnetic materials for applications in magnonics was discussed [164, 165].

Also, it may be worth considering again the phase diagram of 2D spiral ferromagnets, as our work and the work of Rowland et al. [118] indicate, that in the latest paper on 2D spiral ferromagnets by Güngördü [111], and follow-up review articles such as [15], the AF cone phase may have been missed in the phase diagram.

Part II

High-Energy Magnons of a Skyrmion Lattice

8 Introduction to Collective Spin Excitations of Spiral Magnets

In the introduction to spiral magnets in chapter 1 we have encountered the skyrmion lattice phase, where the spins of a magnetic material form a hexagonal lattice of hedgehog-shaped whirls, the so-called skyrmions. In a certain range of magnetic fields and temperatures, the skyrmion lattice is the ground state, representing the spins' equilibrium configuration.

However, those spins will deviate from their equilibrium position for finite temperature due to thermal fluctuations and start to precess. Since neighboring spins are coupled, this gives rise to spin waves, propagating through the entire material – as collective excitations of a multitude of spins [166, 167]. These excitations can be regarded equivalently as quasiparticles, the magnons, which are the quanta of spin waves. We will therefore use both terms interchangeably.

The dynamics of magnons in spiral magnets opens up a research field on its own, where entire Ph.D. theses could be dedicated to [168]. A decent overview is given by the reviews [169, 170], and we will give a short summary of the key aspects in the following.

8.1 Theoretical Description: Bogoliubov - de Gennes Equation

In the low energy limit, chiral magnets can be described by a continuous order parameter function, the magnetization $\vec{M} = M_s\hat{m}$, where M_s is the saturation magnetization and $|\hat{m}| = 1$. Assuming that amplitude variations can be neglected, the unit magnetization $\hat{m}$ of a generic chiral magnet is governed by the general free energy model

$$\mathcal{L} = \frac{M_s}{\gamma}\vec{\mathcal{A}}(\vec{m}) \cdot \dot{\hat{m}} - \mathcal{F}(\vec{m}, \partial_i\vec{m}) \tag{8.1}$$

$$\mathcal{F}(\vec{m}, \partial_i\vec{m}) = A\partial_i m_j \partial_i m_j + Dm_i\varepsilon_{ijk}\partial_j m_k - \mu_0 H M_s m_3 \tag{8.2}$$

with i, j, k and $1, 2, 3$, respectively, indicating the components x, y, z and summation over repeated indices. $\vec{\mathcal{A}}(\vec{m})$ is the spin-gauge potential with the property $\frac{\partial \mathcal{A}_j}{\partial m_i} - \frac{\partial \mathcal{A}_i}{\partial m_j} = \varepsilon_{ijk}m_k$, determining the dynamic part of the Lagrangian, and $\mathcal{F}(\vec{m}, \partial_i\vec{m})$ is the static energy density. We only consider bulk materials, therefore boundary conditions arising at sample surfaces will be neglected [171–173].

As we have seen in the previous project, the ground state solution can be obtained by minimization of the static energy functional $E = \int \mathrm{d}^3r\, \mathcal{F}(\vec{m}, \partial_i\vec{m})$. Here, we go one step further and consider fluctuations around that ground state. We will therefore assume that

the ground-state solution is given by the magnetization $\hat{m}_0(\vec{r})$, describing a spiral texture of a chiral magnet. Since this is a unit vector, fluctuations will occur only perpendicular to $\hat{m}_0(\vec{r})$, altering its direction, but not its magnitude.

Thus, we need a basis that capture deviations perpendicular to $\hat{m}_0$. Analogously to previous work on the spin-wave spectrum of ferromagnets [174–176], it is useful to introduce the two unit vectors $\hat{e}_1$, $\hat{e}_2$ so that $\hat{e}_1 \times \hat{e}_2 = \hat{m}_0$. In addition, it is convenient to introduce the chiral vectors

$$\hat{e}_\pm = \frac{1}{\sqrt{2}}(\hat{e}_1 \pm i\hat{e}_2) \tag{8.3}$$

which we use to express the magnetization order-parameter in the spin-wave parameterization

$$\hat{m} = \hat{m}_0\sqrt{1 - 2|\psi|^2} + \psi\hat{e}_+ + \psi^*\hat{e}_- \tag{8.4}$$

i.e. as a combination of the ground-state magnetization $\hat{m}_0$ and the two fluctuation fields ψ, ψ^*, which can be combined into the spinor $\vec{\psi} = (\psi, \psi^*)^T$. Using this parameterization, we derive the Lagrangian for magnons of a spiral texture in Appendix D.

The derivation yields a Bogoliubov-de Gennes Lagrangian [104, 168, 169, 177], reading in dimensionful units

$$\mathcal{L} = \frac{1}{2}\vec{\psi}^\dagger \left(\frac{M_s}{\gamma} i\hat{\tau}^z \partial_t - \hat{H} \right) \vec{\psi} \tag{8.5}$$

where $\hat{\tau}^z$ is the third Pauli matrix and $\hat{H}$ is a matrix Hamiltonian (see (9.2), (9.3), and (9.4) for its explicit form). The equations of motion take the form of a bosonic Bogoliubov-de Gennes equation

$$\hat{H}\vec{\psi} = \frac{M_s}{\gamma} i\hat{\tau}_z \partial_t \vec{\psi} \tag{8.6}$$

Since the Hamiltonian is constant in time, only the solutions to the stationary Bogoliubov - de Gennes equation need to be determined. This was solved previously in Fourier space, determining the eigenvalues for various cases: the field-polarized state, a helical/-conical spiral state, and the skyrmion lattice (see the supplementary material of [178] and [168, 169] for details). The following sections summarize the main results from this analysis.

8.2 Magnon Excitations of Spiral Textures

In conventional (ferro-)magnets, the dispersion of magnons is symmetric with respect to an inversion center. However, if there is no inversion center, such as in chiral magnets, the magnon dispersion is generally asymmetric [179, 180]. Consequently, magnons with opposite wave vector $\vec{k}$ and $-\vec{k}$ travel at different group velocities, leading to a nonreciprocal propagation. The following gives a short account of how this nonreciprocity develops for different phases of a typical chiral magnet.

Field-Polarized State

For the field-polarized state $\hat{m}_0 = \hat{z}$, the local dreibein can be chosen according to $\hat{e}_1 = \hat{x}$, $\hat{e}_2 = \hat{y}$. Solving the Bogoliubov-de Gennes equation (8.6) in Fourier space shows that the DMI leads to a shift in the dispersion along k_z [168, 169, 178], as the z-direction is distinguished by the applied magnetic field. Consequently, the eigenfrequency spectrum is non-reciprocal $\omega(-k_z) \neq \omega(k_z)$, and magnons that get absorbed at a given momentum k_z cannot be emitted at the same energy, unlike in conventional ferromagnets. This has been observed in inelastic neutron scattering on MnSi [181–183]. It also implies that the group velocity is finite for $k_z \to 0$, positive for right-handed DMI, and negative for left-handed DMI. This non-reciprocal propagation of magnons at small wave vector has been observed e.g. for Cu_2OSeO_3 [184, 185], $LiFe_5O_8$ [186], FeGe and Co-Zn-Mn alloys [187].

Helical State

In a prototypical chiral magnet, a conical helix state is below the magnetic field H_{c2} (see e.g. phase diagram of MnSi in section 1.2). It is discussed together with the purely helical state (without homogeneous component), and orientation effects due to anisotropies can be neglected, i.e. the helical state is assumed to be aligned with the z-axis. A specialty of the helical state is its continuous screw symmetry, where a translation along the z-axis followed by an appropriate rotation around the z-axis leaves the magnetic texture invariant. The flat helix also possesses a discrete symmetry: it is invariant with respect to a π-rotation of real and spin space around the x-axis.

The helical state generates a periodic potential in z-direction for the magnons, leading to a periodic eigenfrequency spectrum $\omega(\vec{k}+m\vec{Q}) = \omega(\vec{k})$ for $m \in \mathbb{Z}$ and $\vec{Q} = Q\hat{z}$ according to the Bloch theorem. The period $\frac{2\pi}{Q}$ is typically on the order of $20\,\mathrm{nm}$ to $70\,\mathrm{nm}$ [169].

For propagation only along z-direction, i.e. $\vec{k} = k_z\hat{z}$, the Fourier transform of the periodic potential vanishes due to the continuous screw symmetry, and as a result, one obtains the empty lattice model for the magnon propagation [188]. Vice versa, for large perpendicular $|\vec{k}_\perp| \gg Q$, the wave equation takes the form of a Mathieu equation and describes a particle with quadratic dispersion in a periodic cosine potential. Increasing $|\vec{k}_\perp|$ tunes the strength of the periodic potential from weak-binding to tight-binding, and the Bragg scattering becomes very strong so that lower bands become effectively flat (no dispersion in z-direction). Thus, magnons become localized within z-direction [169].

The helimagnon spectrum has been thoroughly investigated for MnSi [182, 189–192]. For Cu_2OSeO_3 it could not be resolved at first by inelastic neutron scattering [193, 194], as those inelastic neutron scattering experiments studied the meV-range band structure of Cu_2OSeO_3 arising due to the crystal lattice constant of about 0.8 nm. The helimagnon spectrum caused by helical spin textures with a pitch of about 60 nm [40, 42] resides in the GHz frequency range ($<$ 0.1 meV), which is highly relevant for magnonic applications but inaccessible to inelastic neutron scattering. The helimagnon spectrum of Cu_2OSeO_3 was finally resolved using broadband magnetic resonance spectroscopy [195]. A recent study [196] showed using Brillouin-zone light scattering that the helical conical phase in Cu_2OSeO_3 shows nonreciprocity for small wave vectors, just like the nonreciprocity mentioned above in the field-polarized phase.

On the level of linear spin-wave theory, the uniform magnetization component of the conical spiral does not vary in time in z-direction, i.e. uniform oscillations of the magnetization are confined to the plane in spin space orthogonal to the magnetic field.

Figure 8.1.: Resonance frequencies of the breathing mode, counterclockwise (CCW), and clockwise (CW) mode of a skyrmion lattice (SkX) for a spherical sample of Cu_2OSeO_3. The CW and CCW modes can be excited by an in-plane ac magnetic field. The breathing mode has a magnetic dipole moment, which can be excited by an out-of-plane magnetic field. The solid black lines show the resonance frequencies of the $\pm Q$ modes of the adjacent conical phase (C). CC-BY Markus Garst et al. [169].

When solving the equations of motion, one finds two eigenmodes labeled $\pm Q$ that have a well-defined helicity if they are non-degenerate (depending on sample geometry). The uniform magnetization oscillates clockwise for the $+Q$ and counterclockwise for the $-Q$ mode.

The two modes are known in literature: They were reported in an early study by Date et al. [197], using electron spin resonance, but without detailed theoretical description. Next, Onose et al reported them for Cu_2OSeO_3 [198], while the connection with theory was made by Schwarze et al. [178]. Subsequently, Stasinopoulos et al. confirmed that the $\pm Q$ modes in Cu_2OSeO_3 are linearly polarized for zero magnetic field [199].

Skyrmion Lattice Phase

The magnon modes of the skyrmion lattice phase in chiral magnets were first investigated by Mochizuki [200]. By solving the Landau-Lifshitz-Gilbert equations of a Heisenberg model, he identified three uniform magnetic modes at the Γ point (i. e. at zero

wave vector): breathing, clockwise (CW), and counterclockwise (CCW) mode. They were subsequently also found in experiments by Onose et al. on Cu_2OSeO_3 [198].

Due to backfolding of the magnon spectrum, there are several modes at the Γ point, but only those three are magnetically active: The breathing mode possesses a macroscopic magnetic dipole moment, which can be excited by an out-of-plane magnetic field, leading to an oscillation in the skyrmion size (therefore "breathing" mode). Its frequency decreases with increasing magnetic field.

The CW and CCW modes feature a uniform magnetization that oscillates clockwise and counterclockwise, respectively, and can be excited by an in-plane ac magnetic field. Generally, the CCW mode has a larger weight, and its frequency increases with increasing magnetic field. The CW mode depends only weakly on the magnetic field strength.

As it was shown in a paper by Schwarze et al. [178], the $\pm Q$ of the helical state, as well as the breathing, CW, and CCW modes of the skyrmion lattice phase, represent universal excitations of these phases. I.e. there are found in materials with various electronic properties, which was demonstrated for MnSi (metal), $Fe_{0.8}Co_{0.2}Si$ (semiconductor) and Cu_2OSeO_3 (insulator).

Single Skyrmions

Single skyrmions can also appear as excitations of a chiral magnet's ferromagnetic state and between the skyrmion lattice and field-polarized phases when the skyrmion density is low. Understanding their internal excitation spectrum may not only be relevant for magnonic applications [75, 76], but also for assessing their stability and rigidity. It was determined by a finite-size diagonalization of the Landau-Lifshitz-Gilbert equation by Lin et al. [202], as well as by Schütte et al. [104, 201] within the continuum approximation by solving the Bogoliubov-de Gennes equation (8.6) introduced above.

A skyrmion in a ferromagnetic background introduces locally a potential for magnons, which supports localized, bound modes (i.e. the internal modes of the skyrmion) below the energy gap to the continuous magnon spectrum of the surrounding ferromagnetic state ('magnon continuum'). Among others, these bound modes include a translational mode, corresponding to translational motion of the skyrmion, as well as several breathing modes capturing different kinds of distortions (square, triangular, uniform, elliptic, and others).

For small magnetic fields, there are several gapless modes [202], which indicate instability of the single skyrmion to the respective deformation: as an eigenfrequency becomes negative, the amplitude of the respective mode increases exponentially in time, and the skyrmion configuration becomes unstable. Hence, the single skyrmion becomes unstable already, when the first mode becomes gapless, i.e. its eigenfrequency vanishes. This is the case for a mode capturing elliptical deformations at about $H_a \sim 0.55 D^2/J_{ex}$ [202], where H_a is the strength of the external magnetic film, applied perpendicular to the chiral magnet, D is the strength of the DMI-vector, and J_{ex} is the strength of exchange.

Note that despite a single skyrmion becoming unstable, the skyrmion lattice phase may still constitute the thermodynamic ground state in the low-field region, as the skyrmion lattice geometry restricts skyrmion deformations, and thus these instabilities are suppressed [202].

For large magnetic fields, a single skyrmion is a locally stable (metastable) excitation of the ferromagnetic ground state, as no additional gapless modes appear. Vice versa, as the skyrmion size shrinks, for larger magnetic fields, it can support only fewer modes. Specifically, three different modes exist for large magnetic fields (see Fig. 8.2): At first, there is the translational mode, which is a zero-energy mode (not displayed in Fig. 8.2). It is well separated from the other modes, which justifies treating a skyrmion as a rigid particle when deriving its equation of motion. In addition, there is an elliptic mode and a uniform breathing mode, which may hybridize [201].

The uniform breathing mode produces an oscillation magnetic dipole moment, which can be excited by an out-of-plane ac magnetic field, just as for the skyrmion lattice phase. It may serve as a tunable microwave signal generator [203]. In addition, the elliptical mode provokes an oscillation electric dipole moment, which could be excited using ac electric fields [201].

In an additional study by Kravchuk et

Figure 8.2.: Magnon spectrum of a single skyrmion excitation in the field-polarized state of a chiral magnet. Below the magnon continuum of the field-polarized state, different kinds of breathing modes are present, which can be classified according to their angular momentum quantum number m: a uniform breathing mode with $m = 0$, an elliptical (quadrupolar) mode with $m = -2$, and a triangular (sextupolar) mode with $m = -3$. The translational mode is not displayed. All rights with the American Physical Society [201].

al. [105] it was later also shown that a high-frequency gyrotropic mode is always present in the spectrum, but its frequency lies on the edge of the magnon continuum. In addition, the asymptotic behavior of different modes for large skyrmion radii was investigated.

Magnon-Skyrmion Scattering

Once the energy of magnons surpassed the gap between the single skyrmion bound states and the magnon continuum, they can be considered as scattering states. How they scatter off the skyrmion is intricately affected by the skyrmion's non-trivial topology: the scattering cross-section is highly asymmetric for scattering in the forward direction ('skew scattering), and it features oscillations in strength ('rainbow scattering') [201, 202, 204].

These properties can be understood from a high-energy approximation [205], where the time evolution of the magnons wave function is governed by the Schrödinger equation

$$i\hbar\partial_t\psi = \left[\frac{(-i\hbar\nabla_\perp - \vec{A}(\vec{r}))^2}{2m} + \varepsilon_{\text{gap}}\right]\psi \tag{8.7}$$

Similar to electrons (with spin $s = \frac{1}{2}$) transversing a skyrmion texture (see section 1.2), also magnons (with spin $s = 1$) experience an emergent electrodynamics: They adjust their local quantization axis to the magnetic texture's direction, picking up a Berry phase, which can be described by a spin connection, entering (8.7) as a vector potential $\vec{A} = (A_x, A_y, 0)^T$. Thus, magnons scatter off the fictitious emergent magnetic flux $B_z = [\nabla \times \vec{A}]_z = \partial_x A_y - \partial_y A_x \sim \rho_{\text{top}}$ stemming from the topological density ρ_{top} like a charged particle – in the plane perpendicular to this field ($\nabla_\perp = (\partial_x, \partial_y, 0)^T$).

Their trajectory is deflected due to the emergent Lorentz force, leading to an asymmetric scattering cross-section – so-called skew scattering. This may give rise to a topological magnon Hall effect [204].

As the emergent magnetic field only depends on the distance to the skyrmion center, magnons passing the skyrmion with an impact parameter $\pm b$ on either side encounter the same magnetic flux and thus scatter off at the same angle. As their trajectories interfere constructively and destructively, this leads to a characteristic oscillation pattern in the scattering cross-section, known as rainbow scattering.
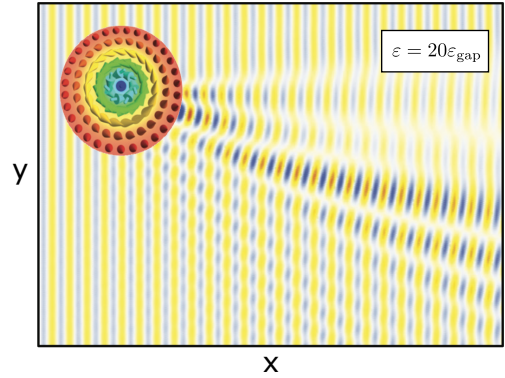
Figure 8.3.: A magnon is coming in from the left side as a plane wave and being scattered off a skyrmion at an energy of $\varepsilon = 20\varepsilon_{\text{gap}}$. Taken from [169], reproduced from [201]; all rights with the American Physical Society.

Skyrmion Strings

Last but not least, also the propagation of spin excitations along a skyrmion tube was investigated, which is mentioned as another exciting research direction that emerged recently.

Here, the center of the skyrmion tube can be modeled as a flexible but robust, one-dimensional string, a so-called skyrmion string, forming a waveguide for spin excitations. The skyrmion string spectrum was studied as a function of wave vector k_z along the magnetic field by Lin et al. [206]. Subsequently, Kravchuk et al. showed by non-linear spin-wave theory that a spin current might also excite solitary excitations of the skyrmion string [207].

Generally, spin excitations propagate along the skyrmion string in a non-linear, non-reciprocal fashion [206, 208, 209]: spin waves propagate with different velocities in either direction, due to the chirality of the texture [208]. Therefore, they may be used as spin-wave channels/diodes, which may allow for information transfer along skyrmion strings.

8.3 Applications in Magnonics

The excitation spectrum of magnetic skyrmion and their interaction with magnons not only add to the list of intriguing skyrmion properties. It is also highly relevant to the emerging field of magnonics [210–216]: the processing of information based on spin waves [217–222]. As spin waves transport only angular momentum and no electric charges, spin-wave-based devices could avoid Joule heating and thus may operate at reduced power consumption. Several studies were dedicated to magnonic logic circuits [223–226] and demonstrating proof-of-concept devices such as a magnon transistor [227], or a magnonic holographic memory [228].

One of the materials that has taken a key role in magnonics in recent years is the insulating ferrimagnet ytrium iron garnet $Y_3Fe_5O_{12}$ (YIG) [210], which features sharp resonances and a very low damping parameter ($\alpha = 3 \times 10^{-5}$ at room temperature) [229], which is unmatched by metals [230].

It is used, for example, in magnonic grating couplers: nanopatterned periodically modulated magnetic materials, which allow the excitation of magnons in a controlled manner by electromagnetic waves. As spins tend to align with an external magnetic field, spin oscillations, and thus magnons, can be induced by an alternating magnetic field. The easiest way to generate an alternating magnetic field is to use electromagnetic waves, whose frequency needs to match the frequency of the magnons, which is typically in the GHz regime. These are microwaves with a typical wavelength of a few centimeters.

However, since the magnon's group velocity is well below the speed of light [231], magnons with wavelengths much shorter than the corresponding wavelength of a microwave can be excited. Their wavelengths need to be smaller than 100 nm to provide an advantage over traditional CMOS computing technology (CMOS: complementary metal-oxide-semiconductor) [219]. Magnons with wavelengths down to 68 nm have been demonstrated e.g. by integrating periodic arrays of metallic ferromagnetic nanodisks into a YIG thin-film serving as a magnonic grating coupler [212].

Chiral magnets hosting periodic magnetic textures are promising candidates to build magnonic grating couplers, as the period of those textures is on the order of the relevant wavelength for magnonics. They offer several advantages over devices tailed by top-down assembly via lamination, heteroepitaxy, or patterning: On the one hand, the periodic spin textures occur spontaneously within a homogenous material, which avoids spurious spin-wave scattering at rough surfaces and allows for bottom-up assembly and tuning the lattice constant of the magnetic nanostructures. On the other hand, those textures occur in systems with a variety of electronic properties, metals, semiconductors, and insulators, which can be exploited to modify the spin textures while processing spin waves, e.g. by applying an electrical current. Here, the most promising material is the insulating chiral ferrimagnet Cu_2OSeO_3, as it features only small damping constant, e.g. $\alpha = 1 \times 10^{-4}$ at 5 K, for the magnon dynamics [232, 233].

9 Modelling & Numerics

9.1 Motivation: Emergent Magnon Landau Levels

This project is inspired by a very recent study by Weber et al. [234] on the magnon dispersion of the skyrmion lattice phase of MnSi. Previous studies used microwave spectroscopy [178] and exploratory inelastic neutron scans [182, 189] to investigated the magnon dispersion at and nearby the Γ-point. In contrast, Weber et al. [234] used polarized inelastic neutron scattering in various setups to determine the magnon dispersion for the first time across the entire Brillouin zone. It turned out that the propagation of magnons in a skyrmion lattice corresponds to that of a charged particle in the emergent magnetic field of the skyrmion texture, leading to topological magnons bands, i.e. that feature a finite Chern number.

Theoretical predictions from solving the Bogoliubov-de Gennes equation (8.6) in Fourier space were complemented by extensive experimental data obtained from three different neutron scattering methods. As an example, Fig.9.1 shows the theoretical prediction for neutron scattering via unpolarized, time-of-flight (ToF) spectroscopy for momentum transfer perpendicular to the skyrmion lattice tubes.

Plot a) depicts the theoretically determined magnon bands as thin gray lines while the spectral weight (dissipative part of the magnetic susceptibility tensor $\chi''_{ij}(q, E)$) is shown in black and green shading for spin-flip (SF) and non-spin-flip scattering (NSF) of an unpolarized neutron beam, respectively.

Plot b) shows the experimental setup, where the external magnetic field H is oriented perpendicular to the skyrmion lattice plane. The six most prominent Bragg peaks of the skyrmion lattice are marked by red dots.

The magnon modes within the skyrmion lattice plane are narrowly spaced and weakly dispersive. However, when plotted in an extended zone scheme as in Fig.9.1 a), the
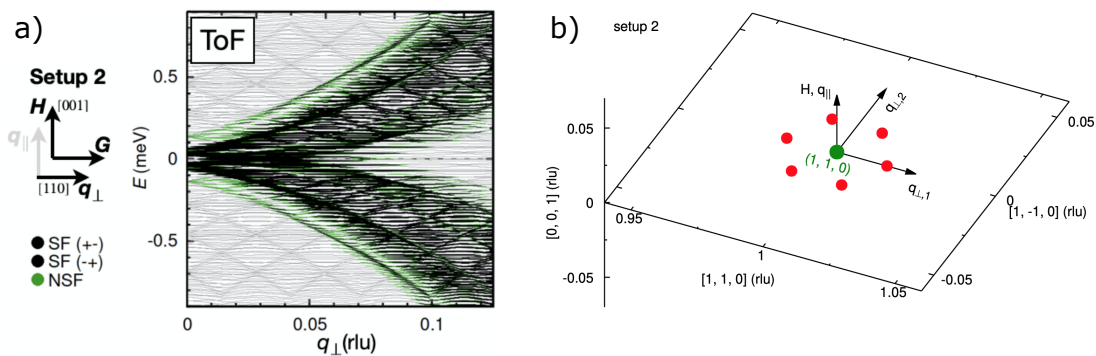
Figure 9.1.: Theoretical prediction for neutron scattering via unpolarized, time-of-flight (ToF) spectroscopy for momentum transfer perpendicular to the skyrmion lattice tubes [234]. Further description in the main text.

magnon bands coalesce to form parabola-shaped superstructures. Even more peculiar: the spectral weight is most pronounced along these parabolas.

This is a curious observation, as a parabola dispersion is typically expected for free particles. However, magnons transversing a skyrmion lattice are subject to a strong emergent magnetic field, as the recent study by Weber et al. suggests. To resolve this conundrum, we develop within this project a high-energy approximation, as it was already done before for magnons scattering off a single skyrmion [205], which will reveal a semiclassical explanation for those parabola superstructures.

9.2 High-Energy Approximation

As introduced in the previous chapter, the motion of magnons in a chiral magnet is governed by a Bogoliubov-de Gennes Lagrangian [104, 168, 169, 177]. Two different derivations are given in appendix D, the result reads in dimensionful units:

$$\mathcal{L} = \frac{1}{2}\vec{\psi}^{\dagger}\left(\frac{M_s}{\gamma}i\hat{\tau}^z\partial_t - \hat{H}\right)\vec{\psi} \tag{9.1}$$

where $\hat{\tau}^z$ is the third Pauli matrix, $\hat{H} = \begin{pmatrix} H^+ & W^- \\ W^+ & H^- \end{pmatrix}$ with $H^{\pm} = -2A\Delta - 2V_0 - 2V^{\pm}$,

and the terms

$$V_0 = -A\vec{m}_0 \cdot (\Delta\vec{m}_0) + D\vec{m}_0 \cdot [\nabla \times \vec{m}_0] - \mu_0 H M_s(\vec{m}_0 \cdot \hat{z})$$
$$+ A\text{Re}(\hat{e}^+ \cdot \Delta\hat{e}^-) - D\text{Re}(\hat{e}^+ \cdot (\nabla \times \hat{e}^-)) \tag{9.2}$$

$$V^{\pm} = 2A(\hat{e}^{\mp}\nabla\hat{e}^{\pm}) \cdot \nabla - D(\hat{e}^{\pm} \times \hat{e}^{\mp}) \cdot \nabla \tag{9.3}$$

$$W^{\pm} = -2A(\hat{e}^{\pm} \cdot \Delta e^{\pm}) + 2D\hat{e}^{\pm} \cdot [\nabla \times \hat{e}^{\pm}] \tag{9.4}$$

In this section, we derive a Schrödinger equation as the high-energy limit of the Bogoliubov-de Gennes equation

$$\hat{H}\vec{\psi} = \frac{M_s}{\gamma}i\hat{\tau}_z\partial_t\vec{\psi} \tag{8.6}$$

as it was previously done in [205]. Writing out the matrix equation yields a system of two

coupled, non-linear partial differential equations

$$H^+\psi + W^-\psi^* = \frac{M_s}{\gamma}i\partial_t\psi \tag{9.5}$$

$$H^-\psi^* + W^+\psi = -\frac{M_s}{\gamma}i\partial_t\psi^* \tag{9.6}$$

where the potentials were defined in (9.2), (9.3), (9.4). Here, $W^\pm$ are anomalous potentials, which contain no gradients or higher-order derivatives. Therefore, they can be neglected in a high-energy approximation, and the two equations (9.5), (9.6) become complex conjugate to each other: Both the time derivative and the spatial gradients in $H^\pm = -2A\Delta - 2V_0 - 2V^\pm$ can be shifted using integration by parts. Thus, we may focus on the first equation (9.5) only, which takes the form

$$i\hbar\partial_t\psi = \frac{\gamma\hbar}{M_s}H^+\psi = \frac{2A\gamma\hbar}{M_s}\left(-\Delta - 2\hat{e}^-(\nabla\hat{e}^+)\cdot\nabla + \frac{D}{A}(\hat{e}^+\times\hat{e}^-)\cdot\nabla - \frac{V_0}{A}\right)\psi \tag{9.7}$$

The terms in V^+ before the gradient can be interpreted as a vector potential $\vec{A}_{\text{tot}}$, with Coulomb gauge $\nabla\cdot\vec{A}_{\text{tot}} = 0$ (this was checked numerically). Thus, the term in the brackets has the general form

$$(-i\nabla - \vec{A}_{\text{tot}})^2 + V = -\Delta + 2i\vec{A}_{\text{tot}}\cdot\nabla + \vec{A}_{\text{tot}}^2 + V \tag{9.8}$$

where

$$2i\vec{A}_{\text{tot}} = -2\hat{e}^-(\nabla\hat{e}^+) + \frac{D}{A}\underbrace{(\hat{e}^+\times\hat{e}^-)}_{=-i\hat{m}_0} \tag{9.9}$$

$$\Rightarrow \vec{A}_{\text{tot}} = i\hat{e}^-(\nabla\hat{e}^+) - \frac{D}{2A}\hat{m}_0 \tag{9.10}$$

and $V = -\frac{V_0}{A} - \vec{A}_{\text{tot}}^2$ captures all of the remaining terms. They will be neglected in our high-energy approximation, as they do not contain any gradients and thus are assumed to be negligible at high energies as compared to terms involving gradients. Thus, the high-energy magnon dynamics in a skyrmion lattice are conjectured to be equivalent to the dynamics of a spin-less, charged particle ($q = 1$) in the magnetic field $\vec{B}_{\text{tot}} = \nabla\times\vec{A}_{\text{tot}}$, governed by the effective Hamiltonian

$$\hat{H} = \frac{1}{2m}\left(\hat{\vec{p}} - \hbar\vec{A}_{\text{tot}}\right)^2 = \frac{2A\gamma\hbar}{M_s}(-i\nabla - \vec{A}_{\text{tot}})^2 \tag{9.11}$$

with the two-dimensional momentum operator $\hat{\vec{p}} = -i\hbar\nabla$ and the mass

$$\frac{\hbar^2}{2m} = \frac{2A\gamma\hbar}{M_s} \Rightarrow m = \frac{\hbar M_s}{4A\gamma} \tag{9.12}$$

Rescaling the vector potential $\vec{A}_{\text{tot}} \to \frac{q}{\hbar}\vec{A}_{\text{tot}}$ and assuming a stationary time-dependence $\psi(\vec{r}, t) = e^{-i\varepsilon t}\psi(\vec{r})$ yields the stationary Schrödinger equation for a charged particle in a magnetic field:

$$\hat{H}\psi(\vec{r}) = \frac{1}{2m}\left(\hat{\vec{p}} - q\vec{A}_{\text{tot}}\right)^2 \psi(\vec{r}) = \varepsilon\psi(\vec{r}) \tag{9.13}$$

Dimensionless Units

In order to solve this Schrödinger equation (9.13) numerically, it is useful to introduce dimensionless units: $\hbar = q = m = 1$. In addition, we measure lengths in units of the distance between two skyrmions $a = \frac{4\pi}{\sqrt{3}k_{\text{skl}}}$, where k_{skl} is the wave vector of the skyrmion lattice. The substitution $\partial_i \to \frac{1}{a}\partial_i$ (highlighted in blue) yields for the Hamiltonian

$$\hat{H} = \frac{1}{2}\left(\frac{1}{a^2}\Delta + 2i\frac{1}{a}\left[-\frac{D}{2A}\hat{m}_0 + i\frac{1}{a}\hat{e}^- \cdot (\nabla\hat{e}^+)\right] \cdot \nabla + \vec{A}_{\text{tot}}^2\right) \tag{9.14}$$

$$= \frac{1}{2a^2}\left(-\Delta + 2i\left[-\underbrace{\frac{Da}{2A}}_{=\delta}\hat{m}_0 + i\hat{e}^- \cdot (\nabla\hat{e}^+)\right] + a^2\vec{A}_{\text{tot}}^2\right) \tag{9.15}$$

with the dimensionless constant ($\frac{k_{\text{skl}}}{k_h} \approx 0.97$ [234])

$$\delta = \frac{D}{2A}\frac{4\pi}{\sqrt{3}k_{\text{skl}}} = \frac{4\pi}{\sqrt{3}}\frac{k_h}{k_{\text{skl}}} \approx 7.48 \tag{9.16}$$

where $k_h = \frac{D}{2A}$ is the helix pitch. We quote our results in terms of the cyclotron frequency

$$\hbar\omega_c = \frac{\hbar q B_u}{m} = \frac{\hbar q}{m}\frac{4\pi\hbar}{qS_{\text{skl}}} = \frac{\sqrt{3}}{\pi}\frac{\hbar^2 k_{\text{skl}}^2}{2m} \tag{9.17}$$

where we have already employed the uniform magnetic field B_u, which will be introduced in the following section, and $S_{\text{skl}} = \frac{\sqrt{3}}{2}a^2$ is the surface of a primitive unit cell of the hexagonal skyrmion lattice.

Many results in the literature [168, 201, 205, 234] are given in terms of the energy scale $E_{c2} = g\mu_B\mu_0 H_{c2}$ ($\omega_{c2} = |\gamma|\mu_0 H_{c2}$), associated with the critical magnetic field H_{c2} at the transition between conical and field-polarized phase for a typical chiral magnet. Here, g is the Landé factor, γ the gyromagnetic ratio, and μ_0 the vacuum permeability. This energy scale can also be expressed in terms of the helix pitch k_h

$$E_{c2} = \frac{\hbar^2 k_h^2}{2m} \tag{9.18}$$

so that the conversion of energy units is given by

$$\frac{\hbar\omega_c}{E_{c2}} = \frac{\sqrt{3}}{\pi}\left(\frac{k_{\text{skl}}}{k_h}\right)^2 \approx 0.52 \tag{9.19}$$

9.3 Vector Potential

In this section, we take a closer look at the vector potential (9.10) we have introduced previously. It consists of two parts

$$\vec{A}_{\text{tot}} = \vec{A}_{\text{DMI}} + \vec{A} \tag{9.20}$$

The first part, $\vec{A}_{\text{DMI}} = -\delta\frac{\hbar}{q}\hat{m}_0$, originates from the DMI. The second part, $\vec{A} = i\frac{\hbar}{q}\hat{e}^- \cdot (\nabla\hat{e}^+)$, is a spin connection, which originates from the exchange interaction and describes the emergent magnetic field

$$\vec{B} = \nabla \times \vec{A} = \frac{4\pi\hbar}{q}\rho_{\text{top}}\hat{z} = \frac{\hbar}{q}\hat{m}_0 \cdot (\partial_x\hat{m}_0 \times \partial_y\hat{m}_0)\hat{z} \tag{9.21}$$

The z-components of the magnetization texture $\hat{m}_z$ and the generated emergent magnetic field are depicted in Fig. 9.2. This ground state configuration was previously determined by Waizner [168] via relaxation in Fourier space within the magnetic field region of the skyrmion lattice phase of MnSi. The emergent magnetic field is the same that electrons experience when transversing a skyrmion lattice (see section 1.2). Its mathematical expression (9.21) is an example of a so-called Mermin-Ho relation [235, 236].

Each skyrmion of the skyrmion lattice carries a topological charge

$$q_{\text{top}} = \int_{\text{WS}} \mathrm{d}^2 r\, \rho_{\text{top}}(\vec{r}) = -1 \tag{9.22}$$
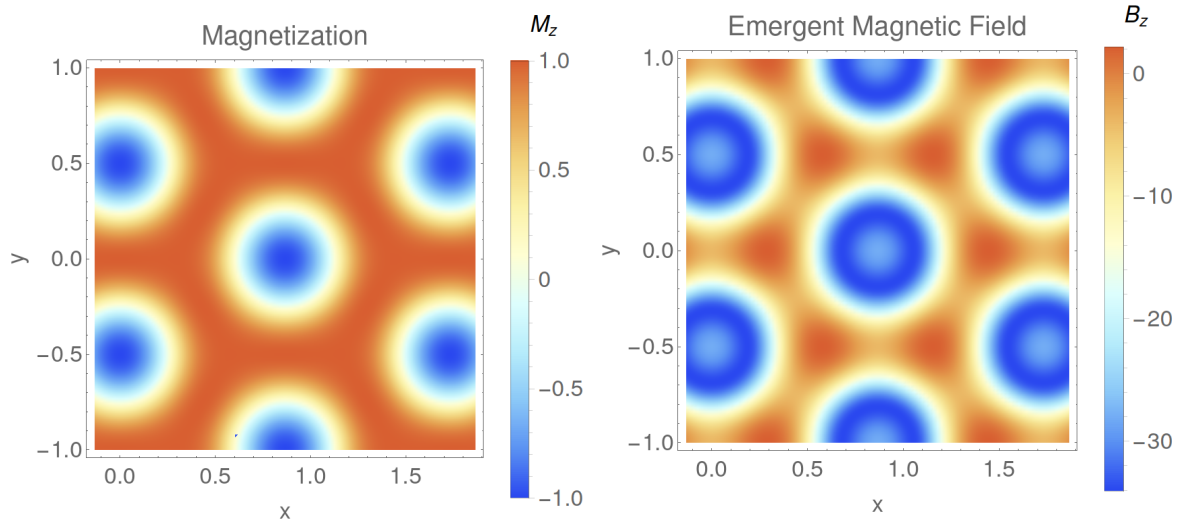
Figure 9.2.: Magnetization distribution of the skyrmion lattice phase in MnSi (left) and the corresponding emergent magnetic field (right).

and thus a magnetic flux of two flux quanta

$$B_u S_{\text{WS}} = \frac{4\pi\hbar}{q} \tag{9.23}$$

where the index 'WS' denotes the Wigner-Seitz cell of the skyrmion lattice, and its area is given by $S_{WS} = \frac{\sqrt{3}}{2}a^2$, where $a = \frac{4\pi}{\sqrt{3}k_{\text{skl}}}$ is the skyrmion distance. Thus, the uniform emergent magnetic field is given by

$$\vec{B}_u = B_u \hat{z} = \frac{8\pi\hbar}{\sqrt{3}\,a^2 q}\hat{z} \tag{9.24}$$

The corresponding vector potential reads in the symmetric gauge

$$\vec{A}_u = \frac{B_u}{2}(-y, x)^T \tag{9.25}$$

The difference to the emergent magnetic field, $\vec{B}_p = \vec{B} - \vec{B}_u$, possesses the periodicity of the two-dimensional hexagonal Bravais lattice L_{hex} with lattice constant a, i.e. $\vec{B}_p(\vec{r} + \vec{R}) = \vec{B}_p(\vec{r})$ with $\vec{R} \in L_{\text{hex}}$. The spatial average of this periodic magnetic field vanishes $\int \mathrm{d}r\, B_p(\vec{r}) = 0$, as all the magnetic flux generated by a single skyrmion is already captured by the uniform magnetic field.
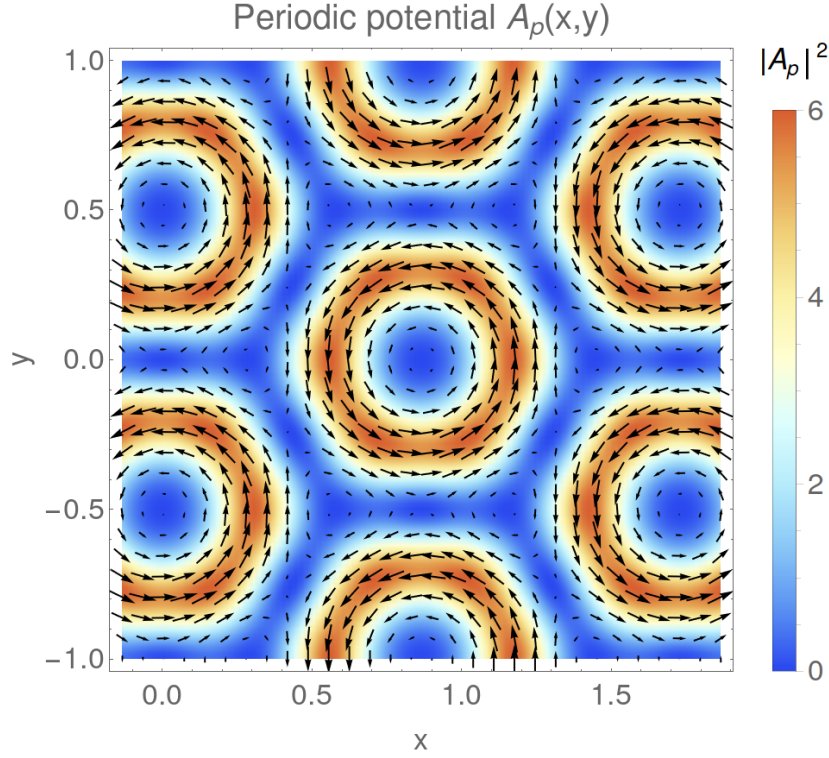
Figure 9.3.: Periodic vector potential $\vec{A}_p$ corresponding to the magnetization texture of the skyrmion lattice plotted in Fig. 9.2.

For a given $B_p(\vec{r})$ the corresponding periodic vector potential can be obtained with the help of the Fourier transform

$$B_p(\vec{r}) = \sum_{\vec{G}} B_p(\vec{G}) e^{i\vec{G}\cdot\vec{r}}, \quad \vec{A}_p^T(\vec{r}) = \sum_{\vec{G}\neq\vec{0}} \frac{i(G_2, -G_1)}{\vec{G}^2} B_p(\vec{G}) e^{i\vec{G}\cdot\vec{r}} \tag{9.26}$$

where $\vec{G}^T = (G_1, G_2, 0)$ is an element of the reciprocal lattice. Fig. 9.3 shows the periodic vector potential for the magnetization texture depicted in Fi.g 9.2.

As the curl is linear and $\vec{B} = \nabla \times \vec{A}$, the vector potential of the emergent magnetic field decomposes into a uniform and a periodic part $\vec{A} = \vec{A}_u + \vec{A}_p$. The DMI-contribution to the vector potential $\vec{A}_{\text{DMI}} = -\delta \hat{m}_0$ trivially possesses the periodicity of the Bravais lattice as well. The uniform vector potential $\vec{A}_u$ will be relevant when considering magnetic translations in order to determine the boundary conditions of our problem in the next section.

9.4 Magnetic Translations

Following the 9th edition of the theory course by Landau and Lifshitz [237], a translation by $\vec{R}$ within a uniform magnetic field described by the vector potential $\vec{A}_u$ lets the wave function $\psi(\vec{r})$ experience the change in the vector potential (assuming symmetric gauge):

$$\vec{A}_u(\vec{r}) \to \vec{A}_u(\vec{r}+\vec{R}) = \vec{A}_u(\vec{r}) + \frac{1}{2}\vec{B}_u \times \vec{R} \tag{9.27}$$

It is a gauge transformation, where $\vec{A}_u(\vec{r}) = \vec{A}_u(\vec{r}+\vec{R}) + \nabla f$ and $f = -\frac{1}{2}\left(\vec{B}_u \times \vec{R}\right)\cdot\vec{r}$ so that the wave function changes by $\psi(\vec{r}) \to \psi(\vec{r}+\vec{R}) = \psi(\vec{r})e^{\frac{i}{\hbar}qf}$. It can be described by introducing the magnetic translation operator $\hat{T}_{\vec{R}}\psi(\vec{r})$, which acts like

$$\hat{T}_{\vec{R}}\psi(\vec{r}) = \psi(\vec{r}+\vec{R})e^{\frac{q}{2}\frac{i}{\hbar}\left(\vec{B}_u \times \vec{R}\right)\cdot\vec{r}} \tag{9.28}$$

It reads explicitly

$$\hat{T}_{\vec{R}} = \exp\left(-\frac{i}{\hbar}(\vec{p}+q\vec{A}_u)\cdot\vec{R}\right) \tag{9.29}$$

and for $\vec{R} \in L_{\text{hex}}$, it is a symmetry of the Hamiltonian, i.e.

$$\left[\hat{T}_{\vec{R}}, \hat{H}\right] = 0 \tag{9.30}$$

Using the Baker-Campbell-Hausdorff formula (9.32), one can show that

$$\hat{T}_{\vec{R}} = \exp\left(-\frac{i}{\hbar}\vec{p}\cdot\vec{R}\right)\exp\left(-\frac{i}{\hbar}q\vec{A}_u\cdot\vec{R}\right) = \exp\left(-\frac{i}{\hbar}q\vec{A}_u\cdot\vec{R}\right)\exp\left(-\frac{i}{\hbar}\vec{p}\cdot\vec{R}\right) \tag{9.31}$$

It gives the solution to the operator equation $e^{\hat{X}}e^{\hat{Y}} = e^{\hat{Z}}$ by

$$\hat{Z} = \hat{X} + \hat{Y} + \frac{1}{2}\left[\hat{X}, \hat{Y}\right] + \frac{1}{12}\left[\hat{X}, \hat{Y}\right]\dots \tag{9.32}$$

We have

$$[\partial_i, (A_u)_j]\,\psi = \partial_i((A_u)_j\psi) - (A_u)_j\partial_i\psi = (\partial_i(A_u)_j)\psi = \frac{\varepsilon_{ij}}{2}B_u\psi \tag{9.33}$$

where $\varepsilon_{ij} = \varepsilon_{ij3}$, and ε_{ijk} is the totally antisymmetric Levi-Civita tensor. Now, regarding the operator's exponents in (9.28), we have

$$[R_i\partial_i, R_j(A_u)_j]\,\psi\psi = R_i\partial_i(R_j(A_u)_j\psi) = R_i\left[(\partial_iR_i)A_j\psi + R_j(\partial_i(A_u)_j)\psi\right]$$

$$= \delta_{ij}R_iA_j\psi + \varepsilon_{ij}R_iR_j\frac{B}{2}\psi = 0 \qquad (9.34)$$

The first term can be checked explicitly with $\vec{A}_u$, and the second term follows since ε_{ij} is antisymmetric. The sum convention applies over repeated indices and δ_{ij} denotes the Kronecker symbol. All the commutators vanish, formula (9.31) holds, and thus the eigenfunctions $\psi_{\vec{k}}(\vec{r})$ with $\vec{k} \in 1.$ BZ (first Brillouin zone) obey

$$\hat{T}_{\vec{R}}\psi_{\vec{k}}(\vec{r}) = \exp\left(-\frac{i}{\hbar}q\vec{A}_u\cdot\vec{R}\right)\psi_{\vec{k}}(\vec{r}+\vec{R}) = \exp\left(i\vec{k}\cdot\vec{R}\right)\psi_{\vec{k}}(\vec{r}) \qquad (9.35)$$

Note that only the uniform part of the vector potential appears in the boundary condition and that these boundary conditions depend on $\vec{r}$, i.e. they are non-constant. This forbids a straightforward solution using one of the standard routines. Instead, we employ our own finite-difference scheme.

9.5 Affine Coordinates

In order to leverage the symmetries of the hexagonal Bravais lattice when solving the Schrödinger equation (9.13), we introduce affine coordinates (a decent introduction is given by [238]). The corresponding covariant basis vectors read in Cartesian coordinates

$$\vec{e}_1 = \left(\frac{\sqrt{3}}{2}, \frac{1}{2}\right)^T, \quad \vec{e}_2 = \left(\frac{\sqrt{3}}{2}, -\frac{1}{2}\right)^T \qquad (9.36)$$

They form the primitive unit cell (PUC) of the skyrmion lattice, depicted in 9.4 a) as purple vectors over the z-component of the periodic part of the emergent magnetic field B_p. In affine coordinates, the skyrmion texture gets distorted, and the PUC becomes a unit square, as shown in 9.4 b).

Distances in the new coordinates are governed by the metric tensor

$$\hat{g}_{\alpha\beta} = \vec{e}_\alpha \cdot \vec{e}_\beta = \begin{pmatrix} 1 & \frac{1}{2} \\ \frac{1}{2} & 1 \end{pmatrix} \qquad (9.37)$$
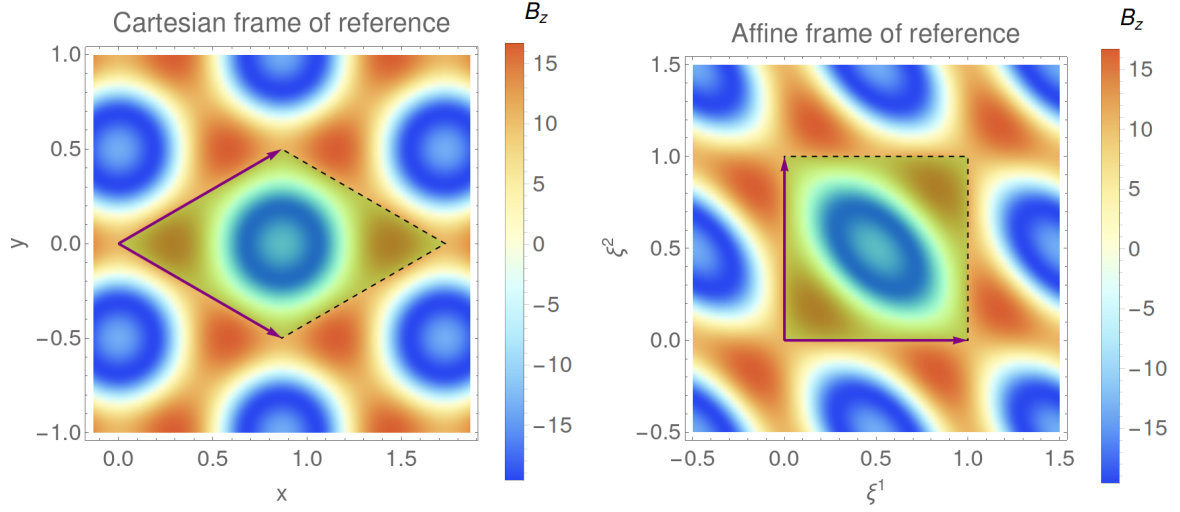
Figure 9.4.: z-component of the periodic part of the emergent magnetic field B_p in Cartesian coordinates (left) and affine coordinates (right).

and the volume of the primitive unit cell is given by $\sqrt{|\hat{g}_{\alpha\beta}|} = \frac{\sqrt{3}}{2}$. The contravariant counterparts of the basis vectors are given by

$$\vec{e}^{\,1} = \left(\frac{1}{\sqrt{3}}, 1\right)^T, \quad \vec{e}^{\,2} = \left(\frac{1}{\sqrt{3}}, -1\right)^T \tag{9.38}$$

from which the reciprocal lattice vectors are constructed as $\vec{g}^{\,1} = 2\pi\vec{e}^{\,1}$ and $\vec{g}^{\,2} = 2\pi\vec{e}^{\,2}$ with $|\vec{g}^{\,1}| = 2\pi\frac{2}{\sqrt{3}} = \frac{4\pi}{\sqrt{3}}$. The first Brillouin zone is a hexagon as well, enlarged and tilted by 30° as compared to the Wigner-Seitz unit cell (see Fig. 10.2 c)). The actual coordinate transformation $(x, y) \to (\xi^1, \xi^2)$ derives from

$$\begin{pmatrix} x \\ y \end{pmatrix} \stackrel{!}{=} \xi^1 \vec{e}_1 + \xi^2 \vec{e}_2 \tag{9.39}$$

which expresses that vectors stay invariant no matter in which coordinates are used.

9.6 Finite-Difference Scheme

Our goal in this section is to develop an explicit finite-difference scheme for solving the Schrödinger equation (9.13) in dimensionless units ($\hbar = 1$, $q = 1$, and here $\varepsilon(\vec{k}) = \omega(\vec{k})$, since $\hbar = 1$). Using Bloch's theorem [167], we can express the wave function through $\psi_{\vec{k}}(\vec{r}) = e^{i\vec{k}\vec{r}}u_{\vec{k}}(\vec{r})$, so that the Schrödinger equation reads

$$\frac{1}{2}\left(-i\nabla + \hbar\vec{k} - \vec{A}_{\text{tot}}\right)^2 u_{\vec{k}}(\vec{r}) = \omega(\vec{k})u_{\vec{k}}(\vec{r}) \tag{9.40}$$

with the boundary conditions (same as (9.35))

$$\exp\left(-i\vec{A}_u(\vec{r}) \cdot \vec{R}\right)u_{\vec{k}}(\vec{r} + \vec{R}) = u_{\vec{k}}(\vec{r}) \tag{9.41}$$

However, the discretization of (9.40) violates the periodicity of the Hamiltonian. Therefore, we work with the original Schrödinger equation

$$\frac{1}{2}\left(-i\nabla - \vec{A}_{\text{tot}}\right)^2 \psi_{\vec{k}}(\vec{r}) = \frac{1}{2}\left(-\Delta\psi + 2i\vec{A}_{\text{tot}} \cdot \nabla\psi + \vec{A}_{\text{tot}}^2\psi\right) = \varepsilon(\vec{k})\psi_{\vec{k}}(\vec{r}) \tag{9.42}$$

In this case, the dependence on $\vec{k}$ is absorbed into the boundary conditions

$$u(\vec{r} + \vec{R}) = \psi_{\vec{k}}(\vec{r} + \vec{R})e^{-i\vec{k}\cdot(\vec{r}+\vec{R})} \overset{!}{=} \psi_{\vec{k}}(\vec{r})e^{-i\vec{k}\cdot\vec{r}}e^{-\frac{i}{2}(\vec{r}\times\vec{R})\cdot\vec{B}_u} = u(\vec{r})e^{\frac{i}{2}(\vec{r}\times\vec{R})\cdot\vec{B}_u} \tag{9.43}$$

and thus (9.35) reads as

$$\psi_{\vec{k}}(\vec{r} + \vec{R}) = \psi_{\vec{k}}(\vec{r})e^{\frac{i}{2}(\vec{r}\times\vec{R})\cdot\vec{B}_u + i\vec{k}\cdot\vec{R}} \tag{9.44}$$

In affine coordinates, the boundary conditions are:

a) $\vec{R} = a(1,0)^T$, $\vec{r} = \xi_2(0,1)^T$ with $\vec{r} \times \vec{R} = -a\xi_2 V_{\text{PUC}}$ leads to

$$\frac{i}{2}(\vec{r} \times \vec{R}) \cdot \vec{B}_u = \frac{i}{2}(-a\xi_2 V_{\text{PUC}})\left(-\frac{4\pi}{V_{\text{PUC}}}\right) = 2\pi i\xi_2 \tag{9.45}$$

b) $\vec{R} = a(0,1)^T$, $\vec{r} = \xi_1(1,0)^T$ with $\vec{r} \times \vec{R} = a\xi_1 V_{\text{PUC}}$ leads to

$$\frac{i}{2}(\vec{r} \times \vec{R}) \cdot \vec{B}_u = \frac{i}{2}(a\xi_1 V_{\text{PUC}})\left(-\frac{4\pi}{V_{\text{PUC}}}\right) = -2\pi i\xi_1 \tag{9.46}$$

The problem is discretized on a grid of $N + 2 \times N + 2$ sites, where the outer sites are ghost cells that allow for the implementation of the boundary conditions so that the resulting finite-difference matrix ends up having $N^2 \times N^2$ entries. The discretized affine coordinates read

$$\xi_1 = (j-1)\Delta a, \quad \xi_2 = (i-1)\Delta a \tag{9.47}$$

with $i, j = 1, \ldots, N$, $\Delta a = 1/N$, and the boundary conditions are implemented by substituting

$$\psi[i, N+1] \to e^{2\pi i(i-1)\Delta a + ik_{\xi_1}} \psi[i, 1], \quad \psi[i, 0] \to e^{-2\pi i(i-1)\Delta a - ik_{\xi_1}} \psi[i, N],$$

$$\psi[N+1, j] \to e^{-2\pi i(j-1)\Delta a + ik_{\xi_2}} \psi[1, j], \quad \psi[0, j] \to e^{2\pi i(j-1)\Delta a - ik_{\xi_2}} \psi[N, j]$$

and

$$\psi[i, N+1] \to e^{i(k_{\xi_1} + k_{\xi_2})} \psi[1, 1], \quad \psi[0, 0] \to e^{-i(k_{\xi_1} + k_{\xi_2})} \psi[N, N],$$

$$\psi[N+1, 0] \to e^{i(-k_{\xi_1} + k_{\xi_2})} \psi[1, N], \quad \psi[0, N+1] \to e^{i(k_{\xi_1} - k_{\xi_2})} \psi[N, 1]$$

with $\vec{k} \cdot \vec{R}_1 = \vec{k} \cdot a(1, 0)^T = k_{\xi_1}$ and $\vec{k} \cdot \vec{R}_2 = \vec{k} \cdot a(0, 1)^T = k_{\xi_2}$. The derivatives are approximated by a central difference scheme, which reads in affine coordinates

$$\nabla\psi[i, j] = \frac{1}{2\Delta a}(\psi[i, j+1] - \psi[i, j-1], \psi[i+1, j] - \psi[i-1, j])^T \tag{9.48}$$

$$\begin{aligned}
\Delta\psi[i, j] = \frac{1}{\Delta a^2}(&\hat{g}^{ab}[0, 0](\psi[i, j+1] - 2\psi[i, j] + \psi[i, j-1]) + \\
&\hat{g}^{ab}[1, 1](\psi[i+1, j] - 2\psi[i, j] + \psi[i-1, j]) + \\
&\frac{1}{2}\hat{g}^{ab}[0, 1](\psi[i+1, j+1] - \psi[i-1, j+1] \\
&- \psi[i+1, j-1] + \psi[i-1, j-1]))
\end{aligned} \tag{9.49}$$

10 Magnon Band Structure

10.1 Magnon Bands

The eigenvalue problem (9.42), (9.41) was solved for a grid of $\vec{k}$-vectors covering the first Brillouin zone (depicted in Fig. 10.2), taking a) just the emergent vector potential $\vec{A}$ and b) taking the total vector potential $\vec{A}_{\text{tot}} = \vec{A} + \vec{A}_{\text{DMI}}$ into account where the latter also includes the DMI contribution $\vec{A}_{\text{DMI}} = -\delta\hat{m}_0$. Thereby, the dynamics of magnons in a skyrmion lattice are modeled by the dynamics of a charged particle in the respective magnetic field: a) the emergent magnetic field $B = [\nabla \times \vec{A}]_z = B_u + B_p$ and b) the total, effective magnetic field $B_{\text{tot}} = [\nabla \times \vec{A}_{\text{tot}}]_z = B + B_{\text{DMI}} = B_u + B_p - D(\partial_x m_y - \partial_y m_x)$. They are displayed in Fig. 10.6, as we get back to them when discussing the classical dynamics in section 10.3.

For each $\vec{k}$, the eigenvalues $\omega(\vec{k})$ of the Hamiltonian in (9.42) were determined. They are displayed as magnon bands over the first Brillouin zone in Fig. 10.1: a) including just the emergent vector potential $\vec{A}$ and b) including the total vector potential $\vec{A}_{\text{tot}} = \vec{A} + \vec{A}_{\text{DMI}}$. Here, only the 14 lowest bands are shown to compare with the work by Waizner [168].

When including only the vector potential $\vec{A}_u$ of the uniform magnetic field B_u, the magnon bands form flat Landau levels at $\frac{\omega}{\omega_c} = n_L + \frac{1}{2}$, where $n_L = 0, 1, 2, \ldots$ counts the number of Landau levels. Each Landau level is double degenerated since the corresponding uniform magnetic field B_u generates two flux quanta (9.23) per Wigner-Seitz cell of the skyrmion lattice.

Including also the periodic vector potential $\vec{A}_p$, the degeneracy is lifted, and two distinct magnon bands form for each Landau level (see Fig. 10.1 a)). Including now also the DMI contribution effectively modifies the periodic vector potential, and thus the effective magnetic field magnons experience (see Fig. 10.6). The degeneracy is further lifted, but the bands are more curved, leading again to near-degenerate points (see Fig. 10.1 b)).

These results are compared to the magnon bands obtained previously by Waizner [168], solving the full Bogoliubov-de Gennes equation (8.6) in Fourier space. They are displayed (without accounting for dipolar interactions) in Fig. 10.1 c), where n is the band index, and C the Chern number of the respective magnon band. The bands 3, 5, and 6 were identified by Waizner [168] with the counterclockwise (CCW), breathing, and clockwise (CW) modes, respectively (see section 8.2). The energy axes are scaled to match the different dimensionless units using (9.19): e.g. $7 \cdot \frac{\sqrt{3}}{\pi}\left(\frac{k_{\text{skl}}}{k_h}\right)^2 \approx 3.6$.

The potential terms that were neglected in our high-energy approximation (see section 9.2) constitute scattering potentials, that may: a) introduce topologically trivial bands (with Chern number $C = 0$) among the topological bands ($C = 1$) originating from Landau levels, b) shift the magnon bands by a constant offset, and c) lead the hybridization and avoided crossings between adjacent modes.
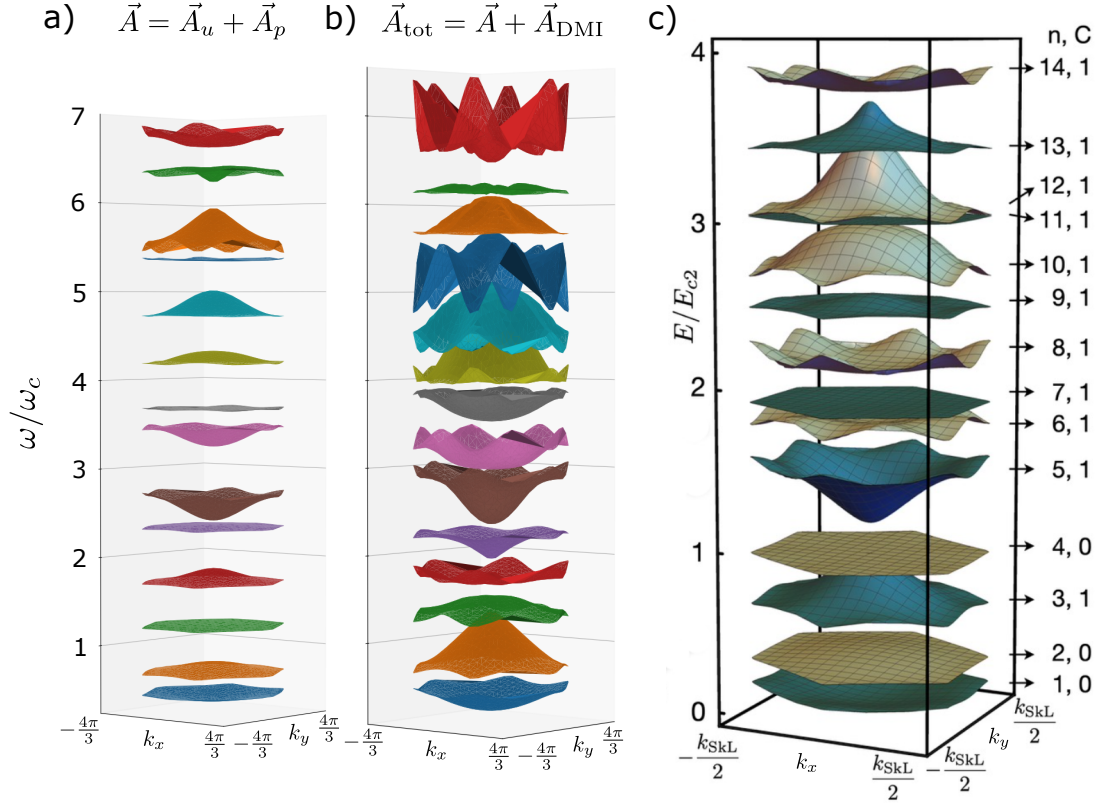
Figure 10.1.: 14 lowest Magnon bands plotted over the first Brillouin zone, a) including just the emergent vector potential $\vec{A}$ and b) including the total vector potential $\vec{A}_{\text{tot}} = \vec{A} + \vec{A}_{\text{DMI}}$. They are compared to the results by Waizner in d), solving the full Bogoliubov-de Gennes equation (8.6) in Fourier space (without dipolar interactions in this example). Here, n indicates the band index, and C the Chern number. The image was taken from [234].

The magnon bands may also be compared when plotted on a path through the high-symmetry points Γ, M, and K of the first Brillouin zone (see Fig.10.2). As before, the plot a) shows the magnon bands including just the emergent vector potential $\vec{A}$ and plot b) when including the total vector potential $\vec{A}_{\text{tot}} = \vec{A} + \vec{A}_{\text{DMI}}$. Red, dotted lines indicate the Landau levels induced by B_u, whose two-fold degeneracy was lifted through the periodic and DMI contributions to the total magnetic field. Nevertheless, the greater curvature induced by the DMI-term and leading to near-degenerate points is clearly visible.

They are compared to the results of Waizner [168] in plot d), which shows the lowest 16 magnon bands plotted along the same path. The axes were scaled to fit as in Fig. 10.1. Several modes can be directly related between plots b) and d): For example, the Goldstone mode (1) in plot d), is also reproduce as mode (1) in b), slightly shifted upwards, which is due to the scattering potentials that were neglected in our high-energy approximation. It features a quadratic dispersion around the Γ point, as the Berry phase contribution to the Lagrangian dominates over the kinetic term in this long-wavelength limit, and the otherwise linear spin-wave dispersion becomes quadratic for propagation within the skyrmion lattice plane [239].
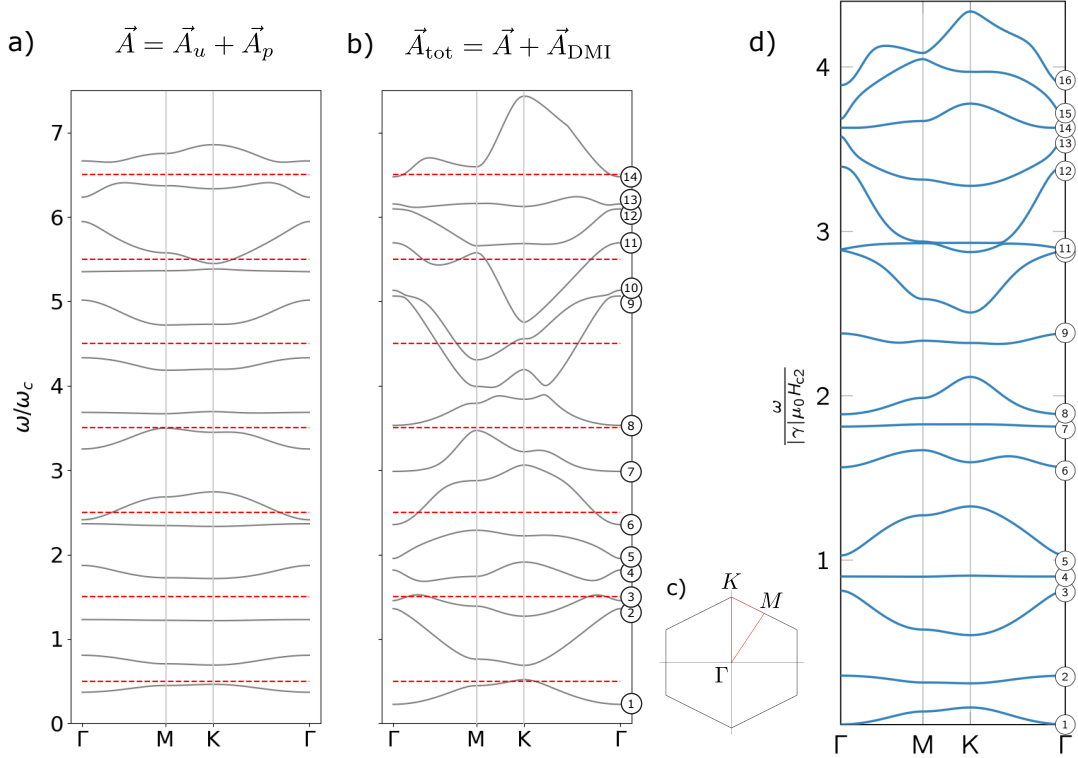
Figure 10.2.: Magnon bands plotted on a path through high-symmetry points of the first Brillouin zone as visualized by plot c): a) includes just the emergent vector potential $\vec{A}$ and b) includes the total vector potential $\vec{A}_{\text{tot}} = \vec{A} + \vec{A}_{\text{DMI}}$. The red, dotted lines indicate the Landau levels induced by B_u, whose two-fold degeneracy was lifted through the periodic and DMI contributions to the total magnetic field. The magnon bands are compared to the results by Waizner [168] in plot d), solving the full Bogoliubov-de Gennes equation (8.6) in Fourier space (without dipolar interactions in this example). The modes (2), (6), and (7) in b) correspond to the CCW (3), breathing (5), and CW (6) modes in d). The plot d) was taken from [168], all rights with Sebastian Waizner.

Mode (2) in b) is reminiscent of mode (3) in d) (CCW mode), mode (6) in b) resembles mode (5) in d) (breathing mode), and mode (7) in b) is qualitatively similar to mode (6) in d) (CW mode). Modes (8) and (9) seem to hybridize, corresponding to modes (8) and (10) in d). Mode (12) in b) is qualitatively similar to mode (12) in d), which hybridizes with mode(11) in d). And, finally, mode (14) in b) resembles mode (16) in d).

10.2 Extended Zone Scheme

In order to make a connection with the predicted and measured magnon spectra from Fig. 9.1 [234], we now go one step further and determine the magnon spectrum beyond the first Brillouin zone up to high energies. The result is shown in Fig. 10.3 for the first 100 magnon bands, a) including just the emergent vector potential $\vec{A}$ and b) including the total vector potential $\vec{A}_{\text{tot}} = \vec{A} + \vec{A}_{\text{DMI}}$. The $\vec{k}$-vector was chosen along in the direction
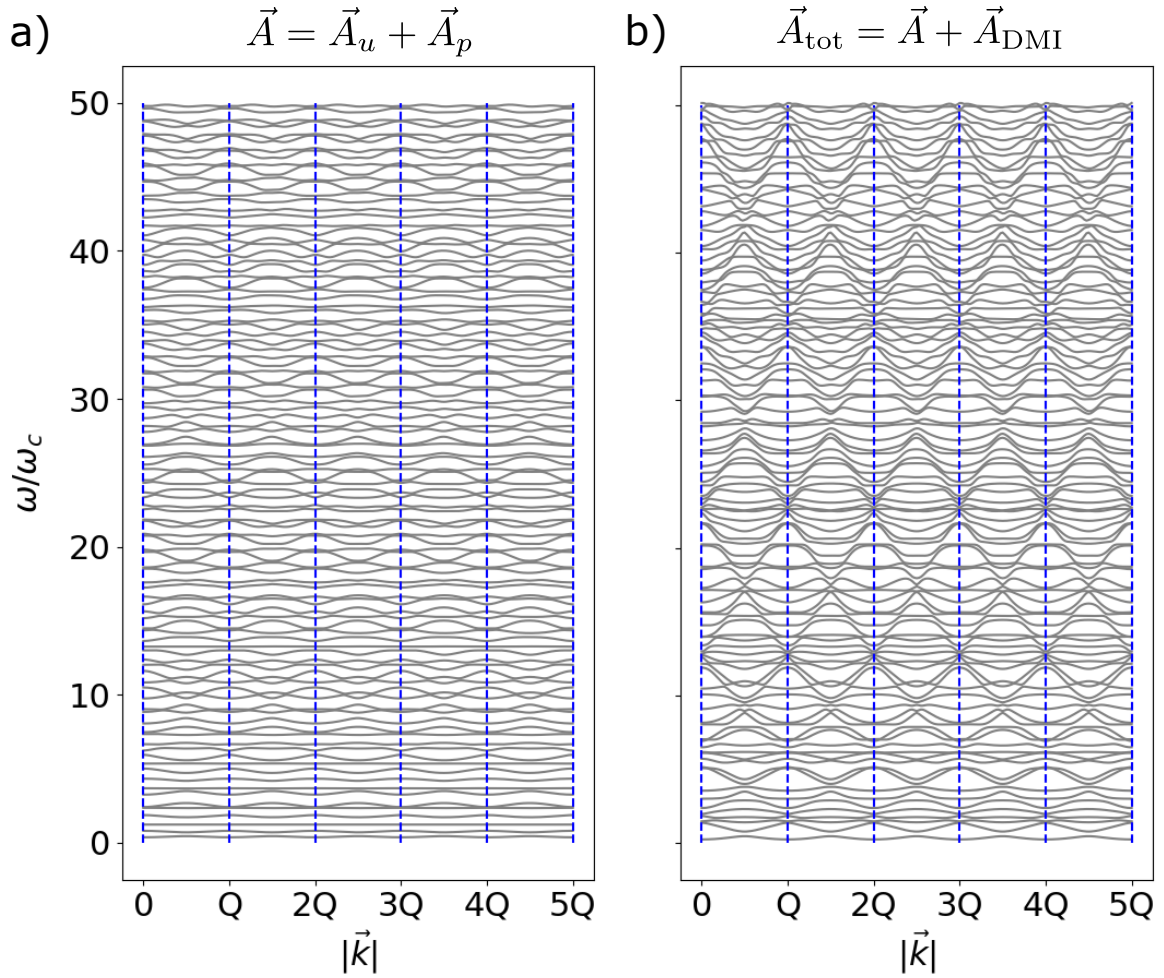
Figure 10.3.: Magnon spectrum in the direction from Γ to M over several Brillouin zones, a) including just the emergent vector potential $\vec{A}$ and b) including the total vector potential $\vec{A}_{\mathrm{tot}} = \vec{A} + \vec{A}_{\mathrm{DMI}}$. The DMI-contribution $\vec{A}_{\mathrm{DMI}}$ not only increases the curvature of the magnon bands, but it does so in a way that the magnon bands align to produce parabola-shaped superstructures, as shown in plot b). Compare with plot 12.7 of [168]

.

$\overrightarrow{\Gamma M}$, i.e. going from the Γ towards to M point and further over several Brillouin zones, where $Q = |\vec{g}^1| = \frac{4\pi}{\sqrt{3}}$ is the magnitude of a reciprocal lattice vector.

In both cases, the magnon spectrum extends, as expected, periodically over the range of Brillouin zones, where the fourteen lowest bands in plot a) and b) in the realm between 0 and $\frac{Q}{2}$ correspond to the magnon bands in the section between Γ and M in Fig. 10.2 a) and b), respectively. All crossings are avoided; especially for higher energies more avoided crossings occur. Comparing these results to the ones by Waizner [168], decent qualitative agreement can be found for $\omega/\omega_c > 10$, i.e. at high energies.

As Fig. 10.3 b) demonstrates, the DMI-contribution $\vec{A}_{\mathrm{DMI}}$ increases the curvature of the magnon bands so that they align in a way that parabola-shaped superstructures appear, when many magnon bands are plotted over many Brillouin zones. They are separated by exactly one reciprocal lattice vector, as one would expect for the empty lattice model, where a particle's wave function is required to fulfill the periodicity of an underlying lattice, but it is otherwise free to move (therefore 'empty lattice'). The parabola's become evident only above a certain energy threshold, which is of the order of $\omega \approx 10\,\omega_c$. It reproduces the parabola superstructures of the predicted magnon spectrum in Fig. 9.1 [234], and gives a first hint that they are originating due to the influence of the DMI.

In the next step, we fitted one of the emergent parabola superstructures, by manually selecting points on the various magnon bands that resembled the steepness of the emergent parabola. Then we applied a least-square fit for a parabola function, shown in red in Fig. 10.4. This resulting parabola corresponds to the dispersion of a free particle carrying the magnon mass (9.12), extracted from the parabola's steepness and accounting for the dimensionless units.

Then we selected various points at and nearby the parabola, green and red points in Fig. 10.4, to analyze the corresponding eigenfunctions: The red dots were chosen where the respective magnon band's steepness resembles the parabola fit; The green dots were chosen slightly of the parabola fit, where the respective magnon bands feature local minima, i.e. are locally flat. The numbers in the square labels indicate the band index of the magnon band at which the respective dot was chosen.

The absolute-value squared of the corresponding eigenfunction, i.e. the probability density, labeled by its band index number is displayed in Fig. 10.5; at the top left also the total magnetic field $B_{\mathrm{tot}} = B + B_{\mathrm{DMI}}$ is plotted as a reminder. The eigenfunctions plotted on the left (green dots/labels) are bound on the skyrmion position's (see number 6 and 28) or its direct surroundings (see number 14). At higher energies, they resembles the interference pattern of random superposition of plane waves (see number 33), which are proposed as a statistical model for describing the eigenfunctions of strongly chaotic systems [240]. It suggests that the corresponding classical dynamics is chaotic and the rational for this statistical model is that a typical classical chaotic trajectory comes close to every point in position space with random directions and 'random phase', i.e. after transversing different trajectory segments of different lengths.
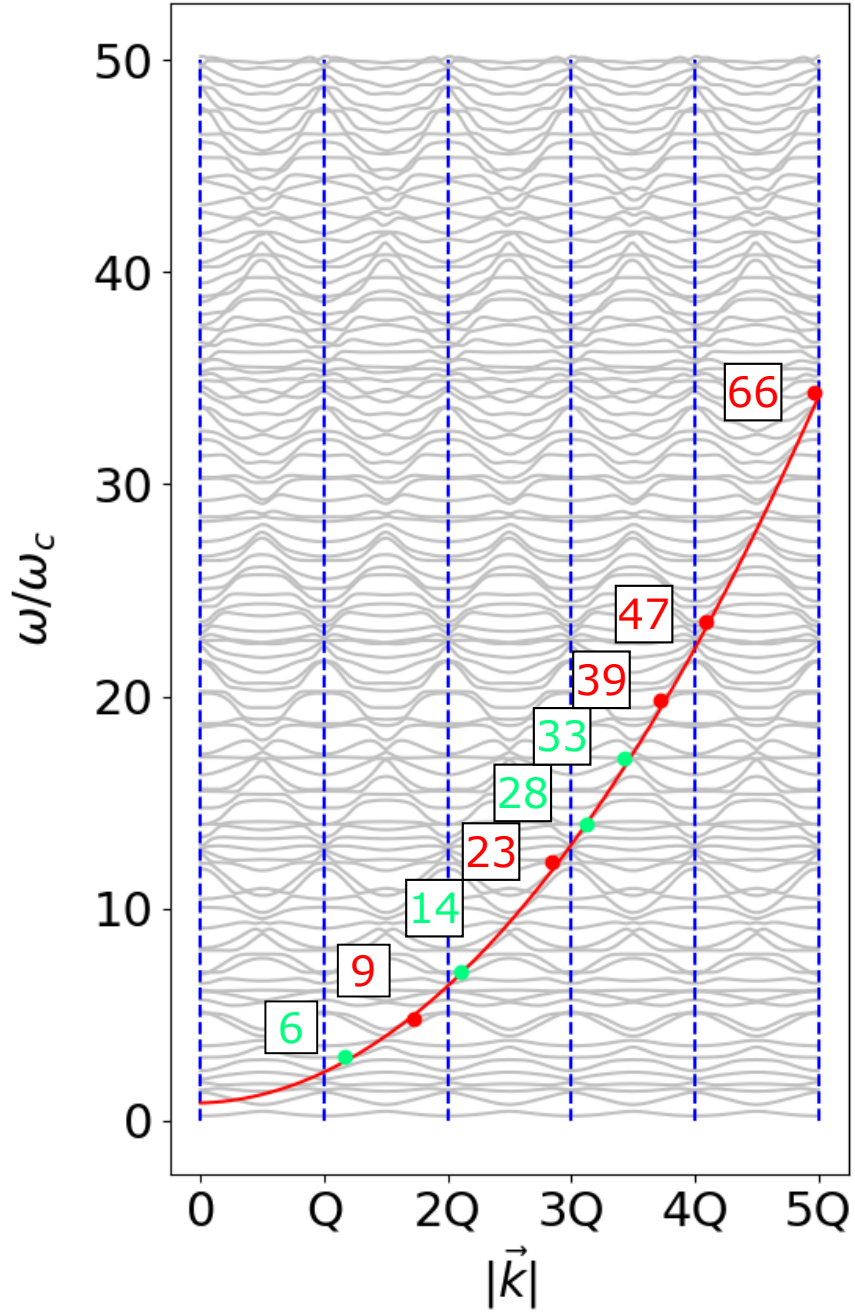
Figure 10.4.: Magnon spectrum in the direction from Γ to M over several Brillouin zones, including the total vector potential $\vec{A}_{\text{tot}} = \vec{A} + \vec{A}_{\text{DMI}}$: the appearing parabola-shaped superstructures were fitted manually; The resulting parabola (red) corresponds to the dispersion of a free particle carrying the magnon mass (9.12). At several points, marked by green and red dots, were the eigenfunctions analyzed and plotted in Fig. 10.5.
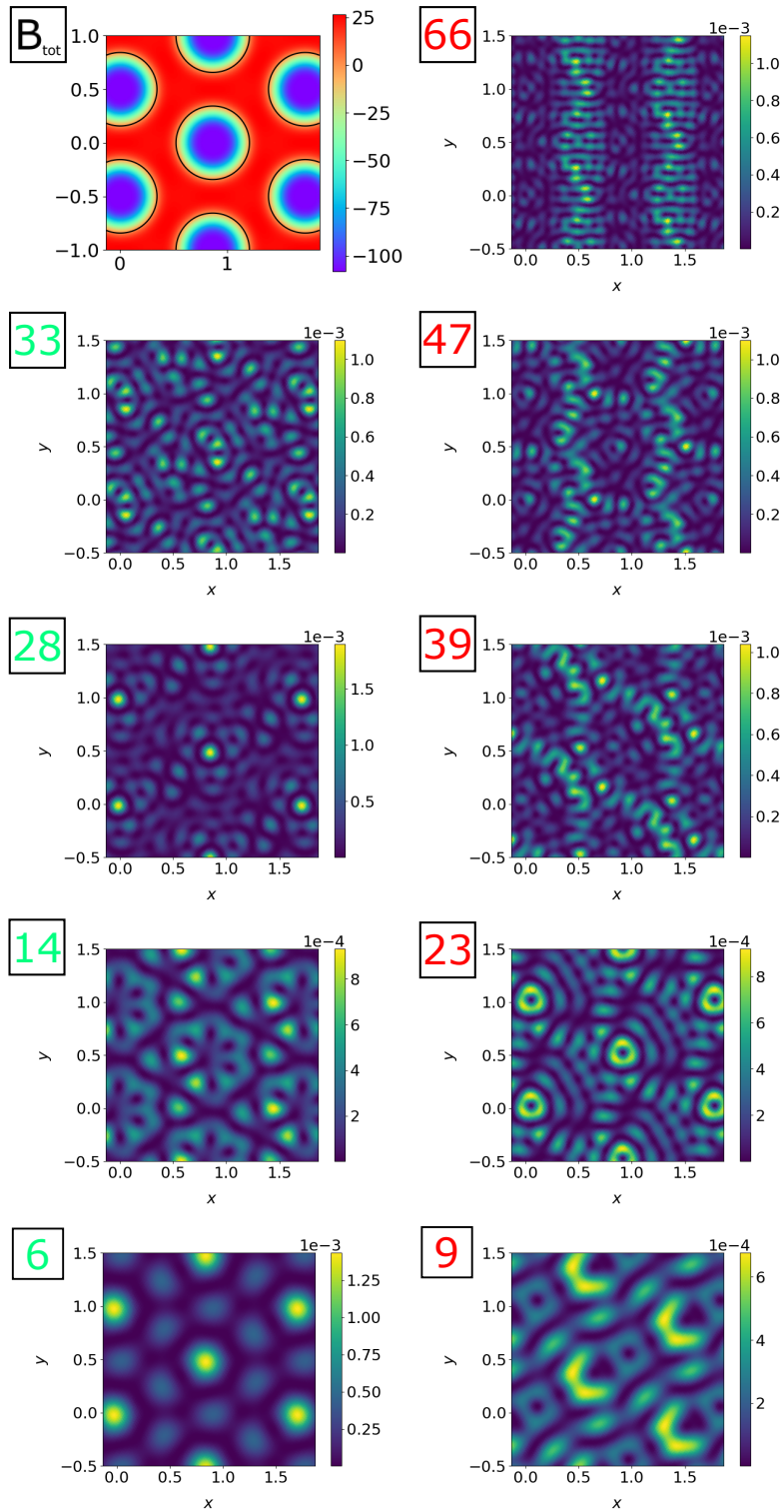
Figure 10.5.: Plots of the absolute value squared of magnon eigenfunctions, where the corresponding wave vector is marked by a green/red dot in Fig. 10.4, and the number corresponds to the band index of the respective magnon band. The red dots were chosen where the magnon band's steepness resembles the parabola, while green dots were chosen slightly off the parabola superstructure, where the magnon bands feature local minima. The total magnetic field $B_{\text{tot}} = B + B_{\text{DMI}}$ is plotted as a reminder at the top.

The eigenfunctions on the right (red dots/labels) were recorded where the magnon bands steepness matches the parabola-superstructures. They concentrate on curved trajectories between the skyrmions, orientated along either of the skyrmion lattice's three directions. At small energies, a decent portion of the eigenfunction's weight is focused at the skyrmion positions (see number 9 or 23). However, this changes as energy increases and eigenfunctions attribute more weight to curved paths skipping between the skyrmions (see number 47 and 66). This is reminiscent of a phenomena called 'scarring' [241–243]: eigenfunctions of mixed chaotic system [244] get enhanced in position space along unstable classical periodic orbits.

The Ehrenfest theorem describes how the expectation values of position and momentum of a particle moving in a scalar potential behave in the classical limit, i.e. that they fulfill the classical equations of motion up to quadratic order of the potential [245, 246]. The semiclassical eigenfunction hypothesis goes one step further, stating that eigenstates concentrate on those regions in phase space a generic classical orbit explores in the long-time limit [240, 247–249]. Thus, for integrable systems, motion is restricted to invariant tori in phase space, and for fully chaotic systems, it is equidistributed on the energy shell. It has been proven for fully chaotic systems [250–255] (a decent introduction is given by [256]), i.e. ergodic systems where spatial and temporal averages agree, by the quantum ergodicity theorem, which states that almost all eigenfunctions become uniformly distributed over phase space in the semiclassical limit.

Restricting ourselves to position space, it means that eigenfunctions focus on those areas in real space that classical trajectories explore in the limit of long times. Thus, it is sensible to also explore the underlying dynamics of the classical problem, a charged particle moving within the effective magnetic field generated by the skyrmion texture and modified by the DMI-contribution, which we present in section 10.3.

10.3 Classical Dynamics

Finally, we study the classical analogon to the quantum mechanical problem we solved in the previous section: the classical dynamics of a charged particle in the total, effective magnetic field $B_{\text{tot}} = B + B_{\text{DMI}} = B_u + B_p - D(\partial_x m_y - \partial_y m_x)$ (see Fig. 10.6 c)). The equations of motion derive from the Lorentz force $\vec{F} = q\vec{v} \times \vec{B}_{\text{tot}}$:

$$\ddot{\vec{r}}(t) = \dot{\vec{r}}(t) \times \vec{B}_{\text{tot}} \tag{10.1}$$

where $\vec{B}_{\text{tot}} = B_{\text{tot}}\hat{z}$, $\vec{v} = \dot{\vec{r}}$ is the velocity vector of the particle, and its mass m and charge q have been set to unity.

A similar problem has been already studied by Waizner [168], by building a model of the skyrmion lattice phase from a superposition of three helices of equal pitch that form a tripod with 120° angles and studying the classical dynamics in the emergent magnetic field of the resulting magnetization pattern. Crucially, only the emergent magnetic field has been taken into account (similar to Fig. 10.6 a)), which is dominated by a large negative magnetic flux through the skyrmions and a comparatively tiny positive flux in
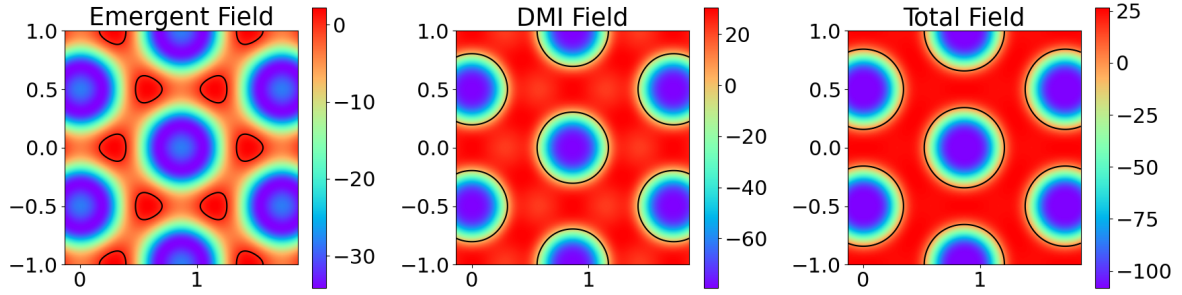
Figure 10.6.: a) Emergent magnetic field B, b) corresponding magnetic field of the DMI-contribution B_{DMI} for $\delta = 7.48$, and c) total magnetic field $B_{\mathrm{tot}} = B + B_{\mathrm{DMI}}$. The black contour lines indicate where the respective magnetic field vanishes.

between them. It means that the dynamics are also dominated by scattering off the skyrmion's magnetic flux, leading to circulating trajectories: the trajectories are bend always just counterclockwise, given a positive charge and the negative magnetic flux through a skyrmion. For special initial conditions, periodic loops are possible, although they may not be true circles. However, altering the initial conditions just slightly leads to chaotic orbits.

The DMI-contribution (see Fig. 10.6 b)) not only enhances the negative magnetic flux through the skyrmions, but it also drastically enhances the positive magnetic flux in between them. Thus, the resulting total magnetic field (see Fig. 10.6 c)) features both a significant positive and negative magnetic flux and bends a charged particle's trajectory not only counterclockwise but also clockwise. This is essential as it leads to completely different dynamics as compared to if only negative magnetic flux were present.

The uniform magnetic field, in rationalized units $B_u = -\frac{8\pi}{\sqrt{3}} \approx -14.51$, is small compared to the variation induced by B_p and B_{DMI}. This is similar to a Chern insulator, featuring broken time-reversal symmetry and topological energy bands despite that no net magnetic flux is present.

We determined the dynamics for ensembles of different initial conditions on the same energy shell, which was set by the total velocity $v = |\vec{v}|$. Due to the hexagonal symmetry of the Wigner-Seitz cell, it is sufficient to restrict oneself when choosing starting points to the triangle spanned by the three high-symmetry points of the Wigner-Seitz cell, i.e. the center point $(0,0)^T$, the top-most point $(0,1)^T$, and the point $(\frac{\sqrt{3}}{4}, \frac{3}{4})^T$ – in analogy to the Γ, K, and M points of the Brillouin zone (see Fig. 10.2 c)). Therefore, we overlayed a grid of 10×10 points with that part of the Wigner-Seitz cell and selected the 23 points lying within the latter. For each of these starting points and for each total velocity v, trajectories with $N = 10$ different initial velocity orientations $\vec{v} = v(\cos(\frac{2\pi \cdot n}{N}), \sin(\frac{2\pi \cdot n}{N}))^T$ with $n = 0, 1, \ldots, N-1$ were advanced for a time interval of $\Delta t = 10$, yielding in total $23 \times 10 = 230$ distinct orbits.

Some representative example trajectories from these ensembles are shown in Fig. 10.7. For a) $v = 4$, the orbits spend most of their time bound to a skyrmion, either bound entirely to a single skyrmion (examples 1) and 2)) or roaming between skyrmions (examples 3) and 4)). Following the semiclassical eigenfunction hypothesis [240, 247–249], these

orbits correspond to the bound magnon eigenfunctions, e.g. number 6 and 14 in Fig. 10.5.

For b) $v = 35$, there still exist orbits bound nearby a single skyrmion (example 1)). However, most orbits show chaotic behavior wandering between skyrmions, which corresponds to chaotic eigenfunction such as number 33 in Fig. 10.5, following the semiclassical eigenfunction hypothesis [240, 247–249]. Already here, it can be seen that orbits follow segments along either of the three directions of the skyrmion lattice over an extended distance, i.e. beyond a few Wigner-Seitz cells.
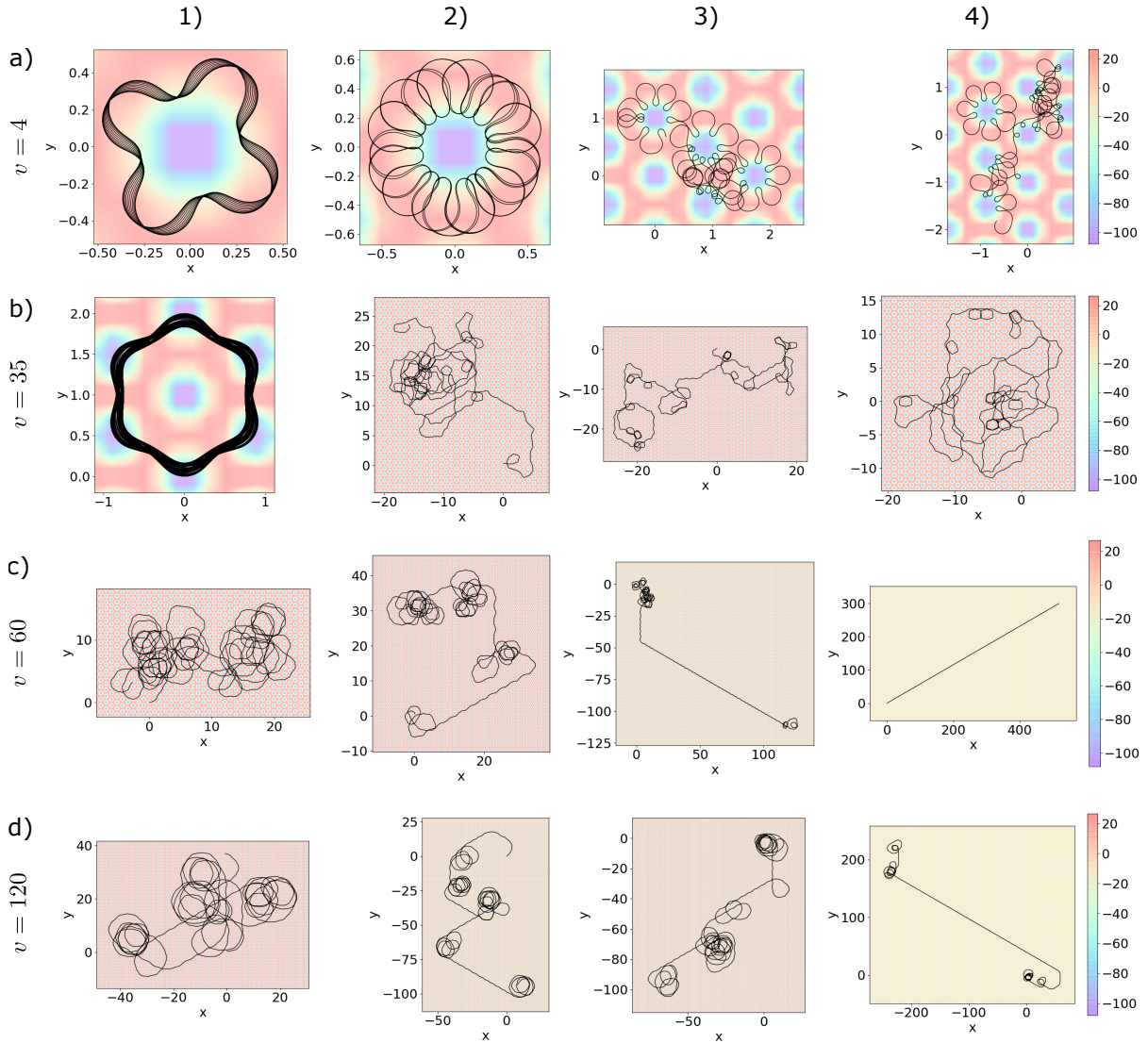
Figure 10.7.: Example trajectories in the total magnetic field $B_{\text{tot}} = B + B_{\text{DMI}}$, consisting of emergent magnetic field B from the topological skyrmion texture, and the contribution of DMI B_{DMI}. For each total velocity v, which sets the energy shell in momentum space four representative examples are shown that we starting at different positions within the Wigner-Seitz cell centered around the origin and for different orientations of the initial velocity. The various orbits are described in the main text.

This phenomenon gets even more pronounced at higher energies, e.g. for c) $v = 60$ or for d) $v = 120$. Magnons spent increasingly more time traveling in almost straight lines along either of the three skyrmion lattice's directions in between scattering events. The reason lies in the modulated magnetic field B_{tot}: while the negative magnetic flux at the skyrmion center bends orbits in a counterclockwise direction, the positive magnetic flux between them bends orbits in a clockwise direction. The influence of both may lead to an almost straight trajectory if an orbit passes a skyrmion with a suitable impact parameter, i.e. when the cyclotron semicircle with a skyrmion matches the cyclotron semicircle outside a skyrmion. This is either the case for very specific initial conditions but may also occur by chance as the result of a scattering event.

Following the semiclassical eigenfunction hypothesis [240, 247–249], eigenfunctions increasingly focus weight on these orbits skipping between skyrmions at higher energies, leading to the patterns observed in the plots on the right in Fig. 10.5. For small energies, still a lot of the eigenfunction's weight is bound to the skyrmion's positions, and only little weight focuses on orbits skipping between skyrmions (see eigenfunctions number 9 and 23 in Fig. 10.5). At higher energies, bound orbits become increasingly rare, and more of the weight is attributed to orbits skipping between skyrmions, which overlay like scars [241–243] a random eigenfunction pattern, originating from chaotic orbits (see eigenfunctions number 47 and 66 in Fig. 10.5).

The trajectories of charged particles traveling in a periodically modulated magnetic field have been already addressed before by Yoshida et al. [257–259] in the context of semiconductor antidot structures and their magnetoresistance. They also found that three types of orbits may occur: pinned orbits that stay bound, chaotic orbits, and so-called runaway orbits skipping through the periodically modulated magnetic field as explained above. The latter have a decisive influence on the peak structure of the magnetoresistance.

Here, runaway orbits can explain the parabola-shaped superstructures in the magnon spectrum: As eigenfunctions attribute weight on runaways orbits/segments following the semiclassical eigenfunction hypothesis [240, 247–249], they behave at high energies effectively like free particles skipping through the skyrmion lattice. As a result, the magnon bands bend at the respective $\vec{k}$-vectors in a way that superimposes the free particle's dispersion with the magnon spectrum, leading to the observed parabola-shaped superstructures.

For this, it is essential that the magnetic field is periodically modulated and sign-alternating since only then runaway orbits may occur. Without the DMI-contribution, no runaway orbits can form in our system, and thus no parabola superstructures occur in the magnon spectrum (see Fig. 10.3). Vice versa, we also calculated for testing purposes the magnon spectrum taking just the periodic vector potential $\vec{A}_p$ into account and observed light parabola superstructures in the magnon spectrum (not shown here). They get more pronounced as the magnetic field's modulation gets enhanced toward positive and negative values by the DMI contribution.

Getting back to the classical dynamics, one can, after all, also characterize the general ensemble behavior by the mean-square displacement $\langle r^2 \rangle$, i.e. were the distance to the origin $r = |\vec{r}(t)|$ squared has been averaged over the entire ensemble of 230 trajectories for a given total velocity v. The results are plotted as a blue line in Fig. 10.8, and they
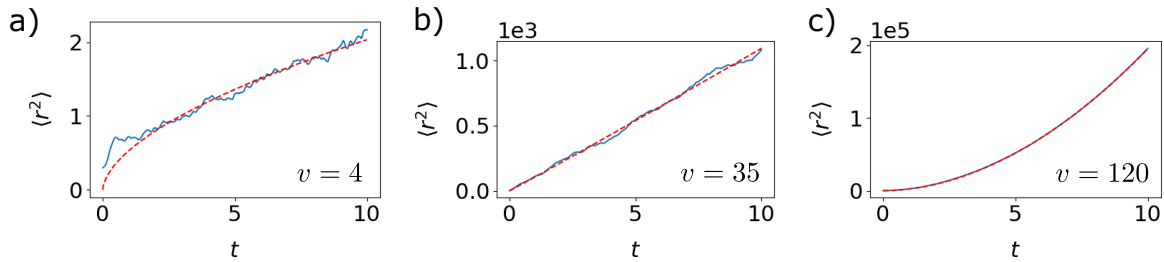
Figure 10.8.: Mean-square displacement (blue) for an ensemble of 230 trajectories as described in the main text. The results were fitted by a power law (red dashed line), which indicates a) subdiffusive behavior at low energies, b) diffusive behavior in a medium range of energies, and c) superdiffusive behavior at high energies.

were fitted by a power-law $f(t) = a \cdot t^b$ (dashed red line).

At small energies, e.g. for small total velocity $v = 4$ in plot a), the mean-square displacement shows subdiffusive behavior ($a = 0.535$, $b = 0.58$), as the exponent $b < 1$ and orbits spend most of their time bound to a skyrmion. The data in the time interval $0 \leq t \leq 1$ has been excluded when obtaining the fit, as the trajectories start at different positions within the Wigner-Seitz cell of the skyrmion lattice, which leads to an initial offset that has been excluded this way. It has been ignored for larger velocities, as orbits do not spend significant time transversing a single Wigner-Seitz cell.

In a medium range of energies, e.g. at total velocity $v = 35$ in plot b), the orbits show diffusive behavior ($a = 104$, $b = 1.02$) as the mean-square displacement is increasing linearly. Some periodic orbits exist that stay near a single skyrmion. However, a slight change in the initial conditions leads to chaotic orbits that spend the majority of their time diffusing between skyrmions.

At high energies, e.g. at a total velocity of $v = 60$ ($a = 1071$, $b = 1.79$) or $v = 120$ in plot c) ($a = 2387$, $b = 1.91$) the orbits feature super-diffusive behavior as $b > 1$ and the mean-square displacement becomes increasingly quadratic for higher energies. The reason is that orbits spend increasingly more time on runaway sections in between scattering events as in the case of a Levy flight, i.e. effectively behaving like a free particle. Still, a stays at a fraction of v^2, because of scattering events and because runaway segments may follow different directions of the skyrmion lattice after scattering events.

11 Summary & Outlook

In summary, we developed a semiclassical explanation for the parabola-shaped superstructures occurring as the energy bands of magnons traversing a skyrmion lattice coalesce at high energies.

Magnons in a chiral magnet are described by a Bogoliubov-de Gennes equation (8.6), which becomes in a high-energy approximation the Schrödinger equation for a charged particle in the emergent magnetic field of the chiral magnet's texture. The emergent magnetic field of the skyrmion lattice texture is characterized by a total magnetic flux of two flux quanta per unit cell. Hence, it can be decomposed into a uniform and a periodic component. While the uniform component leads to double degenerate energy bands and non-uniform boundary conditions, the periodic component lifts the degeneracy and bends the magnon bands. To account for the non-constant boundary conditions, we have implemented our own finite difference scheme for solving the Schrödinger equation and obtaining the magnon energy bands. All bands are expected to be topological, i.e. carry a Chern number of one, which could be verified by future research.

Our results are compared to previous work by Waizner [168] on the full Bogoliubov-de Gennes problem (8.6), who determined the magnon energy spectrum of a skyrmion lattice in Fourier space. As only a limited amount of Fourier components could thereby be taken into account, the spectrum was obtained only for low- to medium-range energies. In contrast, we could obtain the energy spectrum within a high-energy approximation in real space, even up to very high energies.

No parabola-shaped superstructures occur when taking into account only the emergent magnetic field stemming from the exchange interaction. Only when also considering the effect of the DM interaction, the parabola-shaped superstructures could be reproduced that were observed in previous calculations solving the full Bogoliubov-de Gennes equation in Fourier space. The reason for this will become clear below.

Applying a parabola fit to the magnon spectrum featuring those superstructures suggests that the magnon must effectively traverse the skyrmion lattice like free particles, carry exactly the previously determined magnon mass (9.12).

Plotting the magnon eigenfunctions at energy value lying exactly on those parabola-shaped superstructures reveals that they indeed focus on curved paths connecting neighboring skyrmions. Vice versa, eigenfunctions plotted at energies slightly of the parabola-shaped superstructures are either localized or bound to the skyrmion's positions or showing chaotic distributions.

This gave a strong motivation to last but not least investigate the classical dynamics of charged particles moving in the emergent magnetic field of the skyrmion lattice, modified by the influence of the DM interaction. It constitutes a Hamiltonian dynamical system, where the energy shell is set by the magnitude of the initial velocity. The classical dynamics within a periodic, sign-alternating magnetic field had also been determined previously in the context of semiconductor antidot structures, and their magnetoresistance by Yoshida et al. [257–259]. Three different types of dynamics can be observed: pinned

orbits that stay bound to a single skyrmion, chaotic orbits scattering between skyrmion, and so-called runaway orbits skipping between different skyrmions due to the periodic modulation of the magnetic field.

Those runaway orbits only occur if the periodic magnetic field is sign-alternating, i.e. only if the influence of the DM interaction is accounted for, as the orbits need to 'bend back' to skip between adjacent skyrmions. Moreover, those runaway orbits give a semi-classical explanation for the parabola-shaped superstructures occurring in the magnon energy spectrum: Following the semiclassical eigenfunction hypothesis [240, 247–249], eigenfunction at energies lying on those parabolas attribute their weight to those runaway orbits and thus behave at high energies like free particles. Like so-called scars in chaotic quantum systems [241–243], occurring at classically unstable orbits.

Also, the behavior of an ensemble of classical trajectories changes from subdiffusive to diffusive to superdiffusive when increasing the kinetic energy, i.e. more time is spent on runaway orbits, and thus more weight of the magnon eigenfunctions is attributed to those. Consequently, the free particle's dispersion gets superimposed on the magnon band spectrum, leading to the observed parabola-shaped superstructures. Future research may further investigate the levy flight-type, superdiffusive classical dynamics at high energies.

The theoretical prediction for the unpolarized, time-of-flight neutron scattering data (see Fig.9.1) shows that most of the spectral weight is focused at the parabola-shaped superstructures. An intuitive explanation would be that the incoming plane wave function of the neutrons has a greater overlap with the runaway magnon eigenfunctions as compared to the bound or chaotic magnon eigenfunctions, which would need to be investigated in further studies. The runaway magnon states may be used as magnon waveguides, e.g. for applications in magnon computing.

Part III

Chaotic Spin-Torque Nano-Oscillator

12 Introduction to Spin–Torque Nano–Oscillators

Spin currents within a (ferro-)magnetic material exert a spin-transfer torque on the individual magnetic moments [89, 260], and thus compensate magnetic damping and may induce magnetic dynamics. This can lead to either magnetization switching [261–264], which could be employed e.g. for writing processes in memory storage devices, or an oscillation of the magnetization [265–271]. The latter case constitutes a so-called spin-torque oscillator [272, 273] and may, for example, enable the generation of ac signals from dc currents. It may also serve as the building block for various spintronic devices, such as memory elements, field detectors, or microwave generators [274, 275].

Finally, spin-torque oscillators are of interest to neuromorphic computing, which mimics the brains' architecture by means of hardware components [276, 277]: processing units ('neurons') are linked by memory units ('synapses') and emulate a neural network by hardware design. Since actual neurons in the brain fire in rhythmic intervals, various types of non-linear nano-oscillators are considered for building an artificial neuron [278–280]. Among these, spin-torque oscillators are particularly interesting since their dynamical regime can be tuned easily by a dc current. It was already shown in experiments that they can emulate a single neuron [279], or a small neural network [281].

There are different concepts to realize neuromorphic computing based on stochastic (chaotic) oscillator behavior, such as reservoir computing [279, 282–286], spike-based encoding [277, 287–289], and stochastic computing [290, 291].

Chaotic behavior of spin-torque oscillators [290, 292–294] or textures such as merons [295] has been observed before, and its control is crucial for applications.

While ferromagnetic spin-torque oscillators feature output frequencies in the megahertz to gigahertz regime, the typical eigenfrequencies of antiferromagnets are in the terahertz regime [296, 297]. This allows for a much faster operation of antiferromagnetic spin-torque oscillators, enabling the realization of ultra-fast artificial neurons [287]. Antiferromagnets also feature a range of qualities that make them amenable for spintronic applications [298]: insensitivity to magnetic fields, the absence of a skyrmion Hall effect [129, 133, 299], and the presence of the spin Hall effect [300–303]. The latter is employed to generate spin-transfer torques even though most antiferromagnets are insulators. This provides means for building low-dissipation spin Hall nano-oscillators (SHNOs) [126, 304–312].

One of the simplest setups for a spin-torque oscillator is a collinear antiferromagnet (AFM) driven by a spin current, which is essentially a non-linear system with a four-dimensional phase space [304, 313]. This makes such AFM nano-oscillators a natural candidate for the appearance of chaos, a possibility which was recently pointed out by [314]. This project investigates a specific model for such an AFM spin-torque oscillator and shows that it exhibits chaos over a broad range of magnetic fields and spin current strengths.

12.1 Micromagnetic Description of Spin-Transfer Torque

While electrical currents are a flow of charge, spin currents are the flow of electron spin. They occur, for example, when an electrical current is spin-polarized so that all the electron spins point up and charge and spin flow take place at the same time in the same direction. However, spin currents may also occur without any net charge moving around – consider, for example, an electrical current with spin-up polarization in one direction and an electrical current of equal strength and spin-down polarization in the opposite direction, as it is the case for the spin Hall effect (SHE) [303, 315–317].

When a spin current transverses a magnetic material whose magnetization is misaligned with the spin current polarization, the spin current exerts a so-called spin-transfer torque on the material's magnetization. Its microscopic origin is the exchange interaction between conducting spin-polarized electrons (typically s-electrons) and electrons localized on the magnetic atoms of the material (typically in d- or f-orbitals) [318].

In order to generate a spin current in practice, usually, a magnetic multilayer structure is used, consisting of a ferromagnetic layer (also called fixed layer), a metallic/insulating spacer, and another magnetic layer (also called free layer), whose magnetization dynamics will be investigated under the influence of the spin current's torque.

As shown by Slonczewski in 2002 [319], the spin accumulation at the interface of the magnet and nonmagnetic spacer influence the spin-transfer torque (equation (31) in [319], where the difference in electrical resistance at the interface enters through some coefficient λ in the denominator).

In a simplified, micromagnetic picture [320] the spin accumulation $\vec{s}$ adds a contribution to the effective magnetic field $\vec{h}_{\text{eff}} = -\frac{\delta F}{\delta \hat{m}}$ in the Landau-Lifshitz-Gilbert equation (LLG), capturing the dynamics of the free layer magnetization $\hat{m}$

$$\frac{\partial \hat{m}}{\partial t} = -\gamma \hat{m} \times \left(\vec{h}_{\text{eff}} + \frac{J}{\hbar \gamma M_s} \vec{s} \right) + \bar{\alpha} \, \hat{m} \times \frac{\partial \hat{m}}{\partial t} \tag{12.1}$$

with $|\hat{m}| = 1$, the gyromagnetic ratio γ, the Gilbert damping $\bar{\alpha}$, and the exchange strength J between conducting electrons and the magnetization.

The spin accumulation can be expressed in terms of the spin current polarization $\hat{p}$ and the magnetization $\hat{m}$ [320]

$$\vec{s} = a \, \hat{p} \times \hat{m} + b \, (\hat{m} \times \hat{p}) \times \hat{m} + c \, \hat{m} \tag{12.2}$$

which, inserted into the LLG equation, and due to $|\hat{m}| = 1$, results in

$$\frac{\partial \hat{m}}{\partial t} = -\gamma \hat{m} \times \left(\vec{h}_{\text{eff}} + \frac{Jb}{\hbar \gamma M_s} \hat{p} \right) - \hat{m} \times \left(\frac{Ja}{\hbar M_s} \hat{p} \times \hat{m} \right) + \bar{\alpha} \, \hat{m} \times \frac{\partial \hat{m}}{\partial t} \tag{12.3}$$

The first term (with coefficient b) added to the effective magnetic field $\vec{h}_{\text{eff}}$ is called field-like torque. It is usually quite small and will be neglected in our model. The second term (with the coefficient a) is called damping-like torque or spin-transfer torque. Inserting this spin-transfer torque directly into the LLG equation is based on a few assumptions [318] that need to be kept in mind:

a) All the angular momentum transferred from the spin current acts only to reorient the free layer magnetization rather than, for example, to excite short-wavelength magnon modes (in out-of-plane direction) or being transferred to the crystal lattice. With respect to experiments, this seems to be a reasonable approximation.

b) The sign of the spin-transfer torque is important: the spin-transfer torque should enter the LLG equation with a sign opposite to the change in angular momentum, i.e. it should rotate the magnetization of the free layer into the direction of the spin current polarization.

c) Any orbital contribution to the spin-transfer torque is neglected, which may also be a reasonable approximation since orbital moments are typically less than one-tenth of the spin moment, as indicated by the deviation of the Landé g-factor from 2. This is also briefly discussed in [321]

12.2 Nano-Oscillator Model

In this project, we consider a thin-film, uniaxial antiferromagnet, where the magnetic easy-axis is aligned with the surface normal $\hat{n} = \hat{z}$, and the system is driven by a spin current with polarization $\hat{p} = \hat{y}$. We will consider the limit of strong exchange interaction so that the Néel vector (antiferromagnetic order parameter) $\hat{l}$ can be considered as a unit vector $|\hat{l}| = 1$. We denote it for this project by $\hat{l}$, since $\hat{n}$ is reserved for the orientation of the easy-axis.

Based on the corresponding LLG equation (12.3), in appendix E the equations of motion for the Néel vector $\hat{l}$ were derived, which can be regarded as Euler-Lagrange equations stemming from the model (based on [177, 313, 322, 323]):

$$\mathcal{L} = \frac{M_s}{\gamma^2 H_{\text{ex}}} \dot{\hat{l}}^2 - \frac{1}{\gamma H_{\text{ex}}} (\vec{H} \cdot [\hat{l} \times \dot{\hat{l}}]) + \frac{M_s}{H_{\text{ex}}} [\hat{l} \times \vec{H}]^2 - \mathcal{F}_{\text{stat}}(\hat{l}) \tag{12.4}$$

$$\mathcal{R} = \frac{\alpha M_s}{\gamma} \dot{\hat{l}}^2 - \frac{\sigma j M_s}{\gamma} (\hat{p} \cdot [\hat{l} \times \dot{\hat{l}}]) \tag{12.5}$$

where $\mathcal{F}_{\text{stat}}(\vec{l})$ is the static free energy density, $\mathcal{R}$ is the Rayleigh dissipation density function, L is the film thickness, A the exchange stiffness, $H_{\text{ex}} M_s$ is the strength of antiferromagnetic exchange, $K_z = M_s H_{\text{an}}$ the strength of uniaxial anisotropy and the

sum convention applies for the index i. The free energy functional of this is given by

$$F = L \int \mathrm{d}^2r \; \mathcal{F}_{\text{stat}}(\vec{l}) = L \int \mathrm{d}^2r \left[A(\partial_i \hat{l} \cdot \partial_i \hat{l}) - M_s H_{\text{an}}(\hat{l} \cdot \hat{n})^2 \right] \qquad (12.6)$$

which determines the ground state configuration .

Dimensionless Units

Next, we introduce dimensionless units according to table 12.1, which are chosen like in [177]. We start with the Lagrangian

$$\mathcal{L} = \frac{M_s}{H_{\text{ex}}} \left(\frac{1}{\gamma} \dot{\hat{l}} - [\vec{H} \times \hat{l}] \right)^2 - A(\partial_i \hat{l} \cdot \partial_i \hat{l}) + M_s H_{\text{an}}(\hat{l} \cdot \hat{n})^2 \qquad (12.7)$$

and make the switch to dimensionless lengths (highlighted below in blue)

$$\vec{\rho} = \vec{r}/l = \sqrt{\frac{H_{\text{an}} M_s}{A}} r, \quad \nabla_\rho = \sqrt{\frac{A}{H_{\text{an}} M_s}} \nabla_r \qquad (12.8)$$

resulting in

$$\mathcal{L} = \frac{M_s}{H_{\text{ex}}} \left(\frac{1}{\gamma} \dot{\hat{l}} - [\vec{H} \times \hat{l}] \right)^2 - A \frac{H_{\text{an}} M_s}{A} (\partial_i \hat{l} \cdot \partial_i \hat{l}) + M_s H_{\text{an}}(\hat{l} \cdot \hat{n})^2 \qquad (12.9)$$

Next, switching to dimensionless time and dimensionless magnetic fields

$$\tau = \gamma \sqrt{H_{\text{an}} H_{\text{ex}}} t, \quad \vec{h} = \vec{H}/\sqrt{H_{\text{an}} H_{\text{ex}}} \qquad (12.10)$$

leads to

$$\mathcal{L} = \frac{M_s}{H_{\text{ex}}} \left(\frac{1}{\gamma} \gamma \sqrt{H_{\text{an}} H_{\text{ex}}} \dot{\hat{l}} - \sqrt{H_{\text{an}} H_{\text{ex}}} [\vec{h} \times \hat{l}] \right)^2 - H_{\text{an}} M_s(\partial_i \hat{l} \cdot \partial_i \hat{l}) + M_s H_{\text{an}}(\hat{l} \cdot \hat{n})^2 \; (12.11)$$

and, finally, we obtain

$$\mathcal{L} = M_s H_{\text{an}} \left(\left(\dot{\hat{l}} - [\vec{h} \times \hat{l}] \right)^2 - (\partial_i \hat{l} \cdot \partial_i \hat{l}) + (\hat{l} \cdot \hat{n})^2 \right) \qquad (12.12)$$

Table 12.1.: Dimensionless units

Notation	Dimensionless Quantity	Unit of Measurement	Physical Meaning
$\vec{h} = \vec{H}/H_{sf}$	Magnetic field	$H_{sf} = \sqrt{H_{\mathrm{an}}H_{\mathrm{ex}}}$	Spin-flop field
$\tau = t\omega_{\mathrm{AFMR}}$	Time	$\omega_{\mathrm{AFMR}} = \gamma\sqrt{H_{\mathrm{an}}H_{\mathrm{ex}}}$	Uniform AFM resonance
$\vec{\rho} = \vec{r}/l$	Length	$l = \sqrt{A/(H_{\mathrm{an}}M_s)}$	Domain wall width
$\vec{l} = (\vec{M}_1 - \vec{M}_2)/M_0$	Néel vector	$M_0 = 2M_s$	Saturation magnetization
$\alpha = \bar{\alpha}/\xi$	Damping Constant	$\xi = \sqrt{H_{\mathrm{an}}/H_{\mathrm{ex}}}$	Expansion parameter
$j = J/J_0$	Current	$J_0 = \gamma H_{\mathrm{an}}/\sigma$	Spin Current

Switching to dimensionless time yields for the dissipation density function

$$\mathcal{R} = \frac{\bar{\alpha}M_s}{\gamma}\gamma^2 H_{\mathrm{an}}H_{\mathrm{ex}}\dot{\vec{l}}^2 - \frac{\sigma j M_s}{\gamma}\gamma\sqrt{H_{\mathrm{an}}H_{\mathrm{ex}}}(\hat{p}\cdot[\hat{l}\times\dot{\hat{l}}]) \tag{12.13}$$

and introducing a dimensionless current and a dimensionless damping constant

$$\mathcal{R} = \underbrace{\frac{\bar{\alpha}H_{\mathrm{ex}}\gamma}{\gamma\sqrt{H_{\mathrm{ex}}H_{\mathrm{an}}}}}_{=\alpha}\,\gamma\sqrt{H_{\mathrm{ex}}H_{\mathrm{an}}}H_{\mathrm{an}}M_s\dot{\vec{l}}^2$$

$$-J\underbrace{\frac{\sigma\sqrt{\frac{H_{\mathrm{ex}}}{H_{\mathrm{an}}}}}{\gamma\sqrt{H_{\mathrm{ex}}H_{\mathrm{an}}}}}_{=j}\,\gamma\sqrt{H_{\mathrm{ex}}H_{\mathrm{an}}}H_{\mathrm{an}}M_s(\hat{p}\cdot[\hat{l}\times\dot{\hat{l}}]) \tag{12.14}$$

leads to

$$\mathcal{R} = \gamma\sqrt{H_{\mathrm{an}}H_{\mathrm{ex}}}M_s H_{\mathrm{an}}\left(\alpha\dot{\vec{l}}^2 - j(\hat{p}\cdot[\hat{l}\times\dot{\hat{l}}])\right) \tag{12.15}$$

The staggered order parameter may be accompanied by a small, induced magnetization

$\vec{m}$ that reads in dimensionless units

$$\vec{m} = \frac{\dot{\vec{l}} \times \vec{l}}{\gamma H_{\text{ex}}} + \frac{\vec{l} \times (\vec{H} \times \vec{l})}{H_{\text{ex}}} = \frac{\gamma \sqrt{H_{\text{an}} H_{\text{ex}}} \, \dot{\vec{l}} \times \vec{l}}{\gamma H_{\text{ex}}} + \frac{\vec{l} \times (\sqrt{H_{\text{an}} H_{\text{ex}}} \, \vec{h} \times \vec{l})}{H_{\text{ex}}}$$

$$= \xi \left(\dot{\vec{l}} \times \vec{l} + \vec{l} \times (\vec{h} \times \vec{l}) \right) \tag{12.16}$$

The Lagrangian and the Rayleigh dissipation function finally assume in dimensionless units the form

$$\mathcal{L} = \left[\dot{\vec{l}} - (\vec{h} \times \vec{l}) \right]^2 - \mathcal{E}, \quad \mathcal{E} = \sum_{i=x,y,z} (\nabla l_i)^2 - (\vec{l} \cdot \hat{n})^2 \tag{12.17}$$

$$\mathcal{R} = \alpha \dot{\vec{l}}^2 - j\hat{p} \cdot (\vec{l} \times \dot{\vec{l}}) \tag{12.18}$$

They determine the equations of motion

$$\left(\frac{\delta L}{\delta \vec{l}} - \frac{\partial}{\partial t} \frac{\delta L}{\delta \dot{\vec{l}}} - \frac{\delta R}{\delta \dot{\vec{l}}} \right) \times \vec{l} = \vec{0} \tag{12.19}$$

where $L = \int \mathrm{d}^3 r \, \mathcal{L}$ and $R = \int \mathrm{d}^3 r \, \mathcal{R}$ are the Lagrange and Rayleigh functions, respectively. They takes the form (E.26) for the staggered order parameter $\hat{l}$. As we consider the free layer of our nano-oscillator to be deep within the antiferromagnetic phase we have $|\hat{l}| = 1$ and it is convenient to enforce this constraint using spherical coordinates, rather than solving (E.26) directly.

Spherical Coordinates & Equations of Motion

In the following, we consider the special case $\vec{h} = h\hat{z}$, $\hat{n} = \hat{z}$ and $\hat{p} = \hat{y}$ as introduced above. Using the spherical parameterization $\vec{l} = \sin(\theta) (\cos(\phi)\hat{x} + \sin(\phi)\hat{y}) + \cos(\theta)\hat{z}$, one obtains for the Lagrangian

$$\mathcal{L} = \dot{\theta}^2 + \sin^2(\theta) \left(\dot{\phi} - h \right)^2 - \mathcal{E}, \quad \mathcal{E} = (\nabla\theta)^2 + \sin^2(\theta) \left[1 + (\nabla\phi)^2 \right] \tag{12.20}$$

and for the dissipation density

$$\mathcal{R} = \alpha \left(\dot{\theta}^2 + \sin^2(\theta)\dot{\phi}^2 \right) - j \left(\dot{\theta} \cos(\phi) - \dot{\phi}\sin(\theta)\cos(\theta)\sin(\phi) \right) \tag{12.21}$$

The equations of motion for our model are now determined from

$$\frac{\partial \mathcal{L}}{\partial \theta} - \partial_i \frac{\partial \mathcal{L}}{\partial(\partial_i \theta)} - \partial_t \frac{\partial \mathcal{L}}{\partial \dot{\theta}} - \frac{\partial \mathcal{R}}{\partial \dot{\theta}} \stackrel{!}{=} 0 = 2\sin(\theta)\cos(\theta)\left(\dot{\phi} - h\right)^2$$

$$- 2\sin(\theta)\cos(\theta)\left[1 + (\nabla\phi)^2\right] - 2\nabla\cdot(-\nabla\theta) - 2\partial_t\dot{\theta} - 2\alpha\dot{\theta} + j\cos(\phi) \tag{12.22}$$

leading to

$$\sin(\theta)\cos(\theta)\left[1 + (\nabla\phi)^2 - \left(\dot{\phi} - h\right)^2\right] - \Delta\theta + \ddot{\theta} + \alpha\dot{\theta} = \frac{j}{2}\cos(\phi) \tag{12.23}$$

and

$$\frac{\partial \mathcal{L}}{\partial \phi} - \partial_i \frac{\partial \mathcal{L}}{\partial(\partial_i \phi)} - \partial_t \frac{\partial \mathcal{L}}{\partial \dot{\phi}} - \frac{\partial \mathcal{R}}{\partial \dot{\phi}} \stackrel{!}{=} 0 = -2\nabla\cdot\left[-\nabla\phi\sin^2(\theta)\right]$$

$$- \partial_t\left(2\sin^2(\theta)(\dot{\phi} - h)\right) - 2\alpha\dot{\phi}\sin^2(\theta) - j\sin(\theta)\cos(\theta)\sin(\phi) \tag{12.24}$$

leading to

$$\nabla\cdot\left[\nabla\phi\sin^2(\theta)\right] - \partial_t\left(\sin^2(\theta)(\dot{\phi} - h)\right) - \alpha\dot{\phi}\sin^2(\theta) = \frac{j}{2}\sin(\theta)\cos(\theta)\sin(\phi) \tag{12.25}$$

Finally, they assume the form

$$\ddot{\theta} - \Delta\theta + \alpha\dot{\theta} + \sin(\theta)\cos(\theta)\left[1 + (\nabla\phi)^2 + (\dot{\phi} - h)^2\right] = \frac{j}{2}\cos(\phi) \tag{12.26}$$

$$\partial_t\left[\sin^2(\theta)(\dot{\phi} - h)\right] - \nabla\cdot\left[\sin^2(\theta)\nabla\phi\right] + \alpha\sin^2(\theta)\dot{\phi} = -\frac{j}{2}\sin(\theta)\cos(\theta)\sin(\phi) \tag{12.27}$$

In this project, we will only consider uniform solutions, where the staggered order parameter is oriented uniformly in the same direction throughout the entire material. Thus, all spatial derivatives drop, and the resulting equations of motion read

$$\ddot{\theta} + \alpha\dot{\theta} + \sin(\theta)\cos(\theta)\left[1 - (\dot{\phi} - h)^2\right] = \frac{j}{2}\cos(\phi) \tag{12.28}$$

$$\ddot{\phi} + 2\cot(\theta)\dot{\theta}(\dot{\phi} - h) + \alpha\dot{\phi} = -\frac{j}{2}\cot(\theta)\sin(\phi) \tag{12.29}$$

Rotated Frame of Reference

Some orbits of the spin-torque oscillator pass through the poles of the unit sphere, leading to unwanted singularities in the derivative of ϕ. Therefore, we employ for $h \leq 1$ a rotated frame of reference, where

$$\vec{l} = \sin(\theta)\left(\cos(\phi)\hat{z} + \sin(\phi)\hat{x}\right) + \cos(\theta)\hat{y} \tag{12.30}$$

The Lagrangian is now given by

$$\begin{aligned}
\mathcal{L} = & h^2 \sin^2(\theta)(\sin^2(\phi) - 1) + h^2 + 2h\sin(\phi)\dot{\theta} + 2h\sin(\theta)\cos\phi\cos\theta\dot{\phi} \\
& + (\dot{\phi}^2 + 1 - \sin^2(\phi))\sin^2(\theta) + \dot{\theta}^2
\end{aligned} \tag{12.31}$$

and the dissipation density reads

$$\mathcal{R} = \alpha \sin^2(\theta)\dot{\phi}^2 + \alpha\dot{\theta}^2 - j\sin^2(\theta)\dot{\phi} \tag{12.32}$$

The equations of motion for uniform states assume the form

$$\ddot{\theta} = -\alpha\dot{\theta} + \sin(\theta)\left[(h^2 - 1)\cos(\theta)\cos^2(\phi) + 2h\cos(\phi)\sin(\theta) - \cos(\theta)\dot{\theta}^2\right] \tag{12.33}$$

$$\ddot{\phi} = \frac{j}{2} - \alpha\dot{\phi} + (h^2 - 1)\cos(\phi)\sin(\phi) - (2\cot(\theta)\dot{\phi} - 2h\cos(\phi))\dot{\theta} \tag{12.34}$$

112

13 Theoretical Tools for Dissipative Dynamical Systems

A dynamical system is called chaotic if initially proximate orbits separate exponentially fast over time. Thus, uncertainties in the initial conditions grow into exponentially large errors, rendering any long-term prediction meaningless. Despite the fact that deterministic equations of motion govern such systems, their trajectory cannot be predicted in the long run.

This so-called sensitive dependence on initial conditions is due to instabilities arising from hyperbolic fixed points, dividing the phase space of a generic dynamical system into regular and chaotic regions. Here, chaos is the rule, spreading over vast parts of phase space, called the 'chaotic sea,' and regular motion is the exception, confined to small 'regular islands.'

This chapter will introduce Lyapunov exponents as a tool to quantify the term 'sensitive dependence on initial conditions' and bifurcation diagrams as a tool to map out the transition from regular motion into chaos.

13.1 Lyapunov Exponents

Initially introduced by A. M. Lyapunov in 1892 [324], Lyapunov exponents are a tool to quantify the characteristic sensitive dependence on initial conditions for chaotic dynamical systems (further reading: [325]).

Let $\vec{x}(0)$ be the initial state of a chaotic dynamical system in phase space and let $\vec{x}(0) + \vec{\delta}_0$ be a set of nearby initial states, where $||\vec{\delta}_0||$ is very small (on the order of $||\vec{\delta}_0|| \sim 10^{-15}$ determined by floating point accuracy). In numerical studies one finds, that the distance between such initially close orbits can be described by

$$||\vec{\delta}(t)|| \sim ||\vec{\delta}_0|| e^{\Lambda t} \tag{13.1}$$

Here, Λ is the Lyapunov exponent, more specifically, the largest Lyapunov exponent.

Positive Lyapunov exponents indicate that initially close orbits separate exponentially fast and thus indicate sensitive dependence on initial conditions. Negative or zero Lyapunov exponents hint at fixed points or stable, periodic orbits.

However, for a N-dimensional dynamical system, the phase-space needs to be described by an N-dimensional basis of orthogonal basis vectors. Thus, there are N distinct either expanding, contracting, or invariant directions and therefore an entire spectrum of N distinct Lyapunov exponents.

Let's consider an infinitesimally small hypersphere of initial states with main axes δx_0^i and $i = 1, \ldots, N$. Over time this hypersphere will deform into an ellipsoid due to the

presence of expanding and contracting directions, whose main axes are given by δx_t^i. From this, the Lyapunov exponents can be defined via

$$\Lambda_i = \lim_{t \to \infty} \frac{1}{t} \ln \left(\frac{\delta x_t^i}{\delta x_0^i} \right) \tag{13.2}$$

According to the Multiplicative Ergodic Theorem, also called Oseledecs theorem, as it was first proven by Valery Oseledec in 1965 [326], the Lyapunov exponents are independent of the initial conditions. More precisely, they are the same for all trajectories belonging to one attractor. This theorem was also subject to several theoretical studies [327–330].

However, this definition is not very practical for calculating Lyapunov exponents, mainly due to the nature of a chaotic system. We cannot guarantee that our hypersphere stays infinitesimally small over the time scale needed to converge the Lyapunov spectrum. Therefore we will pursue an alternative numerical approach in the following.

Standard Method using Gram-Schmidt Orthogonalization

We are using the standard method to determine the Lyapunov spectrum, initially developed by Benettin et al. [331]. For a more pedagogical introduction and an extension to time series data, have a look at the work of Wolf et al. [332] and recent textbooks, such as [325, 333, 334].

Following [332], we will consider the time evolution of one particular initial state according to the non-linear equations of motion, yielding the fiducial trajectory. However, instead of an infinitesimally small hypersphere of initial conditions, we will consider equivalently the time evolution of an orthonormal vector basis via the linearized equations anchored on the fiducial trajectory.

To be specific, let our N-dimensional dynamical system be described by the N-component, non-linear equation of motion

$$\dot{\vec{x}} = \vec{f}(\vec{x}) \tag{13.3}$$

yielding the fiducial trajectory $\vec{x}^*(t)$. Then each of the orthonormal basis (ONB) vectors $\vec{e}_i$ with $i = 1, \ldots, N$ evolves according to the linearized equations of motion

$$\dot{\vec{e}}_i = \hat{A} \vec{e}_i \tag{13.4}$$

with $\hat{A} = \frac{d\vec{f}}{d\vec{x}}\big|_{\vec{x} = \vec{x}^*}$ being evaluated on the fiducial trajectory, yielding $N \times N$ additional equations of motion. Thus, the entire system of N plus $N \times N$ equations is solved simultaneously. We used $\vec{e}_i$ instead of $\hat{e}_i$ for the notation, as these vectors do not stay normalized during time evolution. Vice versa, even the linearized time evolution suffers from two numerical issues:

a) With time, the vectors $\vec{e}_i$ will grow exponentially large/small for positive/negative Lyapunov exponents.

b) Over time, the vectors $\vec{e}_i$ will collapse along the direction of greatest expansion.

To overcome these two issues, we make repeated use of the Gram-Schmidt orthonormalization procedure on the vector basis (alternatively, we may apply some other QR-decomposition method like a Householder transformation [335]).

Thus, the system of $N + N \times N$ equations of motion is evolved for a certain time Δt (typically on the order of one orbital period), starting with the initial ONB $\vec{e}^i = [\vec{e}_1^i, \ldots, \vec{e}_N^i]$ and finally obtaining the set of vectors $\vec{u}^i = [\vec{u}_1^i, \ldots, \vec{u}_N^i]$ during the i-th iteration. This system is orthogonalized using Gram-Schmidt yielding the set of vectors $\vec{v}^i = [\vec{v}_1^i, \ldots, \vec{v}_N^i]$. And that system is finally normalized and used as an initial ONB for the next round of iteration.

The Gram-Schmidt orthogonalization never alters the direction of the first vector in the system. Therefore, it seeks out the most rapidly growing direction (characterized by the largest Lyapunov exponent).

Due to the GS-orthogonalization procedure, the second vector has its component along the direction of greatest expansion removed. Throughout the iteration process, its direction is constantly changing, so that it is also not free to seek out the second most rapidly expanding direction. However, the vectors $\vec{u}_1$, $\vec{u}_2$ span the same two-dimensional subspace as the vectors $\vec{v}_1$, $\vec{v}_2$. So despite repeated vector replacements, these two vectors explore the two-dimensional subspace whose area is growing most rapidly. This area is governed by the largest and second-largest Lyapunov exponent and grows according to $e^{(\Lambda_1 + \Lambda_2)t}$ [331].

Thus, by monitoring the length of the largest vector, proportional to $e^{\Lambda_1 t}$, and the area spanned by the first two vectors, both Lyapunov exponents can be determined. In practice, since vectors $\vec{v}_1$ and $\vec{v}_2$ are orthogonal, we can determine Λ_2 directly from the mean growth rate of vector $\vec{v}_2$.

This reasoning can be generalized to the k-volume spanned by the first k vectors, which grows according to e^μ where $\mu = \sum_{i=1}^k \Lambda_i t$, and thus the mean grow rates of the k-first vectors provide an estimate for the k largest Lyapunov exponents Λ_k:

$$\Lambda_k = \frac{1}{N} \sum_{i=1}^N \frac{\ln|\vec{v}_k^i|}{\Delta t} = \frac{1}{N\Delta t} \sum_{i=1}^N \ln|\vec{v}_k^i| \tag{13.5}$$

In practice, we found $\delta t = 5$ and $N = 5000$ as a good choice with respect to convergence of the Lyapunov spectrum and the numerical effort for the nano-oscillator model considered in this project.

While the largest Lyapunov exponent is an indicator of chaos and characterizes single trajectories, the entire Lyapunov spectrum characterizes the dynamical system as a whole. Employing the binary logarithm, the Lyapunov exponents give the rates of information loss (positive exponent) or gain (negative exponent) in bits/second.

A beautiful example is given by [332]: If the initial state of the Lorenz attractor is prepared with an accuracy of 20 bits (one part in a million) and the largest Lyapunov exponent $\Lambda_1 = 2.16$ represents the rate of information loss, after about $9\,\text{s} = 20\,\text{bits}/(2.16\,\text{bits/s})$ the uncertainty about its state has spread over the entire attractor.

Kaplan-Yorke Conjecture

The Lyapunov spectrum can also be used to approximate the fractal dimension of a strange attractor according to the Kaplan-Yorke conjecture [336, 337].

Let the Lyapunov exponents of a strange attractor in an N-dimensional phase space be arranged from greatest to smallest $\Lambda_1 \geq \Lambda_2 \geq \cdots \geq \Lambda_N$ and let j be the index for which

$$\sum_{i=1}^{j} \Lambda_i \geq 0 \quad \text{and} \quad \sum_{i=1}^{j+1} \Lambda_i \leq 0 \tag{13.6}$$

Then according to the Kaplan-Yorke conjecture, the Lyapunov dimension

$$D = j + \frac{\sum_{i=1}^{j} \Lambda_i}{|\Lambda_{j+1}|} \tag{13.7}$$

approximates the information dimension D_1, first-order Renyi dimension [336, 337], of the strange attractor: $D = D_1$. It is a remarkable relation between the dynamical properties, as captures by the Lyapunov spectrum, and the geometric properties, measured by D_1, of a strange attractor.

It applies to "typical systems," as it is possible to construct counterexamples that violate the Kaplan-Yorke conjecture but which are pathological in the sense that the slightest change to those systems restores the applicability of the former. Thus, these exceptions have 'zero probability' to occur in practice, and we will assume the applicability of the Kaplan-Yorke conjecture also in this project.

Example: Lorenz System

Consider the Lorenz attractor at $\sigma = 10$, $r = 28$, $b = 8/3$, which features the Lyapunov spectrum $\Lambda_1 = 0.9$, $\Lambda_2 = 0.0$ and $\Lambda_3 = -14.46$ [334]. According to Kaplan-Yorke conjecture its Lyapunov dimension is thus approximated by

$$D = 2 + \frac{\Lambda_1 + \Lambda_2}{|\Lambda_3|} = 2.06 \tag{13.8}$$

So this attractor is flat (close to dimension 2).

Example: Chaotic Nano-Oscillator

Given the Lyapunov exponents $\Lambda_1 = 0.1$, $\Lambda_2 = 0.0$, $\Lambda_3 = -0.02$ and $\Lambda_4 = -0.12$, one could estimate the Lyapunov dimension to be

$$D = 3 + \frac{\Lambda_1 + \Lambda_2 + \Lambda_3}{|\Lambda_4|} = 3.66 \tag{13.9}$$

This attractor is highly non-flat.

13.2 Bifurcation Diagrams

Another tool for understanding and mapping out a dynamical system's transition into chaos is a bifurcation diagram.

The bifurcation diagram essentially visualizes the mapping between an external parameter, the bifurcation parameter that provokes the bifurcation, and the values assumed by some characteristic property of the dynamical system, such as an order parameter component or an oscillator frequency. It indicates when the system undergoes a bifurcation: when a smooth, slight change in the bifurcation parameters leads to a drastic, qualitative (topological) change of the system's orbit, e.g. changing from a single-period to a double-period orbit.

To be concrete, let us consider a three-dimensional dynamical system of the form

$$\dot{\vec{x}} = \vec{f}(\vec{x}, r) \tag{13.10}$$

where $\vec{x}(t) = (x(t), y(t), z(t))^T$ and r is some external parameter, such as the reproduction rate for the logistic map. Since we need to construct a one-dimensional mapping, we could, for example, monitor for every value of r, the maxima of the x-component. Thus, plotting the maximal x-component over r creates a bifurcation diagram.

Here, a single value indicates a single period orbit (as there is just one maximal x-value), two points indicate a double periodic orbit, and a whole range of many different values indicates irregular motion. Nevertheless, it is still hard to distinguish this way a quasiperiodic orbit from a genuinely chaotic, aperiodic orbit.

Therefore, another option is plotting the sequence of maxima of the x-component: x_{i+1} over x_i. This yields an almost one-dimensional mapping for almost flat attractors, despite not in a strict mathematical sense since it still has some 'thickness' associated. If this so-called Lorenz map is a unimodal function (U-shaped), the system is guaranteed to be chaotic as Feigenbaum's theory governs the transition of the dynamical system to chaos, and the bifurcation diagram features a period-doubling route. Higher-dimensional attractors can be 'flattened' by large damping (see the book [334] by Strogatz for a more extensive introduction).

Last but not least, let us consider a specific example for this project. Here, the maxima of the angular frequency ω_l of the spin-torque nano-oscillator (characteristic property) was recorded, depending on the external magnetic field h (external control/bifurcation parameter). This is shown in Fig. 13.1: For every magnetic field value, the orbit of the spin-torque nano-oscillator, i.e. the trajectory of the Néel vector $\vec{l}$ on the unit sphere, depicted in plot b) in red, was evolved until relaxation. Subsequently, all local maxima in the angular frequency of the trajectory were recorded (see plot c)). These were plotted over the magnetic field strength, yielding the bifurcation diagram in plot a). This is demonstrated by the red dotted lines between plot a) and plot c) for the example $h = 0.59$. Note that the orbit is two-periodic, but as inversion symmetry is broken, four local maxima in the angular frequency at $h = 0.59$ show up in this figure. The physics of this bifurcation diagram is discussed in section 14.3; it is plotted again in Fig. 14.19 a).
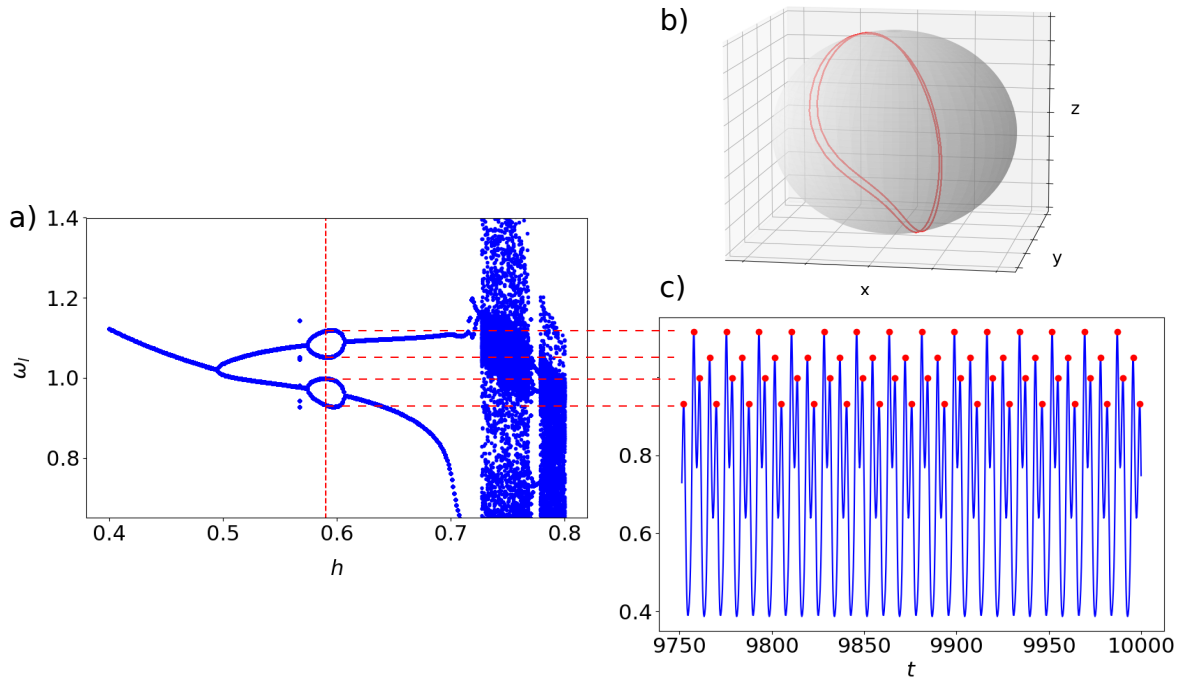
Figure 13.1.: Example of a bifurcation diagram of the spin-torque nano-oscillator considered in this project: Plot a) shows the maxima in the angular frequency ω_l of the nano-oscillator, depending on the external magnetic field h (the bifurcation parameter in this case). It is obtained by evolving the nano-oscillators orbits until relaxation, as shown in plot b), and subsequently recording all local maxima in the oscillator's angular frequency (see plot c)). Note that the orbit is two-periodic, but as inversion symmetry is broken, four local maxima in the angular frequency at $h = 0.59$ show up in this figure.

14 Dynamics of the Spin-Torque Nano-Oscillator

14.1 Regular Dynamics

Fixed Points

Rewriting equations (12.28, 12.29) as a dynamical system of the form $\partial_t \vec{x} = \vec{f}(\vec{x})$ with $\vec{x} = (\theta, \dot{\theta}, \phi, \dot{\phi})^T$ results in

$$\vec{f}(\vec{x}) = \begin{pmatrix} \dot{\theta} \\ \frac{j}{2}\cos(\phi) - \alpha\dot{\theta} - \sin(\theta)\cos(\theta)\left[1 - (\dot{\phi} - h)^2\right] \\ \dot{\phi} \\ -\frac{j}{2}\cot(\theta)\sin(\phi) - 2\cot(\theta)\dot{\theta}(\dot{\phi} - h) - \alpha\dot{\phi} \end{pmatrix} \tag{14.1}$$

As a first step, we look for fixed points, i.e. static, uniform solutions x^*, where $\vec{f}(\vec{x}^*) = \vec{0}$. From this follows $\dot{\theta}, \dot{\phi} = 0$, and our system reduces to

$$\vec{f}_{\text{red}}(\vec{x}^*) = \begin{pmatrix} \frac{j}{2}\cos(\phi) - \sin(\theta)\cos(\theta)\left[1 - h^2\right] \\ -\frac{j}{2}\cot(\theta)\sin(\phi) \end{pmatrix} \overset{!}{=} \vec{0} \tag{14.2}$$

and we end up with the following two equations

$$j\cos(\phi) = \sin(2\theta)\left[1 - h^2\right] \tag{14.3}$$

$$\frac{j}{2}\cot(\theta)\sin(\phi) = 0 \tag{14.4}$$

Zero Current

For zero current $j = 0$, the z-axis is distinguished by the direction of the magnetic field, and the problem has rotational symmetry in x-y-plane. The second equation is trivially fulfilled, and the first equation reduces to

$$\left[1 - h^2\right] \sin(2\theta) = 0 \tag{14.5}$$

Mathematically there are three different solutions for $h \neq 1$: $\theta = 0$, $\theta = \pi$, and $\theta = \frac{\pi}{2}$. As we are going to see from the linear stability analysis, at $h < 1$, the first two solutions are stable, i.e. the Néel vector resides at either pole, which corresponds to the same physical state. This is consistent with the two minima in the uniaxial anisotropy term in $\mathcal{E}$ for (anti-)parallel alignment with the z-axis, which dominates for small h. The third solution describes a manifold of physical states with arbitrary φ around the equator that is unstable and corresponds to the energy maximum of the uniaxial anisotropy term for $h < 1$.

At $h = 1$, a spin-flop transition occurs, as the coupling of the Néel vector to the external magnetic field, which favors orthogonal alignment with the latter, starts to dominate over the uniaxial anisotropy energy term.

The dynamics are entirely regular, starting with an initially oscillatory behavior and settling in the long run in either stable equilibrium due to damping. Fig. 14.1 shows the stable (unstable) fixed points through green (red) markers, as well as a stream plot of $\vec{f}_{\text{red}}(\vec{x})$ in blue ($\dot{\theta} = \dot{\phi} = 0$), which represents a two-dimensional cut of the full four-dimensional phase portrait. It represents the acceleration the dynamical system experiences at zero velocity, and it can give some intuition for the low-velocity dynamics in the vicinity of fixed points.

The first example at $h = 0.9$ in a) shows that the equilibria at the poles attract the system while the ones at the equator repel it. The second example at $h = 1.1$ in b) shows the influence of the spin-flop transition, as the dynamical system is now repelled from the poles (unstable equilibria) and attracted towards the equator (stable equilibria).
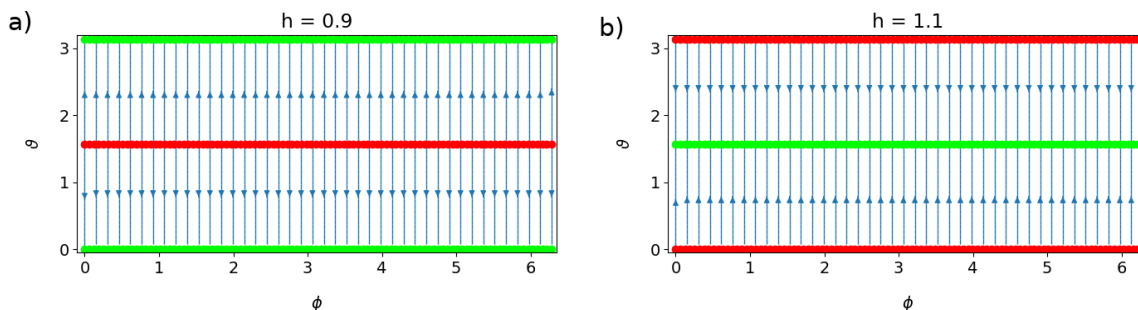
Figure 14.1.: Phase portrait cut at zero velocity and for $h = 0.9$ (left side) and $h = 1.1$ (right side). The dynamics are entirely regular, unstable equilibria (red points) repel the dynamical system towards stable equilibria (green points).

Finite Current

Applying a spin current breaks the rotational symmetry. Going back to the two equations (14.3, 14.4), we see that there are six different mathematical solutions. They correspond to three different physical states, since solutions with $\theta' = \pi - \theta$, $\phi' = \phi + \pi$ describe the same physical state of an antiferromagnet. There are the non-trivial solutions

$$
\begin{aligned}
\phi = 0 \qquad &\theta = \frac{1}{2} \arcsin\left(\frac{j}{1 - h^2} \right) \\[2mm]
\phi = \pi \qquad &\theta = \frac{1}{2} \left(2\pi - \arcsin\left(\frac{j}{1 - h^2} \right) \right)
\end{aligned}
\tag{A}
$$

$$
\begin{aligned}
\phi = 0 \qquad &\theta = \frac{1}{2} \left(\pi - \arcsin\left(\frac{j}{1 - h^2} \right) \right) \\[2mm]
\phi = \pi \qquad &\theta = \frac{1}{2} \left(\pi + \arcsin\left(\frac{j}{1 - h^2} \right) \right)
\end{aligned}
\tag{A$'$}
$$

The staggered order parameter $\hat{l}$ is orthogonal to the polarization of the spin current $\hat{p}$. Thus, the second term in the Rayleigh dissipation unfolds its maximum impact, leading to stable and unstable fixed points (depending on the orientation of $\hat{p}$, $\hat{l}$, $\dot{\hat{l}}$, and thus on whether energy is gained or lost from the interaction with the spin current in the linearized dynamics).

Last but not least, there is the trivial solution, where both hands of the equations are equally zero, which is given by

$$
\theta = \frac{\pi}{2}, \quad \phi = \pm\frac{\pi}{2}
\tag{B}
$$

This corresponds to (anti-)parallel alignment of the staggered order parameter $\hat{l}$ with the polarization of the spin current $\hat{p}$, and thus the second term in the Rayleigh dissipation function vanishes, and no energy is gained or lost from the spin-current (local maximum in energy below and global minimum in energy above the critical current).

The arcsin, occurring for the non-trivial solutions, is only defined when $j \leq j_c = |1 - h^2|$. This defines for any given h the critical current j_c, or vice versa for any given j there are two critical magnetic fields $h_{c_1} = \sqrt{1 - j}$ and $h_{c_2} = \sqrt{1 + j}$, beyond which the physical states (A, A$'$) do not exist. This is indicated by the black line in Fig. 14.2. In addition, for each of the three solutions, the region of linear stability (blue region) or instability (red region) are displayed for damping $\alpha = 0$. For $\alpha > 0$, only the boundary separating the stable and unstable region for solution B at $h \geq 1$ becomes slightly steeper. However, for reasonably small values of α, the effect is barely visible by the eye.
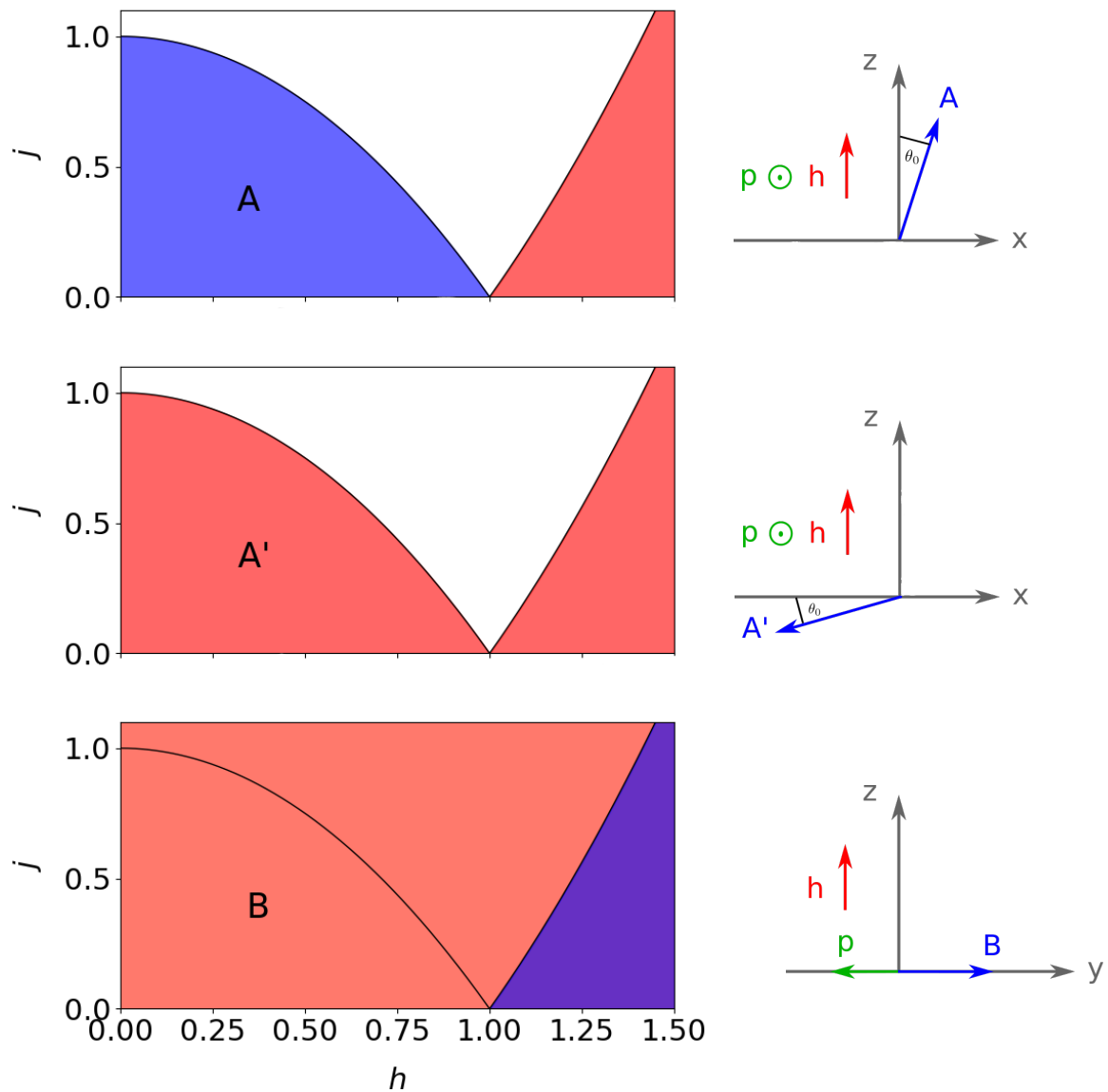
Figure 14.2.: The uniform, static solution exists within the blue parameter region and it is linearly stable with respect to small deviations. These results were determined at $\alpha = 0$ from a linear stability analysis.

As we will see later from cuts of the phase portrait and the actual linear stability analysis, this leads to the following behavior: For $h < 1.0$ and small j, only solution A is stable (with respect to small deviations). As the current j increases, solutions A and A' tilt off the z- and x-axis, respectively, by an angle

$$\theta_0 = \frac{1}{2} \arcsin\left(\frac{j}{1-h^2}\right) \tag{14.6}$$

When reaching the critical current j_c (black line), both solutions coincide, and the respective fixed points annihilate each other in a saddle-node-bifurcation. Above the critical current, only solution B exists, but it is unstable. Thus, the system is either settling on a limit cycle due to damping or can possibly show chaotic behavior.

The case is similar if we consider the current to be fixed but small $j < 1.0$ and let the magnetic field increase. As before, solution A is linearly stable and collides with the unstable solution A′ in a saddle-node-bifurcation upon reaching the first critical magnetic field h_{c_1} (first branch of the black line). In between the two critical fields, only solution B exists and is unstable, leading to limit cycles and possibly chaos. However, upon reaching the second critical magnetic field h_{c_2}, solution B becomes stable. Thus, the system aligns with the spin current polarization $\hat{p} = \hat{y}$, and solutions A and A′ re-emerge as unstable fixed points.

Phase Portrait Cuts

To better understand the regular dynamics, we have a look at two-dimensional cuts of the four-dimensional phase portrait. Fig. 14.3 and 14.4 show on the left-hand side phase portrait cuts of $\vec{f}$ (14.1) at $\dot{\theta} = \dot{\phi} = 0$ and on the right-hand side phase portrait cuts for $\phi = \pi/2$ and $\dot{\phi} = 0$ as a blue stream plot, both taken at $j = 0.5$. They visualize the acceleration the dynamical system experiences at zero velocity. In addition, green and red markers depict the stable and unstable fixed points, respectively.

As the magnetic field h increases, one can see how the fixed points corresponding to solutions A and A′ approach and eventually annihilate each other in a saddle-node-bifurcation at the first critical magnetic field h_{c_1}. In between the two critical magnetic fields, only solution B exists, but it is unstable. At the second critical magnetic field h_{c_2}, solutions A and A′ re-emerge in a saddle-node bifurcation, but this time they are unstable, and B turns stable (for $\alpha > 0$ even slightly before h_{c_2}).

Note that these two-dimensional cuts might not cover all expanding or contracting directions of the full four-dimensional phase portrait. For example, at $h = 1.0$ in Fig. 14.4, the phase portrait cut on the left in θ and ϕ seemingly depicts an elliptical (stable) fixed point. By comparison with the phase portrait cut on the right in $\dot{\theta}$, θ one sees that the fixed point is actually unstable. Hence, the intuition gained from this phase portrait cuts should be taken with a grain of salt. Stability is ultimately determined from the linear stability analysis, which is presented in the next section.
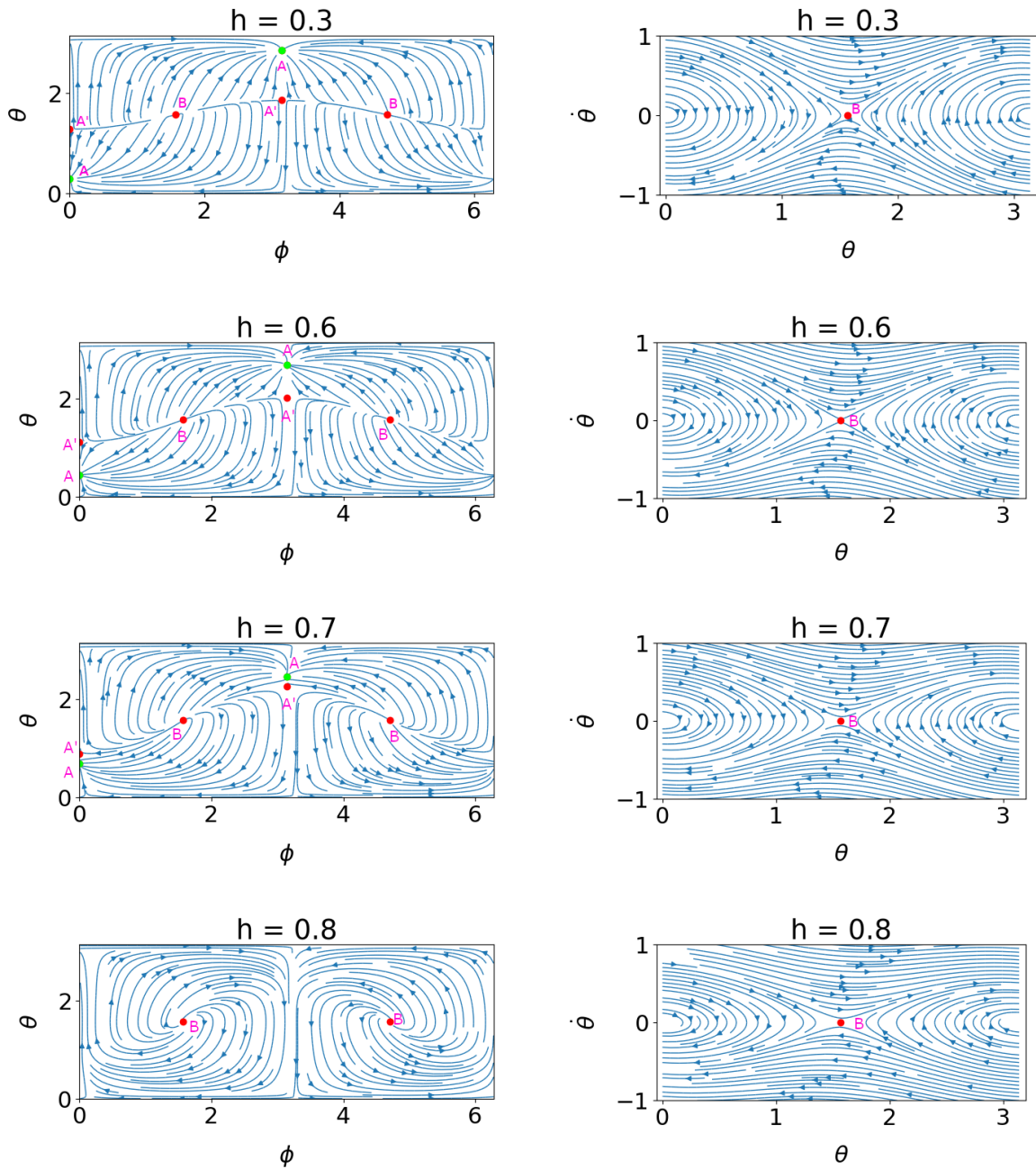
Figure 14.3.: Evolution of phase portrait cuts of $\vec{f}$ at $\dot{\theta} = \dot{\phi} = 0$ (left side) and $\phi = \pi/2$ and $\dot{\phi} = 0$ (right side) for increasing magnetic fields h. One can see that solutions A and A′ annihilate each other in a saddle-node-bifurcation.
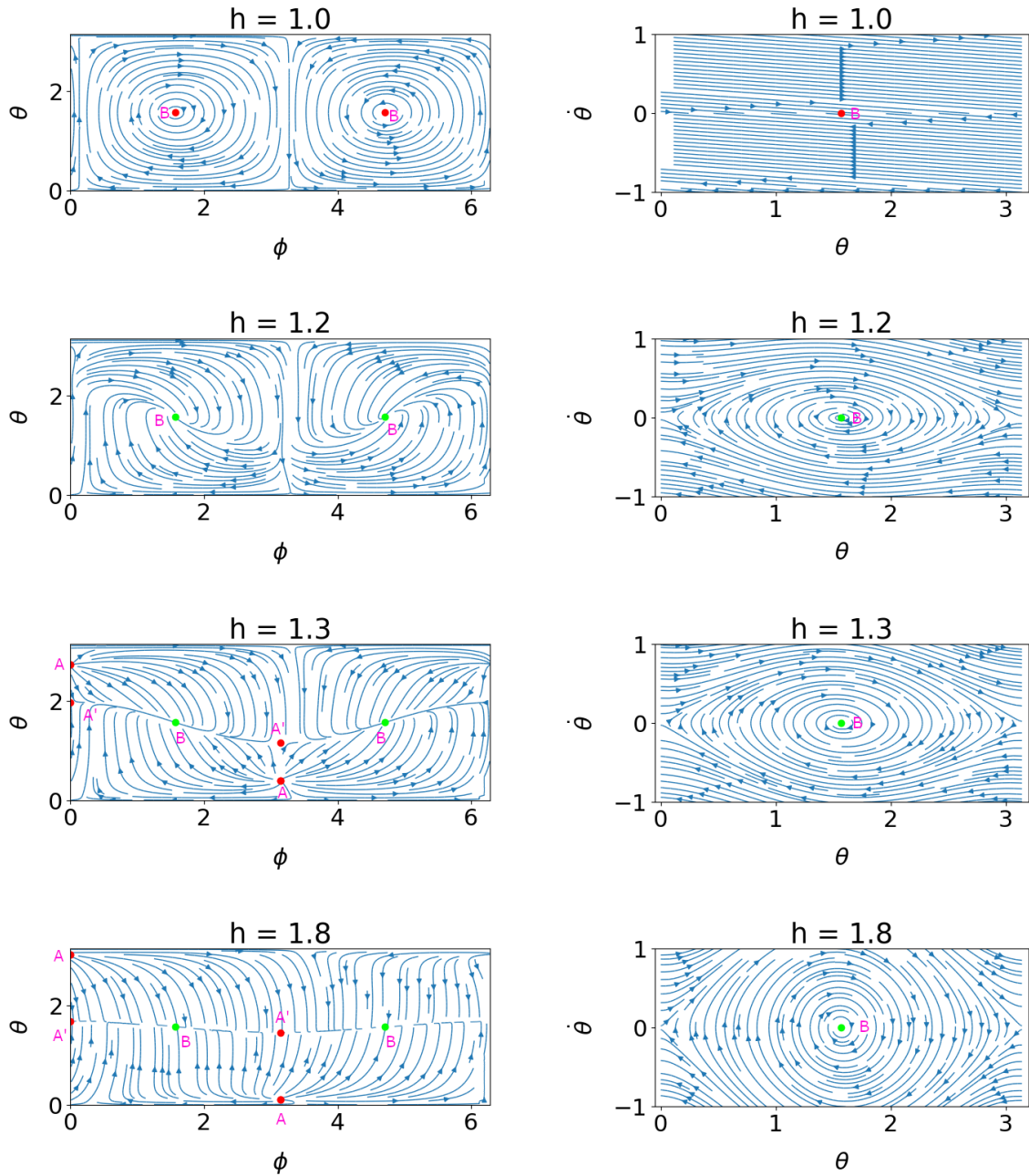
Figure 14.4.: Evolution of phase portrait cuts of $\vec{f}$ at $\dot{\theta} = \dot{\phi} = 0$ (left side) and $\phi = \pi/2$ and $\dot{\phi} = 0$ (right side) for increasing magnetic fields h. One can see that solutions A and A′ re-emerge in a saddle-node-bifurcation.

Linear Stability Analysis

The intuitive picture obtained from the phase portraits is now complemented by a linear stability analysis. Therefore $\vec{f}$ is developed into a Taylor series at a given fixed point $\vec{x}^*$

$$\vec{f}(\vec{x}) = \underbrace{\vec{f}(\vec{x}^*)}_{=\vec{0}} + \underbrace{\frac{\partial \vec{f}}{\partial \vec{x}}\bigg|_{\vec{x}^*}}_{=\hat{L}} \cdot (\vec{x} - \vec{x}^*) + \dots \tag{14.7}$$

The dynamics in the neighborhood of the fixed point $\vec{x}^*$ are then determined by the eigenvalues of

$$\hat{L} = \begin{pmatrix} 0 & 1 & 0 & 0 \\ \left(1 - (v-h)^2\right)\sin^2(\theta) - \left(1 - (v-h)^2\right)\cos^2(\theta) & -\alpha & -\frac{1}{2}j\sin(\phi) & 2(v-h)\sin(\theta)\cos(\theta) \\ 0 & 0 & 0 & 1 \\ 2u(v-h)\csc^2(\theta) + \frac{1}{2}j\csc^2(\theta)\sin(\phi) & -2(v-h)\cot(\theta) & -\frac{1}{2}j\cot(\theta)\cos(\phi) & -\alpha - 2u\cot(\theta) \end{pmatrix} \tag{14.8}$$

where $\csc(x) = 1/\sin(x)$ is the cosecant. The eigenvalues are complex $\varepsilon = \mathrm{Re}(\varepsilon) + i\,\mathrm{Im}(\varepsilon)$ and determine the damping $\tilde{\alpha} = \mathrm{Re}(\varepsilon)$ and the eigenfrequency $\tilde{\omega} = \mathrm{Im}(\varepsilon)$ of the nano-oscillator. The eigenvalues for solutions A and A$'$ assume cumbersome analytical expressions and are therefore not quoted. The eigenvalues for solution B can be easily determined analytically from

$$\hat{L} = \begin{pmatrix} 0 & 1 & 0 & 0 \\ 1 - h^2 & -\alpha & -\frac{j}{2} & 0 \\ 0 & 0 & 0 & 1 \\ \frac{j}{2} & 0 & 0 & -\alpha \end{pmatrix} \tag{14.9}$$

leading to

$$\varepsilon_{1,2,3,4} = -\frac{\alpha}{2} \pm \frac{1}{2}\sqrt{2j_\mathrm{c} \pm 2\sqrt{j_c^2 - j^2} + \alpha^2} \tag{14.10}$$

At first, we look in more detail into the eigenfrequencies of the nano-oscillator (imaginary part) before coming back to the full spectrum of eigenvalues. Fig. 14.5 shows in black the eigenfrequencies at $j = 0.0$: for small magnetic fields $h < 1.0$, there are two branches of the stable solution A that separate linearly according to $\omega_{1,2} = 1 \pm h$. At $h = 1.0$, the system undergoes a spin-flop transition, and now solution B becomes the stable solution.

Here, one eigenvalue is zero, reflecting the rotational symmetry around the z-axis, and the other one behaves like $\omega = \sqrt{h^2 - 1}$ and captures out-of-plane oscillations of the Néel vector.

For $j = 0.1$ and $\alpha = 0.1$, the eigenvalues are plotted in grey. A gap opens between the two critical magnetic fields $h_{c_1} = \sqrt{1 - j}$ and $h_{c_2} = \sqrt{1 + j}$, and near this gap, the behavior of the eigenfrequencies deviates significantly from the case $j = 0.0$: For A, the lower branch reaches the x-axis earlier, at the gap opening. The upper branch even turns toward lower values near the gap opening. Inside the gap, there are no stable fixed points, and thus no eigenfrequencies are plotted.

Beyond the gap, B becomes stable, and its upper branch quickly approaches the branch at $j = 0.0$, as out-of-plane oscillations are less affected by the spin current and damping. The second lower branch gets lifted off the x-axis, as rotational symmetry is broken, but reaches the x-axis again at a finite magnetic field. This indicates the point where the in-plane oscillations become overdamped. (For $\alpha = 0.0$, it approaches but never reaches the x-axis as h increases.)

In the following sections, we will take a closer look at the eigenvalue spectra of the individual solutions.
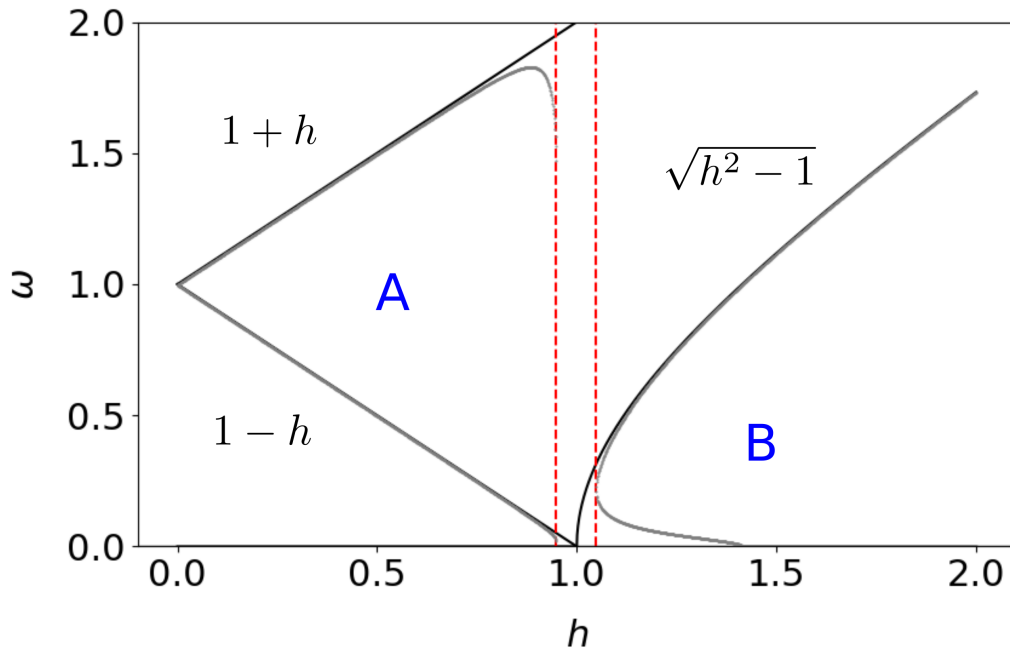
Figure 14.5.: Eigenfrequencies of the nano-oscillator (imaginary part of the eigenvalues of the respective stable solution) plotted for $j = 0.0$, $\alpha = 0.0$ in black, and for $j = 0.1$, $\alpha = 0.1$ in grey. It is further discussed in the main text.

Eigenvalues of Solution A

The entire eigenvalue spectrum of solution A can be seen in Fig. 14.6. Plot a) depicts the evolution of the spectrum with h for $j = 0.1$ and $\alpha = 0.5$, showing a linear splitting of the real and imaginary part, intercepted by a gap between the two critical magnetic fields h_{c_1} and h_{c_2} (indicated by red lines). For $h < 1.0$, both branches of the real part are negative, for $h > 1.0$, one branch becomes positive, which is known as 'dynamic instability' and captures the destabilizing effect of damping: while the real part was zero for zero damping, it acquires a finite, positive value, as soon as the slightest damping applies.

Plots c) and d) depict the evolution with j until the critical current j_c, marked by a red line, at $\alpha = 0.5$ and $h = 0.5$ and $h = 1.2$, respectively. Also here, the dynamical instability can be seen: for $h < 1.0$, both branches of the real part stay negative, while for $h > 1.0$, one branch becomes positive.
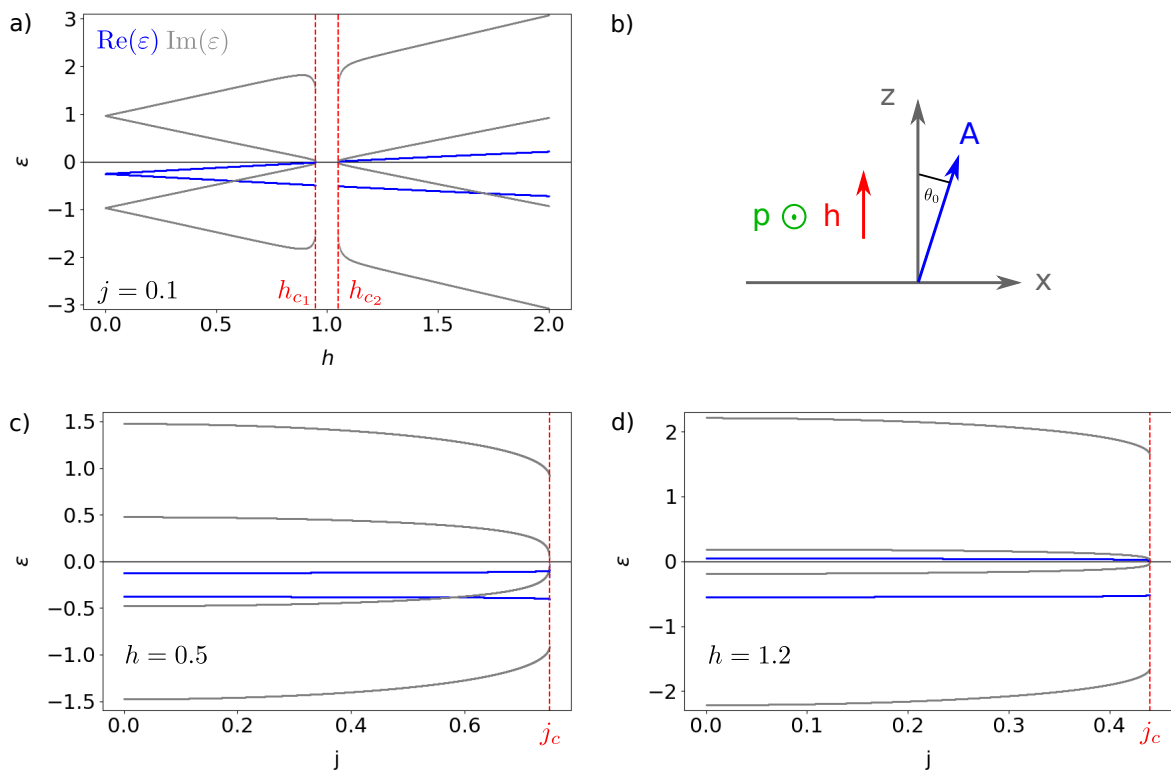
Figure 14.6.: Evolution of the eigenvalue spectrum of solution A with magnetic field h and current j for $\alpha = 0.5$ and a) $j = 0.1$, c) $h = 0.5$, and d) $h = 1.2$. The real part $\mathrm{Re}(\varepsilon)$ (blue) shows a dynamic instability, acquiring a positive value for $h > 1.0$, as soon as the damping constant $\alpha > 0.0$.

Eigenvalues of Solution A$'$

Next, the eigenvalue spectrum of solution A$'$ is depicted in Fig. 14.7, showing that there is always one eigenvalue with a positive real part, and thus solution A$'$ is never stable. Plot a) shows the evolution with h, with a gap between the two critical magnetic fields h_{c_1} and h_{c_2} (indicated by red lines). Plots c) and d) depict the evolution with j up to the critical current j_c for $\alpha = 0.1$ and $h = 0.5$ and $h = 1.2$, respectively. Plot c) shows that for $h < h_{c_1}$, the real part undergoes a bifurcation at $j_{\mathrm{osc}} < j_c$. At the same time, the imaginary part becomes zero, indicating the threshold of in-plane oscillations of solution A$'$. The critical current j_{osc} is determined below.
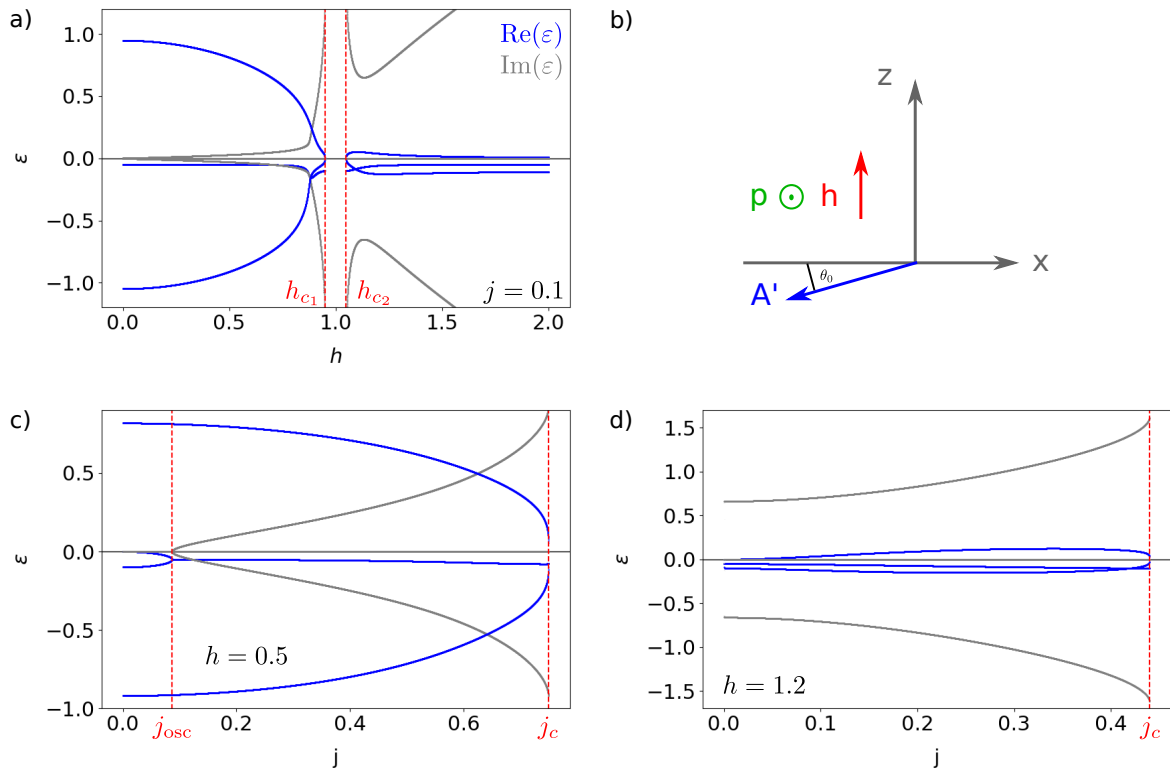
Figure 14.7.: Evolution of the eigenvalue spectrum of solution A$'$ with magnetic field h and current j for $\alpha = 0.1$ and a) $j = 0.1$, c) $h = 0.5$, and d) $h = 1.2$. The real part $\mathrm{Re}(\varepsilon)$ (blue) is always positive, indicating that solution A$'$ is never stable.

Eigenvalues of Solution B

Finally, the eigenvalue spectrum of solution B is shown in Fig. 14.8. Plot a) depicts the evolution with h for $\alpha = 0.1$. The real and imaginary part undergo two bifurcations with increasing magnetic field h. The associated linear fixed point dynamics change from a hyperbolic saddle point to a (hyperbolic) stable focus. For $h > h_{c_2}$, the real part settles at $\mathrm{Re}(\varepsilon) = -\frac{\alpha}{2} = -0.05$. For $h_{\mathrm{osc}} > h_{c_2}$, the real part undergoes a bifurcation, and at the same time, one branch of the imaginary part becomes zero, indicating the threshold of in-plane oscillations of solution A′. The critical field h_{auto} is determined below; it is related to the critical current j_{osc}.

Plots c) and d) depict the evolution with j for $\alpha = 0.1$. In plot c) the real (imaginary) part of ε undergoes with increasing spin current j just one pitch-fork bifurcation, the real part $\mathrm{Re}(\varepsilon)$ keeps increasing with larger spin current j. For positive real part $\mathrm{Re}(\varepsilon_+)$, there is one acoustic branch, with $\mathrm{Re}(\varepsilon_+)(h = 0) = 0$, and one optical branch of the real part, which eventually merge into just one optical branch. This is consistent with [304].

In plot d), the threshold of in-plane oscillations is indicated by the same $j_{\mathrm{osc}} < j_{\mathrm{c}}$, as for solution A′. The real part undergoes a bifurcation for increasing j, becoming positive only at $j > j_{\mathrm{c}}$, which captures the stabilizing effect of damping.
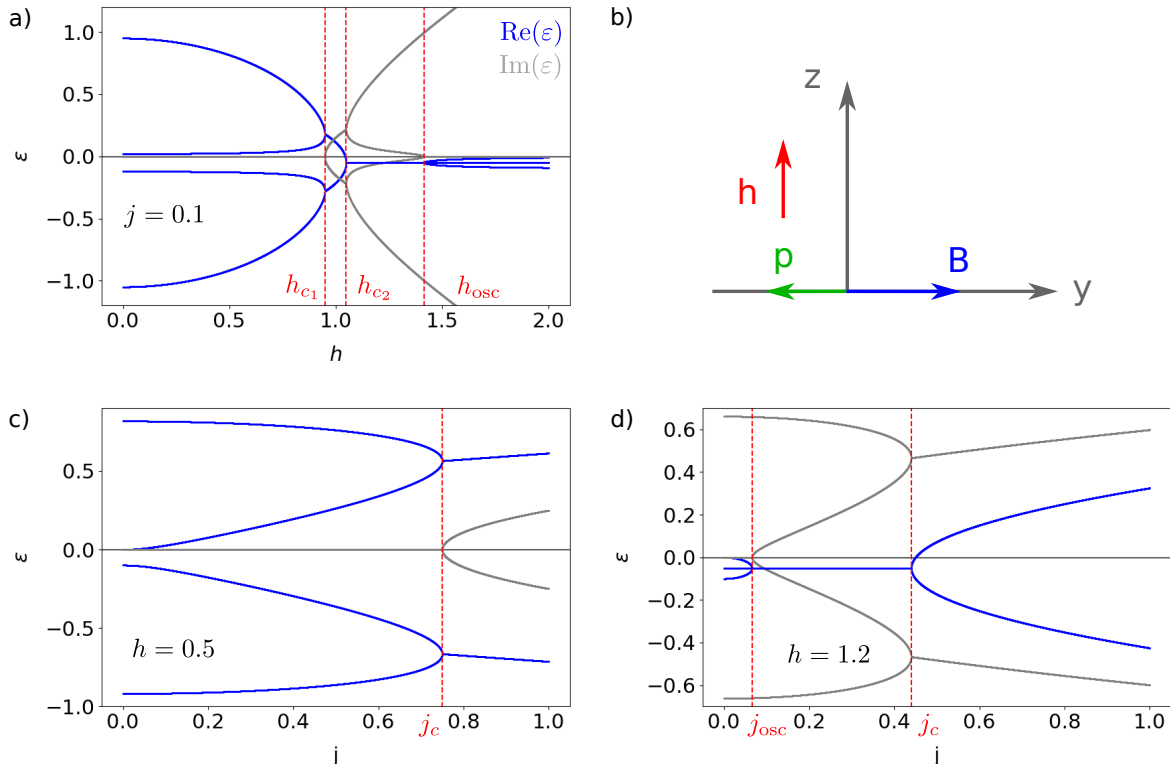
Figure 14.8.: Evolution of the eigenvalue spectrum of solution B with magnetic field h and current j for $\alpha = 0.1$ and a) $j = 0.1$, c) $h = 0.5$, and d) $h = 1.2$. In plot d), the real part becomes positive only at $j > j_{\mathrm{c}}$, indicating the stabilizing effect of damping.
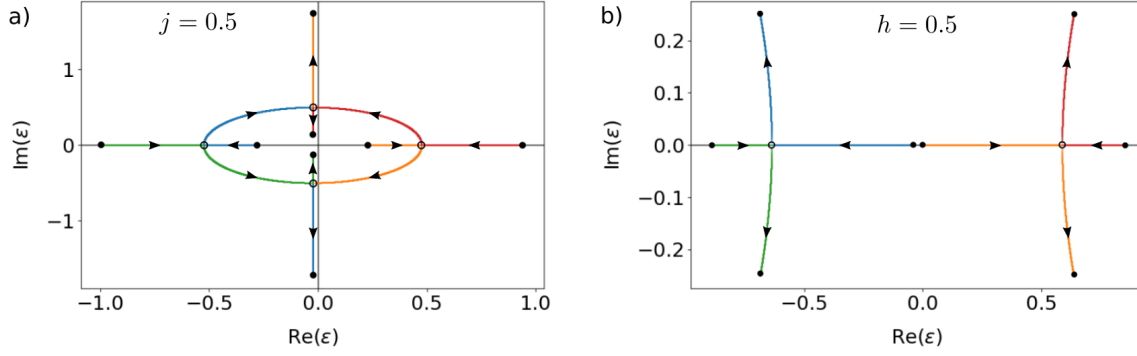
Figure 14.9.: Eigenvalues of solution B within the complex plane for $\alpha = 0.05$: a) shows the evolution for $j = 0.5$ and increasing h from 0. to 2, b) shows the evolution for $h = 0.5$ and increasing j from 0 to 1.

Fig. 14.9 a) shows how the pairs of eigenvalues for solution B collide in a reversible Hopf-bifurcation (open markers) with increasing h at $j = 0.5$. This is analogous to the upward Ziegler double pendulum, which also shows a two-by-two reversible Hopf-bifurcation, depending on the follower load [338, 339]. In the range $h_{c_1} < h < h_{c_2}$, solution B experiences a flutter instability, where the Néel vector follows a limit cycle or shows chaotic behavior. At $h = h_{c_2}$, solution B becomes stable.

Plot b) shows the evolution with increasing current j at $h = 0.5$, where the two pairs of eigenvalues collide on the real axis and then escape into the complex plane for $j > j_c$ (compare with Fig. 14.8 c)).

Threshold of In-plane Oscillations

For $h > 1$, i.e. $1 - h^2 < 0$, and $j_c^2 - j^2 > 0$, there is a threshold when the imaginary part of one of the eigenvalues of solution B vanishes. It corresponds to the threshold of oscillations within the x-y-plane, as the current gets too low and the in-plane oscillations get overdamped. Starting from

$$\varepsilon_{1,2,3,4} = -\frac{\alpha}{2} \pm \frac{1}{2}\sqrt{\underbrace{\alpha^2 - 2j_c}_{=-C} \pm \underbrace{2\sqrt{j_c^2 - j^2}}_{=D}} \tag{14.11}$$

we define two constants that are positive in the given parameter region $C, D \in \mathbb{R}^+$. At $C = D$, a bifurcation in the real part occurs, which determines the threshold of in-plane oscillations. Thus, we get the condition

$$\alpha^2 - 2j_c = 2\sqrt{j_c^2 - j^2} \tag{14.12}$$

131

leading to

$$j_{\text{osc}} = \sqrt{j_{\text{c}}^2 - \frac{(\alpha^2 - 2j_{\text{c}})^2}{4}}$$ (14.13)

and, using $j_{\text{c}} = h^2 - 1$ for $h > 1$, we get

$$h_{\text{osc}} = \sqrt{1 + \frac{\alpha^4 + 4j^2}{4\alpha^2}}$$ (14.14)

14.2 Transition to Chaos (Small Damping)

Below the critical current, the stable solution A lies within the x-z-plane. Using the parameterization

$$\hat{l} = \sin(\Theta)\hat{x} + \cos(\Theta)\hat{z}$$ (14.15)

one could express solutions A and A′ by

$$\Theta = \Theta_0, \quad \Theta = \pi + \Theta_0 \quad \text{with} \quad \Theta_0 = \frac{1}{2}\arcsin\left(\frac{j}{1 - h^2}\right)$$ (14.16)

and $0 \leq \Theta_0 \leq \frac{\pi}{4}$. Beyond the critical current j_{c} and for $h = 0.0$, the second equation of motion (12.29) becomes

$$\ddot{\Theta} + \alpha\dot{\Theta} + \sin(\Theta)\cos(\Theta) = \frac{j}{2}$$ (14.17)

Thus, the Néel vector settles on a limit cycle within x-z-plane for $j > j_{\text{c}} = 1$. If $j \gg j_{\text{c}}$, we have $\Theta(t) \approx \Omega t$, and the oscillators' frequency is given by $\Omega = \frac{j}{2\alpha}$.

For finite magnetic fields, the dynamics become a lot more complicated. Below the critical current, we expect the dynamics to be regular, settling at either stable fixed point due to damping (i.e. a static, uniform solution exists).

Above the critical current and for $h < 1.0$, the stable fixed points vanish (i.e. the static, uniform solution ceases to exist), and the Néel vector might settle on some limit cycle, which is explored in Fig. 14.10. It shows trajectories starting at the equator at $\theta(0) = \pi$, $\phi(0) = 0$ for $j = 1.1$ and a) $h = 0.0$, b) $h = 0.05$, and c) $h = 0.5$. Shown are the first 200 time steps that form a limit circle which lies in a) within x-z-plane and which is tilted by some angle in b). However, for larger magnetic fields, e.g. in plot c),

the motion becomes chaotic and never settles on some regular limit circle but forms a so-called strange attractor.

As we are going to see later, even below the critical current, there is chaotic dynamics for suitable initial conditions, dividing phase space into basins of attraction and a chaotic sea. An example for such a chaotic orbit is shown in d) at $j = 0.3$, $h = 0.5$, and the specific initial conditions $\theta(0) = 1.5$, $\phi(0) = 1.5$.

In order to prove that there is genuine chaos, the Lyapunov spectrum of the strange attractor was determined, using the standard method originally developed by Benettin et al. [331] which is considering the evolution of linear deviation vectors and repeated Gram-Schmidt orthogonalization (see the previous chapter or [333] for a pedagogical introduction).
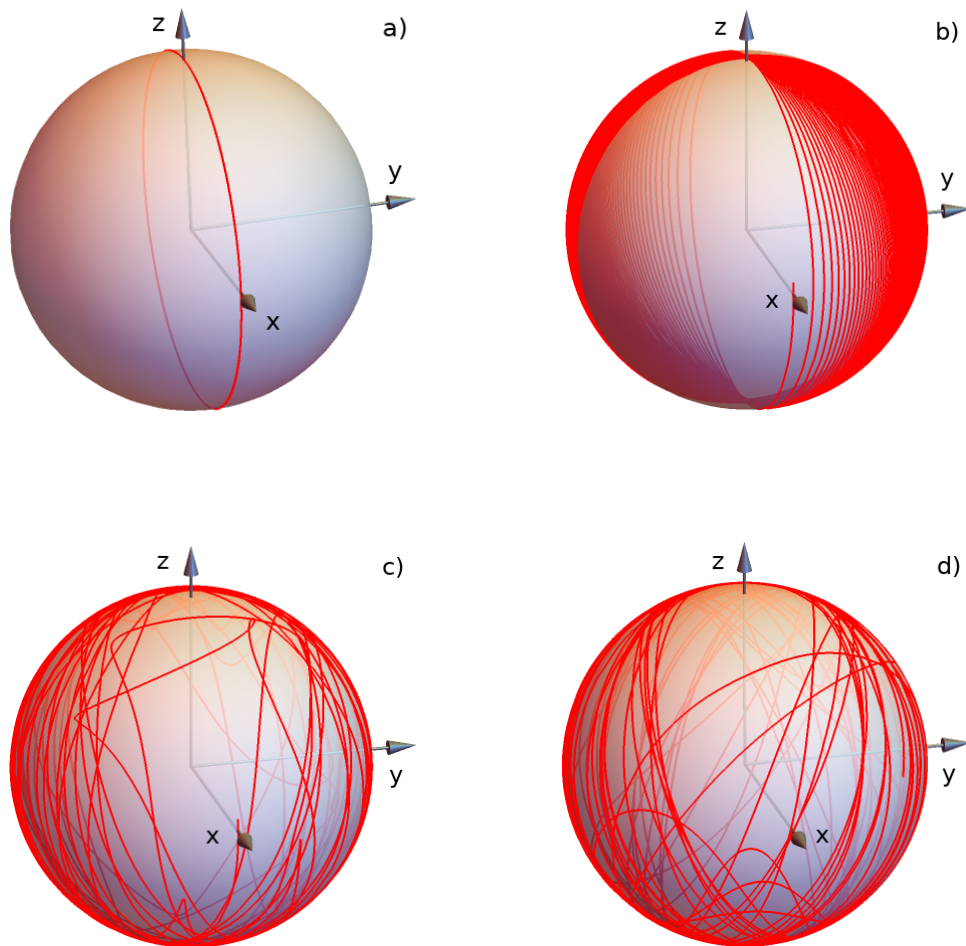
Figure 14.10.: Example trajectories of the AFM nano-oscillator for the first 200 time steps. Above the critical current at $j = 1.1$ and starting at the equator at $\theta(0) = \pi$, $\phi(0) = 0$, there is regular dynamics for a) $h = 0.0$ and b) $h = 0.05$. However, for larger magnetic field s, such as at c) $h = 0.5$, the dynamics become chaotic. Even below the critical current at $j = 0.3$, $h = 0.5$, there are chaotic dynamics for specific initial conditions as depicted in d) for the exemplary initial conditions $\theta(0) = 1.5$, $\phi(0) = 1.5$.

Turning Angle of the Limit Cycle

Above the critical current $j > j_\mathrm{c}$ and for a small magnetic field h, the limit cycle, which we have identified earlier on at $h = 0.0$ within x-z-plane, assumes a finite turning angle ϕ with the x-axis for $h > 0.0$. This can be seen from a) and b) in Fig. 14.10. Thus, the motion can be separated into a fast oscillation in θ and a slow motion in ϕ. Using the ansatz $\theta(t) \approx \Omega t$ (uniform, fast oscillation in ϑ), the equations of motion (12.28) and (12.29) read

$$\dot{\Omega} + \alpha\Omega + \sin(\Omega t)\cos(\Omega t)\left[1 - (\dot{\phi} - h)^2\right] = \frac{j}{2}\cos(\phi) \tag{14.18}$$

$$\ddot{\phi} + 2\cot(\Omega t)\Omega(\dot{\phi} - h) + \alpha\dot{\phi} = -\frac{j}{2}\cot(\Omega t)\sin(\phi) \tag{14.19}$$

Since $h \ll 1$ and because the motion in ϕ is slow, we have $\dot{\phi} \ll 1$ and $\ddot{\phi} \ll 1$, and since the term $\sin(\Omega t)\cos(\Omega t)$ is bound to the interval $[-0.5, 0.5]$, while Ω is large, the terms marked in red will be neglected.

The first equation then yields for the frequency of the fast oscillation

$$\Omega = \frac{j}{2\alpha}\cos(\phi) \tag{14.20}$$

Plugging this into the second equation, we arrive at the equation

$$\dot{\phi} = h - \frac{\alpha}{2}\tan(\phi) \tag{14.21}$$

This equation is non-linear, of first order, and can be separated and integrated using $\eta = \frac{\alpha}{2h}$

$$\int \frac{d\phi}{1 - \eta\tan(\phi)} = \frac{\phi - \eta\ln[\cos(\phi) - \eta\sin(\phi)]}{1 + \eta^2} = ht + C = \int h\,dt \tag{14.22}$$

Introducing $\tan(\psi) = \eta$, we arrive at the implicit relation

$$\left(1 + \eta^2\right)ht = \phi - \eta\ln[\sqrt{1 + \eta^2}\cos(\phi + \psi)] \tag{14.23}$$

For $t \to \infty$, the limit cycle approaches the turning angle $\phi = \frac{\pi}{2} - \psi$, which is plotted in red as analytical solution in Fig. 14.11. It is compared to numerical data plotted in blue, which were obtained the following way: First, orbits starting at zero velocity at $\theta(0) = 0.5$, $\phi(0) = 0.0$, $\dot{\theta}(0) = 0.0$, $\dot{\phi}(0) = 0.0$, for $j = 1.1$ and $\alpha = 0.1$, and various h
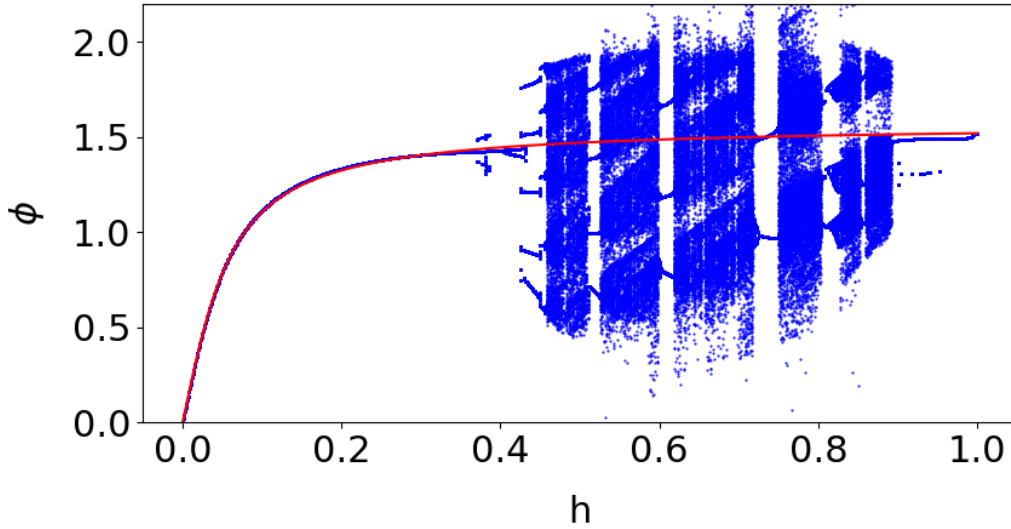
Figure 14.11.: Turning angle with respect to the x-axis of the limit cycle for $j = 1.1 > j_c$ depending on the magnetic field h. The initial parameters are $\theta(0) = 0.5$, $\phi(0) = 0.0$, $\alpha = 0.1$ and 200 values were taken into account.

were advanced for 10,000 time steps to achieve relaxation. Next, 200 values of the turning angle ϕ at the intersection with x-y-plane for $\phi < \pi$ (i.e. $z = 0$, $y < 0$) were recorded and plotted.

Until $h \approx 0.37$, the numerical and analytical results align, but the limit cycle becomes unstable for larger magnetic fields, resulting in period-doubling bifurcations and eventually chaotic regions, which again are intercepted by periodic windows. Here, the numerical data spread broadly around the analytical solution, and this bifurcation diagram gives an intuition for the transition into chaos that we encounter.

Stability of the Limit Cycle

For $h = 1.0$, the limit cycle that was derived in the previous section is an exact solution of the equations of motion. It is again summarized here:

$$\theta(t) = \Omega t, \qquad \Omega = \frac{j}{2\alpha} \cos(\phi), \qquad \phi = \arctan\left(\frac{2}{\alpha}\right) \tag{14.24}$$

Its stability can be determined from the absolute values $|\lambda_i|$, the so-called Floquet multipliers, of the limit cycle's monodromy matrix $\hat{M}$. If one Floquet multiplier is greater than one, i.e. $|\lambda_i| > 1$, the limit cycle becomes unstable [340].

Since this limit cycle passes through the poles of the unit sphere, we employ the rotated frame of reference to avoid singularities, where

$$\vec{l} = \sin\left(\tilde{\theta}\right)\left(\sin\left(\tilde{\phi}\right)\hat{z} + \cos\left(\tilde{\phi}\right)\hat{z}\right) + \cos\left(\tilde{\theta}\right)\hat{y} \tag{12.30}$$

The exact solution can be expressed in the rotated frame of reference via

$$\cos\left(\tilde{\theta}\right) = \sin(\Omega_0 t)\sin(\phi_0) \tag{14.25}$$

$$\sin\left(\tilde{\theta}\right)\sin\left(\tilde{\phi}\right) = \sin(\Omega_0 t)\cos(\phi_0) \tag{14.26}$$

$$\sin\left(\tilde{\theta}\right)\cos\left(\tilde{\phi}\right) = \cos(\Omega_0 t) \tag{14.27}$$

The monodromy matrix corresponds to the fundamental matrix $\hat{\Phi}$ of the linearized dynamical system $\dot{\vec{x}} = \hat{L}\vec{x}$, evaluated at the orbit period $T = \frac{2\pi}{\Omega}$ of the limit cycle: $\hat{M} = \hat{\Phi}(T)$. In order to determine it, the matrix $\hat{L} = \left.\frac{\partial \vec{f}}{\partial \vec{x}}\right|_{\vec{x}=\vec{x}_{\text{cycle}}}$ is evaluated at the exactly known solution of the limit cycle, in the rotated frame of reference. The monodromy matrix is now given by the matrix exponential

$$\hat{M}(T) = \exp\left(\int_0^T dt\, \hat{L}\right) \tag{14.28}$$

However, since this integration cannot be performed analytically, the linearized system was integrated numerically. The fundamental matrix $\hat{\Phi}(t)$ was determined for one orbit period T starting from $\hat{\Phi}(0) = \hat{1}$.

The evolution of the monodromy matrix eigenvalues $\hat{M}$ with the current j is shown in Fig. 14.12. It indicates that the limit cycle is remarkably stable with just one island of instability at $1.615 < j < 1.824$, where the greatest Floquet multiplier is larger than one. This is consistent with a small island of chaos, where the greatest Lyapunov exponent is greater than zero (see Fig. 14.16 a)). The presence of this stable limit cycle explains that chaos is largely absent at $h = 1$ in the Lyapunov spectrum.

There are only two more areas of instability for larger current: $2.366 < j < 3.073$ and $4.265 < j < 6.953$. Note that even for small current j, the smallest Floquet multiplier is not exactly zero, but of the order 10^{-10}, as a zero Floquet multiplier would correspond to a Lyapunov exponent of minus infinity.

For $j = 0$, we have $|\lambda_1| = |\lambda_2| = 1$, which means that the two largest Lyapunov exponents $\Lambda_1 = \Lambda_2 = 0$, and thus the trajectory unfolds on a torus in phase space.

The evolution of the greatest Floquet multiplier at $h = 1.0$ with j and α is depicted in Fig. 14.13. With increasing damping α the regions of instability, where $|\lambda_0| > 1.0$, vanish. For small damping, they get more nuanced.
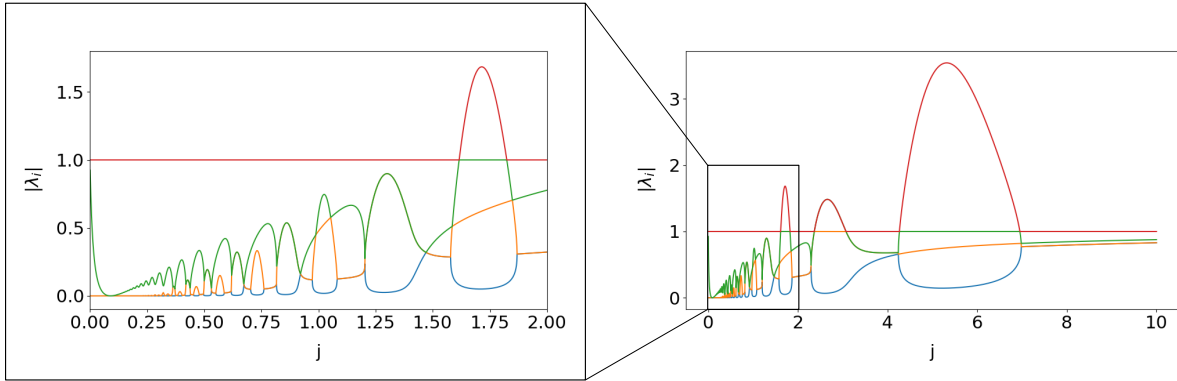
Figure 14.12.: Evolution of the Floquet multipliers (absolute value $|\lambda_i|$ of the eigenvalues of the monodromy matrix) for the limit cycle at $h = 1.0$ and $\alpha = 0.1$: The limit cycle is remarkably stable with just one island of instability $1.615 < j < 1.824$, where the greatest Floquet multiplier is larger than one. There are only two more areas of instability for larger current: $2.366 < j < 3.073$ and $4.265 < j < 6.953$.
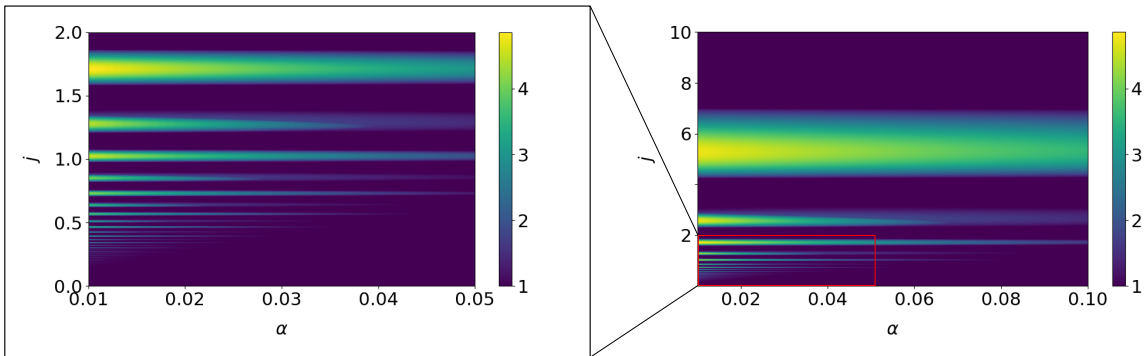
Figure 14.13.: Evolution of the greatest Floquet multiplier for the limit cycle at $h = 1.0$ with j and α. With increasing damping α the regions of instability, where $|\lambda_0| > 1.0$, vanish. For small damping, they get more nuanced.

Lyapunov Spectrum over Phase Space

To investigate how chaos emerges below the critical current, we determined the Lyapunov spectrum over a phase space cut at zero velocity ($\dot{\theta} = 0$ and $\dot{\phi} = 0$) for $h = 0.3$, $j = 0.5$, and $\alpha = 0.02$, which is plotted in Fig. 14.14 b) - e). There are four distinct Lyapunov exponents Λ_i ($i = 1, 2, 3, 4$ from greatest to smallest), since our dynamical system, and thus the phase space is four-dimensional.

It is divided into basins of attraction, related to the two stable fixed points (green dots in plot b)), which correspond to the same physical state since we deal with an antiferromagnet, and the chaotic sea, which is triggered by the unstable fixed points (red dots in plot b)). Here, the largest Lyapunov exponent is positive, correspondingly the smallest
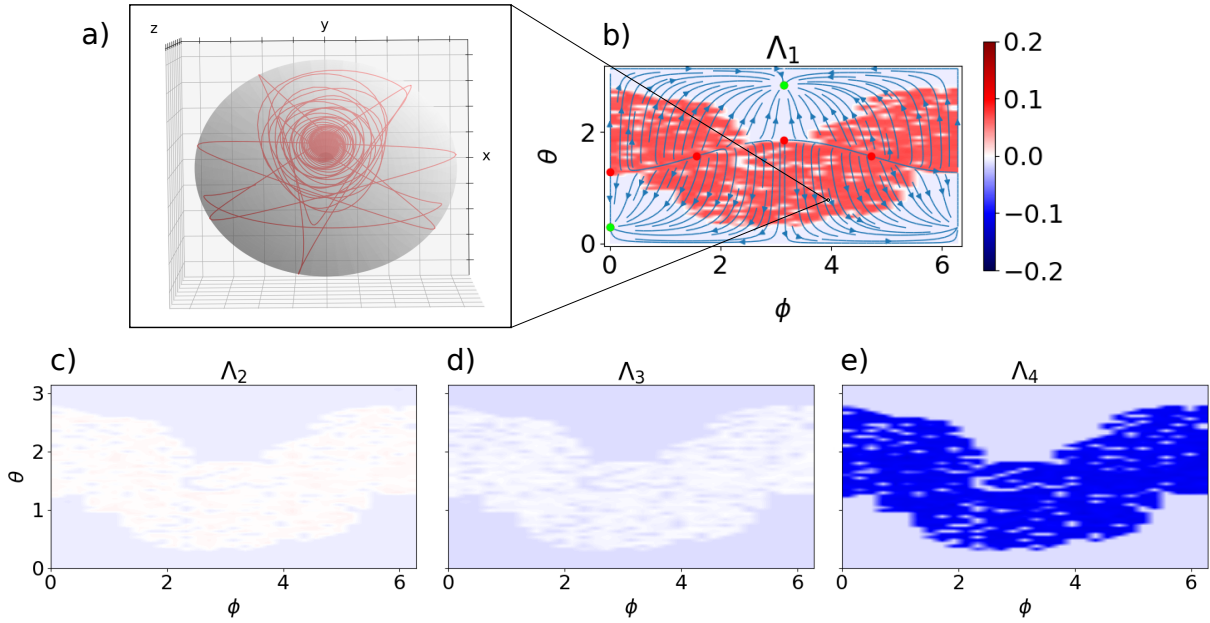
Figure 14.14.: Lyapunov spectrum b) - e) over a cut of phase space at zero velocity and for $h = 0.3$, $j = 0.5$ and $\alpha = 0.02$. Phase space is divided into basins of attraction, surrounding the stable fixed points (green dots in b)), and a chaotic sea as indicated by a positive largest Lyapunov exponent Λ_1 (red area in b)). The latter is intercepted by small regular islands of regular dynamics forming a fractal pattern, where all four Lyapunov exponents are negative due to damping and the orbits are converging the either fixed points as for the example shown in a).

Lyapunov exponent is negative, and the remaining two Lyapunov exponents are zero, which is the signature of a strange attractor. Due to damping, all four Lyapunov exponents are negative within the basins of attraction and small regular islands, intercepting the chaotic sea and forming a fractal structure. For these particular initial conditions, the orbits converge to either fixed point, as shown by the example orbit in plot a). These regular islands vanish upon increased damping α.

Plot b) shows, in addition, the phase portrait plot of $\vec{f}_{\text{red}}$, depicted by blue arrow lines flowing from the unstable towards the stable fixed points. They visualize the acceleration the Néel vector experiences at zero velocity and give some intuition about the linear dynamics around the fixed points as discussed above.

To further elucidate the onset of chaos depending on the initial conditions on the unit sphere, we took a cut at $\phi = 1.5$, for $j = 0.5$ and $\alpha = 0.02$ as before and iterated the Lyapunov spectrum over the magnetic field h and the angle θ. The result is displayed in Fig. 14.15 b) - e). In addition, plot a) shows the values of the largest Lyapunov exponent Λ_1 at $\theta = 1.58$. These plots indicate another critical magnetic field $h_{c_0} \approx 0.17$, where the largest Lyapunov exponent Λ_1 jumps from zero to a positive value and chaos occurs. Within the chaotic sea, its value increases linearly, apart from regular islands that we observed before, where orbits are regular or at least Λ_1 is greatly reduced for these particular initial conditions. As expected, Λ_1 stays negative in the surrounding basins

of attraction. The chaotic sea is growing with increased magnetic field h, at first slowly but then rather quickly, taking over the entire unit sphere even before reaching the first critical magnetic field $h_{c_1} = \sqrt{1-j} = \frac{1}{\sqrt{2}} \approx 0.7071$.
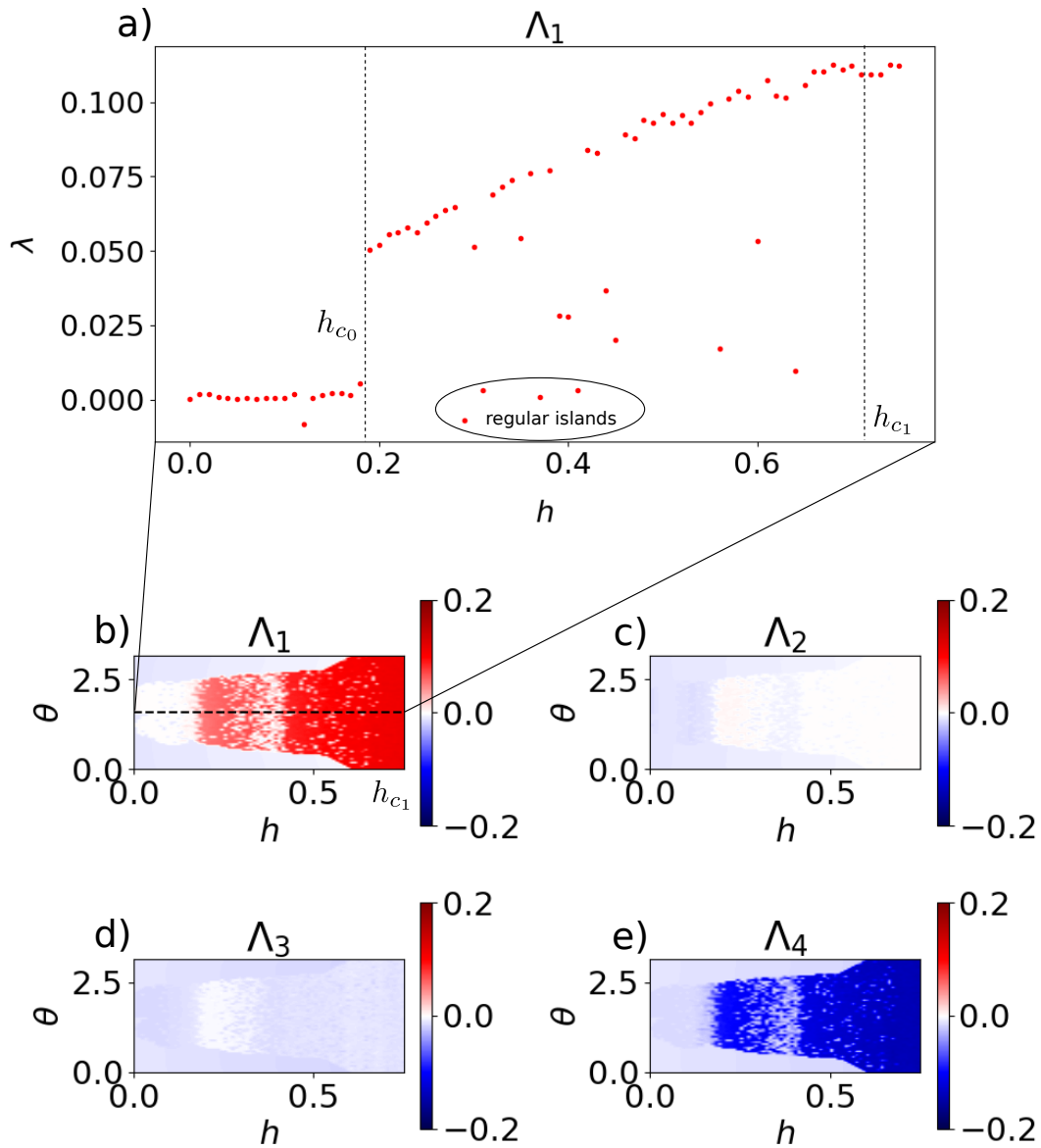
Figure 14.15.: Transition to chaos shown by the Lyapunov spectrum in b) - e) for $\varphi = 1.5$, $j = 0.5$, and $\alpha = 0.02$. In addition, the value of the largest Lyapunov exponent Λ_1 is plotted in a). Chaos appears rather abruptly at an additional critical magnetic field h_{c_0}, where Λ_1 jumps from zero to a positive value and increases linearly from there on – apart from regular islands for particular initial conditions.

Lyapunov Spectrum over Parameter Space

Next, we determined the Lyapunov spectrum over parameter space for $\alpha = 0.1$, which is the main result of this project. This was done just for a single representative damping value due to the tremendous numerical effort involved.

To avoid singularities in the numerics due to limit cycles passing through the poles at small magnetic field h, the rotated frame of reference was employed for $0 \leq h \leq 1$ with initial conditions $\tilde{\theta}(0) = \frac{\pi}{2}$, $\tilde{\phi}(0) = 0$ corresponding to solution A at zero current j. Standard spherical coordinates were employed for $h > 1.0$ with initial conditions $\theta(0) = \frac{\pi}{2}$, $\phi(0) = 0$, as the manifold of solutions B for zero current coincides with the equator.

The result is displayed in Fig. 14.16, where the boundary of linear stability (critical current $j_{\mathrm{c}} = |1 - h^2|$) is indicated as a solid black line and the threshold of in-plane oscillations j_{osc} is plotted as a dashed black line. The Lyapunov exponents characterize different dynamical regimes according to their signature, i.e. whether they are positive, zero, or negative: $(-, -, -, -)$ indicates a fixed point, $(0, -, -, -)$ a limit cycle, $(0, 0, -, -)$ quasi-periodic dynamics on a torus, $(+, 0, -, -)$ chaotic dynamics on a strange attractor, and $(+, +, 0, -)$ indicates hyper-chaos.

For small magnetic field h/small currents j, the initial condition lie within a basin of attraction, and all four Lyapunov exponents are negative. However, as we saw from the investigation of the Lyapunov spectrum over phase space, the chaotic sea grows upon increasing the magnetic field h (or the current j), and at some point, the initial conditions start lying within the chaotic sea. Thus, the largest Lyapunov exponent turns positive even below the critical current (solid black line). Choosing different initial conditions would advance or postpone the onset of chaos and alter Fig. 14.16. They were chosen here in a way to model actual experiments observing the nano-oscillators dynamics after switching on a spin current j.

For $h > 1.0$ and below the critical current j_{c} (solid black line), the dynamics are regular, i.e. the largest Lyapunov exponent is negative, but it turns zero below j_{osc}, indicating the onset of in-plane oscillations.

Above the critical current j_{c} there are two regimes: for small magnetic fields, the largest Lyapunov exponent is zero, and the remaining Lyapunov exponents are negative, as the Néel vector settles on the previously determined limit circle. For larger magnetic fields, the largest Lyapunov exponent Λ_1 turns positive, as the limit cycle becomes unstable, and a vast chaotic region takes up parameters space above j_{c}. The transition from this limit cycle into the chaotic region is investigated in the following section by means of bifurcation diagrams. The chaotic realm is intercepted by periodic windows, where Λ_1 turns zero, and the spin-torque oscillator settles on some limit circle.

The same limit cycle as for small magnetic fields and $j > j_c$ is present right at the spin-flop transition $h = 1$. Its stability over a large range of spin currents strengths j was previously shown by analyzing the Floquet multipliers of the monodromy matrix. Here, it appears as a vertical, white stripe in the plot of Λ_1; There is only one chaotic section for $1.615 < j < 1.824$ in agreement with Fig. 14.12.
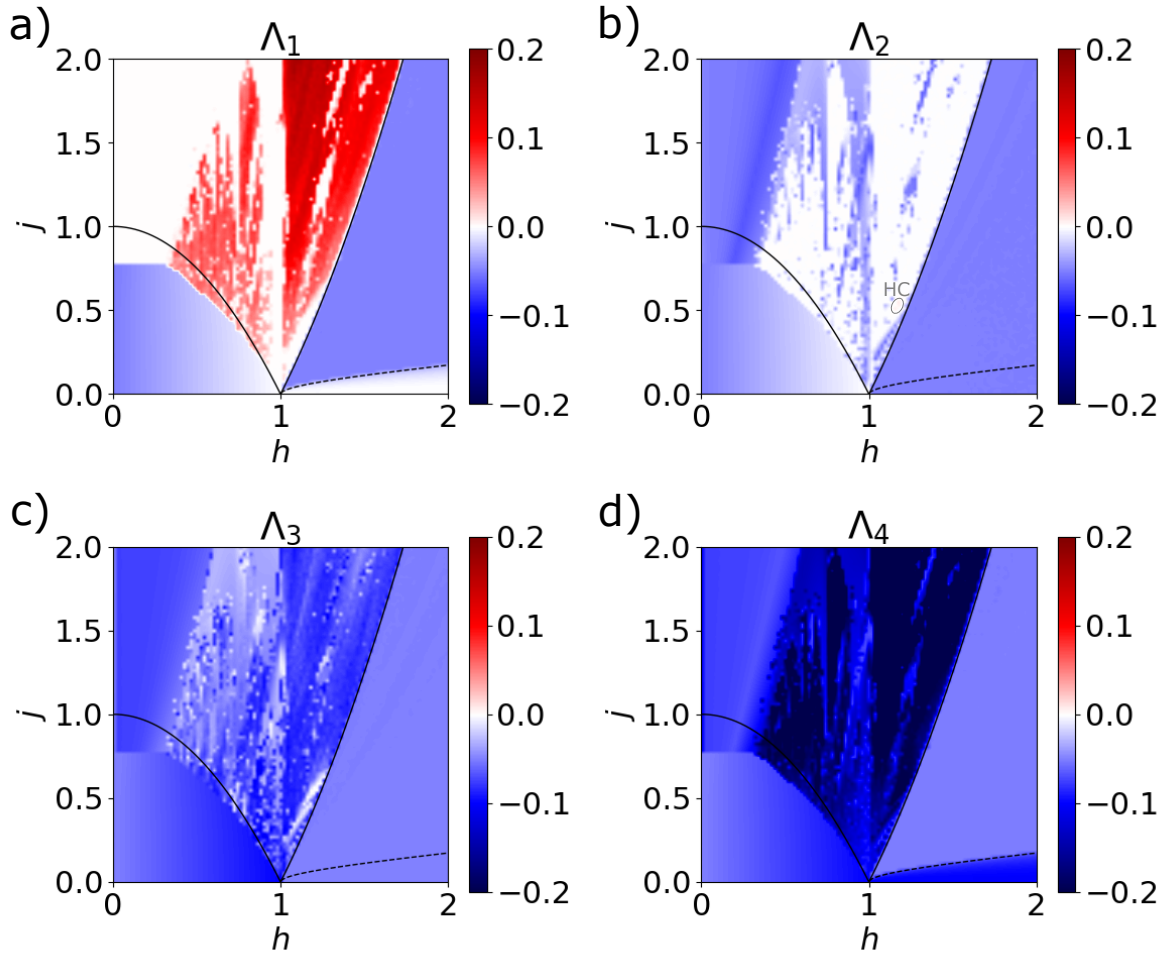
Figure 14.16.: Lyapunov Spectrum Λ_i over parameter space for $\alpha = 0.1$, where the critical current j_c (boundary of linear stability) is plotted as a solid black line and the threshold of in-plane oscillations j_{osc} is plotted as a dashed black line. Below j_c, the dynamics are mostly regular (negative largest Lyapunov exponent in plot a)), while above j_c, the Néel vector either settles on some limit circle (zero largest Lyapunov exponent) or forms a strange attractor (positive largest Lyapunov exponent in plot a)). A small region of hyper-chaos is marked by a grey circle and "HC". Further description and details on the numerics are given in the main text.

As the critical current vanishes at the spin-flop transition, the threshold current for the appearance of chaos is particularly low within its vicinity. In addition, there is a small region of hyper-chaos, denoted in Fig. 14.16 by a grey circle and 'HC.' The transition to chaos in this realm, involving different limit cycles, quasiperiodic dynamics, Andronov-Hopf and Neimark-Sacker bifurcations, and the small region of hyper-chaos, was investigated in our publication [341].

Average Magnetization

Different regimes of dynamics in parameter space can be characterized according to the average magnetization induced by the external magnetic field and the motion of the Néel vector $\hat{l}$. Unlike $\hat{l}$, $\vec{m}$ can be probed in experiments, and its dynamics are reflected in the frequency spectrum of the electromagnetic radiation emitted by the nano-oscillator.

In dimensionless units, equation (E.23) takes the form

$$\vec{m} = (\dot{\vec{l}} + \vec{l} \times \vec{h}) \times \vec{l} \tag{14.29}$$

i.e. the strength of the average magnetization is driven by large external magnetic fields $\vec{h} = h\hat{z}$ and large spin currents, i.e. a high frequency of oscillation, and thus a large $\dot{\vec{l}}$. The strength and the components of the average magnetization are plotted over parameter space in Fig. 14.17 for $\alpha = 0.1$; the critical current j_c (boundary of linear stability) is plotted as a solid black line.

According to (14.29), the static solution A possesses the static magnetization

$$\vec{m}_A = \frac{h}{2}\left[-\frac{j}{j_c}\hat{x} + \left(1 - \sqrt{1 - \frac{j^2}{j_c^2}}\right)\hat{z} \right] \tag{14.30}$$

Likewise, the static solution B possesses the static magnetization $\vec{m}_B = h\hat{z}$. Their increase with h can be seen by the color gradient below the critical current in Fig. 14.17 b) and c); $|\vec{m}_B|$ is noticeably larger and exactly parallel to the external magnetic field. The limit cycle (14.24), which is present for small h and large j, and at $h = 1.0$, induces according to (14.29) the time-dependent magnetization

$$\vec{m}_{LC} = \Omega(\hat{\varepsilon} \times \hat{z}) - \frac{h}{2}\sin(2\Omega t)\hat{\varepsilon} + h\sin^2(\Omega t)\hat{z} \tag{14.31}$$

with $\hat{\varepsilon} = \cos(\phi_0)\hat{x} + \sin(\phi_0)\hat{y}$. If the doubled frequency 2Ω is present in the spectra of the nano-oscillator's emitted electromagnetic radiation, its dynamics follow the limit cycle (14.24). The time-average magnetization is given by the first term and is oriented perpendicular to the external magnetic field.

Within chaotic regimes, the magnetization dynamics are more complicated; an example is shown in Fig. 14.17 a). However, the strength and orientation of the average magnetization are solely determined by the control parameters h, j, and α, i.e. they are a unique property of the respective attractor.
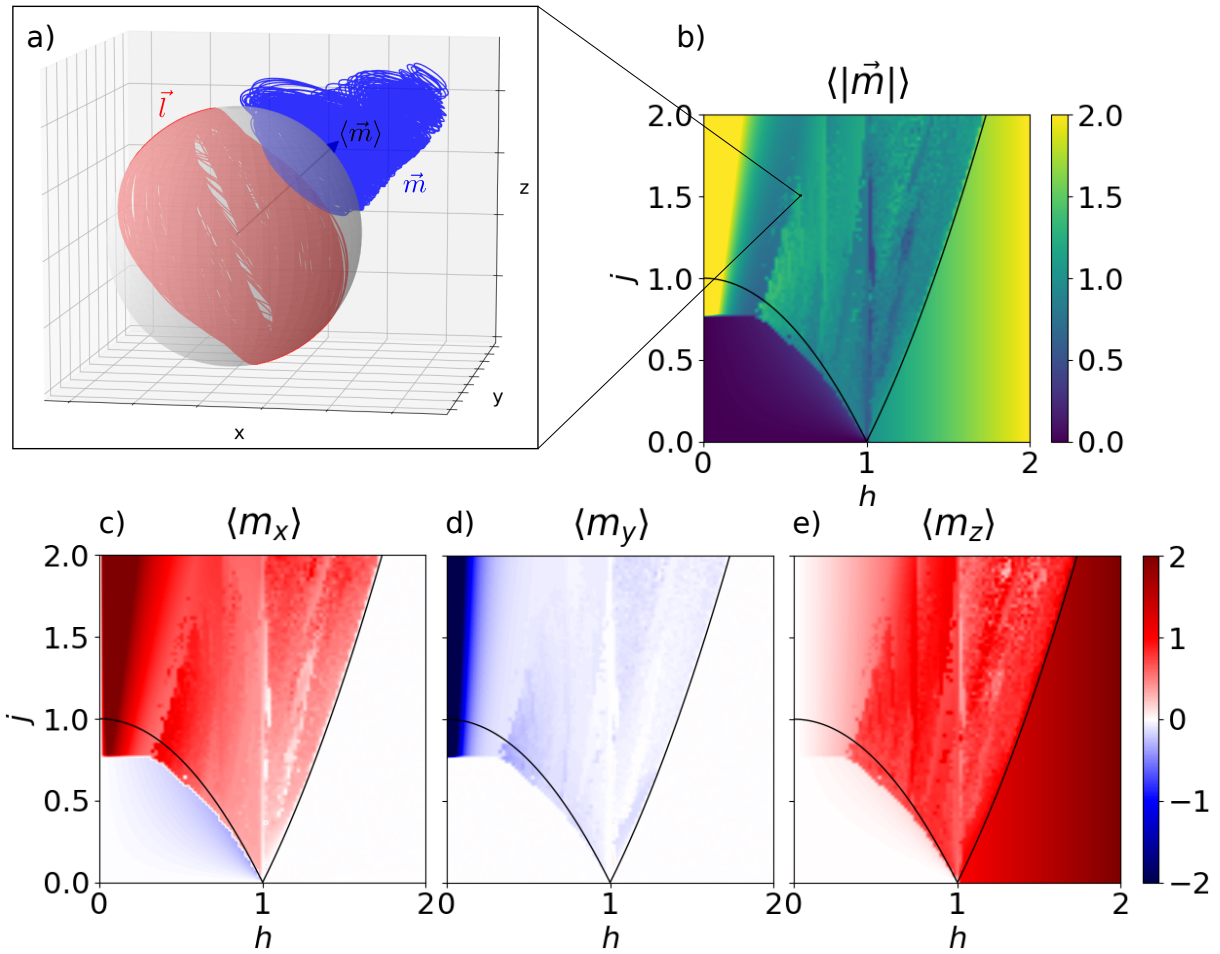
Figure 14.17.: a) Example trajectory and induced magnetization within the chaotic region at $h = 0.6$, $j = 1.5$, $\alpha = 0.05$. b) - e) Average magnetization over parameter space for $\alpha = 0.1$, where the critical current j_c (boundary of linear stability) is plotted as a solid black line. Different dynamical regimes, i.e. static solutions, stable limit cycles, and chaotic dynamics can be distinguished by the generated average magnetization.

Bifurcation Diagrams

The transition to chaos can be mapped out using bifurcation diagrams, which were recorded for the oscillators angular frequency ω_l. Using the parameterization $\vec{l}(t) = (\cos(\phi)\hat{x} + \sin(\phi)\hat{y})\sin(\theta) + \cos(\theta)\hat{z}$, it is given by

$$\omega_l = |\dot{\vec{l}}(t)| = \sqrt{\dot{\theta}^2 + \dot{\phi}^2 \sin^2(\theta)} \tag{14.32}$$

Orbits were evolved in time, and after relaxation (about 10,000 time steps), the maxima in the oscillator's frequency were recorded (the last 200 maxima in the time series), which was done for various initial conditions. Here, a single point corresponds to just one maximal frequency, i.e. an orbit with a single period. Two points correspond to two

different maximal frequencies and thus a two-periodic orbit or a single-periodic orbit with two maxima in the frequency. On the contrary, many points indicate a range of frequencies and thus unstable, chaotic motion.

The results for $j = 1.5$, $\alpha = 0.02$, and initial conditions $\theta(0) = 1.5$, $\phi(0) = 1.8$ within the chaotic sea are shown in Fig. 14.18. The nano-oscillator is tuned for increasing magnetic fields from a limit circle (1) into a chaotic regime (2). The bifurcation diagram in the maximal oscillator's frequency in plot a) reveals an abrupt transition to a strange attractor. The simultaneously recorded Lyapunov spectrum shows in plot b) that the largest Lyapunov exponent turns positive within the chaotic realm. It is intercepted by windows of regular limit cycles (3) with a period of three or higher. The transition is qualitatively the same below the critical current and when tuning the current strength j.
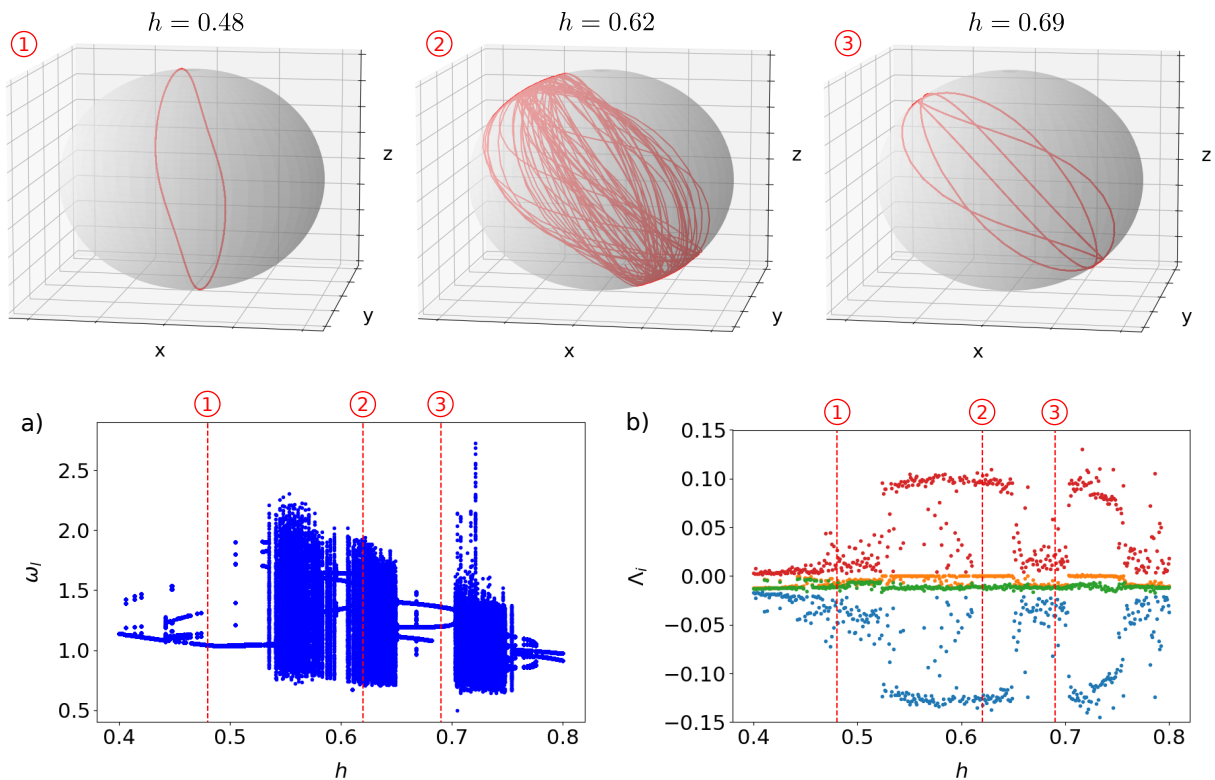
Figure 14.18.: Transition to chaos at $j = 1.5$, $\alpha = 0.02$ and starting points within the chaotic sea at $\theta(0) = 1.5$, $\phi(0) = 1.8$: Plot a) shows a bifurcation diagram in the maximal oscillator frequency. Plot b) shows the corresponding Lyapunov spectrum. The largest Lyapunov exponent is zero for a limit cycle (1) and becomes positive within the chaotic regime (2), which is intercepted by periodic windows (3).

14.3 Control of Chaos (Large Damping)

Period Halving

As the damping constant α increases, we observe that chaos gets controlled by period halving bifurcations. Revisiting the bifurcation diagram of the maximal oscillator's frequency for $\alpha = 0.2$ leads to the plot displayed in Fig. 14.19 a). Plot b) shows the corresponding Lyapunov spectrum.

At small magnetic fields, a limit cycle (1) is present. At around $h = 0.5$, a bifurcation occurs, leading to two distinct maxima in the oscillator's frequency, as the symmetry $\hat{l} \rightarrow -\hat{l}$ of limit cycle (1) gets broken and the limit cycle (2) occurs. There are two distinct attractors present, which are energetically equivalent and induce the same magnetization $\vec{m}$. Either of them is reached depending on the initial conditions, and one of them is shown in (2).
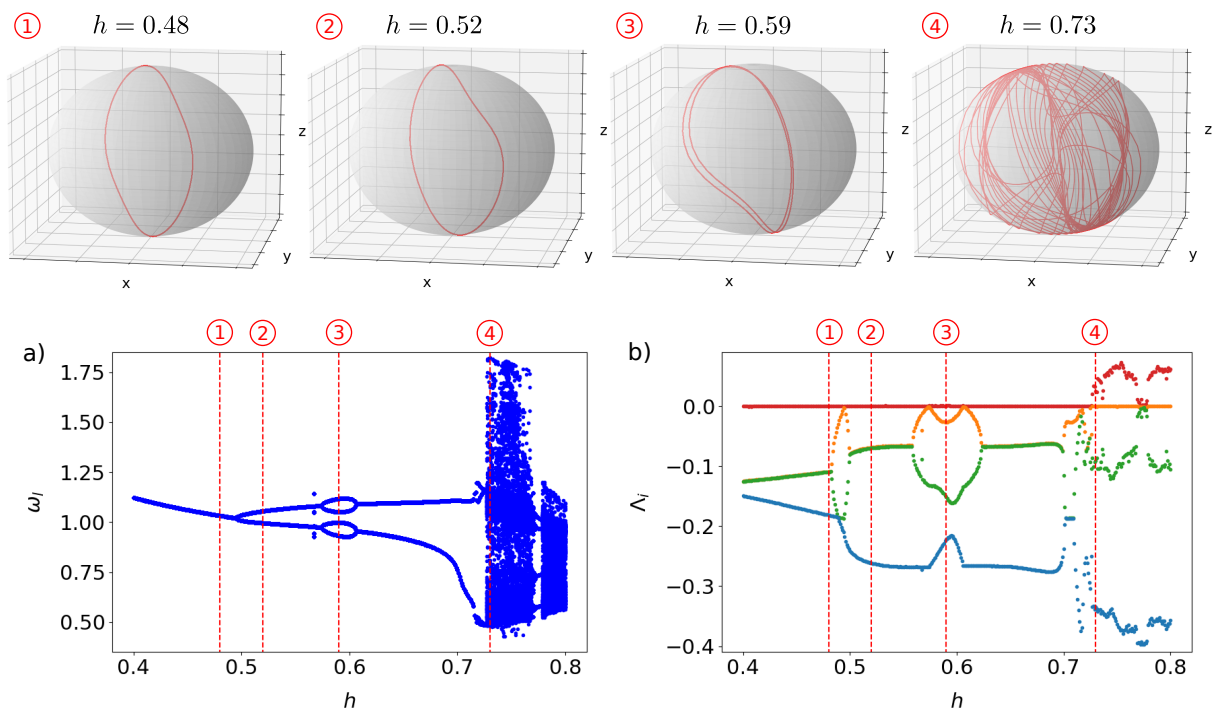
Figure 14.19.: Control of chaos demonstrated for $j = 1.5$, $\alpha = 0.2$ and starting points within the chaotic sea at $\theta(0) = 1.5$, $\phi(0) = 1.8$: a) Bifurcation diagram of the oscillator frequency ω_l in arbitrary units. b) Corresponding Lyapunov spectrum: only for larger magnetic field the largest Lyapunov exponent becomes positive which coincides with the onset of chaos (4) in the bifurcation diagram. At small magnetic fields, a limit cycle (1) is present, whose inversion symmetry gets broken (2) by the first bifurcation. The second bifurcation leads to period-doubling (3), while a subsequent third bifurcation leads to period-halving. The red lines indicate the magnetic fields of the example orbits (1) - (4), not the position of the bifurcations.

At about $h = 0.58$, an actual period-doubling bifurcation occurs, i.e. the limit cycle (2) doubles its period and results in the limit cycle (3). This is followed by a period-halving bifurcation at $h = 0.6$, which gives the original limit cycle (2) and indicates control of chaos. Similarly, the Lyapunov spectrum in plot b) shows that the largest Lyapunov exponent remains zero in this entire regime.

Only when the magnetic field h is increased further, at about $h = 0.72$, an abrupt transition to chaos occurs in a), accompanied by the largest Lyapunov exponent becoming positive in b). The chaotic region is then a four-period window, where the largest Lyapunov exponent drops back to zero.

Period halving bifurcations have been observed before, e.g. in [342] for an ecological model of immigration, represented by a 1D map. If the 1D map has the shape of a universal function, Feigenbaum's theory describes the period-doubling route to chaos. However, if the 1D map has a plateau for large values, instead, period-halving bifurcations occur as the corresponding fixed point regains stability.

Continuous systems can be related to 1D maps by taking an appropriate Poincaré section within the chaotic realm, which leads to a Lorenz map. If this Lorenz map is shaped like a universal function, then also the chaotic behavior of the continuous system is described by Feigenbaum's theory [334, 343, 344].

For our spin-torque nano-oscillator, we face two issues in this respect: On the one hand, the Poincaré section can only be taken within the chaotic regime, i.e. not in the realm where the period-halving bifurcation occurs. This prevents checking whether the resulting Lorenz map had a plateau. On the other hand, plotting the Lorenz map within the chaotic region led to a point cloud rather than a clearly defined function, which gave us a hint that the Lorenz map might not be one-dimensional and that also the strange attractor within the chaotic regime might not be flat (two-dimensional). Therefore, we will look at the attractor's Lyapunov dimension in the following section.

Lyapunov Dimension

We determined the Lyapunov dimension from the Lyapunov exponents, arranged from greatest to smallest $\Lambda_1 \geq \Lambda_2 \geq \cdots \geq \Lambda_n$ so that according to the Kaplan-Yorke conjecture [336, 337, 345, 346]

$$D = j + \frac{\sum_{i=1}^{j} \Lambda_i}{|\Lambda_{j+1}|} \tag{14.33}$$

where j is the index for which $\sum_{i=1}^{j} \Lambda_i \geq 0$ and $\sum_{i=1}^{j+1} \Lambda_i < 0$. The Lyapunov dimension gives a lower bound for the informational dimension D_1 of the strange attractor.

In Fig. 14.20 the evolution of the Lyapunov dimension with increasing damping constant α for a) $h = 0.3$, $j = 0.5$ (below the critical current) and b) $h = 1.1$, $j = 1.8$ (above the critical current) is displayed. In case a) the attractor becomes almost flat around $\alpha = 0.09$ (the regime where Feigenbaum theory may apply). However, due to the large damping period-doubling bifurcations are followed by period-halving bifurcations, as we have seen

in Fig. 14.19, and for even larger α chaos breaks down, i.e. the orbits settle on some fixed point, and the Lyapunov dimension becomes zero. In case b), the strange attractor remains non-flat even for large α, giving rise to non-Feigenbaum chaotic behavior.

These two examples are illustrative of the general oscillator dynamics. Within the chaotic regime, both above and below the critical current, the strange attractor remains high-dimensional. Here, Feigenbaum theory does not apply, and the chaos mechanisms for higher-dimensional attractors are yet to be investigated further. In our publication [341] we found that a series of Andronov-Hopf and Neimark-Sacker bifurcations lead to the occurrence of chaos and even hyperchaos.

The strange attractor may also become increasingly flat. However, since the damping is very high, period-halving instead of period-doubling bifurcations occur, leading to control and, finally, even to the breakdown of chaos.
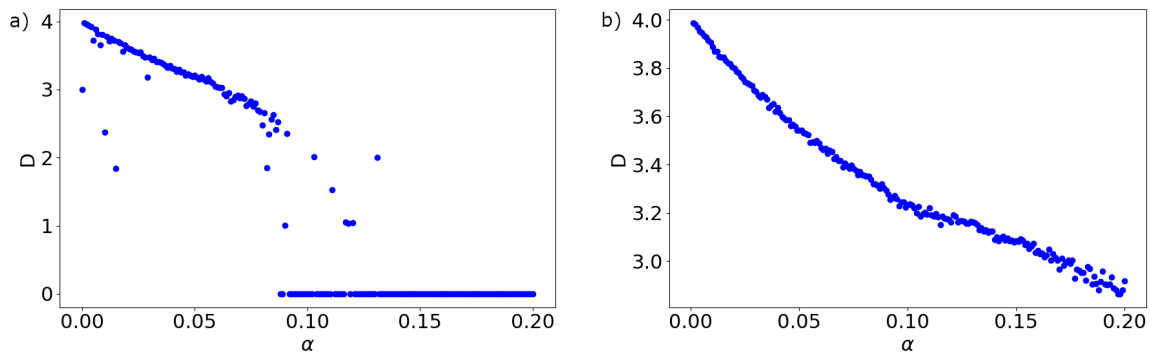
Figure 14.20.: Lyapunov dimension depending on the damping α for a) $h = 0.3$, $j = 0.5$ (below the critical current) and b) $h = 1.1$, $j = 1.8$ (above the critical current). In case a) the attractor becomes almost flat around $\alpha = 0.1$, but due to the large damping period-doubling bifurcations are followed by period-halving bifurcations, and for even larger α chaos breaks down, and the orbits settle on some fixed point (the Lyapunov dimension becomes zero). In case b), the strange attractor remains non-flat even for large α, giving rise to non-Feigenbaum chaotic behavior.

15 Summary & Outlook

In summary, the dynamical regimes of an AFM spin-torque nano-oscillator were investigated theoretically, where the spin current polarization points perpendicular to an external magnetic field and the magnetic field is applied along an easy axis. Within this setup, different limit cycles, quasiperiodic dynamics, and even chaos and hyperchaos develop intrinsically.

At first, we investigated the static, uniform ground state solutions of the antiferromagnet. Without a spin current, the Néel vector points along the easy-axis in z-direction, which represents a stable equilibrium. The equator corresponds to a manifold of unstable equilibria. At a magnetic field of $h = 1$, a spin-flop transition occurs, the Néel vector flips into the x-y-plane due to the easy-plane anisotropy induced by the magnetic field. It possesses in-plane rotational symmetry and corresponds to a manifold of stable equilibria. The same spin-flop transition was already investigated in the first project in a different context (see section 2.1).

A finite spin current with polarization $\hat{p}$ along the $-y$-axis breaks this rotational symmetry and leads to three distinct physical states below a critical current j_c: the stable ground state solution A gets tilted off the easy axis by an angle θ_0. Simultaneously, the manifold of unstable equilibria around the equator breaks up, and two distinct unstable solutions remain: Solution A′ lies within x-z-plane and is tilted off the x-axis by $-\theta_0$, while solution B is anti-parallel to the spin current polarization $\hat{p}$ and points in y-direction (see Fig. 14.2 for an overview of all three solutions).

The spin current also introduces the critical current $j_c = |1 - h^2|$, beyond which no stable static solution prevails, and different regimes of regular and chaotic motion occur. Looking at two-dimensional phase portrait cuts of the four-dimensional dynamic system our nano-oscillator constitutes, one can see that solutions A and A′ collide in a saddle-node-bifurcation upon reaching the critical current j_c.

The stability realm of these three equilibria was established by a linear stability analysis, which also determined the eigenfrequency spectrum of the nano-oscillator (eigenfrequency of the respective stable solution), displayed in Fig. 14.5. For zero magnetic field, the eigenfrequency $\omega = 1$ as it is measured in units of the uniform antiferromagnetic resonance. With spin current, without damping, and for increasing magnetic field h, two branches separate linearly according to $\omega = 1 \pm h$. Above the spin-flop transition, there are two gapless modes: one increases like $\omega = \sqrt{h^2 - 1}$ and the other stays zero, reflecting the in-plane rotational symmetry of solution B around the equator.

This rotational symmetry gets broken for finite spin current, and the corresponding branch gets lifted off the x-axis while approaching the latter for $h \to \infty$. Interestingly, for finite damping, this mode becomes zero again already at a finite magnetic field h_{osc}, as in-plane oscillations become overdamped. A finite spin current also opens up a gap in the eigenfrequency spectrum between the two critical fields $h_{c_1} = \sqrt{1 - j}$ and $h_{c_2} = \sqrt{1 + j}$, which derive directly from the critical current j_c, as no stable ground state solution exist.

Above the critical current j_c, various dynamical regimes exist, which we characterized by calculating the Lyapunov spectrum over a vast range of parameters (see Fig. 14.16), which is the main result of this project. Since the nano-oscillator constitutes a four-dimensional dynamical system, there are four distinct Lyapunov exponents Λ_i ($i = 1, 2, 3, 4$ from greatest to smallest), and their signature, i.e. whether they are positive, zero, or negative, distinguishes different types of dynamics: $(-, -, -, -)$ indicates a fixed point, $(0, -, -, -)$ a limit cycle, $(0, 0, -, -)$ quasi-periodic dynamics on a torus, $(+, 0, -, -)$ chaotic dynamics on a strange attractor, and $(+, +, 0, -)$ indicates hyper-chaos.

Chaotic dynamics occur for a vast range of magnetic fields h and spin current strengths j, above and also below the critical current: The linear stability just showed that a ground state solution exists that is stable with respect to linear deviations. However, far from it, chaotic dynamics may occur even below the critical current for suitable initials conditions (see Fig. 14.14): phase space gets divided into basins of attraction, where orbits settle at the stable ground state solution, and a chaotic sea, where the largest Lyapunov exponent Λ_1 is positive. Interestingly, the chaotic sea is intercepted by small regular islands that form a fractal pattern and which represent very specific initial conditions for which orbits still settle at the stable equilibrium.

The transition to chaos above the critical current, involving different limit cycles, quasiperiodic dynamics, Andronov-Hopf and Neimark-Sacker bifurcations, and even including a small region of hyper-chaos, was investigated in our publication [341].

The various dynamical regimes could also be characterized by the small magnetization induced by the external magnetic field h and the motion of the Néel vector: its strength and orientation only depend on the external parameters for a given attractor (see Fig. 14.17). The spectrum of the emitted electromagnetic radiation can be directly probed by experiments.

The realm of the spin-flop transition at $h = 1$ is special, as the critical current j_c vanishes, and thus the threshold current for the appearance of chaos is particularly low in its vicinity. However, right at the spin-flop transition, a limit cycle is present, whose stability was confirmed using the monodromy matrix technique for a large range of spin current strengths j (see Fig. 14.12). The same limit cycle occurs above the critical current j_c for tiny magnetic fields $h \ll 1$. It lies initially within the x-z-plane at $h = 0$ and turns its plane of rotation with increasing magnetic field (see Fig. 14.11).

The transition to chaos from this limit cycle for increasing magnetic field h and above the critical current at $j = 1.5$ was investigated using bifurcation diagrams in the maxima of the nano-oscillators frequency. For small damping ($\alpha = 0.02$), chaos sets in abruptly, while being intercepted by periodic windows (see Fig. 14.19). For large damping ($\alpha = 0.2$), chaos gets controlled over a larger range of parameters: As the bifurcation diagram in Fig. 14.19 a) shows, period-doubling bifurcations are followed by period-halving bifurcations, preventing the onset of chaos.

A calculation of the Lyapunov dimension, approximating the informational dimension of a strange attractor according to the Kaplan-Yorke conjecture [336, 337, 345, 346], showed that the chaos in this realm is high-dimensional for small damping. For larger damping, the attractors become increasingly flat, i.e. their Lyapunov dimension is reduced. In the realm of damping, where the strange attractors are quasi-two-dimensional, and chaos

could possibly be explained through Feigenbaum's theory of period-doubling bifurcations, the latter gets controlled by period-halving bifurcations or chaos even breaks down – due to the large damping.

The various dynamics of the antiferromagnetic nano-oscillator investigated in this project are not only interesting from a fundamental point of view, e.g. for understanding how chaos unfolds in high-dimensional dynamical systems. Particularly interesting to applications is the realm of the spin-flop transition. Here, a stable limit cycle is present, but at the same time, the threshold current for the appearance of chaos is low. As shown in previous studies, a spin-torque nano-oscillator operated on a stable limit cycle may emulate a single neuron [279], or even a small neural network [281]. More recent studies showed that also chaos may assist with magnetic switching in nonvolatile magnetic memory elements [290] or designing novel neural networks based on stochastic computing [291].

In this project, we investigated the dynamics only for the uniform state of an easy-axis antiferromagnet. However, also non-uniform magnetic textures such as antiferromagnetic bimerons [295] feature chaotic dynamics, and future research may investigate e.g. the dynamics of domain walls and other non-uniform magnetic textures that are also directly relevant to applications.

Also, the dynamical system that the nano-oscillator of this project constitutes could be studied more generally, as the Lyapunov spectrum over parameter space (see Fig. 14.16) depends on whether trajectories are starting within a basin of attraction or the chaotic sea. In addition, one could account for biaxial anisotropy, which is always present in experiments and may be relevant for small magnetic fields. We included a short discussion of biaxiality in our publication [341], but it could be further elaborated by future research.

A Point Groups and DMI–Tensor

A point group G is the group of symmetry operations σ that leave at least one point of the crystal lattice unchanged: $\exists x : \forall \sigma \in G : \sigma x = x$. A point group includes rotations, inversions, and combinations thereof and can be represented by matrices whose determinant is ± 1. Thus, the point group defines the symmetry of the crystal lattice, whereas the space group defines the symmetry of the configuration space, i.e. the actual crystal.

In the following, we will give the general form of the DMI tensor $\hat{D}$ for 2D chiral ferromagnets and the structure of the resulting free energy density. This was analyzed previously in [111] for 2D and in [20] for 3D chiral ferromagnets.

Rashba SOC

For Rashba spin-orbit coupling the DMI-tensor takes the form

$$\hat{D} = -D\hat{e}_z \times = -D\hat{J}_z = -D \begin{pmatrix} 0 & -1 & 0 \\ 1 & 0 & 0 \\ 0 & 0 & 0 \end{pmatrix} \tag{A.1}$$

where $\hat{J}_z$ is the generator of rotations around the z-axis. The resulting free energy density reads

$$\mathcal{F}_{\mathrm{cal}} = (M_3 \partial_1 M_1 - M_1 \partial_1 M_3) - (M_2 \partial_2 M_3 - M_3 \partial_2 M_2) \tag{A.2}$$

It corresponds to the 2D-version of the w_1 energy density functional in [20] and it belongs to the C_{nv} point group. As an example, the free energy density is invariant under symmetry operations by the point group C_{4v}:

1) two vertical mirror planes σ_v

- reflection at the y-z-plane: $\partial_1 \to -\partial_1$, $M_1 \to -M_1$

- reflection at the x-z-plane: $\partial_2 \to -\partial_2$, $M_2 \to -M_2$

2) two diagonal mirror planes σ_d

- reflection at the $x = y$ diagonal: $\partial_1 \to \partial_2$, $M_1 \to M_2$, $\partial_2 \to \partial_1$, $M_2 \to M_1$

- reflection at the $x = -y$ diagonal: $\partial_1 \to -\partial_2$, $M_1 \to -M_2$, $\partial_2 \to -\partial_1$, $M_2 \to -M_1$

3) C_4-rotational symmetry around the z-axis: $\vec{M}' = \hat{C}_4 \vec{M}$ with

$$\hat{C}_n = \begin{pmatrix} \cos\left(\frac{2\pi}{n}\right) & \sin\left(\frac{2\pi}{n}\right) & 0 \\ -\sin\left(\frac{2\pi}{n}\right) & \cos\left(\frac{2\pi}{n}\right) & 0 \\ 0 & 0 & 1 \end{pmatrix} \tag{A.3}$$

Dresselhaus SOC

For Dresselhaus spin-orbit coupling the DMI tensor takes the form

$$\hat{D} = -D\hat{\lambda}_1 = -D \begin{pmatrix} 0 & 1 & 0 \\ 1 & 0 & 0 \\ 0 & 0 & 0 \end{pmatrix} \tag{A.4}$$

The resulting free energy density reads

$$\mathcal{F}_{\text{DMI}} = -(M_3 \partial_1 M_1 - M_1 \partial_1 M_3) - (M_2 \partial_2 M_3 - M_3 \partial_2 M_2) \tag{A.5}$$

It corresponds to the 2D-version of the w_2' energy density functional in [20] and it is invariant under symmetry operations by the point group D_{2d}, which are given here as an another example:

1) two diagonal mirror planes σ_d

- reflection at the $x = y$ diagonal: $\partial_1 \to \partial_2$, $M_1 \to M_2$, $\partial_2 \to \partial_1$, $M_2 \to M_1$

- reflection at the $x = -y$ diagonal: $\partial_1 \to -\partial_2$, $M_1 \to -M_2$, $\partial_2 \to -\partial_1$, $M_2 \to -M_1$

2) C_2-rot. symmetry around the z-axis: $\partial_1 \to -\partial_1$, $M_1 \to -M_1$, $\partial_2 \to -\partial_2$, $M_2 \to -M_2$
3) C_2'-rotational symmetry

- around the x-axis: $\partial_2 \to -\partial_2$, $M_2 \to -M_2$, $\partial_3 \to -\partial_3$, $M_3 \to -M_3$

- around the y-axis: $\partial_1 \to -\partial_1$, $M_1 \to -M_1$, $\partial_3 \to -\partial_3$, $M_3 \to -M_3$

4) S_4-symmetry (C_4-rotation followed by inversion) around the z-axis:
$\partial_1 \to \partial_2$, $\partial_2 \to -\partial_1$, $\partial_3 \to -\partial_3$, $M_1 \to M_2$, $M_2 \to -M_1$, $M_3 \to -M_3$

In-Plane $SO(2)$-symmetry

Here the DMI tensor reads $\hat{D} = -D\hat{1}$ and the resulting energy density functional is

$$\mathcal{F}_{\mathrm{DMI}} = -(M_2\partial_1 M_3 - M_3\partial_1 M_2) - (M_3\partial_2 M_1 - M_1\partial_2 M_3) \tag{A.6}$$

It corresponds to the 2D-version of the w_2 energy density functional in [20].

Mixed Rashba + Dresselhaus SOC

For mixed Rashba and Dresselhaus spin-orbit coupling the DMI tensor takes the form

$$\hat{D} = -D_R\hat{J}_z - D_D\hat{\lambda}_1 = \begin{pmatrix} 0 & D_R - D_D & 0 \\ -D_R - D_D & 0 & 0 \\ 0 & 0 & 0 \end{pmatrix} \tag{A.7}$$

and $D = \sqrt{D_D^2 + D_R^2}$. The resulting free energy density reads

$$\mathcal{F}_{\mathrm{DMI}} = (D_R - D_D)(M_3\partial_1 M_1 - M_1\partial_1 M_3) - (D_R + D_D)(M_2\partial_2 M_3 - M_3\partial_2 M_2) \tag{A.8}$$

It belongs to the C_{2v} point group.

Additional Symmetry classes

There are two more distinguished symmetry classes, which are mentioned for completeness:

- C_2 symmetry with the DMI tensor $\hat{D} = -D_0\hat{1} - D_1\hat{\lambda}_1 - D_z\hat{J}_z$
- reflection symmetry with $\hat{D} = -D\hat{n}_T\times$

B Fourier-Transformation of the Linear sigma model

To employ variational minimization (see section 3.2), the order parameter $\vec{\phi}$ is developed into a Fourier series. Together with the integral contained in the free energy $F = \int d^2r \, \mathcal{F}[\vec{\phi}]$ this effectively corresponds to a Fourier transformation. In the following, the Fourier transforms of the terms in the linear sigma model (3.1) are derived.

$$\int \mathrm{d}^2r \, \vec{\phi}^2(\vec{r}) = \int \mathrm{d}^2r \sum_{\vec{k_1},\vec{k_2}} e^{i\vec{k_1}\cdot\vec{r}+i\vec{k_2}\cdot\vec{r}} \vec{\phi}_{\vec{k_1}} \vec{\phi}_{\vec{k_2}} = \sum_{\vec{k_1},\vec{k_2}} \delta_{\vec{k_1}+\vec{k_2},\vec{0}} \, \vec{\phi}_{\vec{k_1}} \vec{\phi}_{\vec{k_2}} \tag{B.1}$$

$$\int \mathrm{d}^2r \, (\vec{\phi}^2(\vec{r}))^2 = \int \mathrm{d}^2r \sum_{\vec{k_1},\vec{k_2},\vec{k_3},\vec{k_4}} e^{i\vec{k_1}\cdot\vec{r}+i\vec{k_2}\cdot\vec{r}+i\vec{k_3}\cdot\vec{r}+i\vec{k_4}\cdot\vec{r}} \vec{\phi}_{\vec{k_1}} \vec{\phi}_{\vec{k_2}} \vec{\phi}_{\vec{k_3}} \vec{\phi}_{\vec{k_4}}$$
$$= \sum_{\vec{k_1},\vec{k_2},\vec{k_3},\vec{k_4}} \delta_{\vec{k_1}+\vec{k_2}+\vec{k_3}+\vec{k_4},\vec{0}} \, \vec{\phi}_{\vec{k_1}} \vec{\phi}_{\vec{k_2}} \vec{\phi}_{\vec{k_3}} \vec{\phi}_{\vec{k_4}} \tag{B.2}$$

$$\int \mathrm{d}^2r \, (\vec{\phi}(\vec{r}) \cdot \vec{h})^2 = \int \mathrm{d}^2r \sum_{\vec{k_1},\vec{k_2}} e^{i\vec{k_1}\cdot\vec{r}+i\vec{k_2}\cdot\vec{r}} (\vec{\phi}_{\vec{k_1}} \cdot \vec{h})(\vec{\phi}_{\vec{k_2}} \cdot \vec{h})$$
$$= \sum_{\vec{k_1},\vec{k_2}} \delta_{\vec{k_1}+\vec{k_2},\vec{0}} (\vec{\phi}_{\vec{k_1}} \cdot \vec{h})(\vec{\phi}_{\vec{k_2}} \cdot \vec{h}) \tag{B.3}$$

$$\int \mathrm{d}^2r \, (\partial_m \vec{\phi})^2 = \int \mathrm{d}^2r \left(i(\vec{k_1})_m \sum_{\vec{k_1}} e^{i\vec{k_1}\cdot\vec{r}} \vec{\phi}_{\vec{k_1}} \right) \left(i(\vec{k_2})_m \sum_{\vec{k_2}} e^{i\vec{k_2}\cdot\vec{r}} \vec{\phi}_{\vec{k_2}} \right)$$
$$= \sum_{\vec{k_1},\vec{k_2}} (-(\vec{k_1})_m(\vec{k_2})_m) \, \delta_{\vec{k_1}+\vec{k_2},\vec{0}} \, \vec{\phi}_{\vec{k_1}} \vec{\phi}_{\vec{k_2}} \tag{B.4}$$

$$\int \mathrm{d}^2 r \; \partial_m \vec{\phi} \cdot (\vec{e}_n \times \vec{\phi}) = \int \mathrm{d}^2 r \left(-i(\vec{k}_1)_m \sum_{\vec{k}_1} e^{i\vec{k}_1 \cdot \vec{r}} \vec{\phi}_{\vec{k}_1} \right) \cdot \vec{e}_n \times \left(\sum_{\vec{k}_2} e^{i\vec{k}_2 \cdot \vec{r}} \vec{\phi}_{\vec{k}_2} \right)$$

$$= \sum_{\vec{k}_1, \vec{k}_2} (-i(\vec{k}_1)_m) \, \delta_{\vec{k}_1 + \vec{k}_2, \vec{0}} \; \vec{\phi}_{\vec{k}_1} \cdot (\vec{e}_n \times \vec{\phi}_{\vec{k}_2})$$

(B.5)

The linear sigma model was extended in (6.3) by a term accounting for weak ferromagnetism to describe the properties of $Ba_2CuGe_2O_7$. Its Fourier transform reads

$$\int \mathrm{d}^2 r \, (\vec{h} \times \vec{e}_3) \cdot \vec{\phi}(\vec{r}) = (\vec{h} \times \vec{e}_3) \cdot \int \mathrm{d}^2 r \, \vec{\phi}(\vec{r}) e^{-i\vec{k} \cdot \vec{r}} \bigg|_{\vec{k} = \vec{0}} = (\vec{h} \times \vec{e}_3) \cdot \vec{\phi}_{\vec{k} = \vec{0}}$$

(B.6)

Throughout the derivations we have made use of the identity

$$\delta(\vec{k}) = \int_{-\infty}^{\infty} \mathrm{d}^2 r \, e^{i\vec{k} \cdot \vec{r}}$$

(B.7)

As we consider discrete k-vectors, these δ-distributions turn out as Kronecker delta, which represent momentum conservation.

C Flat-Spiral Solution of the Chovan-Model

The properties of the flat spiral solution of chiral antiferromagnets were investigated analytically already by Chovan et al [143]. Here, the calculation is reproduced for educational purpose. The full non-linear sigma model for the unit staggered order parameter $\hat{n}$ that Chovan considered to describe the properties of $Ba_2CuGe_2O_7$ reads [142, 143]

$$\mathcal{L} = \mathcal{L}_0 - \mathcal{F}; \quad \mathcal{L}_0 = \frac{1}{2}\partial_0\hat{n} \cdot \partial_0\hat{n} + \vec{h} \cdot (\hat{n} \times \partial_0\hat{n});$$

$$\mathcal{F} = \frac{1}{2}\left(\partial_1\hat{n} - \vec{e_2} \times \hat{n}\right)^2 + \frac{1}{2}\left(\partial_2\hat{n} - \vec{e_1} \times \hat{n}\right)^2 + \frac{1}{2}(\hat{n} \cdot \vec{h})^2 + d_z(\vec{h} \times \vec{e_3}) \cdot \hat{n}$$

(2.5)

The free energy density for magnetic fields in z-direction $\vec{h} = h\vec{e_3}$ becomes

$$\mathcal{F} = \frac{1}{2}\left[(\partial_1 n_1)^2 + (\partial_2 n_2)^2 + (1 + h^2)n_3^2 + 1\right]$$

$$- \left[(\partial_1 n_1 - \partial_2 n_2)n_3 - (n_1\partial_1 - n_2\partial_2)n_3\right]$$

(C.1)

Choosing a spherical parameterization for the order parameter

$$\hat{n} = (\sin(\phi)\sin\vartheta, \cos(\vartheta), \cos(\phi)\sin(\vartheta))^T$$

(C.2)

one can simplify the free energy density, resulting in

$$\mathcal{F} = \frac{1}{2}\left[(\partial_1\phi)^2 \sin^2\vartheta + (\partial_1\vartheta)^2 + \gamma^2 \cos^2\phi\sin^2\vartheta + 1\right] - \partial_1\phi\sin^2\vartheta$$

(C.3)

The Euler-Lagrange-equations assume the following form

$$\partial_1^2\phi = -\frac{2(\partial_1\phi - 1)\cos\vartheta\partial_1\vartheta + \gamma^2\cos\phi\sin\phi\sin\vartheta\partial_1\phi}{\sin\vartheta}$$

$$\partial_1^2\vartheta = \left((\partial_1\phi)^2 + \gamma^2\cos^2\phi - 2\partial_1\phi\right)\sin\vartheta\cos\vartheta$$

(C.4)

Ansatz

By setting $\vartheta = \frac{\pi}{2}$, the order parameter becomes $\hat{n} = (\sin\phi, 0, \cos\phi)^T$ and the free energy density (C.3) reduces to

$$\mathcal{F} = \frac{1}{2}\left[(\partial_1\phi)^2 + \gamma^2\cos^2(\phi) + 1\right] - \partial_1\phi \tag{C.5}$$

While the second Euler-Lagrange-equation is fulfilled automatically, the first one becomes

$$\partial_1^2\phi + \gamma^2\cos\phi\sin\phi = 0 \tag{C.6}$$

The first integration can be performed analytically by multiplying the equation with $\partial_1\phi$ and then integrating straightforwardly (this procedure is also called energy method). The resulting equation

$$\partial_1\phi = \sqrt{\delta^2 + \gamma^2\cos^2\phi} \tag{C.7}$$

can be rearranged using separation of variables, giving the expression

$$x = \int_0^\phi \frac{\mathrm{d}\varphi}{\sqrt{\delta^2 + \gamma^2\cos^2\varphi}} \tag{C.8}$$

From this, the pitch length of the flat spiral

$$L = \int_0^{2\pi} \frac{\mathrm{d}\phi}{\sqrt{\delta^2 + \gamma^2\cos^2\phi}} \tag{C.9}$$

and the average energy density can be defined

$$w = \frac{F}{L} = \frac{1}{L}\int_0^L \mathrm{d}x\,\mathcal{F}(\phi(x)) \tag{C.10}$$

The integration constant δ is determined by the condition, that the average energy density is minimal. To evaluate this, we first rewrite the average energy density

$$w = \frac{1}{L}\int_0^L \mathrm{d}x\,\mathcal{F}(\phi(x)) = \frac{1}{L}\int_0^{2\pi} \mathrm{d}\phi\,\frac{1}{\frac{\mathrm{d}\phi}{\mathrm{d}x}}\mathcal{F}(\phi(x)) = \frac{1}{L}\int_0^{2\pi} \mathrm{d}\phi\,\frac{\mathcal{F}(\phi(x))}{\sqrt{\delta^2 + \gamma^2\cos^2\phi}} \tag{C.11}$$

Next, we insert $\mathcal{F}(\phi(x))$ (C.5) and $\partial_1\phi(x)$ (C.7) and then rearrange terms

$$w = \frac{1}{L}\int_0^{2\pi} d\phi \left[\frac{\delta^2 + 2\gamma^2\cos^2\phi + 1}{2\sqrt{\delta^2 + \gamma^2\cos^2\phi}} - 1 \right] \tag{C.12}$$

$$= \frac{1}{L}\int_0^{2\pi} d\phi \left[\sqrt{\delta^2 + \gamma^2\cos^2\phi} + \frac{1}{2}\frac{1 - \delta^2}{\sqrt{\delta^2 + \gamma^2\cos^2\phi}} - 1 \right] \tag{C.13}$$

We perform two of the integrals, resulting in

$$w = \frac{1}{L}\int_0^{2\pi} d\phi \sqrt{\delta^2 + \gamma^2\cos^2\phi} + \frac{1 - \delta^2}{2} - \frac{2\pi}{L} \tag{C.14}$$

To find the minimum with respect to δ, we take the derivative

$$\frac{\partial w}{\partial \delta} = \frac{\partial}{\partial \delta}\left[\frac{1}{L}\int_0^{2\pi} d\phi \sqrt{\delta^2 + \gamma^2\cos^2\phi} \right] + \frac{\partial}{\partial \delta}\frac{1 - \delta^2}{2} - \frac{\partial}{\partial \delta}\frac{2\pi}{L} \tag{C.15}$$

$$= \frac{1}{L}\int_0^{2\pi} d\phi \frac{\delta}{\sqrt{\delta^2 + \gamma^2\cos^2\phi}} + \left(-\frac{L'}{L^2}\right)\int_0^{2\pi} d\phi \sqrt{\delta^2 + \gamma^2\cos^2\phi}$$

$$- \delta - 2\pi\left(-\frac{L'}{L^2}\right) \tag{C.16}$$

Then, we use the expression for the pitch length (C.9) and collect terms to get

$$\frac{\partial w}{\partial \delta} = \left(-\frac{L'}{L^2}\right)\left[\int_0^{2\pi} d\phi \sqrt{\delta^2 + \gamma^2\cos^2\phi} - 2\pi\right] \overset{!}{=} \tag{C.17}$$

Dividing by $\left(-\frac{L'}{L^2}\right) \neq 0$ yields the minimization condition

$$\frac{1}{2\pi}\int_0^{2\pi} d\phi \sqrt{\delta^2 + \gamma^2\cos^2\phi} = 1 \tag{C.18}$$

And from (C.14) one can conclude

$$w = \frac{1 - \delta^2}{2} \tag{C.19}$$

Critical Magnetic Field

At the critical field, the pitch length L diverges and the spiral turns into a uniform spin-flop state. Therefore $\delta = 0$, and one can calculate starting from (C.18)

$$\int_0^{2\pi} \sqrt{\gamma^2 \cos^2 \phi} = \gamma \int_0^{2\pi} |\cos^2 \phi| = 4\gamma \stackrel{!}{=} 2\pi \tag{C.20}$$

Thus, it follows

$$\gamma = \frac{\pi}{2} \quad \text{and} \quad h_c = \sqrt{\gamma^2 - 1} = \sqrt{\frac{\pi^2}{4} - 1} \approx 1.21 \tag{C.21}$$

Energy Density Curve

To calculate the average energy density (C.19), the integration constant δ needs to be determined from condition (C.18). It can be evaluated in terms of the second elliptic integral

$$E_2(\phi, m) = \int_0^\phi d\varphi \sqrt{1 - m^2 \sin^2 \varphi} \tag{C.22}$$

which leads to

$$2\pi = \int_0^{2\pi} d\phi \sqrt{\delta^2 + \gamma^2 \cos^2 \phi} = \int_0^{2\pi} d\phi \sqrt{\delta^2 + \gamma^2 - \gamma^2 \sin^2 \phi} \tag{C.23}$$

$$= \sqrt{\delta^2 + \gamma^2} \int_0^{2\pi} d\phi \sqrt{1 - \frac{\gamma^2}{\delta^2 + \gamma^2} \sin^2 \phi} \tag{C.24}$$

$$= \sqrt{\delta^2 + \gamma^2} \left(E_2\left(2\pi, \frac{\gamma^2}{\delta^2 + \gamma^2}\right) - E_2\left(0, \frac{\gamma^2}{\delta^2 + \gamma^2}\right) \right) \tag{C.25}$$

As $E_2\left(0, \frac{\gamma^2}{\delta^2 + \gamma^2}\right) = 0$, the δ-parameter is determined by the following equation

$$2\pi = \sqrt{\delta^2 + \gamma^2} \, E_2\left(2\pi, \frac{\gamma^2}{\delta^2 + \gamma^2}\right) \tag{C.26}$$

From this, the energy density curve $w(h)$ is obtained, which is displayed in in Fig. C.1 a).
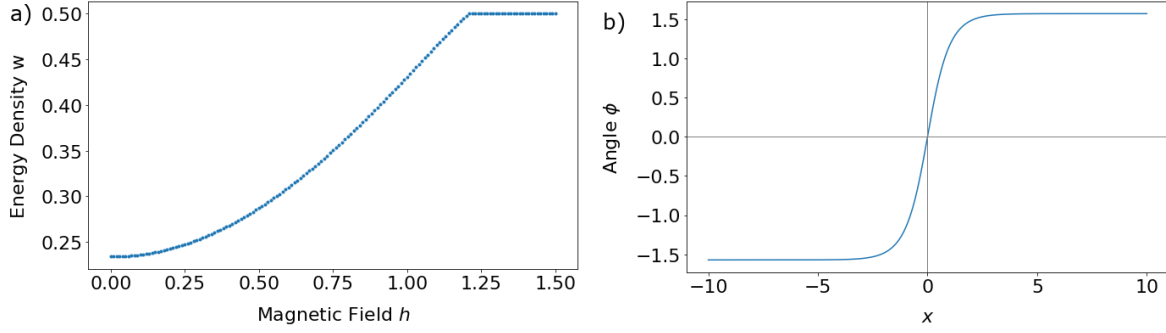
Figure C.1.: a) Energy density w of the flat spiral solution. b) Single kink solution, indicating the instability of the spin-flop phase at about $h_c \approx 1.21$.

Single Kink Solution

At the critical magnetic field $h_c \approx 1.21$ the spin-flop phase becomes unstable and develops into a spiral phase. This starts out by a single kink, evolving into a series of kinks, and finally developing into a spiral. By considering the single kink solution one can derive the value of the critical magnetic field. So we take $\delta = 0$ and tackle equation (C.8) analytically:

$$x - x_0 = \int_0^\phi \mathrm{d}\varphi \, \frac{1}{\sqrt{\gamma^2 \cos^2 \phi}} \tag{C.27}$$

Solving the integral leads to

$$x(\phi) = x_0 + \frac{1}{\gamma} \ln \left(1 + \frac{2}{\cot \frac{\phi}{2} - 1} \right) \tag{C.28}$$

and from this we get as the single kink solution for the order parameter

$$\phi(x) = 2 \operatorname{arccot} \left(\frac{1 + e^{\gamma(x - x_0)}}{-1 + e^{\gamma(x - x_0)}} \right) \tag{C.29}$$

which is displayed for $x_0 = 0$ and $\gamma = \frac{\pi}{2}$ in Fig. C.1 b). The free energy density of the flat spiral is given by

$$\mathcal{F} = \frac{1}{2} \left[(\partial_1 \phi)^2 + \gamma^2 \cos^2(\phi) + 1 \right] - \partial_1 \phi \tag{C.5}$$

$$= \frac{1}{2} (1 + \gamma^2 \cos^2 \phi) = -\frac{2\gamma e^{\gamma x} (1 + e^{2\gamma x} - 2\gamma e^{\gamma x})}{(1 + e^{2\gamma x})^2} \tag{C.30}$$

The average energy density (for diverging pitch length L) is therefore

$$w = \int_{-\infty}^{\infty} dx\, \mathcal{F}(x) = -2\gamma \left[\frac{1}{1 + e^{2\gamma x}} + \frac{\arctan(e^{\gamma x})}{\gamma} \right]_{-\infty}^{\infty}$$

$$= -2\gamma \left(\left[\frac{\pi/2}{\gamma} \right] - \left[1 + \frac{0}{\gamma} \right] \right) = 2\gamma - \pi \qquad (C.31)$$

Below the critical magnetic field h_c and $\gamma = \frac{\pi}{2}$, the single kink solution is favorable in energy.

D Linear Fluctuations of the Skyrmion Lattice

We are considering the model

$$\mathcal{L} = \frac{M_s}{\gamma}\vec{\mathcal{A}}(\vec{m}) \cdot \dot{\vec{m}} - \mathcal{F}(\vec{m}, \partial_i \vec{m}) \tag{8.1}$$

$$\mathcal{F}(\vec{m}, \partial_i \vec{m}) = A\partial_i m_j \partial_i m_j + Dm_i \varepsilon_{ijk}\partial_j m_k - \mu_0 H M_s m_3 \tag{8.2}$$

with i, j, k and $1, 2, 3$ indicating the components x, y, z, respectively. $\vec{\mathcal{A}}(\vec{m})$ is the spin-gauge potential with $\frac{\partial \mathcal{A}_j}{\partial m_i} - \frac{\partial \mathcal{A}_i}{\partial m_j} = \varepsilon_{ijk}m_k$, determining the dynamic part of the Lagrangian, and $\mathcal{F}(\vec{m}, \partial_i \vec{m})$ is the static free energy density.

D.1 Hard-Spin Model: Derivation from the Lagrangian

The linear fluctuations of model (8.1), (8.2) are described by a Bogoliubov-de Gennes (BdG) equation. We are reproducing here the derivation from Kravchuk et al. [177] for educational purpose. Therefore, we employ a local frame of reference $(\hat{e}_1, \hat{e}_2, \hat{m}_0)$, where $\hat{m}_0$ is the normalized ground state magnetization (i.e. $|\hat{m}_0| = 1$) and the other two basis vector fulfill $\hat{e}_1 \times \hat{e}_2 = \hat{m}_0$. Together, they for an orthonormal basis, i.e.e a local dreibein, which accompanies the magnetization texture $\hat{m}_0$.

In addition, we introduce the chiral vectors $\hat{e}_{\pm} = \frac{1}{\sqrt{2}}(\hat{e}_1 \pm i\hat{e}_2)$ with $\hat{e}_+ \cdot \hat{e}_+ = \hat{e}_- \cdot \hat{e}_- = 0$, $\hat{e}_+ \cdot \hat{e}_- = 1$, and $\hat{e}_{\pm} \cdot \hat{m}_0 = 0$.

Spin-wave Parameterization

Within a hard-spin model, the magnetization order parameter, including linear fluctuations, stays normalized and therefore we adopt the following spin-wave parameterization

$$\hat{m} = \hat{m}_0 \sqrt{1 - 2|\psi|^2} + \psi\hat{e}_+ + \psi^*\hat{e}_- \tag{D.1}$$

where $\psi\hat{e}_+ + \psi^*\hat{e}_-$ describes the linear fluctuations and we have introduce a normalization factor. Its time derivative can be approximated up to second order via

$$\dot{\hat{m}} = \frac{-(\psi\dot{\psi}^* + \dot{\psi}\psi^*)}{\sqrt{1 - 2|\psi|^2}}\hat{m}_0 + \dot{\psi}\hat{e}_+ + \dot{\psi}^*\hat{e}_- \approx -(\psi\dot{\psi}^* + \dot{\psi}\psi^*)\hat{m}_0 + \dot{\psi}\hat{e}_+ + \dot{\psi}^*\hat{e}_- \tag{D.2}$$

In the following, we are going to develop the respective terms of the Lagrangian up to second order in the fluctuation fields ψ, ψ^*. Accordingly, the spin gauge potential reads (sum convention over repeated indices applies)

$$\vec{\mathcal{A}}(\hat{m}) = \vec{\mathcal{A}}(\hat{m}_0\sqrt{1-2|\psi|^2} + \psi\hat{e}_+ + \psi^*\hat{e}_-)$$

$$\approx \vec{\mathcal{A}}(\hat{m}_0) + \psi\left[\frac{\partial\vec{\mathcal{A}}}{\partial m_i}\frac{\partial m_i}{\partial\psi}\right]_{\psi,\psi^*=0} + \psi^*\left[\frac{\partial\vec{\mathcal{A}}}{\partial m_i}\frac{\partial m_i}{\partial\psi^*}\right]_{\psi,\psi^*=0}$$

$$= \vec{\mathcal{A}}(\hat{m}_0) + \psi\frac{\partial\vec{\mathcal{A}}}{\partial m_i}(\hat{e}_+)_i + \psi^*\frac{\partial\vec{\mathcal{A}}}{\partial m_i}(\hat{e}_-)_i \tag{D.3}$$

Inserting this into the dynamical part of the Lagrangian

$$\vec{\mathcal{A}}(\hat{m})\cdot\dot{\vec{m}} = \left[\vec{\mathcal{A}}(\hat{m}_0) + \psi\frac{\partial\vec{\mathcal{A}}}{\partial m_i}(\hat{e}_+)_i + \psi^*\frac{\partial\vec{\mathcal{A}}}{\partial m_i}(\hat{e}_-)_i\right]\left[-(\psi\dot{\psi}^* + \dot{\psi}\psi^*)\hat{m}_0 + \dot{\psi}\hat{e}_+ + \dot{\psi}^*\hat{e}_-\right] \tag{D.4}$$

and keeping only second order terms without full time derivatives leads to

$$\vec{\mathcal{A}}(\hat{m})\cdot\dot{\vec{m}} \approx \psi\dot{\psi}^*(\hat{e}_-)_j\frac{\partial\mathcal{A}_j}{\partial m_i}(\hat{e}_+)_i + \psi^*\dot{\psi}(\hat{e}_+)_j\frac{\partial\mathcal{A}_j}{\partial m_i}(\hat{e}_-)_i \tag{D.5}$$

$\downarrow$ adding a total time derivative vanishes under the integral

$$= \left[\psi\dot{\psi}^* - \partial_t(\psi\psi^*)\right](\hat{e}_-)_i\frac{\partial\mathcal{A}_i}{\partial m_j}(\hat{e}_+)_j + \psi^*\dot{\psi}(\hat{e}_+)_j\frac{\partial\mathcal{A}_j}{\partial m_i}(\hat{e}_-)_i \tag{D.6}$$

$$= \psi^*\dot{\psi}(\hat{e}_+)_j(\hat{e}_-)_i\left[\frac{\partial\mathcal{A}_j}{\partial m_i} - \frac{\partial\mathcal{A}_i}{\partial m_j}\right] \tag{D.7}$$

$$= \psi^*\dot{\psi}(\hat{e}_+)_j(\hat{e}_-)_i\,\varepsilon_{ijk}m_k = \psi^*\dot{\psi}(\hat{e}_-\times\hat{e}_+)\cdot\vec{m} \tag{D.8}$$

$$= \frac{\psi^*\dot{\psi}}{2}\left[(\hat{e}_1 - i\hat{e}_2)\times(\hat{e}_1 + i\hat{e}_2)\right] = i\psi^*\dot{\psi} \tag{D.9}$$

$\downarrow$ symmetrize by adding a suitable total time derivative

$$= \frac{i}{2}\left[\psi^*\dot{\psi} - \dot{\psi}^*\psi\right] = \frac{i}{2}\vec{\psi}^\dagger\hat{\tau}_z\dot{\vec{\psi}} \tag{D.10}$$

where we have introduced in the last step the the spinor $\vec{\psi} = (\psi, \psi^*)^T$ and $\hat{\tau}_z$ is the third Pauli matrix.

Symmetric Exchange Term

Next, we are going to evaluate the first term in the static energy density, describing symmetric exchange:

$$\partial_i m^j \partial_i m^j = \partial_i \left(\sqrt{1 - 2|\psi|^2} m_0^j + \psi \left(\hat{e}_+ \right)_j + \psi^* \left(\hat{e}_- \right)_j \right)$$

$$\partial_i \left(\sqrt{1 - 2|\psi|^2} m_0^j + \psi \left(\hat{e}_+ \right)_j + \psi^* \left(\hat{e}_- \right)_j \right) \tag{D.11}$$

$$\approx \partial_i \left((1 - \psi\psi^*) m_0^j + \psi \left(\hat{e}_+ \right)_j + \psi^* \left(\hat{e}_- \right)_j \right)$$

$$\partial_i \left((1 - \psi\psi^*) m_0^j + \psi \left(\hat{e}_+ \right)_j + \psi^* \left(\hat{e}_- \right)_j \right) \tag{D.12}$$

We keep only second order terms in ψ

$$= -2\partial_i m_0^j \partial_i (m_0^j \psi\psi^*) + \partial_i \left[\psi \left(\hat{e}_+ \right)_j \right] \partial_i \left[\psi \left(\hat{e}_+ \right)_j \right] + \partial_i \left[\psi \left(\hat{e}_+ \right)_j \right] \partial_i \left[\psi^* \left(\hat{e}_- \right)_j \right]$$

$$+ \partial_i \left[\psi^* \left(\hat{e}_- \right)_j \right] \partial_i \left[\psi \left(\hat{e}_+ \right)_j \right] + \partial_i \left[\psi^* \left(\hat{e}_- \right)_j \right] \partial_i \left[\psi^* \left(\hat{e}_- \right)_j \right] \tag{D.13}$$

Then we use partial integration to shift the derivative and evaluate the resulting second-order derivative

$$= 2(\hat{m}_0 \cdot \Delta\hat{m}_0)\psi\psi^* - \psi \left(\hat{e}_+ \right)_j \partial_i^2 \left[\psi \left(\hat{e}_+ \right)_j \right] - \psi^* \left(\hat{e}_- \right)_j \partial_i^2 \left[\psi \left(\hat{e}_+ \right)_j \right]$$

$$- \psi \left(\hat{e}_+ \right)_j \partial_i^2 \left[\psi^* \left(\hat{e}_- \right)_j \right] - \psi^* \left(\hat{e}_- \right)_j \partial_i^2 \left[\psi^* \left(\hat{e}_- \right)_j \right] \tag{D.14}$$

$$= 2(\hat{m}_0 \cdot \Delta\hat{m}_0)\psi\psi^* - \psi \left(\hat{e}_+ \right)_j [\psi\partial_i^2 \left(\hat{e}_+ \right)_j {\color{red} + \left(\hat{e}_+ \right)_j \partial_i^2 \psi} + 2\partial_i \left(\hat{e}_+ \right)_j \partial_i \psi$$

$$+ \psi^* \partial_i^2 \left(\hat{e}_- \right)_j + \left(\hat{e}_- \right)_j \partial_i^2 \psi^* + 2\partial_i \left(\hat{e}_- \right)_j \partial_i \psi^*]$$

$$- \psi^* \left(\hat{e}_- \right)_j [\psi\partial_i^2 \left(\hat{e}_+ \right)_j + \left(\hat{e}_+ \right)_j \partial_i^2 \psi + 2\partial_i \left(\hat{e}_+ \right)_j \partial_i \psi$$

$$+ \psi^* \partial_i^2 \left(\hat{e}_- \right)_j {\color{red} + \left(\hat{e}_- \right)_j \partial_i^2 \psi^*} + 2\partial_i \left(\hat{e}_- \right)_j \partial_i \psi^*] \tag{D.15}$$

The red terms cancel, since $\hat{e}_+ \cdot \hat{e}_+ = \hat{e}_- \cdot \hat{e}_- = 0$ and we obtain

$$= 2(\hat{m}_0 \cdot \Delta\hat{m}_0)\psi\psi^* - \psi\psi^* (\hat{e}_+ \cdot \Delta\hat{e}_-) - \psi\psi^* (\hat{e}_- \cdot \Delta\hat{e}_+) - \psi\Delta\psi^* - \psi^*\Delta\psi$$

$$- \psi^2 (\hat{e}_+ \cdot \Delta\hat{e}_+) - \psi^{*2} (\hat{e}_- \cdot \Delta\hat{e}_-)$$

$$\color{red}{-2\psi\hat{e}_+ \cdot [\nabla\hat{e}_+ \cdot \nabla\psi]} - 2\psi\hat{e}_+ \cdot [\nabla\hat{e}_- \cdot \nabla\psi^*]$$

$$- 2\psi^*\hat{e}_- \cdot [\nabla\hat{e}_+ \cdot \nabla\psi] \color{red}{-2\psi^*\hat{e}_- \cdot [\nabla\hat{e}_- \cdot \nabla\psi^*]} \tag{D.16}$$

Again, the red terms drop, this time because

$$\hat{e}_+ \cdot \partial_i\hat{e}_+ = \frac{1}{2}(\hat{e}_1 + i\hat{e}_2) \cdot \partial_i(\hat{e}_1 + i\hat{e}_2) = \frac{i}{2}(\hat{e}_1 \cdot \partial_i\hat{e}_2) + \frac{i}{2}(\hat{e}_2 \cdot \partial_i\hat{e}_1) = \frac{i}{2}\partial_i(\hat{e}_1 \cdot \hat{e}_2) = 0 \tag{D.17}$$

Finally, we obtain as a result

$$= [2(\hat{m}_0 \cdot \Delta\hat{m}_0) - \hat{e}_+ \cdot \Delta\hat{e}_- - \hat{e}_- \cdot \Delta\hat{e}_+]\psi\psi^* - \psi\Delta\psi^* - \psi^*\Delta\psi$$

$$- \psi^2 (\hat{e}_+ \cdot \Delta\hat{e}_+) - \psi^{*2} (\hat{e}_- \cdot \Delta\hat{e}_-) - 2\psi\hat{e}_+ \cdot [\nabla\hat{e}_- \cdot \nabla\psi^*] - 2\psi^*\hat{e}_- \cdot [\nabla\hat{e}_+ \cdot \nabla\psi] \tag{D.18}$$

and thus

$$\partial_i m^j \partial_i m^j = \begin{pmatrix} \psi^* & \psi \end{pmatrix} \begin{pmatrix} -\Delta + v_0 - v^+ & -(\hat{e}_- \cdot \Delta\hat{e}_-) \\ -(\hat{e}_+ \cdot \Delta\hat{e}_+) & -\Delta + v_0 - v^- \end{pmatrix} \begin{pmatrix} \psi \\ \psi^* \end{pmatrix} \tag{D.19}$$

with

$$v_0 = \hat{m}_0 \cdot \Delta\hat{m}_0 - \frac{\hat{e}_+ \cdot \Delta\hat{e}_- + \hat{e}_- \cdot \Delta\hat{e}_+}{2} \tag{D.20}$$

$$v^\pm = 2\hat{e}_\mp \cdot [\nabla\hat{e}_\pm \cdot \nabla] \tag{D.21}$$

Antisymmetric Exchange Term

Next, we are going to evaluate the second term in the static energy density with

$$m^i \varepsilon_{ijk} \partial_j m^k = \varepsilon_{ijk} \left(\sqrt{1 - 2|\psi|^2}\, m_0^i + \psi \left(\hat{e}_+ \right)_i + \psi^* \left(\hat{e}_- \right)_i \right)$$

$$\partial_j \left(\sqrt{1 - 2|\psi|^2}\, m_0^k + \psi \left(\hat{e}_+ \right)_k + \psi^* \left(\hat{e}_- \right)_k \right) \tag{D.22}$$

$$\approx \varepsilon_{ijk} \left((1 - \psi\psi^*) m_0^i + \psi \left(\hat{e}_+ \right)_i + \psi^* \left(\hat{e}_- \right)_i \right)$$

$$\partial_j \left((1 - \psi\psi^*) m_0^k + \psi \left(\hat{e}_+ \right)_k + \psi^* \left(\hat{e}_- \right)_k \right) \tag{D.23}$$

Again, we keep only second-order terms in the fluctuation fields ψ, ψ^*

$$= \varepsilon_{ijk} \{ - m_0^i \partial_j (m_0^k \psi\psi^*) - m_0^i \psi\psi^* \partial_j m_0^k + \left(\hat{e}_+ \right)_i \psi \partial_j \left[\psi \left(\hat{e}_+ \right)_k \right]$$

$$+ \left(\hat{e}_+ \right)_i \psi \partial_j \left[\psi^* \left(\hat{e}_- \right)_k \right] + \left(\hat{e}_- \right)_i \psi^* \partial_j \left[\psi \left(\hat{e}_+ \right)_k \right] + \left(\hat{e}_- \right)_i \psi^* \partial_j \left[\psi^* \left(\hat{e}_- \right)_k \right] \} \tag{D.24}$$

Finally, since $\hat{e}_+ \times \hat{e}_+ = \hat{e}_- \times \hat{e}_- = 0$, this leads to

$$= -2\hat{m}_0 \cdot [\nabla \times \hat{m}_0] \psi\psi^* + \hat{e}_+ \cdot [\nabla \times \hat{e}_+] \psi^2 + \hat{e}_+ \cdot [\nabla \times \hat{e}_-] \psi\psi^*$$

$$+ \hat{e}_- \cdot [\nabla \times \hat{e}_+] \psi\psi^* + \hat{e}_- \cdot [\nabla \times \hat{e}_-] \psi^{*2}$$

$$+ \hat{e}_+ \cdot [\nabla \psi^* \times \hat{e}_-] \psi + \hat{e}_- \cdot [\nabla \psi \times \hat{e}_+] \psi^* \tag{D.25}$$

and thus

$$m^i \varepsilon_{ijk} \partial_j m^k = \begin{pmatrix} \psi^* & \psi \end{pmatrix} \begin{pmatrix} u_0 + u^+ & \hat{e}_- \cdot [\nabla \times \hat{e}_-] \\ \hat{e}_+ \cdot [\nabla \times \hat{e}_+] & u_0 + u^- \end{pmatrix} \begin{pmatrix} \psi \\ \psi^* \end{pmatrix} \tag{D.26}$$

with

$$u_0 = -\hat{m}_0 \cdot [\nabla \times \hat{m}_0] + \frac{\hat{e}_+ \cdot [\nabla \times \hat{e}_-] + \hat{e}_- \cdot [\nabla \times \hat{e}_+]}{2} \tag{D.27}$$

$$u^\pm = [\hat{e}_\pm \times \hat{e}_\mp] \cdot \nabla \tag{D.28}$$

Zeeman Term

For the Zeeman term we consider the third component of the spin-wave paramterization of $\vec{m} = (m_1, m_2, m_3)^T$

$$m_3 \approx m_0^3(1 - \psi\psi^*) + \psi\,(\hat{e}_+)_3 + \psi^*\,(\hat{e}_-)_3 \tag{D.29}$$

As we keep only second order terms im the fluctuation fields ψ, ψ^*, this yields

$$m_3 \approx -m_0^3\psi\psi^* = \begin{pmatrix} \psi^* & \psi \end{pmatrix} \begin{pmatrix} -\frac{m_0^3}{2} & 0 \\ 0 & -\frac{m_0^3}{2} \end{pmatrix} \begin{pmatrix} \psi \\ \psi^* \end{pmatrix} \tag{D.30}$$

Bogoliubov-de Gennes Lagrangian

Putting it all together, we arrive at the Bogoliubov-de Gennes Lagrangian

$$\mathcal{L} = \frac{M_s}{\gamma}\frac{i}{2}\vec{\psi}^\dagger\hat{\tau}^z\partial_t\vec{\psi} - \vec{\psi}^\dagger\hat{H}\vec{\psi} \tag{9.1}$$

where $\hat{\tau}^z$ is the third Pauli matrix, $\hat{H} = \begin{pmatrix} H^+ & W^- \\ W^+ & H^- \end{pmatrix}$ with $H^\pm = -A\Delta - V_0 - V^\pm$, and

the terms

$$V_0 = Av_0 + Du_0 = -A\vec{m}_0 \cdot (\Delta\vec{m}_0) + D\vec{m}_0 \cdot [\nabla \times \vec{m}_0] - \mu_0 H M_s(\vec{m}_0 \cdot \hat{z})$$

$$+ A\mathrm{Re}(\hat{e}^+ \cdot \Delta\hat{e}^-) - D\mathrm{Re}(\hat{e}^+ \cdot (\nabla \times \hat{e}^-)) \tag{9.2}$$

$$V^\pm = Av^\pm + Du^\pm = 2A\hat{e}^\mp(\nabla\hat{e}^\pm \cdot \nabla) - D(\hat{e}^\pm \times \hat{e}^\mp) \cdot \nabla \tag{9.3}$$

$$W^\pm = -A(\hat{e}^\pm \cdot \Delta e^\pm) + D\hat{e}^\pm \cdot \left[\nabla \times \hat{e}^\pm\right] \tag{9.4}$$

Dimensionless Units

In accordance with [177] we introduce, finally, dimensionless units and measure lengths in units of $[x, y, z] = l = \frac{2A}{D}$ ($Q = \frac{D}{2A}$ corresponds to the pitch length of a spiral texture

in our model). Thus, the static free energy density in dimensionless units reads

$$\mathcal{F}(\vec{m}, \partial_i \vec{m}) = A \frac{D^2}{4A^2} \partial_i m_j \partial_i m_j + D \frac{D}{2A} m_i \varepsilon_{ijk} \partial_j m_k - \mu_0 H M_s m_3 \qquad \text{(D.31)}$$

$$= \frac{D^2}{4A} \left[\partial_i m_j \partial_i m_j + 2 m_i \varepsilon_{ijk} \partial_j m_k - 2b m_3 \right] \qquad \text{(D.32)}$$

where the substitution $\partial_i \to \frac{D}{2A} \partial_i$ has been highlighted in blue and we have introduced the dimensionless magnetic field $b = \frac{\mu_0 2 A M_s H}{D^2}$. Putting everything we derived in the previous sections for the terms in the square-brackets together, and introducing the frequency scale $\omega_c = \frac{\gamma D^2}{2A M_s}$, we arrive at the Bogoliubov-de Gennes Lagrangian

$$\mathcal{L} = \frac{M_s}{\gamma} \frac{i}{2} \vec{\psi}^\dagger \hat{\tau}^z \partial_t \vec{\psi} - \frac{D^2}{4A} \vec{\psi}^\dagger \hat{H} \vec{\psi} = \frac{D^2}{2A} \left[\frac{1}{2} \vec{\psi}^\dagger \left(\frac{i}{\omega_{c_2}} \hat{\tau}^z \partial_t - \hat{H} \right) \vec{\psi} \right] \qquad \text{(D.33)}$$

which reads in dimensionless units

$$\mathcal{L} = \frac{1}{2} \vec{\psi}^\dagger \left(i \hat{\tau}^z \partial_t - \hat{H} \right) \vec{\psi} \qquad \text{(D.34)}$$

where $\hat{\tau}^z$ is the third Pauli matrix, $\hat{H} = \begin{pmatrix} H^+ & W^- \\ W^+ & H^- \end{pmatrix}$ with $H^\pm = -\Delta - V_0 - 2V^\pm$, and

the terms

$$V_0 = -\vec{m}_0 \cdot (\Delta \vec{m}_0) + 2 \vec{m}_0 \cdot [\nabla \times \vec{m}_0] - b(\vec{m}_0 \cdot \hat{z})$$

$$+ \operatorname{Re}(\hat{e}^+ \cdot \Delta \hat{e}^-) - 2 \operatorname{Re}(\hat{e}^+ \cdot (\nabla \times \hat{e}^-)) \qquad \text{(D.35)}$$

$$V^\pm = \hat{e}^\mp (\nabla \hat{e}^\pm \cdot \nabla) - (\hat{e}^\pm \times \hat{e}^\mp) \cdot \nabla \qquad \text{(D.36)}$$

$$W^\pm = -(\hat{e}^\pm \cdot \Delta e^\pm) + 2 \hat{e}^\pm \cdot [\nabla \times \hat{e}^\pm] \qquad \text{(D.37)}$$

The only free parameter of this theory is the dimensionless magnetic field $b = \frac{\gamma \mu_0 H}{\omega_c}$.

Spherical Parameterization

The constraint $|\hat{m}_0| = 1$ can be enforced using a spherical parameterization [177]

$$\vec{m}_0 = \sin(\theta)\hat{\varepsilon} + \cos(\theta)\hat{z} \tag{D.38}$$

$$\vec{e}_1 = \partial_\phi \hat{\varepsilon} = -\sin(\phi)\hat{x} + \cos(\phi)\hat{y} \tag{D.39}$$

$$\vec{e}_2 = -\partial_\theta \vec{m}_0 = -\cos(\theta)\hat{\varepsilon} + \sin(\theta)\hat{z} \tag{D.40}$$

with $\hat{\varepsilon} = \cos(\phi)\hat{x} + \sin(\phi)\hat{y}$. The potentials now assume the form

$$V_0 = \frac{(\nabla\theta)^2}{2} + \left(1 - 3\cos^2(\theta)\right)\frac{(\nabla\phi)^2}{2} + (\nabla\theta \times \hat{\varepsilon})_z$$
$$+ 3\sin(\theta)\cos(\theta)(\hat{\varepsilon} \cdot \nabla\phi) - h\cos(\theta) \tag{D.41}$$

$$V^\pm = \pm i\left[(\vec{m}_0 - \cos(\theta)\nabla\phi) \cdot \nabla\right] \tag{D.42}$$

$$W^\pm = -\frac{(\nabla\theta)^2}{2} + \sin^2(\theta)\frac{(\nabla\phi)^2}{2} + (\hat{\varepsilon} \times \nabla\theta)_z + \sin(\theta)\cos(\theta)(\hat{\varepsilon} \cdot \nabla\phi)$$
$$\mp i\nabla \cdot \vec{m}_0 \pm i\sin(\theta)\left[2(\hat{\varepsilon} \times \nabla\phi) - \nabla\theta \cdot \nabla\phi\right] \tag{D.43}$$

D.2 Derivation of the Landau-Lifshitz-Gilbert equation

The Bogoliubov-de Gennes equation for magnons in a skyrmion lattice can be derived as well from the Landau-Lifshitz-Gilbert (LLG) equation within a so-called soft-spin model, which describes the temporal dynamics of a magnetization vector $\vec{m} = M_s\hat{m}$ with $|\hat{m}| = 1$ and is given in its general form by

$$\frac{\partial\vec{m}}{\partial t} = -\gamma\left(\vec{m} \times \left(\frac{-1}{M_s}\frac{\delta F}{\delta\vec{m}}\right)\right) \tag{D.44}$$

In a soft-spin model, the length of the magnetization order parameter is not constraint to unity (therefore 'soft spin'). We are going to derive the specific form of the LLG equation for the model (8.1), (8.2) in this section. In the following section we derive again the Bogoliubov-de Gennes equation from this LLG equation. At first, our main task will be to evaluate the functional derivative $\frac{\delta F}{\delta\vec{m}}$.

For our soft-spin model we need to introduce an additional term $f(\vec{m})$ into the free

energy functional F, where the latter represents the static part of the Lagrangian (8.2)

$$F = \int d^3 r\, \mathcal{F}, \quad \mathcal{F} = A(\partial_i m_j)(\partial_i m_j) + D m_i \varepsilon_{ijk} \partial_j m_k - \mu_0 M_s H m_3 + f(\vec{m}) \qquad \text{(D.45)}$$

Here, $\vec{m}$ is the magnetization, i, j, k are indicating the respective components x, y, z, summation over repeated indices is assumed, and $\vec{H} = H \hat{e}_3$ is an external magnetic field.

Typically, the additional term takes the form $f(\vec{m}) = (1 - \vec{m}^2)^2$. However, the crucial point here is that it involves a quartic term with a positive coefficient, which ensures the stability of the soft-spin model: If energy can be gained from the quadratic terms, i.e. if their energy contribution is negative overall, and as the length of $\vec{m}$ is not normalized to unity, this would lead to a divergence of the length of $\vec{m}$ and the soft-spin model would energetically not be bound from below.

First-order Variation Approach

The functional derivative $\frac{\delta F}{\delta \vec{m}}$ can be obtained directly from first-order variation

$$\frac{\delta F}{\delta \vec{m}_j} = \frac{\partial \mathcal{F}}{\partial \vec{m}_j} - \partial_i \frac{\partial \mathcal{F}}{\partial (\partial_i \vec{m}_j)} \qquad \text{(D.46)}$$

where

$$\frac{\partial \mathcal{F}}{\partial \vec{m}_j} = 2\vec{m} f'(\vec{m}^2) - \mu_0 M_s H \delta_{j,3} \qquad \text{(D.47)}$$

and

$$\partial_i \frac{\partial \mathcal{F}}{\partial (\partial_i \vec{m}_j)} = \partial_i \frac{\partial}{\partial (\partial_i \vec{m}_j)} \left[A(\partial_a m_b)(\partial_a m_b) + D m_a \varepsilon_{abc} \partial_b m_c \right]$$

$$= \partial_i \left[2A \delta_{ia} \delta_{jb} (\partial_a m_b) + D m_a \varepsilon_{abc} \delta_{bi} \delta_{cj} \right]$$

$$= 2A \partial_i \partial_j m_j + \underbrace{D \varepsilon_{aij} \partial_i m_a}_{= -D \varepsilon_{jia} \partial_i m_a} = 2A \Delta \vec{m}_j - D(\nabla \times \vec{m})_j$$

so, in the end, we obtain

$$\frac{\delta F}{\delta \vec{m}} = -2A \Delta \vec{m} + 2D(\nabla \times \vec{m}) - \mu_0 M_s \vec{H} + 2\vec{m} f'(\vec{m}^2) \qquad \text{(D.48)}$$

We expand the order parameter $\vec{m}$ up to linear order $\vec{m} = \hat{m}_0 + \vec{\mu}$, where $\hat{m}_0$ is the normalized ground state magnetization ($|\hat{m}_0| = 1$). Also, we have

$$\left.\frac{\delta F}{\delta \vec{m}_j}\right|_{\hat{m}_0} = -2A\Delta\hat{m}_0 + 2D(\nabla \times \hat{m}_0) - \mu_0 M_s \vec{H} + 2\hat{m}_0 f'(\hat{m}_0^2) = 0 \tag{D.49}$$

$$\Rightarrow \underbrace{\hat{m}_0^2}_{=1} f'(\hat{m}_0^2) = A\hat{m}_0 \cdot \Delta\hat{m}_0 - D\hat{m}_0 \cdot (\nabla \times \hat{m}_0) - \frac{1}{2}\mu_0 M_s \vec{H} \cdot \hat{m}_0 \tag{D.50}$$

Next, we expand the LLG equation up to linear order in $\vec{\mu}$

$$\frac{M_s}{\gamma}\frac{\partial \vec{m}}{\partial t} = (\hat{m}_0 + \vec{\mu}) \times [-2A\Delta(\hat{m}_0 + \vec{\mu}) + 2D(\nabla \times (\hat{m}_0 + \vec{\mu})) - \mu_0 M_s \vec{H}$$

$$+ 2(\hat{m}_0 + \vec{\mu})f'(\vec{m}^2)]$$

$$= (\hat{m}_0 + \vec{\mu}) \times [\underbrace{-2A\Delta\hat{m}_0 + 2D\nabla \times \hat{m}_0 - \mu_0 M_s \vec{H} + 2\hat{m}_0 f'(\hat{m}_0^2)}_{=0} \tag{D.51}$$

$$- 2A\Delta\vec{\mu} + 2D\nabla \times \vec{\mu} + 2\vec{\mu}f'(\hat{m}_0^2)]$$

$$= \hat{m}_0 \times [-2A\Delta\vec{\mu} + 2D\nabla \times \vec{\mu} + 2\vec{\mu}f'(\hat{m}_0^2)] \tag{D.52}$$

D.3 Soft-Spin Model

The LLG equation we derived in the previous section reads in dimensionless units (see previous section and formula (D.32))

$$\partial_t \vec{\mu} = \hat{m}_0 \times [-\Delta\vec{\mu} + 2\nabla \times \vec{\mu} - \vec{\mu}\mathcal{F}_0] \tag{D.53}$$

$$\mathcal{F}_0 = -\hat{m}_0 \cdot \Delta\hat{m}_0 + 2\hat{m}_0 \cdot (\nabla \times \hat{m}_0) - 2b\hat{m}_3 \tag{D.54}$$

We employ the spin-wave parameterization

$$\vec{m} = \hat{m}_0 + \vec{\mu} = \hat{m}_0 + \psi\hat{e}_+ + \psi^*\hat{e}_- \tag{D.55}$$

This time, the magnitude of $\vec{m}$ is not constraint to unity (therefore, it is called soft-spin model). In order to obtain the Bogoliubov-de Gennes equation for the two-component spinor $\vec{\psi}$ from the three-component LLG equation, we project the latter onto the chiral

vectors

$$\hat{e}_+ \cdot \partial_t \vec{\mu} = \hat{e}_+ \cdot (\dot{\psi}\hat{e}_+ + \dot{\psi}^*\hat{e}_-) = \dot{\psi}^* \stackrel{!}{=} \hat{e}_+ \cdot (\hat{m}_0 \times [-\Delta\vec{\mu} + 2\nabla \times \vec{\mu} - \vec{\mu}\mathcal{F}_0]) \qquad (\text{D}.56)$$

$$\hat{e}_- \cdot \partial_t \vec{\mu} = \hat{e}_- \cdot (\dot{\psi}\hat{e}_+ + \dot{\psi}^*\hat{e}_-) = \dot{\psi} \stackrel{!}{=} \hat{e}_- \cdot (\hat{m}_0 \times [-\Delta\vec{\mu} + 2\nabla \times \vec{\mu} - \vec{\mu}\mathcal{F}_0]) \qquad (\text{D}.57)$$

Rewriting the triple product and using $\hat{e}_\pm \times \hat{m}_0 = \pm i\hat{e}_\pm$ leads to

$$\dot{\psi} = -i\hat{e}_- \cdot [-\Delta\vec{\mu} + 2\nabla \times \vec{\mu} - \vec{\mu}\mathcal{F}_0] \qquad (\text{D}.58)$$

$$\dot{\psi}^* = i\hat{e}_+ \cdot [-\Delta\vec{\mu} + 2\nabla \times \vec{\mu} - \vec{\mu}\mathcal{F}_0] \qquad (\text{D}.59)$$

Inserting the spin-wave parameterization also for the square-bracket term

$$[\dots] \equiv -\Delta\vec{\mu} + 2\nabla \times \vec{\mu} - \vec{\mu}\mathcal{F}_0 = -\Delta(\psi\hat{e}_+ + \psi^*\hat{e}_-) + 2\nabla \times (\psi\hat{e}_+ + \psi^*\hat{e}_-)$$
$$- (\psi\hat{e}_+ + \psi^*\hat{e}_-)\mathcal{F}_0 \qquad (\text{D}.60)$$

and using the identities

$$\nabla \times (f(\vec{r})\vec{e}(\vec{r})) = \nabla f(\vec{r}) \times \vec{e}(\vec{r}) + f(\vec{r})\nabla \times \vec{e}(\vec{r}) \qquad (\text{D}.61)$$

$$\Delta(f(\vec{r})\vec{e}(\vec{r})) = \Delta f(\vec{r})\vec{e}(\vec{r}) + 2(\nabla f(\vec{r}) \cdot \nabla)\vec{e}(\vec{r}) + f(\vec{r})\Delta\vec{e}(\vec{r}) \qquad (\text{D}.62)$$

where $f(\vec{r})$ is a scalar- and $\vec{e}(\vec{r})$ is a vector-valued function of space, we obtain

$$[\dots] = -\Delta\psi\hat{e}_+ - 2(\nabla\psi \cdot \nabla)\hat{e}_+ - \psi\Delta\hat{e}_+ - \Delta\psi^*\hat{e}_- - 2(\nabla\psi^* \cdot \nabla)\hat{e}_- - \psi^*\Delta\hat{e}_-$$
$$+ 2[\nabla\psi \times \hat{e}_+ + \psi\nabla \times \hat{e}_+] + 2[\nabla\psi^* \times \hat{e}_- + \psi^*\nabla \times \hat{e}_-] + (\psi\hat{e}_+ + \psi^*\hat{e}_-)\mathcal{F}_0 \quad (\text{D}.63)$$

Thus, we obtain for (D.58)

$$i\dot{\psi} = \hat{e}_- \cdot [\dots] = -\Delta\psi - 2\hat{e}_- \cdot (\nabla\psi \cdot \nabla)\hat{e}_+ - \psi\hat{e}_- \cdot \Delta\hat{e}_+ \textcolor{red}{-2\hat{e}_- \cdot (\nabla\psi^* \cdot \nabla)\hat{e}_-}$$
$$- \psi^*\hat{e}_- \cdot \Delta\hat{e}_- + 2[\hat{e}_- \cdot (\nabla\psi \times \hat{e}_+) + \psi\hat{e}_- \cdot (\nabla \times \hat{e}_+)]$$
$$+ 2[\underbrace{\hat{e}_- \cdot (\nabla\psi^* \times \hat{e}_-)}_{=\nabla\psi^* \cdot (\hat{e}_- \times \hat{e}_-)=0} + \psi^*\hat{e}_- \cdot (\nabla \times \hat{e}_-)] - \psi\mathcal{F}_0 \qquad (\text{D}.64)$$

where the first red term drops, since $\hat{e}_+ \cdot \partial_i \hat{e}_+ = 0$ following (D.17), which finally leads to

$$i\dot{\psi} = [-\Delta \underbrace{-\mathcal{F}_0 - \hat{e}_- \cdot \Delta\hat{e}_+ + 2\hat{e}_- \cdot (\nabla \times \hat{e}_+)}_{=V_0} \underbrace{-2\hat{e}_- \cdot (\nabla\hat{e}_+ \cdot \nabla) + 2(\hat{e}_+ \times \hat{e}_-) \cdot \nabla}_{=V^+}]\psi$$

$$+ [\underbrace{-\hat{e}_- \cdot \Delta\hat{e}_- + 2\hat{e}_- \cdot (\nabla \times \hat{e}_-)}_{=W^-}]\psi^* \tag{D.65}$$

Similarly, we obtain for (D.59)

$$-i\dot{\psi}^* = \hat{e}_+ \cdot [\ldots] = \color{red}{-2\hat{e}_+ \cdot (\nabla\psi \cdot \nabla)\hat{e}_+} \color{black}{- \psi\hat{e}_+ \cdot \Delta\hat{e}_+ - \Delta\psi^* - 2\hat{e}_+ \cdot (\nabla\psi^* \cdot \nabla)\hat{e}_-}$$

$$- \psi^*\hat{e}_+ \cdot \Delta\hat{e}_- + 2[\underbrace{\hat{e}_+ \cdot (\nabla\psi \times \hat{e}_+)}_{=\nabla\psi\cdot(\hat{e}_+\times\hat{e}_+)=0} + \psi\hat{e}_+ \cdot (\nabla \times \hat{e}_+)]$$

$$+ 2[\hat{e}_+ \cdot (\nabla\psi^* \times \hat{e}_-) + \psi^*\hat{e}_+ \cdot (\nabla \times \hat{e}_-)] - \psi^*\mathcal{F}_0 \tag{D.66}$$

where the first red term drops, since $\hat{e}_- \cdot \partial_i \hat{e}_- = 0$ following (D.17), which finally leads to

$$-i\dot{\psi}^* = [-\Delta \underbrace{-\mathcal{F}_0 - \hat{e}_+ \cdot \Delta\hat{e}_- + 2\hat{e}_+ \cdot (\nabla \times \hat{e}_-)}_{=V_0} \underbrace{-2\hat{e}_+ \cdot (\nabla\hat{e}_- \cdot \nabla) + 2(\hat{e}_- \times \hat{e}_+) \cdot \nabla}_{=V^-}]\psi^*$$

$$+ [\underbrace{-\hat{e}_+ \cdot \Delta\hat{e}_+ + 2\hat{e}_+ \cdot (\nabla \times \hat{e}_+)}_{=W^+}]\psi \tag{D.67}$$

In identifying V_0 we have used that

$$\nabla \cdot (\hat{e}_+ \times \hat{e}_-) = 0 = \hat{e}_- \cdot (\nabla \times \hat{e}_+) - \hat{e}_+ \cdot (\nabla \times \hat{e}_-) \tag{D.68}$$

$$\Rightarrow \hat{e}_- \cdot (\nabla \times \hat{e}_+) = \hat{e}_+ \cdot (\nabla \times \hat{e}_-) \tag{D.69}$$

In addition, we have

$$\Delta(\hat{e}_+ \cdot \hat{e}_-) = 0 = \hat{e}_+\Delta\hat{e}_- + 2\nabla\hat{e}_+\nabla\hat{e}_- + \hat{e}_-\Delta\hat{e}_+ \tag{D.70}$$

and using partial integration

$$0 = \hat{e}_+\Delta\hat{e}_- - 2\hat{e}_+\Delta\hat{e}_- + \hat{e}_-\Delta\hat{e}_+ \tag{D.71}$$

this leads to $\hat{e}_+\Delta\hat{e}_- = \hat{e}_-\Delta\hat{e}_+$.

D.4 Gauge-Transformations of the Bogoliubov - de Gennes Equation

A gauge transformation $\vec{A} \rightarrow \vec{A} - \nabla\chi$ transforms the spinor $\vec{\psi}$ and the chiral vectors according to

$$\begin{pmatrix} \psi \\ \psi^* \end{pmatrix} \rightarrow e^{i\hat{\tau}_z \chi} \begin{pmatrix} \psi \\ \psi^* \end{pmatrix}, \quad \hat{e}_+ \rightarrow e^{-i\chi}\hat{e}_+, \quad \hat{e}_- \rightarrow e^{i\chi}\hat{e}_-, \tag{D.72}$$

The Lagrangian, and in particular $\hat{H}$, needs to be invariant under this gauge transformation. Writing it out in components

$$\begin{pmatrix} \psi^* \\ \psi \end{pmatrix} \begin{pmatrix} H^+ & W^- \\ W^+ & H^- \end{pmatrix} \begin{pmatrix} \psi \\ \psi^* \end{pmatrix} = \psi^* H^+ \psi + \psi W^+ \psi + \psi^* W^- \psi^* + \psi H^- \psi^* \tag{D.73}$$

one sees, that the off-diagonal terms must acquire a phase, i.e. they are not gauge-invariant: $W^\pm \rightarrow e^{\mp 2i\chi}W^\pm$.

Invariant Terms

While this is evident for diagonal terms involving only $\hat{m}_0$ that they being gauge-invariant, this is less clear for terms involving the chiral vectors $\hat{e}_+$, $\hat{e}_-$. We will express the former in terms of the chiral vectors and thereby show which diagonal terms involving the chiral vectors are gauge invariant. For this we will use index notation, assume summation over repeated indices, and use upper indices, e.g. $\hat{m}^0 = i\varepsilon_{ijk}e_j^+ e_k^-$ instead of $\hat{m}_0$:

$$-\hat{m}^0 \cdot \Delta\hat{m}^0 = -m_i^0 \partial_j \partial_j m_i^0 = -i\varepsilon_{imn}e_m^+ e_n^- \partial_j \partial_j [i\varepsilon_{iab}e_a^+ e_b^-] \tag{D.74}$$

$$= \varepsilon_{imn}\varepsilon_{iab}e_m^+ e_n^- [(\partial_j \partial_j e_a^+)e_b^- + 2(\partial_j e_a^+)(\partial_j e_b^-) + e_a^+(\partial_j \partial_j e_b^-)] \tag{D.75}$$

$$= (\delta_{ma}\delta_{nb} - \delta_{mb}\delta_{na})\, e_m^+ e_n^- [(\partial_j \partial_j e_a^+)e_b^- + 2(\partial_j e_a^+)(\partial_j e_b^-) + e_a^+(\partial_j \partial_j e_b^-)] \tag{D.76}$$

$$= e_a^+ e_b^- (\partial_j \partial_j e_a^+)e_b^- + 2e_a^+ e_b^- (\partial_j e_a^+)(\partial_j e_b^-) + e_a^+ e_b^- e_a^+ (\partial_j \partial_j e_b^-)$$

$$- e_b^+ e_a^- (\partial_j \partial_j e_a^+)e_b^- - 2e_b^+ e_a^- (\partial_j e_a^+)(\partial_j e_b^-) - e_b^+ e_a^- e_a^+ (\partial_j \partial_j e_b^-) \tag{D.77}$$

We use $e_b^- e_b^- = e_a^+ e_a^+ = 0$, $e_b^+ e_b^- = 1$, and $e_a^+(\partial_j e_a^+) = e_b^-(\partial_j e_b^-) = 0$ (see (D.17)), which results in

$$-\hat{m}^0 \cdot \Delta\hat{m}^0 = -e_a^-(\partial_j\partial_j e_a^+) - 2e_a^-(\partial_j e_a^+)e_b^+(\partial_j e_b^-) - e_b^+(\partial_j\partial_j e_b^-) \tag{D.78}$$

$$= -\hat{e}^- \cdot \Delta\hat{e}^+ - \hat{e}^+ \cdot \Delta\hat{e}^- - 2\hat{e}^-(\nabla\hat{e}^+)\hat{e}^+(\nabla\hat{e}^-) \tag{D.79}$$

$$= -2\operatorname{Re}(\hat{e}^- \cdot \Delta\hat{e}^+) + 2(\hat{e}^-(\nabla\hat{e}^+))^2 \tag{D.80}$$

as $\hat{e}^- \cdot \Delta\hat{e}^+ = \hat{e}^+ \cdot \Delta\hat{e}^-$ and $\hat{e}^-(\nabla\hat{e}^+) = -\hat{e}^+(\nabla\hat{e}^-)$ (see section D.3 for details). Similarly, we get

$$\hat{m}^0 \cdot (\nabla \times \hat{m}^0) = m_i^0 \varepsilon_{ijk}\partial_j m_k^0 = i\varepsilon_{imn}e_m^+ e_n^- \varepsilon_{ijk}\partial_j[i\varepsilon_{klp}e_l^+ e_p^-] \tag{D.81}$$

In order to mix the outer terms $e_m^+ e_n^-$ with the square bracket terms $\partial_j[e_l^+ e_p^-]$ we use the identity

$$\varepsilon_{imn}\varepsilon_{klp} = \delta_{ik}\delta_{ml}\delta_{np} + \delta_{il}\delta_{mp}\delta_{nk} + \delta_{ip}\delta_{mk}\delta_{nl} - \delta_{ik}\delta_{mp}\delta_{nl} - \delta_{ip}\delta_{ml}\delta_{nk} - \delta_{il}\delta_{mk}\delta_{np} \tag{D.82}$$

The resulting terms that involve δ_{ik} give zero as they identify two indices of the remaining Levi-Civita symbol ε_{ijk}.

$$\hat{m}^0 \cdot (\nabla \times \hat{m}^0) =$$

$$= -\{e_m^+ e_k^- \varepsilon_{ijk}\partial_j[e_i^+ e_m^-] + e_k^+ e_n^- \varepsilon_{ijk}\partial_j[e_n^+ e_i^-]$$

$$- e_m^+ e_k^- \varepsilon_{ijk}\partial_j[e_m^+ e_i^-] - e_k^+ e_n^- \varepsilon_{ijk}\partial_j[e_i^+ e_n^-]\} \tag{D.83}$$

$$= -\{e_m^+ e_k^- \varepsilon_{ijk}[(\partial_j e_i^+)e_m^- + e_i^+(\partial_j e_m^-)] + e_k^+ e_n^- \varepsilon_{ijk}[(\partial_j e_n^+)e_i^- + e_n^+(\partial_j e_i^-)]$$

$$- e_m^+ e_k^- \varepsilon_{ijk}[(\partial_j e_m^+)e_i^- + e_m^+(\partial_j e_i^-)] - e_k^+ e_n^- \varepsilon_{ijk}[(\partial_j e_i^+)e_n^- + e_i^+(\partial_j e_n^-)]\} \tag{D.84}$$

Again, using $e_m^+ e_m^+ = e_n^- e_n^- = 0$, $e_m^+ e_m^- = 1$, and $e_m^+(\partial_j e_m^+) = e_n^-(\partial_j e_n^-) = 0$ (see (D.17)), we obtain

$$\hat{m}^0 \cdot (\nabla \times \hat{m}^0) =$$

$$= -\{e_k^- \varepsilon_{ijk}(\partial_j e_i^+) + e_m^+ e_k^- \varepsilon_{ijk} e_i^+ (\partial_j e_m^-) + e_k^+ e_n^- \varepsilon_{ijk}(\partial_j e_n^+)e_i^- + e_k^+ \varepsilon_{ijk}(\partial_j e_i^-)\} \tag{D.85}$$

$$= e_k^- \varepsilon_{kji} \partial_j e_i^+ + e_k^+ \varepsilon_{kji} \partial_j e_i^- + e_m^+(\partial_j e_m^-)\varepsilon_{jik} e_i^+ e_k^- - e_n^-(\partial_j e_n^+)\varepsilon_{jki} e_k^+ e_i^- \tag{D.86}$$

$$= \hat{e}^- \cdot (\nabla \times \hat{e}^+) + \hat{e}^+ \cdot (\nabla \times \hat{e}^-) + \hat{e}^+(\nabla \hat{e}^-) \cdot (\hat{e}^+ \times \hat{e}^-) - \hat{e}^-(\nabla \hat{e}^+) \cdot (\hat{e}^+ \times \hat{e}^-) \tag{D.87}$$

$$= 2\,\mathrm{Re}(\hat{e}^+ \cdot (\nabla \times \hat{e}^-)) - 2i\hat{e}^+(\nabla \hat{e}^-) \cdot \hat{m}_0 \tag{D.88}$$

where we have used that $\hat{e}^- \cdot (\nabla \times \hat{e}^+) = \hat{e}^+ \cdot (\nabla \times \hat{e}^-)$ (see section D.3 for details). As the emergent vector potential $\vec{A} = i\hat{e}^+(\nabla \hat{e}^-)$ is orthogonal to the ground state magnetization $\hat{m}_0$, the last term vanishes and we have

$$\hat{m}^0 \cdot (\nabla \times \hat{m}^0) = 2\,\mathrm{Re}(\hat{e}^+ \cdot (\nabla \times \hat{e}^-)) \tag{D.89}$$

D.5 Remarks on Solving the Full Bogoliubov-de Gennes Equation in Real Space

Solving the full Bogoliubov-de Gennes equation in real space is a hard problem, which was attempted within this thesis but did not succeed due to time constraints. The challenges associated with this originate from the fact that to practically implement the Bogoliubov-de Gennes equation (8.6), one needs to find an explicit representation of the chiral vectors $\hat{e}_\pm$ for the given ground state magnetization $\hat{m}_0$.

As $\hat{m}_0(\vec{r})$ covers the entire unit sphere over a unit cell, employing spherical coordinates (θ, ϕ) to express the terms in $\hat{H}^\pm$, $\hat{W}^\pm$ leads to singularities in the derivative of ϕ, as the polar angle gets ill-defined at the poles (coordinate singularity). However, even working with an explicit representation of the chiral vectors $\hat{e}_\pm$ leads to unwanted singularities in the derivatives of $\hat{e}_\pm$, which are independent on the coordinates of the specific representation, but a general feature of the representation $\hat{m}_0 = i\hat{e}_+ \times \hat{e}_-$ being singular.

This can be understood from the hairy ball theorem: there is no continuous tangent vector field for even-dimensional n-spheres. Loosely speaking, there is no way to comb a vector field around that unit sphere without producing a cowlick for the ordinary 2-sphere. Let $\hat{m}_0$ indicate the position on the unit sphere, then $\hat{e}_+$ can be regarded as a tangent vector field, while $\hat{e}_- = \hat{m}_0 \times \hat{e}_+$ completes the tripod. However, due to the hairy ball theorem, the tangent vector field $\hat{e}_+$, and therefore also $\hat{e}_-$, cannot be chosen in a continuous way, and there will be at least one point on the unit sphere, where the derivatives of the chiral vectors $\hat{e}_\pm$ will get singular – this is an inherent feature of the parameterization that cannot be avoided.

However, all physical quantities that derive from this parameterization must not be affected, i.e. must not feature any singularities. Likewise, the Bogoliubov - de Gennes equation can be written in gauge-invariant form, which does not feature singularities – apart from the vector potential $\vec{A}$, which is not gauge-invariant. However, dealing even with those singularities in $\vec{A}$ is numerically challenging and leads to erroneous results when implemented straightforwardly in a central difference scheme.

It may be solved involving more advanced numerics such as the spectral method: At first, solving the Laplace equation with the respective non-constant boundary conditions and then using the resulting eigenfunctions as a basis. Next, the (yet unknown) solutions of the full Bogoliubov - de Gennes problem can be developed into this basis. Inserting it into the Bogoliubov - de Gennes equation, integrating it, and using the orthonormality of the basis functions leads to a set of linear equations, which constitutes an eigenvalue problem that could be solved.

E Derivation of the Spin–Torque Nano-Oscillator Model

In the following section, we will rederive a Lagrangian theory based on [177, 313, 322, 323] in order to describe the dynamics of an antiferromagnet (free layer) that is separated from a FM layer (fixed layer) by a metallic, non-magnetic spacer. An antiferromagnet can be described as a multi-sublattice magnet, in the simplest case being composed of two anti-parallel magnetic sublattices, labeled by $i = 1, 2$ and compensating each other $|\vec{M}_1| = |\vec{M}_2| = M_s$. Following [313], the spin-transfer (damping-like) torque reads

$$\vec{T}_i = \sigma J \left[\hat{m}_i \times (\hat{m}_i \times \hat{p}) \right] \tag{E.1}$$

which corresponds to the second term in (12.3) and where $\hat{m}_i = \frac{\vec{M}_i}{M_s}$ was already normalized to be consistent with our previous considerations. j is the spin current strength polarized in the direction $\hat{p}$ with $|\hat{p}| = 1$ and $\sigma = \frac{\varepsilon \hbar \gamma}{2Ve}$ captures the efficiency ε of scattering processes between the non-magnetic spacer and the AFM-layer, V is the volume of the AFM layer, $\hbar$ the reduced Planck constant, e the electron charge and γ the gyromagnetic ratio. Positive $j > 0$ corresponds to an injection of spin current into the AFM layer. The LLG equations with the classical Slonczewski term for the spin-transfer torque thus read

$$\frac{\partial \hat{m}_i}{\partial t} = -\gamma \, \hat{m}_i \times \vec{h}_{i,\text{eff}} + \sigma J \left[\hat{m}_i \times (\hat{m}_i \times \hat{p}) \right] + \bar{\alpha} \, \hat{m}_i \times \frac{\partial \hat{m}_i}{\partial t} \tag{E.2}$$

where $\vec{h}_{i,\text{eff}} = -\frac{1}{M_s} \frac{\delta \mathcal{F}}{\delta \hat{m}_i}$ is the effective local field acting on the i-th sublattice and $\mathcal{F}$ is the free energy density of the AFM layer. The field-like torque (first term in (12.3)) has been neglected. For an AFM with two sublattices we can rewrite the LLG equation in terms of the (macroscopic) magnetization $\vec{m}$ and the Néel order parameter $\vec{l}$

$$\vec{m} = \frac{\hat{m}_1 + \hat{m}_2}{2} = \frac{\vec{M}_1 + \vec{M}_2}{2M_s}, \quad \vec{l} = \frac{\hat{m}_1 - \hat{m}_2}{2} = \frac{\vec{M}_1 - \vec{M}_2}{2M_s} \tag{E.3}$$

This results in

$$\dot{\vec{m}} = \frac{1}{2}(\dot{\hat{m}}_1 + \dot{\hat{m}}_2) = \frac{\gamma}{2M_s} \left[\hat{m}_1 \times \frac{\delta \mathcal{F}}{\delta \hat{m}_1} + \hat{m}_2 \times \frac{\delta \mathcal{F}}{\delta \hat{m}_2} \right] + \frac{\bar{\alpha}}{2} \left[\hat{m}_1 \times \dot{\hat{m}}_1 + \hat{m}_2 \times \dot{\hat{m}}_2 \right]$$
$$+ \frac{\sigma J}{2} \left[\hat{m}_1 \times \hat{p} \times \hat{m}_1 + \hat{m}_2 \times \hat{p} \times \hat{m}_2 \right] \tag{E.4}$$

Using the chain rule for the functional derivative of two functionals F and G

$$\frac{\delta F[G[\rho]]}{\delta \rho(y)} = \int dx \frac{\delta F[G]}{\delta G(x)} \frac{\delta G[\rho](x)}{\delta \rho(y)} \tag{E.5}$$

we find that

$$\frac{\delta \mathcal{F}}{\delta \hat{m}_1} = \int dr' \left[\frac{\delta \mathcal{F}}{\delta \vec{m}} \underbrace{\frac{\delta \vec{m}}{\delta \hat{m}_1}}_{=\delta(\vec{r}-\vec{r}')/2} + \frac{\delta \mathcal{F}}{\delta \vec{l}} \underbrace{\frac{\delta \vec{l}}{\delta \hat{m}_1}}_{=\delta(\vec{r}-\vec{r}')/2} \right] = \frac{1}{2} \left[\frac{\delta \mathcal{F}}{\delta \vec{m}} + \frac{\delta \mathcal{F}}{\delta \vec{l}} \right] \tag{E.6}$$

$$\frac{\delta \mathcal{F}}{\delta \hat{m}_2} = \int dr' \left[\frac{\delta \mathcal{F}}{\delta \vec{m}} \underbrace{\frac{\delta \vec{m}}{\delta \hat{m}_2}}_{=\delta(\vec{r}-\vec{r}')/2} + \frac{\delta \mathcal{F}}{\delta \vec{l}} \underbrace{\frac{\delta \vec{l}}{\delta \hat{m}_2}}_{=-\delta(\vec{r}-\vec{r}')/2} \right] = \frac{1}{2} \left[\frac{\delta \mathcal{F}}{\delta \vec{m}} - \frac{\delta \mathcal{F}}{\delta \vec{l}} \right] \tag{E.7}$$

and inserting these relations alongside $\hat{m}_1 = \vec{m} + \vec{l}$ and $\hat{m}_2 = \vec{m} - \vec{l}$ leads to

$$\dot{\vec{m}} = \frac{\gamma}{4M_s} \left[(\vec{m} + \vec{l}) \times \left(\frac{\delta \mathcal{F}}{\delta \vec{m}} + \frac{\delta \mathcal{F}}{\delta \vec{l}} \right) + (\vec{m} - \vec{l}) \times \left(\frac{\delta \mathcal{F}}{\delta \vec{m}} - \frac{\delta \mathcal{F}}{\delta \vec{l}} \right) \right]$$

$$+ \frac{\bar{\alpha}}{2} \left[(\vec{m} + \vec{l}) \times (\dot{\vec{m}} + \dot{\vec{l}}) + (\vec{m} - \vec{l}) \times (\dot{\vec{m}} - \dot{\vec{l}}) \right]$$

$$+ \frac{\sigma J}{2} \underbrace{\left[\underbrace{(\hat{m}_1 \cdot \hat{m}_1)}_{=1} \hat{p} - (\hat{m}_1 \cdot \hat{p}) \hat{m}_1 + \underbrace{(\hat{m}_2 \cdot \hat{m}_2)}_{=1} \hat{p} - (\hat{m}_2 \cdot \hat{p}) \hat{m}_2 \right]}_{=2\hat{p} - (\vec{m} + \vec{l})(\vec{m} \cdot \hat{p} + \vec{l} \cdot \hat{p}) - (\vec{m} - \vec{l})(\vec{m} \cdot \hat{p} - \vec{l} \cdot \hat{p})} \tag{E.8}$$

Simplifying these terms leads to

$$\dot{\vec{m}} = \frac{\gamma}{2M_s} \left[\vec{m} \times \frac{\delta \mathcal{F}}{\delta \vec{m}} + \vec{l} \times \frac{\delta \mathcal{F}}{\delta \vec{l}} \right] + \bar{\alpha} \left[\vec{m} \times \dot{\vec{m}} + \vec{l} \times \dot{\vec{l}} \right] + \sigma J \left[\hat{p} - \vec{m}(\vec{m} \cdot \hat{p}) - \vec{l}(\vec{l} \cdot \hat{p}) \right] \tag{E.9}$$

Analogously, one obtains

$$\dot{\vec{l}} = \frac{1}{2}(\dot{\hat{m}}_1 - \dot{\hat{m}}_2) \tag{E.10}$$

$$= \frac{\gamma}{2M_s}\left[\vec{m}\times\frac{\delta\mathcal{F}}{\delta\vec{l}} + \vec{l}\times\frac{\delta\mathcal{F}}{\delta\vec{m}}\right] + \bar{\alpha}\left[\vec{m}\times\dot{\vec{l}} + \vec{l}\times\dot{\vec{m}}\right] - \sigma J\left[\vec{m}(\vec{l}\cdot\hat{p}) + \vec{l}(\vec{m}\cdot\hat{p})\right] \tag{E.11}$$

Introducing $\vec{h}_m = -\frac{1}{M_s}\frac{\partial\mathcal{F}}{\partial\vec{m}}$, an effective magnetic field that includes external magnetic fields, and $\vec{h}_l = -\frac{1}{M_s}\frac{\partial\mathcal{F}}{\partial\vec{l}}$, a magnetic anisotropy conjugate to the Néel order parameter, one can express these equations also in the form

$$\dot{\vec{m}} = \gamma[(\vec{h}_m\times\vec{m}) + (\vec{h}_l\times\vec{l})] + \bar{\alpha}[(\vec{m}\times\dot{\vec{m}}) + (\vec{l}\times\dot{\vec{l}})]$$
$$+ \sigma J\left[\vec{m}\times(\vec{m}\times\hat{p}) + \vec{l}\times(\vec{l}\times\hat{p})\right] \tag{E.12}$$

$$\dot{\vec{l}} = \gamma[(\vec{h}_m\times\vec{l}) + (\vec{h}_l\times\vec{m})] + \bar{\alpha}[(\vec{m}\times\dot{\vec{l}}) + (\vec{l}\times\dot{\vec{m}})]$$
$$+ \sigma J\left[\vec{m}\times(\vec{l}\times\hat{p}) + \vec{l}\times(\vec{m}\times\hat{p})\right] \tag{E.13}$$

Exchange Approximation

In order to proceed, we need to specify the free energy density, describing our bipartite antiferromagnet including uniform and non-uniform exchange, uniaxial anisotropy, and the influence of an external magnetic field via a Zeeman term

$$\mathcal{F} = \mathcal{F}_{\text{ex}} + \mathcal{F}_{\text{an}} + \mathcal{F}_{\text{zee}} \tag{E.14}$$

The individual contributions assume the following expressions

$$\mathcal{F}_{\text{ex}} = \frac{H_{\text{ex}}M_s}{2}\hat{m}_1 \cdot \hat{m}_2 + \sum_{i=x,y,z} \left\{ \frac{A'}{2}\left[(\partial_i\hat{m}_1)^2 + (\partial_i\hat{m}_2)^2\right] + A''\left[\partial_i\hat{m}_1 \cdot \partial_i\hat{m}_2\right] \right\}$$

$$= \frac{H_{\text{ex}}M_s}{2}(\vec{m} + \vec{l}) \cdot (\vec{m} - \vec{l})$$

$$+ \sum_{i=x,y,z} \left\{ \frac{A'}{2}\left[2(\partial_i\vec{m})^2 + 2(\partial_i\vec{l})^2\right] + A''\left[(\partial_i\vec{m} + \partial_i\vec{l}) \cdot (\partial_i\vec{m} - \partial_i\vec{l})\right] \right\}$$

$$= \frac{H_{\text{ex}}M_s}{2}(2\vec{m}^2 - 1) + \sum_{i=x,y,z} \left\{ (A' + A'')(\partial_i\vec{m})^2 + \underbrace{(A' - A'')}_{=A}(\partial_i\vec{l})^2 \right\} \tag{E.15}$$

$$\mathcal{F}_{\text{an}} = -\frac{H_{\text{an}}M_s}{2}\left[(\hat{m}_1 \cdot \hat{n})^2 + (\hat{m}_2 \cdot \hat{n})^2\right] = -H_{\text{an}}M_s\left[(\vec{m} \cdot \hat{n})^2 + (\vec{l} \cdot \hat{n})^2\right] \tag{E.16}$$

$$\mathcal{F}_{\text{zee}} = -M_s\vec{H} \cdot (\hat{m}_1 + \hat{m}_2) = -2M_s\vec{H} \cdot \vec{m} \tag{E.17}$$

with $|\hat{n}| = 1$ as the direction of the uniaxial anisotropy, an external magnetic field $\vec{H}$, and $H_{\text{ex}}M_s$, $H_{\text{an}}M_s$ being the strength of exchange and uniaxial anisotropy, respectively. The functional derivatives are given by

$$\frac{\delta\mathcal{F}}{\delta\vec{m}} = \frac{\partial\mathcal{F}}{\partial\vec{m}} - \sum_{i=x,y,z} \partial_i \frac{\partial\mathcal{F}}{\partial(\partial_i\vec{m})} = 2H_{\text{ex}}M_s\vec{m} - 2H_{\text{an}}M_s(\vec{m} \cdot \hat{n})\hat{n}$$

$$- 2M_s\vec{H} - (A' + A'')\nabla^2\vec{m} \tag{E.18}$$

$$\frac{\delta\mathcal{F}}{\delta\vec{l}} = \frac{\partial\mathcal{F}}{\partial\vec{l}} - \sum_{i=x,y,z} \partial_i \frac{\partial\mathcal{F}}{\partial(\partial_i\vec{l})} = -2H_{\text{an}}(\vec{l} \cdot \hat{n})\hat{n} - A\nabla^2\vec{l} \tag{E.19}$$

Next, they are inserted into the equation of motion (E.13) for $\vec{l}$. Within the exchange approximation all terms proportional to $\vec{m}$ are neglected (displayed in red), apart from the linear term $H_{\mathrm{ex}}M_s\vec{m}$ originating from uniform exchange

$$\dot{\vec{l}} = \frac{\gamma}{2M_s}\left[\vec{m}\times\frac{\delta\mathcal{F}}{\delta\vec{l}} + \vec{l}\times(2H_{\mathrm{ex}}M_s\vec{m}-2H_{\mathrm{an}}M_s(\vec{m}\cdot\hat{n})\hat{n} - 2M_s\vec{H}-(A'+A'')\nabla^2\vec{m})\right]$$

$$+\bar{\alpha}\left[\vec{m}\times\dot{\vec{l}}+\vec{l}\times\dot{\vec{m}}\right] - \sigma J\left[\vec{m}(\vec{l}\cdot\hat{p})+\vec{l}(\vec{m}\cdot\hat{p})\right]$$

$$=\gamma\left[H_{\mathrm{ex}}\vec{l}\times\vec{m} - \vec{l}\times\vec{H}\right] \tag{E.20}$$

Next, we take the cross product with $\vec{l}$ on both sides

$$\vec{l}\times\dot{\vec{l}} = \gamma\left(H_{\mathrm{ex}}\vec{l}\times[\vec{m}\times\vec{l}] - [\vec{l}\times\vec{H}]\times\vec{l}\right) \tag{E.21}$$

and use

$$\vec{l}\times[\vec{m}\times\vec{l}] = \vec{m}\underbrace{\vec{l}^2}_{\approx 1} + \vec{l}\underbrace{(\vec{m}\cdot\vec{l})}_{=0} = \vec{m} \tag{E.22}$$

so that we, finally, arrive at

$$\vec{m} = \frac{\dot{\vec{l}}\times\vec{l}}{\gamma H_{\mathrm{ex}}} + \frac{\vec{l}\times[\vec{H}\times\vec{l}]}{H_{\mathrm{ex}}} \tag{E.23}$$

We can substitute this into the equation of motion (E.12) for $\vec{m}$, this time neglecting terms that are quadratic in $\vec{m}$ (again highlighted in red)

$$\dot{\vec{m}} = \frac{\ddot{\vec{l}}\times\vec{l}}{\gamma H_{\mathrm{ex}}} + \frac{1}{H_{\mathrm{ex}}}\left[\partial_t[\vec{l}\times\vec{H}]\times\vec{l} + [\vec{l}\times\vec{H}]\times\dot{\vec{l}}\right]$$

$$\stackrel{!}{=} \frac{\gamma}{2M_s}\left[\vec{m}\times\left(2H_{\mathrm{ex}}M_s\vec{m} - 2H_{\mathrm{an}}M_s(\vec{m}\cdot\hat{n})\hat{n} - 2M_s\vec{H}-(A'+A'')\nabla^2\vec{m}\right) + \vec{l}\times\frac{\delta\mathcal{F}}{\delta\vec{l}}\right]$$

$$+\bar{\alpha}\left[\vec{m}\times\dot{\vec{m}} + \vec{l}\times\dot{\vec{l}}\right] + \sigma J\left[\hat{p}-\vec{m}(\vec{m}\cdot\hat{p}) - \vec{l}(\vec{l}\cdot\hat{p})\right]$$

$$= -\gamma\left[\vec{m}\times\vec{H}\right] + \frac{\gamma}{2M_s}\vec{l}\times\frac{\delta\mathcal{F}}{\delta\vec{l}} + \bar{\alpha} + \vec{l}\times\dot{\vec{l}} + \sigma J\left[\vec{l}\times\hat{p}\times\vec{l}\right] \tag{E.24}$$

Last but not least we can also express the first term $-\gamma\left[\vec{m}\times\vec{H}\right]$ in (E.24) through $\vec{l}$ using (E.23)

$$-\gamma\left[\vec{m}\times\vec{H}\right] = -\gamma\frac{[\dot{\vec{l}}\times\vec{l}]\times\vec{H}}{\gamma H_{\text{ex}}} - \frac{\gamma}{H_{\text{ex}}}[(\vec{l}\times\vec{H})\times\vec{l}]\times\vec{H}$$

$$= \frac{1}{H_{\text{ex}}}\vec{H}\times[\dot{\vec{l}}\times\vec{l}] - \frac{\gamma}{H_{\text{ex}}}[\vec{H}-\vec{l}(\vec{l}\cdot\vec{H})]\times\vec{H}$$

$$= \frac{1}{H_{\text{ex}}}\vec{H}\times[\dot{\vec{l}}\times\vec{l}] - \frac{\gamma}{H_{\text{ex}}} - [\vec{l}\times\vec{H}](\vec{l}\cdot\vec{H}) \tag{E.25}$$

resulting in the closed-form equation of motion

$$(\ddot{\vec{l}} + \gamma\vec{l}\times\vec{H} + 2\gamma\dot{l}\times\vec{H} + \gamma^2\vec{H}(\vec{l}\cdot\vec{H}) - \frac{\gamma^2 H_{\text{ex}}A}{M_s}\nabla^2\vec{l} - \gamma H_{\text{ex}}H_{\text{an}}(\vec{l}\cdot\hat{n})\hat{n}$$

$$+ \gamma\bar{\alpha}H_{\text{ex}}\dot{\vec{l}} - \gamma J\sigma H_{\text{ex}}[\vec{l}\times\hat{p}])\times\vec{l} = 0 \tag{E.26}$$

It can be regarded as an Euler-Lagrange equation stemming from the Lagrange density

$$\mathcal{L} = \frac{M_s}{\gamma^2 H_{\text{ex}}}\dot{\vec{l}}^2 - \frac{1}{\gamma H_{\text{ex}}}(\vec{H}\cdot[\vec{l}\times\dot{\vec{l}}]) + \frac{M_s}{H_{\text{ex}}}[\vec{l}\times\vec{H}]^2 - \mathcal{F}_{\text{stat}}(\vec{l}) \tag{E.27}$$

and a yet to be determined Rayleigh density $\mathcal{R}$.

Rayleigh Dissipation Function

To account for dissipation, which stems from the last two terms of the original LLG equation (E.2), we determine the rate of energy loss. Getting back to the microscopic level of individual magnetic moments and assuming that dissipation is small and in zeroth approximation

$$\frac{\partial\hat{m}_i}{\partial t} = -\gamma\,\hat{m}_i\times\vec{h}_{i,\text{eff}} \tag{E.28}$$

Using (E.2), the rate of energy loss is given by the time derivative of the free energy density

$$\frac{d\mathcal{F}}{dt} = -\sum_i M_s \vec{h}_{i,\text{eff}} \cdot \frac{\partial \hat{m}_i}{\partial t}$$

$$= -\sum_i M_s \vec{h}_{i,\text{eff}} \cdot \left[-\gamma \hat{m}_i \times \vec{h}_{i,\text{eff}} + \sigma j \left[\hat{m}_i \times (\hat{m}_i \times \hat{p}) \right] + \alpha \, \hat{m}_i \times \frac{\partial \hat{m}_i}{\partial t} \right]$$

$$= -\sum_i M_s \sigma j \, \vec{h}_{i,\text{eff}} \cdot \left[\hat{m}_i \times (\hat{m}_i \times \hat{p}) \right] + \alpha M_s \, \vec{h}_{i,\text{eff}} \cdot \left[\hat{m}_i \times \frac{\partial \hat{m}_i}{\partial t} \right]$$

Using $\frac{\partial \hat{m}_i}{\partial t} = -\gamma \, \hat{m}_i \times \vec{h}_{i,\text{eff}}$ we get for the first term

$$\vec{h}_{i,\text{eff}} \cdot \left[\hat{m}_i \times (\hat{m}_i \times \hat{p}) \right] = -(\hat{m}_i \times \hat{p}) \cdot (\hat{m}_i \times \vec{h}_{i,\text{eff}})$$

$$= \frac{1}{\gamma} (\hat{m}_i \times \hat{p}) \cdot \frac{\partial \hat{m}_i}{\partial t} = -\frac{1}{\gamma} \hat{p} \cdot \left[\hat{m}_i \times \frac{\partial \hat{m}_i}{\partial t} \right] \qquad (E.29)$$

and for the second term

$$\vec{h}_{i,\text{eff}} \cdot \left[\hat{m}_i \times \frac{\partial \hat{m}_i}{\partial t} \right] = -\frac{\partial \hat{m}_i}{\partial t} \cdot \left[\hat{m}_i \times \vec{h}_{i,\text{eff}} \right] = \frac{1}{\gamma} \left(\frac{\partial \hat{m}_i}{\partial t} \right)^2 \qquad (E.30)$$

so that we, finally, arrive at

$$\frac{d\mathcal{F}}{dt} = -\sum_i \frac{\alpha M_s}{\gamma} \left(\frac{\partial \hat{m}_i}{\partial t} \right)^2 - \frac{\sigma j M_s}{\gamma} \hat{p} \cdot \left[\hat{m}_i \times \frac{\partial \hat{m}_i}{\partial t} \right] \qquad (E.31)$$

Switching to a macroscopic picture, in the Lagrangian formalism damping can be described by the Rayleigh dissipation function, which is related to the rate of energy loss via

$$\frac{d\mathcal{F}}{dt} = -\dot{\vec{l}} \cdot \frac{\partial \mathcal{R}_{AFM}}{\partial \dot{\vec{l}}} \qquad (E.32)$$

It reads

$$\mathcal{R}_{AFM} = \frac{\alpha M_s}{\gamma} \dot{\vec{l}}^2 - \frac{\sigma j M_s}{\gamma} (\hat{p} \cdot [\vec{l} \times \dot{\vec{l}}]) \qquad (E.33)$$

This can be shown by calculating

$$-\dot{\vec{l}} \cdot \frac{\partial \mathcal{R}_{AFM}}{\partial \dot{\vec{l}}} = -\dot{\vec{l}} \cdot \left(\frac{2\alpha M_s}{\gamma} \dot{\vec{l}} - \frac{\sigma j M_s}{\gamma} [\hat{p} \times \vec{l}] \right) = -\frac{2\alpha M_s}{\gamma} \dot{\vec{l}}^2 + \frac{\sigma j M_s}{\gamma} \dot{\vec{l}} \cdot [\hat{p} \times \vec{l}] \quad \text{(E.34)}$$

Taking into account $\hat{m}_1 = -\hat{m}_2 = \frac{\vec{l}}{2}$ (valid in the limit of a large exchange field that we consider) we get

$$\frac{d\mathcal{F}}{dt} = -\frac{2\alpha M_s}{\gamma} \dot{\hat{m}}_1^2 + \frac{2\sigma j M_s}{\gamma} \dot{\hat{m}}_1 \cdot [\hat{p} \times \hat{m}_1] \quad \text{(E.35)}$$

which is consistent with expression (E.31) given above.

Summary of the Model

In summary, we have derived the Lagrangian model

$$\mathcal{L} = \frac{M_s}{\gamma^2 H_{\text{ex}}} \dot{\hat{l}}^2 - \frac{1}{\gamma H_{\text{ex}}} (\vec{H} \cdot [\hat{l} \times \dot{\hat{l}}]) + \frac{M_s}{H_{\text{ex}}} [\hat{l} \times \vec{H}]^2 - \mathcal{F}_{\text{stat}}(\hat{l}) \quad \text{(12.4)}$$

$$\mathcal{R}_{AFM} = \frac{\alpha M_s}{\gamma} \dot{\hat{l}}^2 - \frac{\sigma j M_s}{\gamma} (\hat{p} \cdot [\hat{l} \times \dot{\hat{l}}]) \quad \text{(12.5)}$$

describing the dynamics of the Néel vector $\hat{l}$.

Acknowledgements

Bibliography

[1] J. Clayden, N. Greeves, and S. Warren, *Organic chemistry* (Oxford University Press, 2012).

[2] J. Mun, M. Kim, Y. Yang, T. Badloe, J. Ni, Y. Chen, C.-W. Qiu, and J. Rho, Light: Science & Applications **9**, 139 (2020).

[3] J. Campbell, J. Huston, and F. Krauss, *The black book of quantum chromodynamics: a primer for the lhc era* (Oxford University Press, 2018).

[4] A. A. Abrikosov, Journal of Physics and Chemistry of Solids **2**, 199 (1957).

[5] J. F. Annett, *Superconductivity, superfluids, and condensates* (Oxford University Press, 2005).

[6] J. H. Han, J. Zang, Z. Yang, J.-H. Park, and N. Nagaosa, Phys. Rev. B **82**, 094429 (2010).

[7] G. Yin, Y. Li, L. Kong, R. K. Lake, C. L. Chien, and J. Zang, Phys. Rev. B **93**, 174403 (2016).

[8] K. Everschor-Sitte and M. Sitte, Journal of Applied Physics **115**, 172602 (2014).

[9] A. Hirohata and K. Takanashi, Journal of Physics D: Applied Physics **47**, 193001 (2014).

[10] A. Hirohata, K. Yamada, Y. Nakatani, I.-L. Prejbeanu, B. Diény, P. Pirro, and B. Hillebrands, Journal of Magnetism and Magnetic Materials **509**, 166711 (2020).

[11] T. H. R. Skyrme and B. F. J. Schonland, Proceedings of the Royal Society of London. Series A. Mathematical and Physical Sciences **260**, 127 (1961).

[12] T. H. R. Skyrme, Nuclear Physics **31**, 556 (1962).

[13] M. Rho and I. Zahed, eds., *The multifaceted skyrmion* (World Scientific, 2016).

[14] T. H. R. Skyrme, Proceedings of the Royal Society A: Mathematical, Physical and Engineering Sciences **262,** 237 (1961).

[15] A. A. Kovalev and S. Sandhoefner, Frontiers in Physics **6**, 98 (2018).

[16] B. Piette, B. Schroers, and W. Zakrzewski, Nuclear Physics B **439**, 205 (1995).

[17] M. Gell-Mann and M. Lévy, Il Nuovo Cimento (1955-1965) **16**, 705 (1960).

[18] Y. M. Shnir, *Topological and non-topological solitons in scalar field theories* (Cambridge University Press, 2018).

[19] N. Manton and P. Sutcliffe, *Topological solitons* (Cambridge University Press, Cambridge, 2004).

[20] A. N. Bogdanov and D. A. Yablonskii, Sov. Phys. JETP **68**, 101 (1989).

[21] A. Bogdanov and A. Hubert, J. Magn. Magn. Mater. **138**, 255 (1994).

[22] U. K. Rößler, A. N. Bogdanov, and C. Pfleiderer, Nature **442**, 797 (2006).

[23] A. Bogdanov, Sov. Phys. JETP **62**, 247 (1995).

[24] L. Landau and E. Lifshitz, *Statistical physics part 1*, Vol. 5, Course of Theoretical Physics (Oxford: Pergamon, 1980).

[25] I. Dzyaloshinsky, J. Phys. Chem. Solids **4**, 241 (1958).

[26] T. Moriya, Phys. Rev. **120**, 91 (1960).

[27] K. Everschor-Sitte and M. Sitte, Wikimedia, `https://commons.wikimedia.org/wiki/File:2skyrmions.PNG`, Nov. 2015.

[28] P. F. Bessarab, G. P. Müller, I. S. Lobanov, F. N. Rybakov, N. S. Kiselev, H. Jónsson, V. M. Uzdin, S. Blügel, L. Bergqvist, and A. Delin, Scientific Reports **8**, 3433 (2018).

[29] J. Wild, T. N. G. Meier, S. Pöllath, M. Kronseder, A. Bauer, A. Chacon, M. Halder, M. Schowalter, A. Rosenauer, J. Zweck, J. Müller, A. Rosch, C. Pfleiderer, and C. H. Back, Sci Adv **3**, e1701704 (2017).

[30] D. Cortés-Ortuño, W. Wang, M. Beg, R. A. Pepper, M.-A. Bisotti, R. Carey, M. Vousden, T. Kluyver, O. Hovorka, and H. Fangohr, Scientific Reports **7**, 4060 (2017).

[31] S. Mühlbauer, B. Binz, F. Jonietz, C. Pfleiderer, A. Rosch, A. Neubauer, R. Georg, and P. Böni, Science **323**, 915 (2009).

[32] T. Adams, S. Mühlbauer, C. Pfleiderer, F. Jonietz, A. Bauer, A. Neubauer, R. Georgii, P. Böni, U. Keiderling, K. Everschor, M. Garst, and A. Rosch, Phys. Rev. Lett. **107**, 217206 (2011).

[33] M. Janoschek, M. Garst, A. Bauer, P. Krautscheid, R. Georgii, P. Boeni, and C. Pfleiderer, Physical Review B **87**, 134407 (2013).

[34] W. Münzer, A. Neubauer, T. Adams, S. Mühlbauer, C. Franz, F. Jonietz, R. Georgii, P. Böni, B. Pedersen, M. Schmidt, A. Rosch, and C. Pfleiderer, Phys. Rev. B **81**, 041203 (2010).

[35] P. Milde, D. Köhler, J. Seidel, L. M. Eng, A. Bauer, A. Chacon, J. Kindervater, S. Mühlbauer, C. Pfleiderer, S. Buhrandt, C. Schütte, and A. Rosch, Science **340**, 1076 (2013).

[36] X. Z. Yu, Y. Onose, N. Kanazawa, J. H. Park, J. H. Han, Y. Matsui, N. Nagaosa, and Y. Tokura, Nature **465**, 901 (2010).

[37] X. Z. Yu, N. Kanazawa, Y. Onose, K. Kimoto, W. Z. Zhang, S. Ishiwata, Y. Matsui, and Y. Tokura, Nat. Mater. **10**, 106 (2011).

[38] K. Shibata, X. Yu, T. Hara, D. Morikawa, N. Kanazawa, K. Kimoto, S. Ishiwata, Y. Matsui, and Y. Tokura, Nature nanotechnology **8**, 723 (2013).

[39] I. Kézsmárki, S. Bordács, P. Milde, E. Neuber, L. M. Eng, J. S. White, H. M. Rønnow, C. D. Dewhurst, M. Mochizuki, K. Yanai, H. Nakamura, D. Ehlers, V. Tsurkan, and A. Loidl, Nature Materials **14**, 1116 (2015).

[40] T. Adams, A. Chacon, M. Wagner, A. Bauer, G. Brandl, B. Pedersen, H. Berger, P. Lemmens, and C. Pfleiderer, Phys. Rev. Lett. **108**, 237204 (2012).

[41] S. Seki and M. Mochizuki, *Skyrmions in magnetic materials*, SpringerBriefs in Physics (Springer International Publishing, 2016).

[42] S. Seki, J.-H. Kim, D. S. Inosov, R. Georgii, B. Keimer, S. Ishiwata, and Y. Tokura, Phys. Rev. B **85**, 220406 (2012).

[43] Y. S. Lin, P. J. Grundy, and E. A. Giess, Appl. Phys. Lett. **23**, 485 (1973).

[44] T. Garel and S. Doniach, Phys. Rev. B **26**, 325 (1982).

[45] S. Takao, J. Magn. Magn. Mater. **31-34**, 1009 (1983).

[46] M. Ezawa, Phys. Rev. Lett. **105**, 197202 (2010).

[47] T. Okubo, S. Chung, and H. Kawamura, Phys. Rev. Lett. **108**, 017206 (2012).

[48] S. Heinze, K. von Bergmann, M. Menzel, J. Brede, A. Kubetzka, R. Wiesendanger, G. Bihlmayer, and S. Blügel, Nature Physics **7**, 713 (2011).

[49] A. Neubauer, C. Pfleiderer, B. Binz, A. Rosch, R. Ritz, P. G. Niklowitz, and P. Böni, Phys. Rev. Lett. **102**, 186602 (2009).

[50] A. Bauer, M. Garst, and C. Pfleiderer, Phys. Rev. Lett. **110**, 177207 (2013).

[51] A. Bauer and C. Pfleiderer, Phys. Rev. B **85**, 214418 (2012).

[52] Y. Ishikawa, K. Tajima, D. Bloch, and M. Roth, Solid State Communications **19**, 525 (1976).

192

[53] P. Bak and M. H. Jensen, Journal of Physics C: Solid State Physics **13**, L881 (1980).

[54] M. L. Plumer and M. B. Walker, Journal of Physics C: Solid State Physics **14**, 4689 (1981).

[55] O. Nakanishi, A. Yanase, A. Hasegawa, and M. Kataoka, Solid State Communications **35**, 995 (1980).

[56] J. Kindervater, W. Häußler, M. Janoschek, C. Pfleiderer, P. Böni, and M. Garst, Phys. Rev. B **89**, 180408 (2014).

[57] S. A. Brazovskii, Sov. Phys. JETP **41**, 85 (1975).

[58] B. Lebech, P. Harris, J. Skov Pedersen, K. Mortensen, C. I. Gregory, N. R. Bernhoeft, M. Jermy, and S. A. Brown, International Conference on Magnetism **140-144**, 119 (1995).

[59] C. Pfleiderer, D. Reznik, L. Pintschovius, and J. Haug, PRL **99**, 156406 (2007).

[60] Y. Ishikawa and M. Arai, J. Phys. Soc. Jpn. **53**, 2726 (1984).

[61] S. V. Grigoriev, S. V. Maleyev, A. I. Okorokov, Y. O. Chetverikov, and H. Eckerlebe, PRB **73**, 224440 (2006).

[62] B. Lebech, 0 (WORLD SCIENTIFIC, Mar. 1993), pp. 167–178.

[63] T. Adams, M. Garst, A. Bauer, R. Georgii, and C. Pfleiderer, Phys. Rev. Lett. **121**, 187205 (2018).

[64] M. Laver and E. M. Forgan, Nature Communications **1**, 45 (2010).

[65] S. Buhrandt and L. Fritz, Phys. Rev. B **88**, 195137 (2013).

[66] S. D. Yi, S. Onoda, N. Nagaosa, and J. H. Han, Phys. Rev. B **80**, 054416 (2009).

[67] A. Tonomura, X. Yu, K. Yanagisawa, T. Matsuda, Y. Onose, N. Kanazawa, H. S. Park, and Y. Tokura, Nano Lett. **12**, 1673 (2012).

[68] N. Nagaosa and Y. Tokura, Nat. Nanotechnol. **8**, 899 (2013).

[69] K. Everschor-Sitte, J. Masell, R. M. Reeve, and M. Kläui, J. Appl. Phys. **124**, 240901 (2018).

[70] Y. Tokura and N. Kanazawa, Chem. Rev., `10.1021/acs.chemrev.0c00297` (2020).

[71] G. Finocchio, F. Büttner, R. Tomasello, M. Carpentieri, and M. Kläui, Journal of Physics D: Applied Physics **49**, 423001 (2016).

[72] J. H. Han, *Skyrmions in condensed matter*, Springer Tracts in Modern Physics (Springer International Publishing, 2017).

[73] J. P. Liu, Z. Zhang, and G. Zhao, eds., *Skyrmions. topological structures, properties, and applications*, Series in Materials Science and Engineering (CRC Press by Taylor & Francis Group, 2017).

[74] J. Iwasaki, M. Mochizuki, and N. Nagaosa, Nature Nanotechnology **8**, 742 (2013).

[75] J. Sampaio, V. Cros, S. Rohart, A. Thiaville, and A. Fert, Nature Nanotechnology **8**, 839 (2013).

[76] N. Romming, C. Hanneken, M. Menzel, J. E. Bickel, B. Wolter, K. von Bergmann, A. Kubetzka, and R. Wiesendanger, Science **341**, 636 (2013).

[77] H. Y. Yuan and X. R. Wang, Scientific Reports **6**, 22638 (2016).

[78] H. Du, R. Che, L. Kong, X. Zhao, C. Jin, C. Wang, J. Yang, W. Ning, R. Li, C. Jin, X. Chen, J. Zang, Y. Zhang, and M. Tian, Nature Communications **6**, 8504 (2015).

[79] J. Müller, A. Rosch, and M. Garst, New Journal of Physics **18**, 065006 (2016).

[80] T. Yokouchi, S. Sugimoto, B. Rana, S. Seki, N. Ogawa, S. Kasai, and Y. Otani, Nature Nanotechnology **15**, 361 (2020).

[81] R. Wiesendanger, Nature Reviews Materials **1**, 16044 (2016).

[82] A. Fert, N. Reyren, and V. Cros, Nature Reviews Materials **2**, 17031 (2017).

[83] A. Fert, V. Cros, and J. Sampaio, Nat. Nanotechnol. **8**, 152 (2013).

[84] M. V. Berry, Proceedings of the Royal Society of London. A. Mathematical and Physical Sciences **392**, 45 (1984).

[85] T. Schulz, R. Ritz, A. Bauer, M. Halder, M. Wagner, C. Franz, C. Pfleiderer, K. Everschor, M. Garst, and A. Rosch, Nature Physics **8**, 301 (2012).

[86] M. Lee, W. Kang, Y. Onose, Y. Tokura, and N. P. Ong, Phys. Rev. Lett. **102**, 186601 (2009).

[87] R. Ritz, M. Halder, M. Wagner, C. Franz, A. Bauer, and C. Pfleiderer, Nature **497**, 231 (2013).

[88] R. Ritz, M. Halder, C. Franz, A. Bauer, M. Wagner, R. Bamler, A. Rosch, and C. Pfleiderer, Phys. Rev. B **87**, 134424 (2013).

[89] J. C. Slonczewski, Journal of Magnetism and Magnetic Materials **159**, L1 (1996).

[90] K. Everschor, "Current-induced dynamics of chiral magnetic structures: skyrmions, emergent electrodynamics and spin-transfer torques", PhD thesis (Universität zu Köln, 2012).

[91] K. Everschor, M. Garst, B. Binz, F. Jonietz, S. Mühlbauer, C. Pfleiderer, and A. Rosch, PRB **86**, 054432 (2012).

[92] K. Everschor, M. Garst, R. A. Duine, and A. Rosch, PRB **84**, 064401 (2011).

[93] J. Iwasaki, M. Mochizuki, and N. Nagaosa, Nature Communications **4**, 1463 (2013).

[94] F. Jonietz, S. Mühlbauer, C. Pfleiderer, A. Neubauer, W. Münzer, A. Bauer, T. Adams, R. Georgii, P. Böni, R. A. Duine, K. Everschor, M. Garst, and A. Rosch, Science **330**, 1648 (2010).

[95] J. Zang, M. Mostovoy, J. H. Han, and N. Nagaosa, PRL **107**, 136804 (2011).

[96] M. Tsoi, R. E. Fontana, and S. S. P. Parkin, Appl. Phys. Lett. **83**, 2617 (2003).

[97] J. Grollier, P. Boulenc, V. Cros, A. Hamzić, A. Vaurès, A. Fert, and G. Faini, Appl. Phys. Lett. **83**, 509 (2003).

[98] W. Jiang, X. Zhang, G. Yu, W. Zhang, X. Wang, M. Benjamin Jungfleisch, J. E. Pearson, X. Cheng, O. Heinonen, K. L. Wang, Y. Zhou, A. Hoffmann, and S. G. E. te Velthuis, Nature Physics **13**, 162 (2017).

[99] K. Litzius, I. Lemesh, B. Krüger, P. Bassirian, L. Caretta, K. Richter, F. Büttner, K. Sato, O. A. Tretiakov, J. Förster, R. M. Reeve, M. Weigand, I. Bykova, H. Stoll, G. Schütz, G. S. D. Beach, and M. Kläui, Nature Physics **13**, 170 (2017).

[100] T. Yokouchi, F. Kagawa, M. Hirschberger, Y. Otani, N. Nagaosa, and Y. Tokura, Nature **586**, 232 (2020).

[101] N. Nagaosa, Japanese Journal of Applied Physics **58**, 120909 (2019).

[102] D. Kurebayashi and N. Nagaosa, *Electromagnetic response in spiral magnets and emergent inductance*, 2021.

[103] A. Kitaori, N. Kanazawa, T. Yokouchi, F. Kagawa, N. Nagaosa, and Y. Tokura, *Emergent electromagnetic induction beyond room temperature*, 2021.

[104] C. Schütte, "Skyrmions and monopoles in chiral magnets & correlated heterostructures", PhD thesis (Universität Köln, 2014).

[105] V. P. Kravchuk, D. D. Sheka, U. K. Rößler, J. van den Brink, and Y. Gaididei, Phys. Rev. B **97**, 064403 (2018).

[106] S. Sachdev, *Quantum phase transitions*, 2nd ed. (Cambridge University Press, 2011).

[107] P. Hohenberg and A. Krekhov, Physics Reports **572**, 1 (2015).

194

[108] L. D. Landau, Zh. Eksp. Teor. Fiz. **7**, 19 (1937).

[109] V. L. Ginzburg and L. D. Landau, Zh. Eksp. Teor. Fiz. **20**, 1064 (1950).

[110] P. W. Anderson, Phys. Rev. **115**, 2 (1959).

[111] U. Güngördü, R. Nepal, O. A. Tretiakov, K. Belashchenko, and A. A. Kovalev, Phys. Rev. B **93**, 064428 (2016).

[112] S.-W. Cheong and M. Mostovoy, Nat. Mater. **6**, 13 (2007).

[113] M. Mostovoy, Phys. Rev. Lett. **96**, 067601 (2006).

[114] M. Heide, G. Bihlmayer, and S. Blügel, J. Nanosci. Nanotechnol. **11**, 3005 (2011).

[115] S. Banerjee, J. Rowland, O. Erten, and M. Randeria, Phys. Rev. X **4**, 031045 (2014).

[116] A. B. Butenko, A. A. Leonov, U. K. Rößler, and A. N. Bogdanov, Phys. Rev. B **82**, 052403 (2010).

[117] R. Keesman, A. O. Leonov, P. van Dieten, S. Buhrandt, G. T. Barkema, L. Fritz, and R. A. Duine, Phys. Rev. B **92**, 134405 (2015).

[118] J. Rowland, S. Banerjee, and M. Randeria, Phys. Rev. B **93**, 020404 (2016).

[119] S.-Z. Lin, A. Saxena, and C. D. Batista, Phys. Rev. B **91**, 224407 (2015).

[120] L. Smejkal, Y. Mokrousov, B. Yan, and A. H. MacDonald, Nat. Phys. **14**, 242 (2018).

[121] E. V. Gomonay and V. M. Loktev, Low Temperature Physics **40**, 17 (2014).

[122] A. H. MacDonald and M. Tsoi, Philosophical Transactions of the Royal Society A: Mathematical, Physical and Engineering Sciences **369**, 3098 (2011).

[123] S. Fukami, V. O. Lorenz, and O. Gomonay, Journal of Applied Physics **128**, 070401 (2020).

[124] T. Jungwirth, J. Sinova, A. Manchon, X. Marti, J. Wunderlich, and C. Felser, Nature Physics **14**, 200 (2018).

[125] M. B. Jungfleisch, W. Zhang, and A. Hoffmann, Physics Letters A **382**, 865 (2018).

[126] A. Kurenkov, S. Fukami, and H. Ohno, Journal of Applied Physics **128**, 010902 (2020).

[127] A. N. Bogdanov, U. K. Rößler, M. Wolf, and K.-H. Müller, Phys. Rev. B **66**, 214410 (2002).

[128] C. Jin, C. Song, J. Wang, and Q. Liu, Appl. Phys. Lett. **109**, 182404 (2016).

[129] X. Zhang, Y. Zhou, and M. Ezawa, Sci. Rep. **6**, 24795 (2016).

[130] H. Velkov, O. Gomonay, M. Beens, G. Schwiete, A. Brataas, J. Sinova, and R. A. Duine, New J. Phys. **18**, 075016 (2016).

[131] A. Bogdanov and A. Shestakov, Phys. Solid State **40**, 1350 (1998).

[132] O. Gomonay, V. Baltz, A. Brataas, and Y. Tserkovnyak, Nat. Phys. **14**, 213 (2018).

[133] J. Barker and O. A. Tretiakov, Phys. Rev. Lett. **116**, 147203 (2016).

[134] T. Jungwirth, X. Marti, P. Wadley, and J. Wunderlich, Nature Nanotechnology **11**, 231 (2016).

[135] V. Baltz, A. Manchon, M. Tsoi, T. Moriyama, T. Ono, and Y. Tserkovnyak, Rev. Mod. Phys. **90**, 015005 (2018).

[136] A. Salimath, F. Zhuo, R. Tomasello, G. Finocchio, and A. Manchon, Phys. Rev. B **101**, 024429 (2020).

[137] C. A. Akosa, O. A. Tretiakov, G. Tatara, and A. Manchon, Phys. Rev. Lett. **121**, 097204 (2018).

[138] H. D. Rosales, D. C. Cabra, and P. Pujol, PRB **92**, 214439 (2015).

[139] W. Legrand, D. Maccariello, F. Ajejas, S. Collin, A. Vecchiola, K. Bouzehouane, N. Reyren, V. Cros, and A. Fert, Nature Materials **19**, 34 (2020).

[140] S. Gao, H. D. Rosales, F. A. Gómez Albarracín, V. Tsurkan, G. Kaur, T. Fennell, P. Steffens, M. Boehm, P. Čermák, A. Schneidewind, E. Ressouche, D. C. Cabra, C. Rüegg, and O. Zaharko, Nature **586**, 37 (2020).

[141] H. Jani, J.-C. Lin, J. Chen, J. Harrison, F. Maccherozzi, J. Schad, S. Prakash, C.-B. Eom, A. Ariando, T. Venkatesan, and P. G. Radaelli, Nature **590**, 74 (2021).

[142] J. Chovan and N. Papanicolaou, Phys. Rev. B **65**, 064433 (2002).

[143] J. Chovan, M. Marder, and N. Papanicolaou, Phys. Rev. B **88**, 064421 (2013).

[144] S. Mühlbauer, S. Gvasaliya, E. Ressouche, E. Pomjakushina, and A. Zheludev, Phys. Rev. B **86**, 024417 (2012).

[145] A. Zheludev, S. Maslov, G. Shirane, I. Tsukada, T. Masuda, K. Uchinokura, I. Zaliznyak, R. Erwin, and L. P. Regnault, Phys. Rev. B **59**, 11432 (1999).

[146] A. Zheludev, G. Shirane, Y. Sasago, N. Kiode, and K. Uchinokura, Phys. Rev. B **54**, 15163 (1996).

[147] A. Zheludev, G. Shirane, Y. Sasago, N. Koide, and K. Uchinokura, Physica B: Condensed Matter **234-236**, Proceedings of the First European Conference on Neutron Scattering, 546 (1997).

[148] A. Zheludev, S. Maslov, G. Shirane, Y. Sasago, N. Koide, K. Uchinokura, D. A. Tennant, and S. E. Nagler, Phys. Rev. B **56**, 14006 (1997).

[149] A. Zheludev, S. Maslov, G. Shirane, Y. Sasago, N. Koide, and K. Uchinokura, Phys. Rev. Lett. **78**, 4857 (1997).

[150] A. Zheludev, S. Maslov, I. Tsukada, I. Zaliznyak, L. P. Regnault, T. Masuda, K. Uchinokura, R. Erwin, and G. Shirane, Phys. Rev. Lett. **81**, 5410 (1998).

[151] T. A. Kaplan, Z. Phys. B **49**, 313 (1983).

[152] L. Shekhtman, A. Aharony, and O. Entin-Wohlman, Phys. Rev. B **47**, 174 (1993).

[153] J. Chovan and N. Papanicolaou, "Frontiers in magnetic materials", edited by A. N. Narlikar, p. (Springer Berlin, 2005) Chap. Commensurate and Incommensurate Magnetism in Layered Antiferromagnets, pp. 347–384.

[154] S. Mühlbauer, S. N. Gvasaliya, E. Pomjakushina, and A. Zheludev, Phys. Rev. B **84**, 180406 (2011).

[155] R. Keesman, M. Raaijmakers, A. E. Baerends, G. T. Barkema, and R. A. Duine, PRB **94**, 054402 (2016).

[156] B. Göbel, I. Mertig, and O. A. Tretiakov, Physics Reports **895**, 1 (2021).

[157] S. Hayami and R. Yambe, Journal of the Physical Society of Japan **89**, 103702 (2020).

[158] X. Z. Yu, W. Koshibae, Y. Tokunaga, K. Shibata, Y. Taguchi, N. Nagaosa, and Y. Tokura, Nature **564**, 95 (2018).

[159] H. Murakawa, Y. Onose, and Y. Tokura, Phys. Rev. Lett. **103**, 147201 (2009).

[160] L. Shekhtman, O. Entin-Wohlman, and A. Aharony, Phys. Rev. Lett. **69**, 836 (1992).

[161] C. Pfleiderer and A. Rosch, Nature **465**, 880 (2010).

[162] R. Ono, S. Nikolaev, and I. Solovyev, Phys. Rev. B **102**, 064422 (2020).

[163] M. D. Lumsden, B. C. Sales, D. Mandrus, S. E. Nagler, and J. R. Thompson, Phys. Rev. Lett. **86**, 159 (2001).

[164] F. J. dos Santos, M. dos Santos Dias, and S. Lounis, Phys. Rev. B **102**, 104436 (2020).

[165] S.-J. Lee, D.-K. Lee, and K.-J. Lee, Phys. Rev. B **101**, 064422 (2020).

[166] P. Nowik-Boltyk, *Magnon bose einstein condensation for non-physicists*, CC-BY-NC-SA 3.0, `https://www.uni-muenster.de/Physik.AP/Demokritov/en/Forschen/Forschungsschwerpunkte/mBECfnP.html`, June 2012.

[167] C. Kittel, *Introduction to solid state physics*, Vol. 8 (Wiley John + Sons, 2004).

[168] J. Waizner, "Spin wave excitations in magnetic helices and skyrmion lattices", PhD thesis (Universität zu Köln, 2017).

[169] M. Garst, J. Waizner, and D. Grundler, Journal of Physics D: Applied Physics **50**, 293002 (2017).

[170] H. Yu, J. Xiao, and H. Schultheiss, Physics Reports **905**, Magnetic texture based magnonics, 1 (2021).

[171] S. Rohart and A. Thiaville, Phys. Rev. B **88**, 184422 (2013).

[172] S. A. Meynell, M. N. Wilson, H. Fritzsche, A. N. Bogdanov, and T. L. Monchesky, Phys. Rev. B **90**, 014406 (2014).

[173] S. L. Zhang, G. van der Laan, W. W. Wang, A. A. Haghighirad, and T. Hesjedal, Phys. Rev. Lett. **120**, 227202 (2018).

[174] B. A. Ivanov, JETP Lett. **61**, 917 (1995).

[175] B. A. Ivanov, H. J. Schnitzer, F. G. Mertens, and G. M. Wysin, Phys. Rev. B **58**, 8464 (1998).

[176] D. D. Sheka, B. A. Ivanov, and F. G. Mertens, Phys. Rev. B **64**, 024432 (2001).

[177] V. P. Kravchuk, O. Gomonay, D. D. Sheka, D. R. Rodrigues, K. Everschor-Sitte, J. Sinova, J. van den Brink, and Y. Gaididei, Phys. Rev. B **99**, 184429 (2019).

[178] T. Schwarze, J. Waizner, M. Garst, A. Bauer, I. Stasinopoulos, H. Berger, C. Pfleiderer, and D. Grundler, Nature Materials **14**, 478 (2015).

[179] R. L. Melcher, Phys. Rev. Lett. **30**, 125 (1973).

[180] M. Kataoka, J. Phys. Soc. Jpn. **56**, 3635 (1987).

[181] T. J. Sato, D. Okuyama, T. Hong, A. Kikkawa, Y. Taguchi, T.-h. Arima, and Y. Tokura, Phys. Rev. B **94**, 144420 (2016).

[182] T. Weber, J. Waizner, G. S. Tucker, R. Georgii, M. Kugler, A. Bauer, C. Pfleiderer, M. Garst, and P. Böni, Phys. Rev. B **97**, 224403 (2018).

[183] G. Shirane, R. Cowley, C. Majkrzak, J. B. Sokoloff, B. Pagonis, C. H. Perry, and Y. Ishikawa, Phys. Rev. B **28**, 6251 (1983).

[184] S. Seki, Y. Okamura, K. Kondou, K. Shibata, M. Kubota, R. Takagi, F. Kagawa, M. Kawasaki, G. Tatara, Y. Otani, and Y. Tokura, Phys. Rev. B **93**, 235131 (2016).

[185] P. Che, I. Stasinopoulos, A. Mucchietto, J. Li, H. Berger, A. Bauer, C. Pfleiderer, and D. Grundler, *Confined dipole and exchange spin waves in a bulk chiral magnet with dzyaloshinskii-moriya interaction*, 2021.

[186] Y. Iguchi, S. Uemura, K. Ueno, and Y. Onose, Phys. Rev. B **92**, 184419 (2015).

[187] R. Takagi, D. Morikawa, K. Karube, N. Kanazawa, K. Shibata, G. Tatara, Y. Tokunaga, T. Arima, Y. Taguchi, Y. Tokura, and S. Seki, Phys. Rev. B **95**, 220406 (2017).

[188] M. Krawczyk, S. Mamica, M. Mruczkiewicz, J. W. Klos, S. Tacchi, M. Madami, G. Gubbiotti, G. Duerr, and D. Grundler, Journal of Physics D: Applied Physics **46**, 495003 (2013).

[189] M. Janoschek, F. Bernlochner, S. Dunsiger, C. Pfleiderer, P. Böni, B. Roessli, P. Link, and A. Rosch, Phys. Rev. B **81**, 214436 (2010).

[190] M. Kugler, G. Brandl, J. Waizner, M. Janoschek, R. Georgii, A. Bauer, K. Seemann, A. Rosch, C. Pfleiderer, P. Böni, and M. Garst, Phys. Rev. Lett. **115**, 097203 (2015).

[191] T. Weber, J. Waizner, P. Steffens, A. Bauer, C. Pfleiderer, M. Garst, and P. Böni, Phys. Rev. B **100**, 060404 (2019).

[192] T. Weber, J. Waizner, G. S. Tucker, L. Beddrich, M. Skoulatos, R. Georgii, A. Bauer, C. Pfleiderer, M. Garst, and P. Böni, AIP Advances **8**, 101328 (2018).

[193] G. S. Tucker, J. S. White, J. Romhányi, D. Szaller, I. Kézsmárki, B. Roessli, U. Stuhr, A. Magrez, F. Groitl, P. Babkevich, P. Huang, I. Živkovi ć, and H. M. Rønnow, Phys. Rev. B **93**, 054401 (2016).

[194] P. Y. Portnichenko, J. Romhányi, Y. A. Onykiienko, A. Henschel, M. Schmidt, A. S. Cameron, M. A. Surmach, J. A. Lim, J. T. Park, A. Schneidewind, D. L. Abernathy, H. Rosner, J. van den Brink, and D. S. Inosov, Nature Communications **7**, 10725 (2016).

[195] M. Weiler, A. Aqeel, M. Mostovoy, A. Leonov, S. Geprägs, R. Gross, H. Huebl, T. T. M. Palstra, and S. T. B. Goennenwein, Phys. Rev. Lett. **119**, 237204 (2017).

[196] N. Ogawa, L. Köhler, M. Garst, S. Toyoda, S. Seki, and Y. Tokura, Proceedings of the National Academy of Sciences **118**, `10.1073/pnas.2022927118` (2021).

[197] M. Date, K. Okuda, and K. Kadowaki, J. Phys. Soc. Jpn. **42**, 1555 (1977).

[198] Y. Onose, Y. Okamura, S. Seki, S. Ishiwata, and Y. Tokura, Phys. Rev. Lett. **109**, 037603 (2012).

[199] I. Stasinopoulos, S. Weichselbaumer, A. Bauer, J. Waizner, H. Berger, M. Garst, C. Pfleiderer, and D. Grundler, Scientific Reports **7**, 7037 (2017).

[200] M. Mochizuki, Phys. Rev. Lett. **108**, 017601 (2012).

[201] C. Schütte and M. Garst, Phys. Rev. B **90**, 094423 (2014).

[202] S.-Z. Lin, C. D. Batista, and A. Saxena, Phys. Rev. B **89**, 024415 (2014).

[203] Y. Zhou, E. Iacocca, A. A. Awad, R. K. Dumas, F. C. Zhang, H. B. Braun, and J. Åkerman, Nature Communications **6**, 8193 (2015).

[204] J. Iwasaki, A. J. Beekman, and N. Nagaosa, Phys. Rev. B **89**, 064412 (2014).

[205] S. Schroeter and M. Garst, Low Temperature Physics **41**, 817 (2015).

[206] S.-Z. Lin, J.-X. Zhu, and A. Saxena, Phys. Rev. B **99**, 140408 (2019).

[207] V. P. Kravchuk, U. K. Rößler, J. van den Brink, and M. Garst, PRB **102**, 220408 (2020).

[208] S. Seki, M. Garst, J. Waizner, R. Takagi, N. D. Khanh, Y. Okamura, K. Kondou, F. Kagawa, Y. Otani, and Y. Tokura, Nature Communications **11**, 256 (2020).

[209] X. Xing, Y. Zhou, and H. Braun, Phys. Rev. Applied **13**, 034051 (2020).

[210] A. A. Serga, A. V. Chumak, and B. Hillebrands, Journal of Physics D: Applied Physics **43**, 264002 (2010).

[211] H. Yu, O. d'Allivy Kelly, V. Cros, R. Bernard, P. Bortolotti, A. Anane, F. Brandl, R. Huber, I. Stasinopoulos, and D. Grundler, Scientific Reports **4**, 6848 (2014).

[212] H. Yu, O. d'Allivy Kelly, V. Cros, R. Bernard, P. Bortolotti, A. Anane, F. Brandl, F. Heimbach, and D. Grundler, Nature Communications **7**, 11255 (2016).

[213] E. N. Beginin, A. V. Sadovnikov, V. K. Sakharov, A. I. Stognij, Y. V. Khivintsev, and S. A. Nikitov, Journal of Magnetism and Magnetic Materials **492**, 165647 (2019).

[214] V. K. Sakharov, E. N. Beginin, Y. V. Khivintsev, A. V. Sadovnikov, A. I. Stognij, Y. A. Filimonov, and S. A. Nikitov, Appl. Phys. Lett. **117**, 022403 (2020).

[215] C. Liu, J. Chen, T. Liu, F. Heimbach, H. Yu, Y. Xiao, J. Hu, M. Liu, H. Chang, T. Stueckler, S. Tu, Y. Zhang, Y. Zhang, P. Gao, Z. Liao, D. Yu, K. Xia, N. Lei, W. Zhao, and M. Wu, Nature Communications **9**, 738 (2018).

[216] J. Chen, T. Yu, C. Liu, T. Liu, M. Madami, K. Shen, J. Zhang, S. Tu, M. S. Alam, K. Xia, M. Wu, G. Gubbiotti, Y. M. Blanter, G. E. W. Bauer, and H. Yu, Phys. Rev. B **100**, 104427 (2019).

[217] V. V. Kruglyak, S. O. Demokritov, and D. Grundler, Journal of Physics D: Applied Physics **43**, 264001 (2010).

[218] B. Lenk, H. Ulrichs, F. Garbs, and M. Münzenberg, Physics Reports **507**, 107 (2011).

[219] A. V. Chumak, V. I. Vasyuchka, A. A. Serga, and B. Hillebrands, Nature Physics **11**, 453 (2015).

[220] R. L. Stamps, S. Breitkreutz, J. Åkerman, A. V. Chumak, Y. Otani, G. E. W. Bauer, J.-U. Thiele, M. Bowen, S. A. Majetich, M. Kläui, I. L. Prejbeanu, B. Dieny, N. M. Dempsey, and B. Hillebrands, Journal of Physics D: Applied Physics **47**, 333001 (2014).

[221] A. V. Chumak, *Fundamentals of magnon-based computing*, 2019.

[222] A. V. Chumak, A. A. Serga, and B. Hillebrands, Journal of Physics D: Applied Physics **50**, 244001 (2017).

[223] A. Khitun, M. Bao, and K. L. Wang, Journal of Physics D: Applied Physics **43**, 264005 (2010).

[224] T. Schneider, A. A. Serga, B. Leven, B. Hillebrands, R. L. Stamps, and M. P. Kostylev, Appl. Phys. Lett. **92**, 022505 (2008).

[225] M. Krawczyk and D. Grundler, Journal of Physics: Condensed Matter **26**, 123202 (2014).

[226] A. Khitun, Journal of Applied Physics **111**, 054307 (2012).

[227] A. V. Chumak, A. A. Serga, and B. Hillebrands, Nature Communications **5**, 4700 (2014).

[228] F. Gertz, A. Kozhevnikov, Y. Filimonov, and A. Khitun, IEEE Transactions on Magnetics **51**, 1 (2015).

[229] S. Klingler, H. Maier-Flaig, C. Dubs, O. Surzhenko, R. Gross, H. Huebl, S. T. B. Goennenwein, and M. Weiler, Appl. Phys. Lett. **110**, 092409 (2017).

[230] M. A. W. Schoen, D. Thonig, M. L. Schneider, T. J. Silva, H. T. Nembach, O. Eriksson, O. Karis, and J. M. Shaw, Nature Physics **12**, 839 (2016).

[231] S. R. Boona and J. P. Heremans, Phys. Rev. B **90**, 064421 (2014).

[232] I. Stasinopoulos, S. Weichselbaumer, A. Bauer, J. Waizner, H. Berger, S. Maendl, M. Garst, C. Pfleiderer, and D. Grundler, Appl. Phys. Lett. **111**, 032408 (2017).

[233] V. G. Bar'yakhtar, A. G. Danilevich, and V. N. Krivoruchko, Phys. Rev. B **99**, 104407 (2019).

[234] T. Weber, D. M. Fobes, J. Waizner, P. Steffens, G. S. Tucker, M. Böhm, L. Beddrich, C. Franz, H. Gabold, R. Bewley, D. Voneshen, M. Skoulatos, R. Georgii, G. Ehlers, A. Bauer, C. Pfleiderer, P. Böni, M. Janoschek, and M. Garst, *Emergent landau levels of magnons in a skyrmion lattice*, (unpublished), 2021.

[235] R. D. Kamien, Reviews of Modern Physics **74**, 953 (2002).

[236] N. D. Mermin and T.-L. Ho, Phys. Rev. Lett. **36**, 594 (1976).

[237] E. Lifshitz and L. P. Pitaevskii, *Statistical physics part ii*, Vol. 9 (Pergamon Press, 1980).

[238] P. Grinfeld, *Introduction to tensor analysis and the calculus of moving surfaces* (Springer-Verlag New York, 2013).

[239] O. Petrova and O. Tchernyshyov, Phys. Rev. B **84**, 214433 (2011).

[240] M. V. Berry, Journal of Physics A: Mathematical and General **10**, 2083 (1977).

[241] E. J. Heller, Phys. Rev. Lett. **53**, 1515 (1984).

[242] E. B. Bogomolny, Physica D: Nonlinear Phenomena **31**, 169 (1988).

[243] M. Berry, Proceedings of the Royal Society of London. A. Mathematical and Physical Sciences **423**, 219 (1989).

[244] L. Markus and K. Meyer, Memoirs of the American Mathematical Society, Providence, Rhode Island (1974).

[245] P. Ehrenfest, Zeitschrift für Physik **45**, 455 (1927).

[246] R. Shankar, *Principles of quantum mechanics*, Vol. 2 (Springer US, 1994).

[247] I. C. Percival, Journal of Physics B: Atomic and Molecular Physics **6**, L229 (1973).

[248] M. V. Berry, "Comportement chaotique des systèmes déterministes — chaotic behaviour of deterministic systems", edited by R. H. G. H. G. Iooss and R. Stora (North-Holland Publishing Company, 1983) Chap. Semiclassical mechanics of regular and irregular motion, pp. 171–271.

[249] A. Voros, Stochastic behavior in classical and quantum hamiltonian systems, edited by G. Casati and J. Ford (1979), pp. 326–333.

[250] A. I. Shnirel'man, Uspekhi Mat. Nauk **29**, 181 (1974).

[251] S. Zelditch, Duke Mathematical Journal **55**, 919 (1987).

[252] Y. Colin de Verdiére, fr, Seminar 'Partial derivative equations (Polytechnique) also called "Seminaire Goulaouic-Schwartz", talk: 13 (1984-1985).

[253] B. Helffer, A. Martinez, and D. Robert, Communications in Mathematical Physics **109**, 313 (1987).

[254] P. Gérard and E. Leichtnam, Duke Mathematical Journal **71**, 559 (1993).

[255] S. Zelditch and M. Zworski, Communications in Mathematical Physics **175**, 673 (1996).

[256] A. Bäcker, R. Schubert, and P. Stifter, Phys. Rev. E **57**, 5425 (1998).

[257] J. Yoshida and T. Ohtsuki, Journal of the Physical Society of Japan **72**, 594 (2003).

[258] J. Yoshida, T. Ohtsuki, and M. Noda, Physica E: Low-dimensional Systems and Nanostructures **18**, 23rd International Conference on Low Temperature Physics (LT23), 153 (2003).

[259] J. Yoshida, T. Ohtsuki, and Y. Ono, Journal of the Physical Society of Japan **67**, 3886 (1998).

[260] L. Berger, Phys. Rev. B **54**, 9353 (1996).

[261] J. Finley, C.-H. Lee, P. Y. Huang, and L. Liu, Adv. Mater. **31**, 1805361 (2019).

[262] J. A. Katine, F. J. Albert, R. A. Buhrman, E. B. Myers, and D. C. Ralph, Phys. Rev. Lett. **84**, 3149 (2000).

[263] L. Liu, O. J. Lee, T. J. Gudmundsen, D. C. Ralph, and R. A. Buhrman, Phys. Rev. Lett. **109**, 096602 (2012).

[264] L. Liu, C.-F. Pai, Y. Li, H. W. Tseng, D. C. Ralph, and R. A. Buhrman, Science **336**, 555 (2012).

[265] Y. Ji, C. L. Chien, and M. D. Stiles, Phys. Rev. Lett. **90**, 106601 (2003).

[266] S. I. Kiselev, J. C. Sankey, I. N. Krivorotov, N. C. Emley, R. J. Schoelkopf, R. A. Buhrman, and D. C. Ralph, Nature **425**, 380 (2003).

[267] W. H. Rippard, M. R. Pufall, S. Kaka, S. E. Russek, and T. J. Silva, Phys. Rev. Lett. **92**, 027201 (2004).

[268] T. J. Silva and W. H. Rippard, Journal of Magnetism and Magnetic Materials **320**, 1260 (2008).

[269] M. Tsoi, A. G. M. Jansen, J. Bass, W.-C. Chiang, M. Seck, V. Tsoi, and P. Wyder, Phys. Rev. Lett. **80**, 4281 (1998).

[270] M. Tsoi, A. G. M. Jansen, J. Bass, W.-C. Chiang, V. Tsoi, and P. Wyder, Nature **406**, 46 (2000).

[271] Z. Zeng, G. Finocchio, B. Zhang, P. K. Amiri, J. A. Katine, I. N. Krivorotov, Y. Huai, J. Langer, B. Azzerboni, K. L. Wang, and H. Jiang, Scientific Reports **3**, 1426 (2013).

[272] J.-V. Kim, *Solid state physics*, Vol. 63, edited by R. E. Camley and R. L. Stamps (Academic Press, Jan. 2012), pp. 217–294.

[273] S. E. Russek, W. H. Rippard, T. Cecil, and R. Heindl, "Handbook of spin transport and magnetism", edited by E. Y. Tsymbal and I. Zutic (CRC Press, 2012) Chap. 38, p. 731.

[274] N. Locatelli, V. Cros, and J. Grollier, Nature Materials **13**, 11 (2013).

[275] R. Cheng, M. W. Daniels, J.-G. Zhu, and D. Xiao, Scientific Reports **6**, 24223 (2016).

[276] D. Marković, A. Mizrahi, D. Querlioz, and J. Grollier, Nature Reviews Physics **2**, 499 (2020).

[277] K. Roy, A. Jaiswal, and P. Panda, Nature **575**, 607 (2019).

[278] K. Segall, M. LeGro, S. Kaplan, O. Svitelskiy, S. Khadka, P. Crotty, and D. Schult, Physical Review E **95**, 032220 (2017).

[279] J. Torrejon, M. Riou, F. A. Araujo, S. Tsunegi, G. Khalsa, D. Querlioz, P. Bortolotti, V. Cros, K. Yakushiji, A. Fukushima, H. Kubota, S. Yuasa, M. D. Stiles, and J. Grollier, Nature **547**, 428 (2017).

[280] M. D. Pickett, G. Medeiros-Ribeiro, and R. S. Williams, Nature Materials **12**, 114 (2012).

[281] M. Romera, P. Talatchian, S. Tsunegi, F. A. Araujo, V. Cros, P. Bortolotti, J. Trastoy, K. Yakushiji, A. Fukushima, H. Kubota, S. Yuasa, M. Ernoult, D. Vodenicarevic, T. Hirtzlin, N. Locatelli, D. Querlioz, and J. Grollier, Nature **563**, 230 (2018).

[282] D. Marković, N. Leroux, M. Riou, F. A. Araujo, J. Torrejon, D. Querlioz, A. Fukushima, S. Yuasa, J. Trastoy, P. Bortolotti, and J. Grollier, Applied Physics Letters **114**, 012409 (2019).

[283] H. Jaeger, Science **304**, 78 (2004).

[284] S. Tsunegi, T. Taniguchi, K. Nakajima, S. Miwa, K. Yakushiji, A. Fukushima, S. Yuasa, and H. Kubota, Applied Physics Letters **114**, 164101 (2019).

[285] J. Choi and P. Kim, Chaos: An Interdisciplinary Journal of Nonlinear Science **29**, 043110 (2019).

[286] T. Kanao, H. Suto, K. Mizushima, H. Goto, T. Tanamoto, and T. Nagasawa, Phys. Rev. Applied **12**, 024052 (2019).

[287] R. Khymyn, I. Lisenkov, J. Voorheis, O. Sulymenko, O. Prokopenko, V. Tiberkevich, J. Akerman, and A. Slavin, Scientific Reports **8**, 15727 (2018).

[288] C. Zhao, W. Danesh, B. T. Wysocki, and Y. Yi, 2015 IEEE symposium on computational intelligence for security and defense applications (CISDA) (2015).

[289] R. Matsumoto, S. Lequeux, H. Imamura, and J. Grollier, Physical Review Applied **11**, 044093 (2019).

[290] E. A. Montoya, S. Perna, Y.-J. Chen, J. A. Katine, M. d'Aquino, C. Serpico, and I. N. Krivorotov, Nature Communications **10**, 543 (2019).

[291] M. W. Daniels, A. Madhavan, P. Talatchian, A. Mizrahi, and M. D. Stiles, Phys. Rev. Applied **13**, 034016 (2020).

[292] T. Taniguchi, AIP Advances **10**, 015112 (2020).

[293] T. Yamaguchi, N. Akashi, K. Nakajima, S. Tsunegi, H. Kubota, and T. Taniguchi, Phys. Rev. B **100**, 224422 (2019).

[294] A. M. Cabanas, L. M. Pérez, and D. Laroze, Journal of Magnetism and Magnetic Materials **460**, 320 (2018).

[295] L. Shen, J. Xia, X. Zhang, M. Ezawa, O. A. Tretiakov, X. Liu, G. Zhao, and Y. Zhou, Phys. Rev. Lett. **124**, 037202 (2020).

[296] F. Keffer and C. Kittel, Phys. Rev. **85**, 329 (1952).

[297] A. J. Sievers and M. Tinkham, Phys. Rev. **129**, 1566 (1963).

[298] J. Železný, P. Wadley, K. Olejník, A. Hoffmann, and H. Ohno, Nature Physics **14**, 220 (2018).

[299] B. Göbel, A. Mook, J. Henk, and I. Mertig, Phys. Rev. B **96**, 060406 (2017).

[300] J. E. Hirsch, Phys. Rev. Lett. **83**, 1834 (1999).

[301] M. I. Dyakonov and V. I. Perel, Sov. Phys. JETP Lett. **13**, 467 (1971).

[302] M. I. Dyakonov, *Spin physics in semiconductors*, Vol. 157, Springer Series in Solid-State Sciences (Springer Nature, 2008).

[303] M. I. Dyakonov and V. I. Perel, Physics Letters A **35**, 459 (1971).

[304] R. Cheng, D. Xiao, and A. Brataas, Phys. Rev. Lett. **116**, 207603 (2016).

[305] J. Bertram, A. Tanwear, A. Rodriguez, G. Paterson, S. McVitie, and H. Heidari, Ieee sensors (Oct. 2019), pp. 1–4.

[306] V. E. Demidov, H. Ulrichs, S. V. Gurevich, S. O. Demokritov, V. S. Tiberkevich, A. N. Slavin, A. Zholud, and S. Urazhdin, Nature Communications **5**, 3179 (2014).

[307] V. E. Demidov, S. Urazhdin, H. Ulrichs, V. Tiberkevich, A. Slavin, D. Baither, G. Schmitz, and S. O. Demokritov, Nature Materials **11**, 1028 (2012).

[308] A. Giordano, M. Carpentieri, A. Laudani, G. Gubbiotti, B. Azzerboni, and G. Finocchio, Appl. Phys. Lett. **105**, 042412 (2014).

[309] A. Giordano, R. Verba, R. Zivieri, A. Laudani, V. Puliafito, G. Gubbiotti, R. Tomasello, G. Siracusano, B. Azzerboni, M. Carpentieri, A. Slavin, and G. Finocchio, Scientific Reports **6**, 36020 (2016).

[310] B. Jiang, W. Zhang, H. Zhong, Y. Zhang, S. Yu, G. Han, S. Xiao, G. Liu, S. Yan, J. Li, and S. Kang, Journal of Magnetism and Magnetic Materials **490**, 165470 (2019).

[311] L. Liu, C.-F. Pai, D. C. Ralph, and R. A. Buhrman, Phys. Rev. Lett. **109**, 186602 (2012).

[312] H. Ulrichs, V. E. Demidov, and S. O. Demokritov, Appl. Phys. Lett. **104**, 042407 (2014).

[313] H. V. Gomonay and V. M. Loktev, Phys. Rev. B **81**, 144427 (2010).

[314] A. Parthasarathy, E. Cogulu, A. D. Kent, and S. Rakheja, Phys. Rev. B **103**, 024450 (2021).

[315] W. Han, S. Maekawa, and X.-C. Xie, Nature Materials **19**, 139 (2020).

[316] J. Sinova, S. O. Valenzuela, J. Wunderlich, C. H. Back, and T. Jungwirth, Rev. Mod. Phys. **87**, 1213 (2015).

[317] J. Shi, P. Zhang, D. Xiao, and Q. Niu, Phys. Rev. Lett. **96**, 076604 (2006).

[318] D. C. Ralph and M. D. Stiles, Journal of Magnetism and Magnetic Materials **320**, 1190 (2008).

[319] J. C. Slonczewski, Journal of Magnetism and Magnetic Materials **247**, 324 (2002).

[320] C. Abert, H. Sepehri-Amin, F. Bruckner, C. Vogler, M. Hayashi, and D. Suess, Phys. Rev. Applied **7**, 054007 (2017).

[321] P. M. Haney, D. Waldron, R. A. Duine, A. S. Núñez, H. Guo, and A. H. MacDonald, Phys. Rev. B **76**, 024404 (2007).

[322] I. Bar'yakhtar and B. Ivanov, Sov. J. Low Temp. Phys. **5**, 361 (1979).

[323] A. M. Kosevich, B. A. Ivanov, and A. S. Kovalev, Physics Reports **194**, 117 (1990).

[324] A. M. Lyapunov, Int. J. Control **55**, English translation from the French: Liapounoff A (1907) Probléme général de la stabilité du mouvement. Annal. Fac. Sci. Toulouse 9, 203–474. The French text was reprinted in Annals Math. Studies Vol. 17 Princeton Univ. Press (1947). The original was published in Russian by the Mathematical Society of Kharkov in 1892, 531 (1992).

[325] J. C. Vallejo and M. A. F. Sanjuan, *Predictability of chaotic dynamics* (Springer International Publishing AG, 2017).

[326] V. Oseledec, Trans. Moscow Math. Soc. **19**, 197 (1968).

[327] P. Walters, Trans. Amer. Math. Soc. **335**, 245 (1993).

[328] D. Ruelle, IHES Publ. Math. **50**, 275 (1979).

[329] M. S. Raghunathan, Israel Journal of Mathematics **32**, 356 (1979).

[330] R. A. Johnson, K. J. Palmer, and G. R. Sell, SIAM J. Math. Anal **18**, 1 (1987).

[331] G. Benettin, L. Galgani, A. Giorgilli, and J.-M. Strelcyn, Meccanica **15**, 9 (1980).

[332] A. Wolf, J. B. Swift, H. L. Swinney, and J. A. Vastano, Physica D: Nonlinear Phenomena **16**, 285 (1985).

[333] C. Skokos, "Dynamics of small solar system bodies and exoplanets", Vol. 790, edited by J. J. Souchay and R. Dvorak, Lecture Notes in Physics 1 (Springer-Verlag Berlin Heidelberg, 2010) Chap. The Lyapunov Characteristic Exponents and Their Computation, pp. 63–135.

[334] S. H. Strogatz, *Nonlinear dynamics and chaos: with applications to physics, biology, chemistry, and engineering* (CRC Press, 2015).

[335] K. Geist, U. Parlitz, and W. Lauterborn, Progress of Theoretical Physics **83**, 875 (1990).

[336] P. Frederickson, J. L. Kaplan, E. D. Yorke, and J. A. Yorke, Journal of Differential Equations **49**, 185 (1983).

[337] K. J.L. and Y. J.A., "Functional differential equations and approximation of fixed points.", Vol. 730, edited by P. HO. and W. HO., Lecture Notes in Mathematics (Springer, Berlin, Heidelberg, 1979) Chap. Chaotic behavior of multidimensional difference equations. P. 228.

[338] I. Mascolo, Frontiers in Applied Mathematics and Statistics **5**, 51 (2019).

[339] H. Ziegler, Ingenieur-Archiv **20**, 49 (1952).

[340] J. Argyris, G. Faust, M. Haase, and R. Friedrich, *An exploration of dynamical systems and chaos* (Springer-Verlag Berlin Heidelberg, 2015).

[341] B. Wolba, O. Gomonay, and V. P. Kravchuk, Phys. Rev. B **104**, 024407 (2021).

[342] L. Stone, Nature **365**, 617 (1993).

[343] M. J. Feigenbaum, Los Alamos Science **1**, 4 (1980).

[344] P. Collet, J. P. Eckmann, and O. E. Lanford, Commun Math Phys **76**, 211 (1980).

[345] F. Ledrappier, Comm. Math. Phys. **81**, 229 (1981).

[346] L.-S. Young, Ergodic Theory and Dynamical Systems **2**, 109 (1982).

[347] H. T. Yi, Y. J. Choi, S. Lee, and S.-W. Cheong, Appl. Phys. Lett. **92**, 212904 (2008).

[348] A. Zheludev, T. Sato, T. Masuda, K. Uchinokura, G. Shirane, and B. Roessli, Phys. Rev. B **68**, 024428 (2003).

[349] T. Sato, T. Masuda, and K. Uchinokura, Proceedings of the 23rd International Conference on Low Temperature Physics **329-333**, 880 (2003).

[350] A. N. Bogdanov, U. K. Rößler, M. Wolf, and K.-H. Müller, Proceedings of the International Conference on Magnetism (ICM 2003) **272-276**, 332 (2004).

[351] J. Chovan and N. Papanicolaou, Ukr. J. Phys. **50**, 747 (2005).

[352] S. Mühlbauer, G. Brandl, M. Månsson, and M. Garst, Phys. Rev. B **96**, 134409 (2017).

[353] M. N. Wilson, A. B. Butenko, A. N. Bogdanov, and T. L. Monchesky, Phys. Rev. B **89**, 094411 (2014).

[354] H. Murakawa, Y. Onose, S. Miyahara, N. Furukawa, and Y. Tokura, Phys. Rev. B **85**, 174106 (2012).

[355] E. G. Tveten, T. Müller, J. Linder, and A. Brataas, Phys. Rev. B **93**, 104408 (2016).

[356] N. Kumar, S. K. Dhar, A. Thamizhavel, P. Bonville, and P. Manfrinetti, Phys. Rev. B **81**, 144414 (2010).

[357] M. Sandri, The Mathematica Journal **6**, 78 (1996).

[358] G. Bertotti, C. Serpico, I. D. Mayergoyz, A. Magni, M. d'Aquino, and R. Bonin, Phys. Rev. Lett. **94**, 127206 (2005).

[359] R. Cheng, J. Xiao, Q. Niu, and A. Brataas, Phys. Rev. Lett. **113**, 057601 (2014).

[360] M. W. Daniels, W. Guo, G. M. Stocks, D. Xiao, and J. Xiao, New Journal of Physics **17**, 103039 (2015).

[361] O. Gomonay, T. Jungwirth, and J. Sinova, Phys. Status Solidi RRL **11**, 1700022 (2017).

[362] Y. Kajiwara, K. Harii, S. Takahashi, J. Ohe, K. Uchida, M. Mizuguchi, H. Umezawa, H. Kawai, K. Ando, K. Takanashi, S. Maekawa, and E. Saitoh, Nature **464**, 262 (2010).

[363] L. Liu, T. Moriyama, D. C. Ralph, and R. A. Buhrman, Phys. Rev. Lett. **106**, 036601 (2011).

[364] R. H. Liu, W. L. Lim, and S. Urazhdin, Phys. Rev. Lett. **110**, 147601 (2013).

[365] Z. Yang, S. Zhang, and Y. C. Li, Phys. Rev. Lett. **99**, 134101 (2007).

[366] X. Zhang, Y. Zhou, and M. Ezawa, Scientific Reports **6**, 24795 (2016).

[367] M. Hoffmann, B. Zimmermann, G. P. Müller, D. Schürhoff, N. S. Kiselev, C. Melcher, and S. Blügel, Nature Communications **8**, 308 (2017).

[368] J. Beille, J. Voiron, and M. Roth, Solid State Communications **47**, 399 (1983).

[369] B. Lebech, J. Bernhard, and T. Freltoft, J. Phys.: Condens. Matter **1**, 6105 (1989).

[370] J. K. Asbóth, L. Oroszlány, and A. Pályi, Lecture Notes in Physics, `10.1007/978-3-319-25607-8` (2016).

[371] X. Zhang, M. Ezawa, and Y. Zhou, Scientific Reports **5**, 9400 (2015).

[372] S. Zhang, J. Wang, Q. Zheng, Q. Zhu, X. Liu, S. Chen, C. Jin, Q. Liu, C. Jia, and D. Xue, New Journal of Physics **17**, 023061 (2015).

[373] W. Kang, Y. Huang, X. Zhang, Y. Zhou, and W. Zhao, Proceedings of the IEEE **104**, 2040 (2016).

[374] H. Kantz and T. Schreiber, *Nonlinear time series analysis*, 2nd ed. (Cambridge University Press, 2003).

[375] Y. B. Pesin, Russian Mathematical Surveys **32**, 55 (1977).

[376] Z. Wang, Y. Su, S.-Z. Lin, and C. D. Batista, PRB **103**, 104408 (2021).